



TECHNISCHE UNIVERSITÄT MÜNCHEN

Lehrstuhl für Technische Chemie II

Mechanistic studies of reactions of polyaromatic compounds on metal sulfide catalysts

Eva Christina Schachtl

Vollständiger Abdruck der von der Fakultät für Chemie der Technischen Universität München zur Erlangung des akademischen Grades eines

Doktors der Naturwissenschaften (Dr. rer. nat.)

genehmigten Dissertation.

Vorsitzender: Univ.-Prof. Dr. K.-O. Hinrichsen

Prüfer der Dissertation: 1. Univ.-Prof. Dr. J. A. Lercher

2. Univ.-Prof. Dr. T. Nilges

Die Dissertation wurde am 27.10.2015 bei der Technischen Universität München eingereicht und durch die Fakultät für Chemie am 14.12.2015 angenommen.

*“Success is the ability
to go from one failure to another
with no loss of enthusiasm.”*

Winston Churchill

Acknowledgements

After all, my thesis is finished. Of course there are many people who contributed to this success, supported and encouraged me, and I like to take this opportunity to say thank you.

First I want to thank Prof Johannes A. Lercher for the opportunity to work in his group and for giving me this interesting and challenging research topic. I enjoyed the freedom of research you granted me, as well as the guidance you offered and our scientific discussions, which were always inspiring. During this time I had some great experiences and got the chance to evolve not only as a scientist, but also personally.

Further thanks go to my project partner, Chevron Energy Technology Company, for the financial support of my thesis, and for granting me the possibility to visit their site in San Francisco. In particular I want to mention my project partners, Alex Kuperman, Axel Brait and Jinyi Han, thank you for your support, your input and the wonderful telephone meetings. It was always a pleasure to talk to you, to exchange ideas and experiences, and it was at all times helpful and motivating.

Special thanks I owe to my supervisor, Oliver Y. Gutiérrez. It was a pleasure to work with you, personally and scientifically. Thank you for all your help, your unlimited enthusiasm and for guiding me in the right direction. We are quite opposite in many ways, and I think that's why we complemented one another very well and what made working together especially interesting, productive and fun. Thank you also for your patience, trust and your open ear for all my troubles, however small. And for granting me so much freedom and independence. Last but not least, thank you for the laughs we shared.

Another very important person during the last years was Jennifer Hein. Thank you, Jenny, for introducing me into the world of sulfides in the beginning, for your help inside and outside the lab and for being a great colleague, and friend. Our discussions were especially helpful, since we shared so many day-to-day problems. I really appreciated your scientific council and believe we made an excellent team. With this I also want to thank the third "sulfur girl", Elena Kondratieva. Your expertise in sulfide materials and IR spectroscopy were a great help, thank you for sharing it with us, and for our time together in the lab, I enjoyed it.

I am very grateful also to Andreas Jentys. Thank you for your counsel and assistance with the IR setup, the XAFS measurements and all other technical support. Your caring but strict attitude towards the students is refreshing and made teaching really enjoyable. I especially relish your direct and honest nature.

There are of course many more people who assisted me throughout my thesis and without whom work would have been a good deal harder. Xaver, thank you for all your support in the lab, with the setups, pumps, gases, GC... and besides, the little chats in between. You're the memory and the soul of TCII. Special thanks go to our secretaries, Steffi and Uli, for the

organizational work you take off our shoulders, but also for your very exhilarant and open spirits, and the cheering and funny moments in between. In addition, I very much appreciate the help of Bettina, Martin, Andreas and Karen, thank you.

During my thesis I required many TEM measurements, that's why I would like to express some extra gratitude to the TEM people, Marianne Hanzlik, Hui Shi, Sabine, Liesl, Sebastian G., Marco and Ehrmi, thank you for all the time you invested in my samples. Since I myself was responsible for SEM, I like to thank my team, Katia Rodewald, Martin, Christian and Sebastian, it was fun working with all of you.

Many students did a great job and contributed to the present work. I would like to thank Edith Ball, Ferdi Vogelgsang, Ludovik Lacroix, Daniel Melzer, Marta Muratori Sosa, Julia Hager, Marco Decker, Wolfgang Reitingner, Alexandra Ranner and Guan Jing.

Now, special thanks to all my colleagues at TCII. Thank you for creating this nice atmosphere at work, it was really great to be part of such an international group. Thanks to my first office mates, Anna, Sabine, Florian, Xianyong, Baoxiang, Herui, and later Jeongnam, Sebastian, Tobias, Stan, Marco, Rocky and Gabriella. I enjoyed our funny, sometimes weird talks and discussions, especially the non-scientific stuff. I am also very grateful to all people of the "sulfur sub-group", Jenny, Elena, Lei, Sylvia, Oliver, Anastasia, Manu, Wenhao and of course Wanqiu, keep up the good work. Outside the office I like to mention in addition Steffi, Moni, Stefan, Christian, Linus, Liesl, Pamina, Wenji, Robin, Max, Claudia, Dani, Sonja (who already left TCII) and Martina, Ehrmi, Daniel and Kai, thank you for simply everything. Thanks also to all those who joined for Mensa and "Grieche", and thus made lunch break a pleasant daily diversion. Finally I want to point out some special people, Jenny, Steffi, Moni, Stefan, Sebastian, Anna, Sylvia, Oliver, you were my rocks in the turbulent waters of TCII.

Of course life outside work is equally important, and I like to thank all those who shared my ups and downs over the last years and kept me busy and distracted, especially Yves, Uli, Stefan, Martin and Ruben. My godchild Paul and his brothers Aron & Noah also had a significant role in distracting me, thank you Uli and Micha for being there, your open ears at all times and for cheering me up whenever necessary.

Very special thanks also go to my partner Felix. Thank you for a wonderful time, your support and patience, and for making me laugh no matter what. And last but not least, I want to thank my family. Mama, Papa thank you for your support throughout my studies, you're the best. Katrin and Tessi, thank you for being always there.

Thank you very much to all of you!

Abstract

Ni promotion improves the dispersion of MoS₂ and concentration of defect sites. Spectroscopic techniques point to two Ni species, Ni cations and small NiS_x cluster at the perimeter of MoS₂. Isotopic experiments display an increase of active surface hydrogen in presence of Ni. Kinetic investigations show that hydrogenation of phenanthrene is faster on Ni-MoS₂/Al₂O₃ and that selectivity shifts towards deeper hydrogenated products compared to MoS₂/Al₂O₃ because of changes in the rate determining step.

Kurzzusammenfassung

Als Promoter erhöht Ni die Dispersion, sowie die Konzentration an Fehlstellen in MoS₂. Ni tritt dabei an den Kanten von MoS₂ sowohl als Kation, als auch in Form kleiner NiS_x Cluster auf. Isotopenexperimente zeigen einen Anstieg an aktivem H an der Oberfläche von Ni-MoS₂/Al₂O₃. Die Hydrierung von Phenanthren wird durch Ni beschleunigt und zugleich verändert sich die Selektivität hin zu stärker hydrierten Produkten, was auf eine Veränderung des geschwindigkeitsbestimmenden Schritts zurückzuführen ist.

Abbreviations

A	Absorption
Al ₂ O ₃	aluminium oxide, alumina
asymOHPhe	asymmetric- or 1,2,3,4,4a,9,10,10a-octahydrophenanthrene
BAS	Brønsted acid sites
BET	<i>Brunauer–Emmett–Teller</i>
CO	Carbon monoxide
DDN	direct denitrogenation
DDS	direct desulfurization
DFT	density functional theory
DiHPhe	9,10-dihydrophenanthrene
4,6-DMDBT	4,6-dimethyldibenzothiophene
DMP	2,6-dimethylpyridine
DOS	density of states
E ₀	inner potential
EXAFS	extended x-ray absorption fine structure
f or f _{Mo}	dispersion of Mo
FCC	fluid catalytic cracking
GC	gas chromatography
H/C	hydrogen-to-carbon
HDA	hydrodearomatisation
HDM	hydrodemetallization
HDN	hydrodenitrogenation
HDO	hydrodeoxygenation
HDS	hydrodesulfurization
HYD	hydrogenation
IR	infrared
k _i	reaction rate constant
K _c	equilibrium concentration ratio
K _{eq}	equilibrium constant
K _i	adsorption constant
LAS	Lewis acid sites
LCF	linear combination fitting

L-H	Langmuir-Hinshelwood
LPG	liquefied petroleum gas
MS	mass spectrometry
N	coordination number
$Ni \cdot (Mo+Ni)^{-1}$ or $Ni/(Mo+Ni)$	ratio of Ni to total metal
NO	nitric oxide
O_h	octahedral
PAH	polycyclic aromatic hydrocarbon
Phe	phenanthrene
Q	quinolone
r_i	reaction rate
R	distance
rds	rate determining step
STEM	scanning transmission electron microscopy
STM	scanning tunneling microscopy
<i>sym</i> OHPhe	symmetric- or 1,2,3,4,5,6,7,8-octahydrophenanthrene
σ^2	Debye-Waller factor
T_d	tetrahedral
TEM	transmission electron microscopy
TetHPhe	1,2,3,4-tetrahydrophenanthrene
TMS	transition metal sulfides
TPS	temperature programmed sulfidation
T_{red}	reduction temperature
UV-Vis DR	Ultraviolet-visible diffuse reflectance
vdW	van der Waals
VGO	vacuum gas oil
vol.-%	volume percent
wt.-%	weight percent
XANES	X-ray absorption near edge structure
XAS	X-ray absorption spectroscopy
XRD	X-ray diffraction

Table of Contents

Chapter 1

General Introduction	1
1.1. Oil – a balance between growing demand and environment protection.....	1
1.2. Hydrotreating	3
1.2.1. Relevance in oil refining	3
1.2.2. Removal of heteroatoms	5
1.2.3. Hydrogenation of aromatic compounds	7
1.3. Transition metal sulfides	11
1.3.1. Material characteristics.....	11
1.3.2. Brief history of sulfide catalysis	12
1.3.3. Catalytically active sites of MoS ₂	14
1.3.4. Infrared spectroscopy of sulfide materials	15
1.4. Scope of the thesis	17
1.5. References	19

Chapter 2

Understanding Ni promotion of MoS ₂ /γ-Al ₂ O ₃ and its implications for the hydrogenation of phenanthrene	23
2.1. Introduction.....	24
2.2. Experimental Section.....	25
2.2.1. Material Synthesis.....	25
2.2.2. Catalyst characterization	26
2.2.3. Kinetic measurements.....	28
2.3. Results	29
2.3.1. Catalyst characterization	29
2.3.2. Hydrogenation of Phenanthrene.....	39
2.4. Discussion	42
2.4.1. State of Ni and its effect on the structure of MoS ₂ /γ-Al ₂ O ₃	42
2.4.2. Structure-activity correlations for (Ni)MoS ₂ /γ-Al ₂ O ₃	45
2.5. Conclusions	47
2.6. References	48
2.7. Supporting Information.....	51

Chapter 3

Pathways for H ₂ activation on (Ni)-MoS ₂ catalysts	69
3.1. Introduction	70
3.2. Results and Discussion.....	70
3.3. Conclusions	74
3.4. References	76
3.5. Supporting Information.....	77

Chapter 4

Mechanistic implications of Ni promotion on the hydrogenation of phenanthrene over MoS ₂ /γ-Al ₂ O ₃	85
4.1. Introduction	86
4.2. Experimental part.....	87
4.2.1. Material synthesis and characterization	87
4.2.2. Kinetic measurements	87
4.3. Results.....	88
4.3.1. Catalyst characterization	88
4.3.2. Hydrogenation of phenanthrene and dihydrophenanthrene	89
4.3.3. Determination of activation energies for phenanthrene hydrogenation	94
4.3.4. Determination of reaction orders	94
4.4. Discussion	98
4.5. Conclusions	102
4.6. References	103
4.7. Supporting Information.....	105

Chapter 5

Summary and Conclusions	115
-------------------------------	-----

Chapter 6

Zusammenfassung	119
-----------------------	-----

Appendix.....	123
---------------	-----

Curriculum Vitae	127
------------------------	-----

List of Publications	129
----------------------------	-----

Chapter 1

General Introduction

1.1. Oil – a balance between growing demand and environment protection

Oil is the most important energy source of our time, accounting for a third of the global energy consumption. And the demand is growing, in 2014 by 0.8 million barrels per day (0.8%). Looking at the last 25 years, oil consumption increased by about 25 million barrels daily. Over time, the regional distribution of consumers changed, as is graphically presented in Figure 1-1. The largest growth is recorded for the Asia Pacific region, with China in the leading position, amounting to an increase of 390,000 barrels oil per day in 2014. Regarding total consumption, that region overtook North America already in 2006. Indeed, in North America as well as in Europe & Eurasia the demand for oil is rather decreasing.¹

The production of oil at the same time is expanding, particularly in North America, the US taking over from Saudi Arabia as the world's largest oil producer in 2014. New technologies allow for ever more resources to become available. The distribution of proven oil reserves is given in Figure 1-1. The largest oil reservoirs are located in Middle East, whereas the region with the highest oil demand shows the minimum store, i.e. Asia Pacific.¹

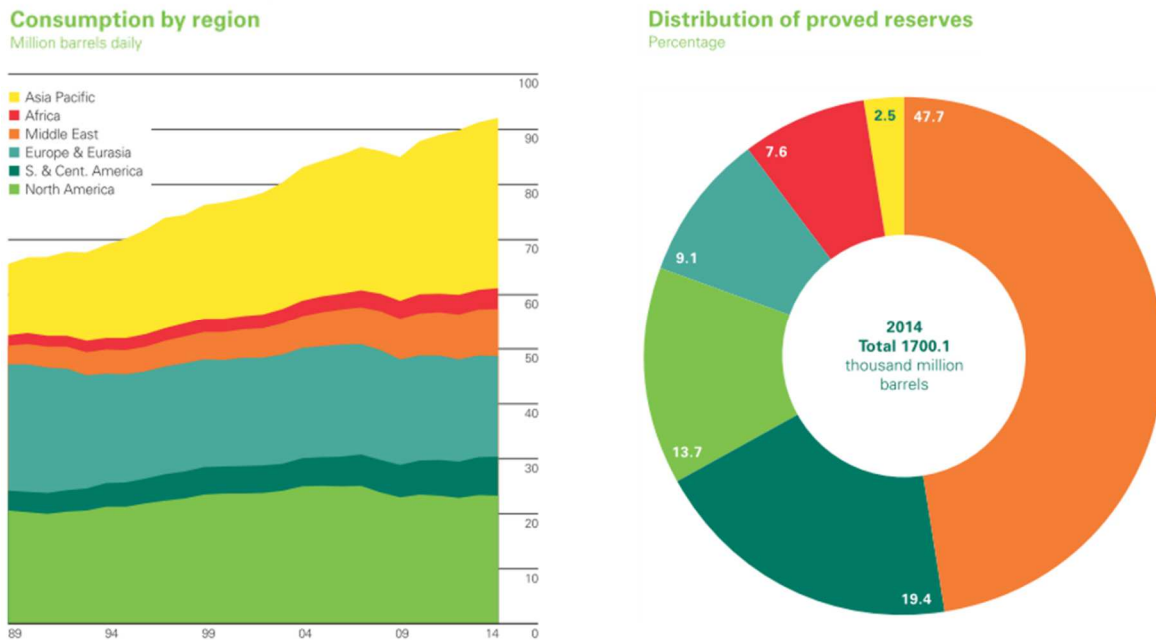


Figure 1-1. Worldwide oil consumption between 1989 and 2014 in million barrels daily (left) and distribution of proved oil reserves for 2014 in percent (right). Pictures are taken from the 'BP Statistical Review of World Energy 2015'.¹

The access to new oil reserves is accompanied by a change in oil quality. Crude oils produced from Canadian tar sands, for example, contain much more S, N and aromatic compounds as conventional resources.² In Table 1-1 key properties of various types of oils are listed. The API gravity describes the density of oil in comparison to water. A high API gravity describes light, low density oil, whereas an API gravity <10 means the oil is more dense than water and sinks. The differences in properties between light and heavy crudes are tremendous. The content of asphaltenes, e.g., can reach from 0 to 40%, while impurities like S differ between 0 and 6%.³ As lighter oil reserves inevitably become rare, refineries have to adopt their processes in order to keep product quality stable and output high. Especially since in parallel light distillates are the fastest-growing refined product category worldwide.¹

Table 1-1. Main properties of different types of crude oils.³

	Extra light	Light crude	Heavy crude	Extra heavy
API gravity	>50	22-32	10-22	<10
Hydrocarbons				
Asphaltenes, wt.-%	0 – <2	<0.1 – 12	11 – 25	15 - 40
Resins, wt.-%	0.05 – 3	3 – 22	14 – 39	-
Oils, wt.-%	-	67 – 97	24 - 64	-
Impurities				
S, wt.-%	0.02 – 0.2	0.05 – 4.0	0.1 – 5.0	0.8 – 6.0
N, wt.-%	0 – 0.01	0.02 – 0.5	0.2 – 0.8	0.1 – 1.3
Ni+V, ppm	<10	10 – 200	50 – 500	200 - 600

Another factor enhancing the demand on refineries is increasingly strict environmental regulations, especially for transportation fuels. Limitations for the S content of fuels were implemented in Europe for the first time in 1994, starting at 2000 ppm. Since then, the EU fuel specifications have been revised several times, until in 2009 the Euro 5 regulation took effect, limiting S to 10 ppm for gasoline and diesel. Similar regulations exist all over the world. In USA the limit for S is 15 ppm for diesel and 10 ppm for gasoline. Even Beijing and Shanghai have adopted 10 ppm as the target limit for S in all fuels, which will be expanded nationwide in 2017. Although those values are not yet realistic, a direction for the future is set.⁴

Of course greenhouse emissions are regulated as well. Currently the EU standard for CO₂ is 130 g/km, but it will be lowered to 95 g/km by 2020. Limits for gasoline exhaust are 0.06 g/kg for NO_x, 1.0 g/kg for CO and 0.1 g/kg for hydrocarbons, whereof 0.068 g/km can be non-methane hydrocarbons.⁴

In recent years, a shift in transportation fuels to diesel instead of gasoline has been registered. The reasons are higher fuel efficiency (about 25%), and taxation preferences in many regions worldwide. Environmentally this change is disadvantageous, as diesel exhausts contain 15.5% more greenhouse gases, especially NO and CO₂, and higher amounts of particulate matter.⁵ For refineries the growing demand for diesel in turn means a change in product slate and process control, as diesel contains considerable less aromatics than gasoline.⁴ Hydrocracking and hydrotreating are the key steps in the refining process to cope with these challenges.

1.2. Hydrotreating

Hydrotreating is a catalytic process utilized to remove impurities and other undesired components from crude oil by reaction with hydrogen. Main impurities are S, N, O and various metals (Ni, V). Further undesired compounds are olefins and aromatics, which are saturated to certain degree during hydrotreating, without changing the C-C chain length significantly.⁶

1.2.1. Relevance in oil refining

Crude oil is a very important natural resource for various products, i.e. gasoline, diesel, jet fuel, liquefied petroleum gas (LPG), heavy fuel oil, asphalt, lubricants and as well petrochemicals like ethane, propane, butane and benzene-toluene-xylene (BTX). After the crude is processed by an oil production plant, oil refineries continue with purification and upgrading. In Figure 1-2 an outline of a typical oil refinery is depicted. The heated crude oil undergoes atmospheric distillation, where its components are fractionated by boiling point. Subsequently, the high density bottom products continue to vacuum distillation. The light, gaseous end is led on to a gas plant, producing LPG, various alkanes and sulfur. The middle fraction of the atmospheric distillation is composed of naphtha, diesel, kerosene and jet fuel, which are led on to different

hydrotreating units. Depending on its specific density, the naphtha is further processed either by isomerization, or reforming, before it is fed to the gasoline blending pool. The residuum of vacuum distillation is further processed to asphalt and petroleum coke. The heavy vacuum gas oil (VGO) is treated in a hydrocracker, yielding diesel and gasoline. The light VGO continues on to hydrotreating, followed by a fluid catalytic cracking unit (FCC) and a second hydrotreating process. The light parts of the cracking products from hydrocracker and FCC unit undergo alkylation, before they are fed to the gasoline blending pool as well.^{6,7}

Hydrotreating units are key components of oil refining for various reasons. The removal of S is crucial, on the one hand to protect the following process units from corrosion. On the other hand, the catalysts used in catalytic reforming, cracking and alkylation often contain noble metals like Pt, Ir, Re and Pd, or zeolites, which are very sensitive to poisoning by S, N, O or metals. In addition metals can cause severe coke buildup in further processing units. Severe environmental regulations especially for transportation fuels are another reason to remove impurities from crude oil.^{7,8} And lastly, the performance of fuel is dependent on the right hydrogen-to-carbon (H/C) ratio. For crude oil the H/C ratio is between 1.4 and 1.6 depending on the origin. To get high quality gasoline, e.g., an increase to about 2.0 is mandatory, which can be accomplished by hydrotreating and hydrocracking.⁹

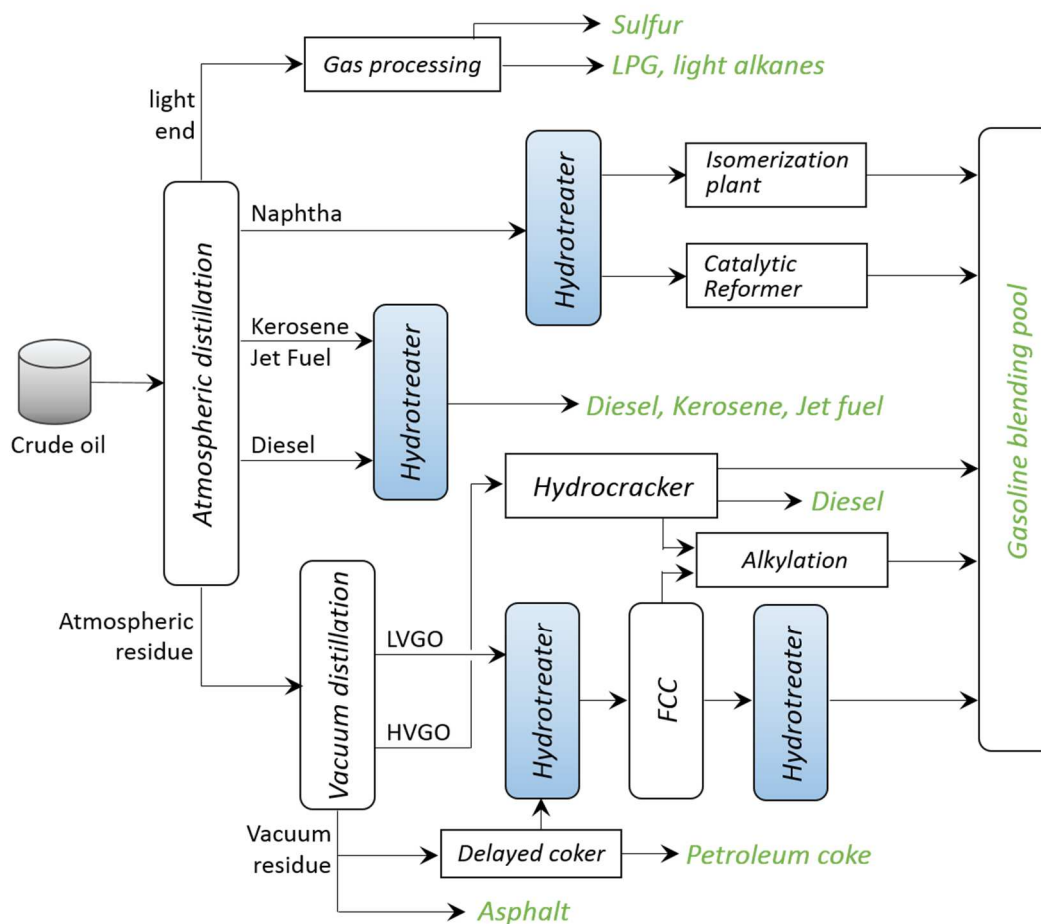


Figure 1-2. Schematic flow diagram showing typical components of an oil refinery.⁷

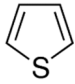
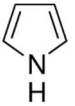
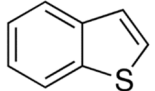
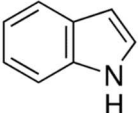
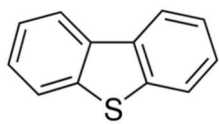
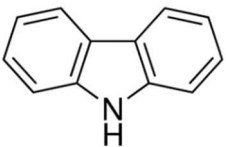
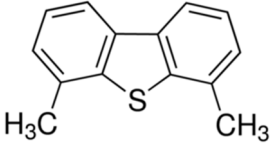
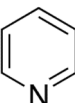
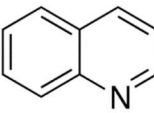
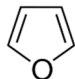
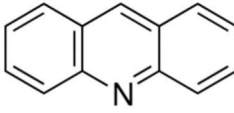
The reactors used for hydrotreating are usually downflow, fixed-bed catalytic reactors operated in trickle-flow regime. Reaction conditions typically are harsh and range from 40 – 160 bar and 260 – 420°C, depending on the composition of the feed and the desired products.¹⁰ As during the reaction large amounts of H₂ are present, and H₂S and NH₃ are formed, the reactor materials need to be corrosion resistant. Austenitic stainless steels possess excellent corrosion resistance against hot sulfuric acid and other aggressive environments and are often used to coat the inside of hydrotreating reactor vessels.⁶

Catalysts employed for hydrotreating in consequence also have to withstand these harsh conditions and at the same time show high activity for S, N, O and metals removal. Transition metal sulfide catalysts are applied to a large extent, particularly Ni-MoS₂, Co-MoS₂ and Ni-WS₂ supported on Al₂O₃.⁸

1.2.2. Removal of heteroatoms

The most abundant undesired element in crude oil is S, with up to 5 wt.-% in heavy crudes.³ Hydrodesulfurization (HDS) is accomplished by catalytic reaction with hydrogen under release of H₂S. Thiols (R-SH), sulfides (R-S-R') and disulfides (R-SS-R') are easily converted, whereas thiophene-like structures are more difficult due to their aromatic character. In Table 1-2 common heterocyclic compounds are shown.^{8,11}

Table 1-2. Typical heterocyclic molecules containing S, N or O found in crude oil.^{8,11}

S compounds		N compounds	
Thiophene C ₄ H ₅ S		Pyrrole C ₄ H ₅ N	
Benzothiophene C ₈ H ₆ S		Indole C ₈ H ₇ N	
Dibenzothiophene C ₁₂ H ₈ S		Carbazole C ₁₂ H ₉ N	
4,6-Dimethyl- dibenzothiophene C ₁₄ H ₁₂ S		Pyridine C ₅ H ₅ N	
O compound		Quinoline C ₉ H ₇ N	
Furan C ₄ H ₄ O		Acridine C ₁₃ H ₉ N	

HDS reactions always comprise a combination of C-S bond cleavage and hydrogen saturation. Hydrogenolysis and hydrogenation are always exothermic reactions. At industrial conditions (high pressures, up to 420°C) sulfur removal is essentially irreversible. However, hydrogenation of aromatic rings is at the border of thermodynamic limitations, resulting in equilibrated reaction steps with conversions below 100%.¹²

4,6-Dimethyldibenzothiophene (4,6-DMDBT) is one of the most difficult molecules to desulfurize, especially causing problems in deep HDS, where sulfur levels below 10 ppm have to be reached. In Figure 1-3 the reaction mechanism for 4,6-DMDBT is shown. Two reaction paths are possible. On the one hand direct desulfurization (DDS) to 3,3'-dimethylbiphenyl, where S is removed without hydrogenating the aromatic rings. On the other hand hydrogenation (HYD) to 4,6-dimethyl-tetrahydrodibenzothiophene and higher hydrogenated molecules, followed by desulfurization. The HYD route is strongly favored in case of 4,6-DMDBT. The reason is its steric demand on adsorption of the S atom. Because of the aromaticity of the molecule, the methyl substituents are in one plane with S and the whole compound is very inflexible. For DDS the molecule is usually adsorbed *via* S at coordinatively unsaturated sites at the edges of the catalyst, thus activating the C-S bonds. For 4,6-DMDBT this kind of adsorption is sterically hindered. Instead adsorption is found to take place preferentially on the basal plane of MoS₂ *via* the aromatic ring system.¹³ After partial hydrogenation, however, the flexibility of the molecule increases accelerating DDS paths.¹⁴

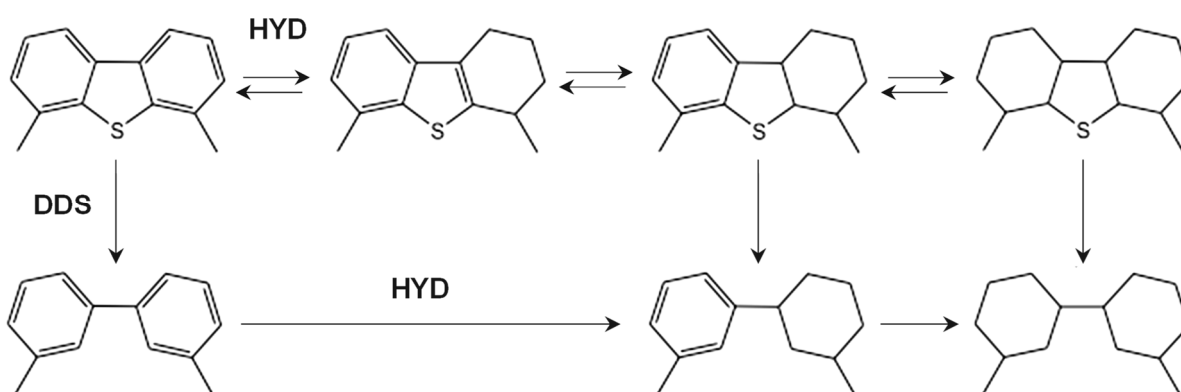


Figure 1-3. Reaction mechanism for HDS of 4,6-dimethyldibenzothiophene.^{11,14}

N-containing molecules are the second most abundant impurity in crude oil. Hydrodenitrogenation (HDN) is accomplished by catalytic reaction with hydrogen, releasing NH₃. Amines (R-NH₂) and non-heterocyclic rings (e.g. aniline) are easily decomposed. Heterocyclic molecules like pyrrole, pyridine and their higher derivatives (see Table 1-2), however, are more difficult to react.^{8,11}

From a thermodynamic point of view, HDN is quite different from HDS, as heterocycles containing N need to be completely hydrogenated before hydrogenolysis can occur. The

reason is the relatively strong C-N bond in aromatic systems, which gets reduced by hydrogenation. Consequently, the thermodynamic of N compounds is governed by hydrogenation, which is often in equilibrium at typical hydrotreating conditions. For non-heterocyclic molecules HDN is usually irreversible.¹²

A popular model compound for HDN is quinolone (Q). Its reaction mechanism is given in Figure 1-4. Before C-N bond cleavage can take place, either one or both aromatic rings of Q are hydrogenated. Subsequently, the heterocycle is broken between position 1 and 2. The removal of N in the following takes place by direct denitrogenation (DDN) without further hydrogenation of the ring system (if not already saturated). The main route for Q HDN is hydrogenation through decahydroquinoline as intermediate, with propylcyclohexane as main product.^{11,15}

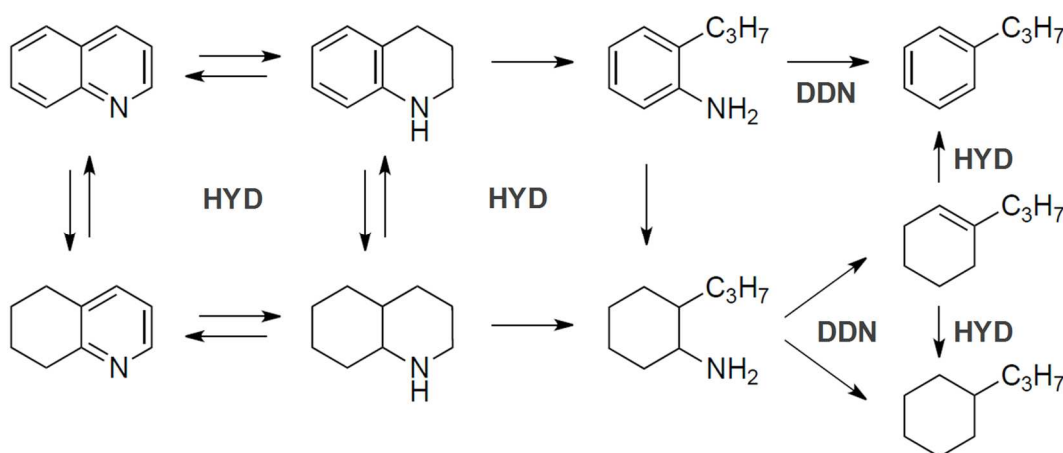


Figure 1-4. Reaction mechanism for HDN of quinolone.^{11,15}

Molecules containing oxygen are less abundant in crude oil. They are usually present as naphthenic acids, phenols or furan. As the share of biomass for transportation fuels increases, hydrodeoxygenation (HDO) is going to become increasingly important.⁸

Metal impurities are predominantly found in heavy crude oils, mostly Ni and V. They originate from plants and are present in porphyrinic structures. During hydrodemetallization (HDM) the metals are deposited onto the catalyst in their sulfide form.⁸


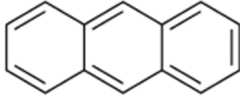
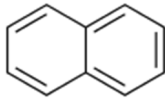
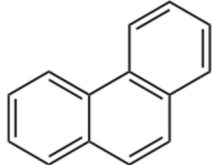
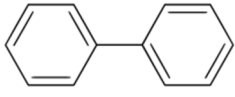
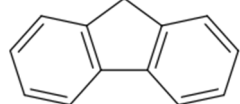
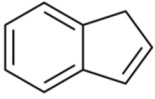
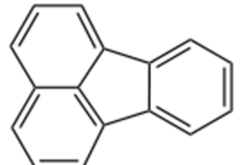
1.2.3. Hydrogenation of aromatic compounds

The content of aromatics, especially polycyclic aromatic compounds in crude oil is increasing as the supply changes from light to heavy feedstock. Typical aromatic molecules found in crudes are listed in Table 1-3, leaving out possible alkyl substituents. Heavy crudes also contain a great concentration of asphaltenes, which are very large arrangements of aromatic systems, S, N and O, as depicted exemplary in Figure 1-5. In the past, this part of the oil was separated and used e.g. as paving material for roads (asphalt). However, as their fraction increases more and more, interest in alternative utilization possibilities gains importance.

Saturation of aromatics by reaction with hydrogen, hydrodearomatization (HDA), is a prominent option.^{12,16,17}

Model compounds are usually employed to investigate the thermodynamic and kinetic behavior of aromatics, e.g. those listed in Table 1-3. The equilibrium constants for the hydrogenation of aromatic compounds are generally below 1 in the temperature range of 260-420°C. Hydrogenation reactions, therefore, are reversible, often showing equilibrium conversions below 100%. As hydrogen addition is an exothermic process, increasing temperatures lead to even lower equilibrium conversions. In order to circumvent equilibrium limitations, high pressures of up to 160 bar are commonly used in industry.¹²

Table 1-3. Typical aromatic molecules found in crude oil.^{12,17}

Aromatic compounds			
Benzene C ₆ H ₆		Anthracene C ₁₄ H ₁₀	
Naphthalene C ₁₀ H ₈		Phenanthrene C ₁₄ H ₁₀	
Biphenyl C ₁₂ H ₁₀		Fluorene C ₁₃ H ₁₀	
Indene C ₉ H ₈		Fluoranthene C ₁₆ H ₁₀	

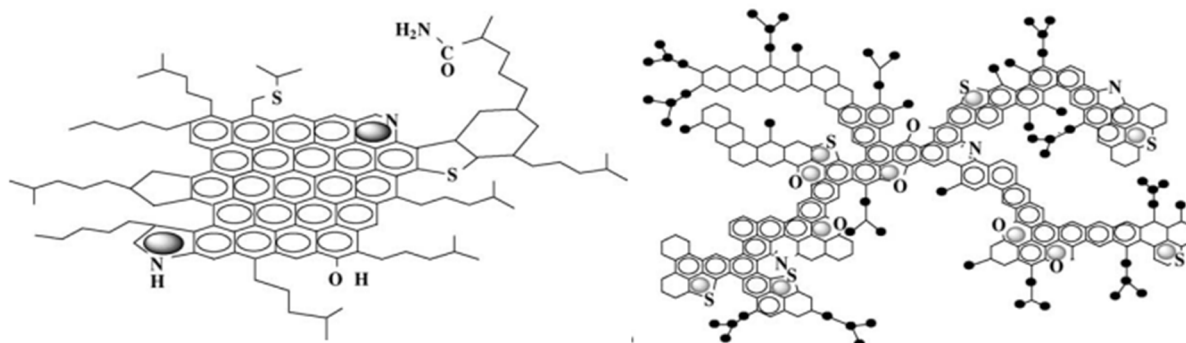


Figure 1-5. Structures proposed for asphaltenes present in heavy crude oil.¹⁶

In terms of reactivity, polycyclic aromatics are considerably faster to hydrogenate than monocyclic compounds, e.g. naphthalene gives rates one order of magnitude higher than benzene.¹² The reason is better resonance stabilization of large aromatic ring systems. This results in stronger interaction of the molecule with the catalytic active site upon adsorption and

most probably also better stabilization of intermediate structures. Indeed, the increase in binding energy for naphthalene compared to benzene adsorption on the basal plane of MoS₂ was shown recently by density functional theory (DFT) calculations.¹⁸ Ongoing developments in DFT and computing capacity allows since 2004 to consider van der Waals (vdW) interactions for the calculation of molecule interactions.^{19,20} It has been shown that vdW forces are essential for binding energies on MoS₂ surfaces and that adsorption of conjugated and aromatic compounds is feasible on the basal plane of MoS₂ merely by physisorption *via* vdW interaction. The aromatic molecules are arranged planar, parallel to the surface at a distance of 3.5 Å. The binding energy calculated for benzene is -0.47 eV and for naphthalene -0.70 eV (vdW-DF functional). A linear correlation exists between the adsorption energy on the basal plane of MoS₂ and the number of main atoms of a molecule, including C, S and N.¹⁸

Hydrogenation of polycyclic aromatic hydrocarbons (PAH) usually proceeds ring by ring. Saturation of the first ring is kinetically most favored, whereas the reaction rates for subsequent rings decrease, the last ring being the slowest to hydrogenate.¹⁷ This renders PAHs as proper model compounds for kinetic studies aiming at a detailed understanding of reaction mechanisms and kinetics of HDA. Their often complex reaction networks can be advantageous to observe the influence of different catalyst materials, reaction conditions, or inhibiting effects, e.g. by H₂S.

Phenanthrene (Phe) is a popular PAH model compound due to its special electronic structure. In Figure 1-6 the distribution of π -electrons in anthracene and Phe is compared. Both molecules own 14 π -electrons. From benzene it is known that π -electrons are very mobile and tend to delocalize, i.e. they can migrate among different double bonds. This delocalization gives benzene its very unique stability, symbolized by a circle drawn inside the hexagon instead of three double bonds.

In anthracene 14 e⁻ are distributed over three linear arranged rings, which leads to 4 e⁻ per ring plus two spare electrons that are mobile. However, there is a certain probability for 6 e⁻ to be localized in one ring, thus adopting very different properties, referred to as “benzenoid”, i.e. very high stability and low reactivity. Adjacent rings with only 4 e⁻ are termed “aromatic” and can have any degree of reactivity. Figure 1-6 (a) illustrates this relation for anthracene; the arrow symbolizes the mobility of 2 e⁻.

Phe features an angular arrangement of its three rings, depicted in Figure 1-6 (b). This induces the possibility to form a second benzenoid 6 e⁻ ring-system, Figure 1-6 (c), resulting in a higher stability of phenanthrene compared to anthracene. Additionally, this leads to very special properties for the 9,10-position in Phe. In formula (b) the middle ring has aromatic character (4 e⁻), whereas it presents merely a double bond containing 2 e⁻ in (c). Apparently, the 9,10-position is the most reactive bond in Phe, showing almost the reactivity of an olefin.²¹

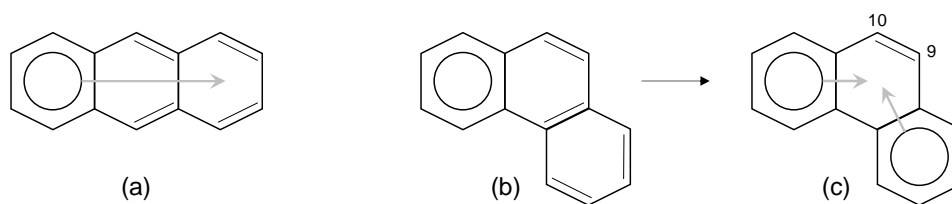


Figure 1-6. Distribution of π -electrons in anthracene (a) and phenanthrene (b,c).²¹

The reaction network of phenanthrene hydrogenation has been investigated before, yet with different outcome.^{22–25} Jiang *et al.*²⁶ recently compared three different reaction systems derived for transition metal sulfide catalysts. In Figure 1-7 all feasible hydrogenation pathways are depicted. The fastest reaction usually is the formation of 9,10-dihydrophenanthrene (DiHPhe), where only two hydrogen atoms are added to Phe. Formation of 1,2,3,4-tetrahydrophenanthrene (TetHPhe) is often slower, depending on the catalyst. Isomerization of DiHPhe and TetHPhe is also observed, but with low rates. Further hydrogenation to 1,2,3,4,5,6,7,8-octahydrophenanthrene (*sym*OHPhe) and 1,2,3,4,4a,9,10,10a-octahydrophenanthrene (*asym*OHPhe) is preferred from TetHPhe. The reason is a larger stabilizing effect and stronger adsorption of the naphthenic ring-system of TetHPhe than of the two benzenoid substituents in DiHPhe. Full hydrogenation to perhydrophenanthrene (PerHPhe) is reached only at high conversion levels at conditions far from equilibrium.

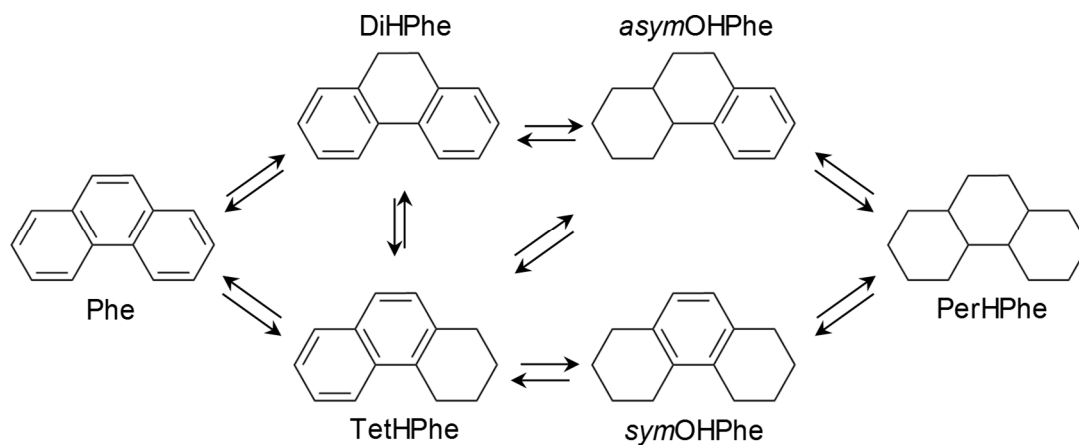


Figure 1-7. Reaction network for the hydrogenation of phenanthrene.^{22–26}

1.3. Transition metal sulfides

1.3.1. Material characteristics

Many non-ferrous metals naturally occur as sulfide minerals. They have various applications in industry, as S source and as catalysts.²⁷ Of special interest are the transition metal sulfides MoS_2 and WS_2 , which are employed as catalysts in hydrotreating reactors – one of the largest processes worldwide based on heterogeneous catalysis.⁸

The structure of MoS_2 and WS_2 is exceptionally alike. Their ion radii are almost identical, i.e. 59 pm for Mo^{6+} and 60 pm for W^{6+} , due to the Lanthanide contraction. Metal sulfide structures have a significant covalent character, in contrast to oxides. Moreover they tend to form chains of single bonded atoms (-S-S-), leading to a preferred formation of layered structures. In case of molybdenite-type structures (MoS_2 , WS_2), these “layers” are usually referred to as “slabs” and are composed of three atomic layers each. Two atomic layers (top and bottom) consist of S in a hexagonal symmetry, stacked AA. In between is a metal layer, with the metal atoms sitting in trigonal prismatic holes. Within each sandwich triple layer, strong covalent interactions exist, whereas only weak van der Waals forces prevail in between slabs. The distance between slabs is 6.1 Å.²⁸ Within one layer the distance between Mo-Mo is 3.16 Å and 2.43 Å for Mo-S.²⁹ Figure 1-8 depicts the structure of the most common form of MoS_2 - anisotropic 2H- MoS_2 - as described above (“2” corresponds to the number of slabs per unit cell, and “H” the hexagonal arrangement of S).^{27,30}

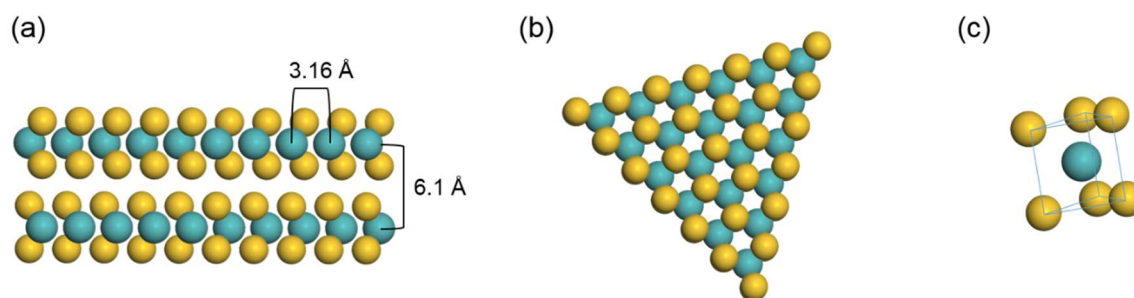


Figure 1-8. Structure of 2H- MoS_2 ; (A) side view, (B) top view, and (C) geometry around Mo. Blue: Mo, yellow: S.

The special structure of MoS_2 makes it a good high temperature lubricant, it is very robust and at the same time the sandwich triple layers slide over each other with little resistance.²⁷ Besides, bulk MoS_2 is a diamagnetic semiconductor with a bandgap of about 1.2 eV, similar to Si.³¹ This opens many possibilities for further application, especial in the field of photo- and electro-catalytic processes.

When MoS_2 (or WS_2) are applied as hydrotreating catalysts, they usually contain Ni or Co as promoting components. Where and how Ni and Co are incorporated into the sulfide slabs is addressed in the following chapters. Naturally, many different stoichiometries of Ni and Co

sulfides exist. The most common forms detected in transition metal sulfide (TMS) catalysts are metal-rich Ni_3S_2 and Co_9S_8 . Ni_3S_2 has a trigonal space group ($R\bar{3}2$) with Ni sitting in a distorted tetrahedral interstice surrounded by S. Co_9S_8 forms a cubic closed pack and has the space group $Fm\bar{3}m$.²⁷

1.3.2. Brief history of sulfide catalysis

At the end of World War I a growing interest in the hydrogenation of local coal supplies to produce liquid fuels developed, with the objective to reduce dependencies on petroleum imports and vulnerable supply lines. Researchers tested various metal catalysts and discovered that S-containing molecules were poisonous to many of them, except Mo and W which retained their activity for hydrogenation. After processing, Mo and W had actually converted to sulfides – the field of transition metal sulfide (TMS) catalysis emerged – and over 6000 different catalytic materials were tested until 1930. Paul Sabatier and Friedrich Bergius were among the leading scientists, and were awarded for their work by a Nobel Prize in 1912 and 1913, respectively.³²

The *Sabatier principle* states that optimum activity is reached for catalysts with an optimal metal-to-reactant bond strength, i.e. not too strong and not too weak. Accordingly, investigations of periodic trends regarding HDS activity of TMS catalysts, as conducted for example by Pecoraro and Chianelli³³, inevitably lead to a “volcano” curve. MoS_2 and WS_2 actually are not the most active TMS materials, however, they are relatively cheap compared to Ru, Re, Pt, Pd and Ir. And the promoting effect of the addition of Ni or Co to MoS_2 and WS_2 , considerably boosting their activity, was discovered early on. First results from 1933 by Pease and Keighton³⁴, however, proved to be irreproducible for a long time, which immediately revealed a strong dependency of these materials on preparation methods and conditions, and was the beginning of a long controversy about the active sites of TMS catalysts.³⁵

Over the years, various models for the promotion of MoS_2 and WS_2 by Ni and Co and the nature of the catalytic active sites have been proposed. Figure 1-9 schematically shows three concepts. One is *pseudo-intercalation*, where the promoting atoms are inserted between alternate sandwich triple layers, close to the edge of MoS_2 . This was assumed to result in surface reconstruction of MoS_2 , leading to more exposed Mo cations and, therefore, to enhanced activity. The effect of intercalation, however, was not deemed sufficient to explain the steep increase in hydrotreating activity usually observed.^{36,37}

Another concept is *contact synergy*. The metals are present in separate phases, as layered MoS_2 and clusters of Co_9S_8 , but are in close contact. The role of the promoter is to provide H atoms, which are spilled-over to MoS_2 . There, reduced Mo sites are created, which in turn are active for hydrogenation. The promoter influences in “remote control” the surface of MoS_2 , and

its activity. Discrepancies, however, were found for samples with very low concentrations of Co, where no Co_9S_8 phase, but high activities were observed; and for samples with very high concentrations of Co_9S_8 , resulting in an actual decrease in activity.^{36,38}

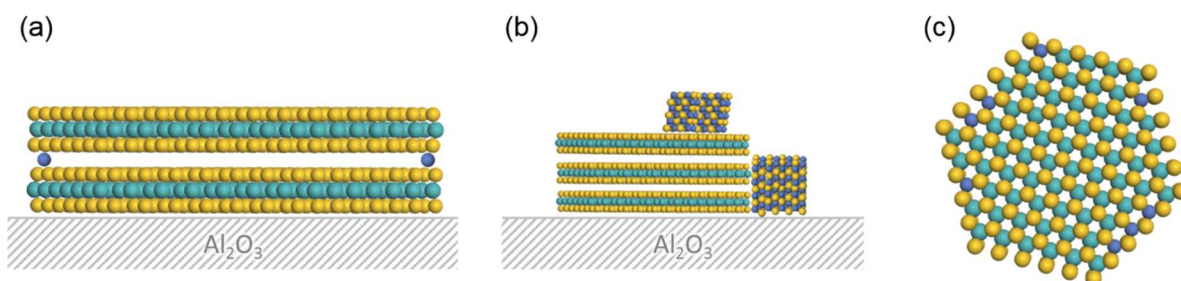


Figure 1-9. Schematic pictures of the location of promoting atoms in MoS_2 according to the *pseudo-intercalation* (a), *contact synergy* (b), and *CoMoS phase* (c) model.^{36–38} Blue: Mo, gray: Ni/Co, yellow: S.

Yet another concept is placing the promoting atoms in one layer with Mo, creating a *CoMoS phase*. First strong indications for the direct incorporation of Co in the MoS_2 slab were gained by Topsøe *et al.*³⁹ using Mössbauer spectroscopy. Direct, visual evidence for the formation of a $\text{Co}(\text{Ni})\text{MoS}$ phase is provided much later by scanning tunneling microscopy (STM)^{40,41} and scanning transmission electron microscopy (STEM, Figure 1-10 a).⁴² Ni and Co are observed predominantly at the edges of MoS_2 slabs, replacing single Mo atoms. The promoting atoms adapt to the layered sandwich structure of MoS_2 by forming a so-called millerite-type structure depicted in Figure 1-10 b. Ni therein is square pyramidal coordinated. Ni is surrounded by five S atoms, whereas four of these S atoms are connected to MoS_2 and a fifth is placed on top of Ni. In the second coordination shell are up to two Mo atoms, and another Ni is found in the third coordination shell.²⁹

The promoting effect of Ni and Co is believed to originate from electron donation to MoS_2 . Charge transfer between Mo and the promoter is possible over shared S atoms, allowing for a transfer of *d*-electrons from Ni/Co to *4d*-orbitals of Mo. The higher electron density at Mo decreases the bond strength to sulfur, and thus, increases the activity.^{37,43}

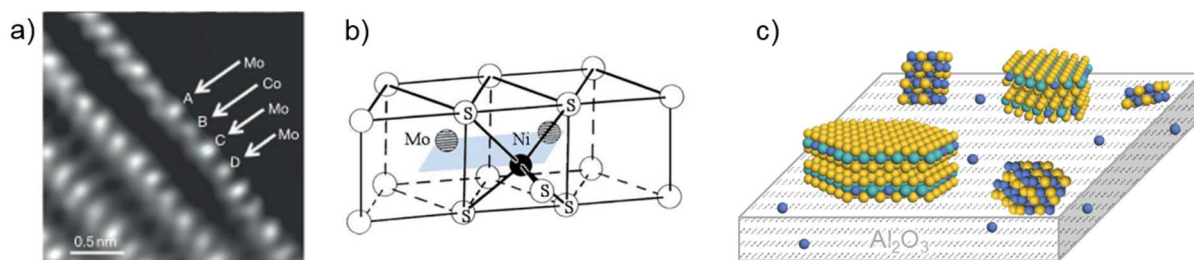


Figure 1-10. Location and coordination of promoting atoms in MoS_2 . (a) Micrograph of bulk CoMoS nanowires as observed in HAADF-STEM.⁴² (b) Millerite-type structure of the Ni-Mo-S phase.²⁹ Schematic picture of the distribution of Co/Ni in $\gamma\text{-Al}_2\text{O}_3$ supported MoS_2 .⁴⁴

Investigations of γ -Al₂O₃ supported Co(Ni)MoS₂ catalysts (which are the most common used form in refining) revealed the simultaneous presence of Co (or Ni) in three different phases: Incorporated in MoS₂ slabs forming a CoMoS phase, as Co₉S₈ clusters, and as spinel CoAl₂O₄ distributed in the support. Figure 1-10 shows a schematic representation of these three options. Only the CoMoS phase - and pure MoS₂ - are active for hydrotreating.⁴⁴

1.3.3. Catalytically active sites of MoS₂

The existence of different types of active sites in MoS₂ was recognized early on. A popular two-site concept developed by Daage and Chianelli⁴⁵ is the “rim-edge”-model. The MoS₂ particle is described as a stack of several slabs, as depicted in Figure 1-11. The perimeter of the top and bottom slab is considered the “rim” and the perimeters of the sandwiched slabs in between are the “edge”. The basal plane on top the MoS₂ stack is supposed to be catalytically inactive. Hydrogenolysis can occur on rim and edges, whereas hydrogenation is limited to the rim region.

As adsorption sites for S, N and aromatic compounds, sulfur vacancies at the edges of MoS₂ were identified. Activation of heteroatom containing molecules was found to take place by coordination *via* the S or N atom to the Lewis acidic sulfur vacancy. Aromatic compounds were reasoned to be harder to activate, thus, requiring larger degrees of unsaturation (stronger Lewis acidity) which is generally found for sulfur vacancies at the “rim” or at corner sites of MoS₂. These conclusions were based on structure-activity correlations, inhibiting experiments and adsorption of probe molecules. Visual evidence of adsorption of dibenzothiophene on the edge of a MoS₂ slab *via* S could now be provided by STM¹³ (see Figure 1-11), and confirmed the already long accepted concept.

An alternative kind of active site was proposed by Topsøe *et al.*^{41,44}. In STM studies the MoS₂ particles exhibit a bright perimeter, which indicates electron enrichment and leads to a metallic character of this region, denoted as “brim” site. The brim is expected to adsorb and activate even large S, N and aromatic molecules, as steric hindrance is small compared to edge sites. In Figure 1-11 a STM image of the adsorption of 4,6-dimethyldibenzothiophene on MoS₂ is depicted.¹³ In addition, DFT calculations showed feasible adsorption energies for various model compounds on the basal plane and the brim sites of MoS₂.^{18,46}

Structural changes of MoS₂ upon promotion with Co or Ni can also be directly observed in STM. The original triangle shape of MoS₂ is exchanged by a truncated hexagon in presence of Co or Ni in model systems. In addition, the brim of Co and Ni substituted edges is brighter, indicating increased electron density and could explain higher activity for hydrotreating reactions due to promotion.⁴⁰

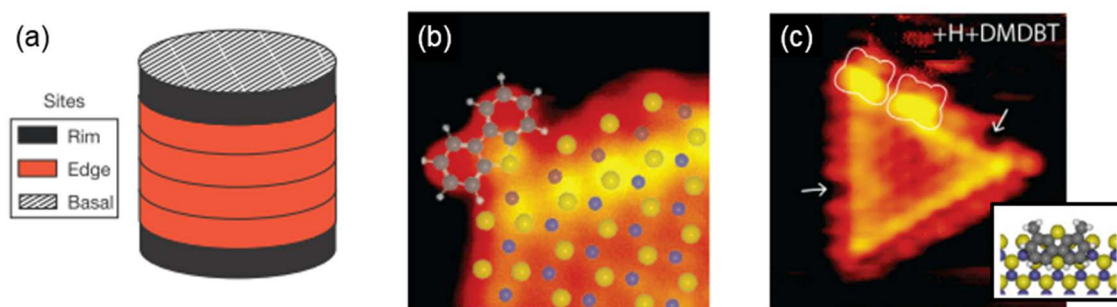


Figure 1-11. Active sites in MoS₂ catalysts. (a) “Rim-edge” model proposed by Daage and Chianelli.⁴⁵ (b, c) STM images of dibenzothiophene adsorbed on a sulfur vacancy and 4,6-dimethyldibenzothiophene on the basal plane of MoS₂.¹³

Of great importance is also the adsorption and activation of hydrogen on the surface of TMS catalysts. Where and how (at sulfur vacancies or at the brim - heterolytic or homolytic splitting) H₂ is activated by MoS₂ is still controversially discussed. At present a certain consensus exists, that SH-groups are the active form of H on the surface, sitting predominantly at the edges of MoS₂.^{47–54}

1.3.4. Infrared spectroscopy of sulfide materials

Infrared (IR) spectroscopy is one of the most frequently used techniques to study sulfide catalysts. This is related to the great variety of information that can be gathered, ranging from characterization of supports, precursors and aged catalysts, to *in situ* information about reaction intermediates and activation mechanism, to the nature of adsorbed species and reactivity of catalysts.⁵⁵ IR was among the first *in situ* techniques applied to sulfide catalysts in the early 1980s.⁵⁶

Stability is a key factor during characterization of sulfide materials, as contact with air easily leads to partial reoxidation of sulfides, resulting in the formation of Mo(W)=O groups, sulfate and thiosulfate-like anions.⁵⁷ This makes *in situ* operations mandatory, which usually means that the materials are sulfided or re-sulfided directly inside the respective measuring equipment. Various designs were developed for IR, where sulfidation in flowing H₂S is possible and later on, vacuum conditions could be applied, without exposing the sample to air.^{56,58–62} Some setups, however, do not allow sulfidation in pressure, which is known to have an impact on the structure of the active catalyst.^{58,63,64} Hence, in this work an IR cell was designed and built with operation limits of pressures up to 20 bar, temperatures up to 400°C and evacuation till 10⁻⁸ mbar and liquid N₂ temperature. The cell is described in the Appendix.

There are two possibilities to study catalysts by IR, i.e. direct and indirect. Direct characterization yields information about functional groups on the surface, like OH and SH, support interactions, distribution and nature of the oxide and sulfide phase, and influence of preparation conditions. Additional information about the catalyst surface can be obtained by

adsorption of probe molecules, i.e. indirect IR characterization. Common probe molecules are CO and NO to study adsorption sites (sulfur vacancies) and, among others, 2,6-dimethylpyridine to study acidic properties. As sulfides are always black powders, transmission is usually low, which makes spectroscopy of bulk materials extremely challenging. Supported samples are much easier to handle, for which reason they comprise the majority of literature.

Direct characterization of Al₂O₃ supported MoS₂ revealed strong support interactions with Al-OH groups. This explains the tendency of MoS₂ to form single layers on alumina, whereas high stacking degrees are common for bulk MoS₂.^{53,65} After addition of Ni or Co, stacking of MoS₂ slabs increases, which is attributed to a weakening of the support interactions by promotion.⁶⁶ Adsorption of NO or CO exclusively takes place at the edge sites of MoS₂. As the frequencies for NO and CO adsorption on promoter atoms differ from Mo, conclusions about the location of promoter atoms are possible. Indeed, by addition of Co or Ni a decrease in the availability of Mo edge atoms can be observed, indicating an atomic dispersion of the promoters in the edge of MoS₂ slabs, forming a mixed CoMoS phase.^{55,67} For Co this phase was previously observed by Mössbauer spectroscopy³⁹, however, similar experiments are not possible for Ni, which makes IR spectroscopy a key technique for the characterization of Ni-promoted MoS₂ catalysts. Furthermore, a direct correlation of CO adsorbed on Co edge atoms with HDS activity was revealed, proving that the CoMoS sites are the active phase for hydrotreating.⁵⁵

The presence of SH-groups on the surface of sulfide catalysts was known, however, IR spectroscopy of pyridine (which is the common probe molecule for OH groups of zeolites), probing mainly Lewis acidic sites (LAS), could hardly provide any evidence for Brønsted acidity.^{68,69} 2,6-Dimethylpyridine (DMP) is a stronger base than pyridine, the pK_b values being 7.4 and 8.7, respectively.⁷⁰ In addition, the steric influence of the two methyl groups close to N lead to a preferred adsorption of DMP on Brønsted acid sited (BAS). Adsorption of DMP on MoS₂ successfully revealed the presence of BAS in addition to LAS. Furthermore, subsequent co-adsorption of H₂S leads to the creation of new BAS, at the expense of LAS. In the presence of Co, both, the concentration of BAS before and after admission of H₂S was increased compared to not-promoted MoS₂.^{62,71,72}

1.4. Scope of the thesis

Transition metal sulfides, particularly Ni-promoted MoS₂ supported on γ -Al₂O₃, are well-established industrial hydrotreating catalysts and have been extensively studied. Detailed reaction pathways and models for active sites exist for hydrodesulfurization.⁵² Knowledge about the manner of hydrogen activation, leading to the formation of active SH-groups at the edges of MoS₂ slabs, however, is rare. The adsorption of polycyclic aromatic hydrocarbons is also hardly investigated, although hydrogenation is becoming more and more important as the relevance of heavy oil conversion grows. Another weak spot in literature is the understanding of high metal concentration Ni-MoS₂/ γ -Al₂O₃ samples. They are a valuable link to understanding bulk sulfide materials, which gain renewed importance in ultra-low sulfur diesel production. Hence, the objective of this thesis is to gain a deeper understanding of hydrogenation reactions over Ni-MoS₂/ γ -Al₂O₃ catalysts on a molecular level. The following tasks were covered:

i. Catalyst synthesis and characterization

Sulfide catalysts with varying Ni/(Mo+Ni) ratios from 0 to 0.7 are synthesized by incipient wetness impregnation of γ -Al₂O₃ followed by sulfidation in H₂S/H₂. Structural information is gathered by UV-Vis spectroscopy, X-ray diffraction and transmission electron microscopy (TEM). The sulfiding process is followed by temperature programmed sulfidation. Indications of the presence of Ni in different phases, as NiAl₂O₄ spinel, Ni₃S₂ clusters, and Ni in close interaction with MoS₂, are obtained.

ii. Evaluation of adsorption sites by spectroscopy

Adsorption of probe molecules like CO and 2,6-dimethylpyridine (DMP) provides valuable information about active sites of sulfide materials. Therefore, an infrared spectroscopy setup for high pressure sulfidation and high vacuum adsorption down to liquid nitrogen temperature is implemented. The influence of Ni on the concentration of sulfur vacancies and Brønsted acidic SH-groups at the edges of MoS₂ is investigated. Additional structural information is gained by extended X-ray absorption fine structure (EXAFS) analysis. The presence of Ni as a mixed Ni-Mo-S phase is confirmed.

iii. Activation of H₂

The mechanism of hydrogen activation is examined by co-adsorption of 2,6-dimethylpyridine with H₂S or H₂, analyzed quantitatively by IR spectroscopy. The relevance of sulfur vacancies for the formation of SH-groups on sulfide catalysts is proved. Isotope exchange experiments using D₂ are executed to substantiate quantitative IR results and amplify the influence of Ni on H₂ activation.

iv. Correlation of structure and reactivity for aromatic hydrogenation

Phenanthrene (Phe), a polycyclic aromatic hydrocarbon consisting of three fused rings, is chosen as model compound to study the hydrogenation activity of sulfide catalysts. Correlations of reactivity and structural features of the catalysts, in particular those interrogated by IR of adsorbed CO and DMP and co-adsorbed H₂S or H₂ and NO adsorption, are used to obtain insight into the active sites for hydrogenation. Analysis of the results from TEM and EXAFS, atomic models of the MoS₂ and Ni-Mo-S phases present on the catalyst surface are created, in consistency with characterization and activity results.

v. Modeling of surface reaction steps by in-depth kinetic investigations

Two catalysts, MoS₂/γ-Al₂O₃ and the most active Ni-MoS₂/γ-Al₂O₃, are chosen for further kinetic experiments. A detailed analysis of the reaction network for phenanthrene hydrogenation is conducted by exploring the hydrogenation of an intermediate, 9,10-dihydrophenanthrene. Furthermore, the activation energy for Phe hydrogenation and reaction orders in H₂, Phe and H₂S are determined. A Langmuir-Hinshelwood model, applied on the kinetic data, allows understanding the rate determining step of the hydrogenation process. The key parameter governing the product distribution is the rate of hydrogen addition, which is increased by Ni promotion, and explains the formation of higher hydrogenated products in Ni-MoS₂/γ-Al₂O₃ compared to MoS₂/γ-Al₂O₃.

1.5. References

- (1) British Petroleum. BP Statistical Review of World Energy. bp.com/statisticalreview (accessed Jul 25, 2015).
- (2) Leliveld, R. G.; Eijsbouts, S. *Catal. Today* **2008**, *130* (1), 183–189.
- (3) Ancheyta, J.; Rana, M. S. Future Technology in Heavy Oil Processing. <http://www.eolss.net/sample-chapters/c08/e6-185-22.pdf> (accessed Jul 25, 2015).
- (4) TransportPolicy <http://transportpolicy.net/> (accessed Jul 25, 2015).
- (5) Harding, M. *The Diesel Differential: Differences in the Tax Treatment of Gasoline and Diesel for Road Use*; OECD Taxation Working papers, 2014.
- (6) Jones, D. S. J.; Pujadó, P. R. *Handbook of Petroleum Processing*; Springer Verlag: Dordrecht, The Netherlands, 2008.
- (7) Ancheyta, J.; Speight, J. G. *Hydroprocessing of Heavy Oils and Residua*; Taylor & Francis Group, 2007.
- (8) Chorkendorff, I.; Niemantsverdriet, J. W. *Concepts of Modern Catalysis and Kinetics*; Wiley-VCH Verlag: Weinheim, 2003.
- (9) Speight, J. G.; Ozum, B. *Petroleum Refining Processes*; CRC Press, 2001.
- (10) Hydrocarbon Processing. 2008 Refining Processes Handbook. http://www.hydrocarbonprocessing.com/handbooks/refining_process_hb.pdf (accessed Jul 25, 2015).
- (11) Hrabar, A. Understanding hydrodenitrogenation on unsupported and supported sulfide based catalysts, Technische Universität München, 2011.
- (12) Girgis, M. J.; Gates, B. C. *Ind. Eng. Chem. Res.* **1991**, *30* (9), 2021–2058.
- (13) Tuxen, A. K.; Füchtbauer, H. G.; Temel, B.; Hinnemann, B.; Topsøe, H.; Knudsen, K. G.; Besenbacher, F.; Lauritsen, J. V. *J. Catal.* **2012**, *295*, 146–154.
- (14) Prins, R.; Egorova, M.; Rothlisberger, A.; Zhao, Y.; Sivasankar, N.; Kukula, P.; Röthlisberger, A.; Zhao, Y.; Sivasankar, N.; Kukula, P. *Catal. Today* **2006**, *111* (1-2), 84–93.
- (15) Prins, R.; Jian, M.; Flechsenhar, M. *Polyhedron* **1997**, *16* (18), 3235–3246.
- (16) Ancheyta, J.; Rana, M. S.; Furimsky, E. *Catal. Today* **2005**, *109* (1-4), 3–15.
- (17) Stanislaus, A.; Cooper, B. *Catal. Rev.* **1994**, *36* (1), 75–123.
- (18) Moses, P. G.; Mortensen, J. J.; Lundqvist, B. I.; Nørskov, J. K. *J. Chem. Phys.* **2009**, *130* (10), 104709.
- (19) Dion, M.; Rydberg, H.; Schröder, E.; Langreth, D. C.; Lundqvist, B. I. *Phys. Rev. Lett.* **2004**, *92* (24), 246401.
- (20) Thonhauser, T.; Cooper, V. R.; Li, S.; Puzder, A.; Hyldgaard, P.; Langreth, D. C. *Phys. Rev. B* **2007**, *76* (12), 125112.
- (21) Clar, E. *Polycyclic Hydrocarbons, Band I*; Academic Press: London-New York, 1964.
- (22) Beltramone, A. R.; Resasco, D. E.; Alvarez, W. E.; Choudhary, T. V. *Ind. Eng. Chem. Res.* **2008**, *47* (19), 7161–7166.

- (23) Ishihara, A.; Lee, J.; Dumeignil, F.; Takashi, M.; Qian, E. W.; Kabe, T. *Energy & Fuels* **2003**, *17* (5), 1338–1345.
- (24) Korre, S. C.; Klein, M. T.; Quann, R. J. *Ind. Eng. Chem. Res.* **1995**, *34* (1), 101–117.
- (25) Girgis, M. J.; Gates, B. C. *Ind. Eng. Chem. Res.* **1994**, *33* (12), 2301–2313.
- (26) Yang, H.; Wang, Y.; Jiang, H.; Weng, H.; Liu, F.; Li, M. *Ind. Eng. Chem. Res.* **2014**, *53* (31), 12264–12269.
- (27) Weber, T.; Prins, R.; van Santen, R. A. *Transition Metal Sulphides: Chemistry and Catalysis*; Springer Science & Business Medis, 2013.
- (28) Wyckoff, R. W. G. *Crystal Structures, Vol. 1*; Interscience: New York, 1963.
- (29) Louwers, S. P. A.; Prins, R. *J. Catal.* **1992**, *133* (1), 94–111.
- (30) Hollemann, A. F.; Wiberg, E. *Lehrbuch der Anorganischen Chemie*, 101st ed.; Walter de Gruyter: Berlin, 1995.
- (31) Kam, K. K.; Parkinson, B. A. *J Phys Chem* **1982**, *86* (4), 463–467.
- (32) Chianelli, R. R.; Berhault, G.; Torres, B. *Catal. Today* **2009**, *147* (3-4), 275–286.
- (33) Pecoraro, T. A.; Chianelli, R. R. *J. Catal.* **1981**, *67* (2), 430–445.
- (34) Pease, R. N.; Keighton, W. B. *J. Ind. Eng. Chem.* **1933**, *25*, 1012.
- (35) Chianelli, R. R.; Daage, M.; Ledoux, M. J. *Adv. Catal.* **1994**, *40*, 177–232.
- (36) Prins, R.; de Beer, V. H. J.; Somorjai, G. A. *Catal. Rev. Sci. Eng.* **1989**, *31* (1-2), 1–41.
- (37) Chianelli, R. R. *Oil Gas Sci. Technol. - Rev. l'IFP* **2006**, *61* (4), 503–513.
- (38) Bensch, W. Hydrotreating: Removal of Sulfur from Crude Oil Fractions with Sulfide Catalysts, In *Comprehensive Inorganic Chemistry II* (2nd Edition), edited by Reedijk J. and Poepelmeier K.; Elsevier, Amsterdam; 2013, 287–321.
- (39) Topsøe, H.; Clausen, B. S.; Candia, R.; Wivel, C.; Mørup, S. *J. Catal.* **1981**, *68* (2), 433–452.
- (40) Lauritsen, J. V.; Kibsgaard, J.; Olesen, G. H.; Moses, P. G.; Hinnemann, B.; Helveg, S.; Nørskov, J. K.; Clausen, B. S.; Topsøe, H.; Laegsgaard, E.; Besenbacher, F. *J. Catal.* **2007**, *249* (2), 220–233.
- (41) Lauritsen, J. V.; Helveg, S.; Lægsgaard, E.; Stensgaard, I.; Clausen, B. S.; Topsøe, H.; Besenbacher, F. *J. Catal.* **2001**, *197* (1), 1–5.
- (42) Deepak, F. L.; Esparza, R.; Borges, B.; Lopez-Lozano, X.; Jose-Yacaman, M. *ACS Catal.* **2011**, *1* (5), 537–543.
- (43) Byskov, L. S.; Hammer, B.; Nørskov, J. K.; Clausen, B. S.; Topsøe, H. *Catal. Letters* **1997**, *47*, 177–182.
- (44) Topsøe, H. *Appl. Catal. A Gen.* **2007**, *322*, 3–8.
- (45) Daage, M.; Chianelli, R. R. *J. Catal.* **1994**, *149*, 414–427.
- (46) Logadóttir, Á.; Moses, P. G.; Hinnemann, B.; Topsøe, N.-Y.; Knudsen, K. G.; Topsøe, H.; Nørskov, J. K. *Catal. Today* **2006**, *111* (1-2), 44–51.
- (47) Breyse, M.; Furimsky, E.; Kasztelan, S.; Lacroix, M.; Perot, G. *Catal. Rev.* **2002**, *44* (4), 651–735.

- (48) Thomas, C.; Vivier, L.; Lemberon, J. L.; Kasztelan, S.; Pérot, G. *J. Catal.* **1997**, *167*, 1–11.
- (49) Kogan, V. M.; Nikulshin, P. a. *Catal. Today* **2010**, *149* (1-2), 224–231.
- (50) Hensen, E. J. M.; Lardinois, G. M. H. J.; de Beer, V. H. J.; van Veen, J. A. R. V; van Santen, R. A. *J. Catal.* **1999**, *187*, 95–108.
- (51) Prodhomme, P.-Y.; Raybaud, P.; Toulhoat, H. *J. Catal.* **2011**, *280* (2), 178–195.
- (52) Moses, P. G.; Hinnemann, B.; Topsøe, H.; Nørskov, J. K. *J. Catal.* **2007**, *248* (2), 188–203.
- (53) Topsøe, N.-Y.; Topsøe, H. *J. Catal.* **1993**, *139*, 641–651.
- (54) Byskov, L. S.; Bollinger, M.; Nørskov, J. K.; Clausen, B. S.; Topsøe, H. *J. Mol. Catal. A* **2000**, *163*, 117–122.
- (55) Topsøe, N.-Y. *Catal. Today* **2006**, *113* (1-2), 58–64.
- (56) Topsoe, N. *J. Catal.* **1980**, *64* (1), 235–237.
- (57) Maugé, F.; Lamotte, J.; Nesterenko, N. S.; Manoilova, O.; Tsyganenko, A. A. *Catal. Today* **2001**, *70* (1-3), 271–284.
- (58) Oliviero, L.; Mariey, L.; Lélías, M. A.; Aiello, S.; Gestel, J.; Maugé, F. *Catal. Letters* **2010**, *135* (1-2), 62–67.
- (59) Zhao, Z.; Diemant, T.; Häring, T.; Rauscher, H.; Behm, R. *J. Rev. Sci. Instrum.* **2005**, *76* (12), 123903.
- (60) Schneider, M. S.; Grunwaldt, J.-D.; Bürgi, T.; Baiker, A. *Rev. Sci. Instrum.* **2003**, *74* (9), 4121.
- (61) Joly, J. F.; Zanier-Szydłowski, N.; Colin, S.; Raatz, F.; Saussey, J.; Lavalley, J. C. *Catal. Today* **1991**, *9* (1-2), 31–38.
- (62) Travert, A.; Maugé, F. *Stud. Surf. Sci. Catal.* **1999**, *127*, 269–277.
- (63) Dugulan, A. I.; Hensen, E. J. M.; van Veen, J. A. R. *Catal. Today* **2008**, *130* (1), 126–134.
- (64) Hensen, E. J. M.; van der Meer, Y.; van Veen, J. A. R.; Niemantsverdriet, J. W. *Appl. Catal. A Gen.* **2007**, *322*, 16–32.
- (65) Topsøe, N.-Y.; Topsøe, H. *J. Catal.* **1993**, *139*, 631–640.
- (66) Gutiérrez, O. Y.; Singh, S.; Schachtl, E.; Kim, J.; Kondratieva, E.; Hein, J.; Lercher, J. A. *ACS Catal.* **2014**, *4* (5), 1487–1499.
- (67) Travert, A.; Dujardin, C.; Maugé, F.; Veilly, E.; Cristol, S.; Paul, J.-F.; Payen, E. *J. Phys. Chem. B* **2006**, *110* (3), 1261–1270.
- (68) Bandyopadhyay, S.; Massoth, F. E.; Pons, S.; Eyring, E. M. *J. Phys. Chem.* **1985**, *89* (12), 2560–2564.
- (69) Topsøe, N.-Y.; Topsøe, H.; Massoth, F. E. *J. Catal.* **1989**, *119* (1), 252–255.
- (70) Rappoport, Z. *CRC Handbook of Tables for Organic Compound Identification*, third.; CRC Press: Boca Raton, Florida, 1984.
- (71) Petit, C.; Maugé, F.; Lavalley, J.-C. *Stud. Surf. Sci. Catal.* **1997**, *106*, 157–166.
- (72) Breyse, M.; Berhault, G.; Kasztelan, S.; Lacroix, M.; Maugé, F.; Perot, G. *Catal. Today* **2001**, *66* (1), 15–22.

Chapter 2

Understanding Ni promotion of MoS₂/γ-Al₂O₃ and its implications for the hydrogenation of phenanthrene

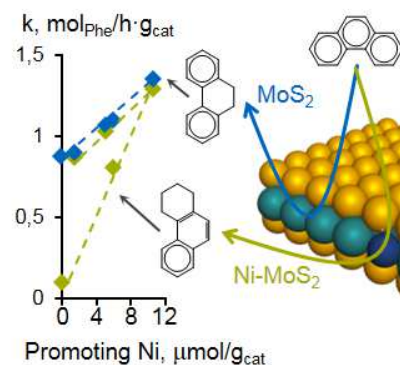
This chapter is based on:

E. Schachtl, E. Kondratieva, L. Zhong, J. Hein, O. Y. Gutiérrez, A. Jentys, and J. A. Lercher
“Understanding Ni promotion of MoS₂/γ-Al₂O₃ and its implications for the hydrogenation of phenanthrene.” *ChemCatChem*, **2015**, 7 (24), pp 4118-4130.
DOI: 10.1002/cctc.201500706R1.

Reprinted with permission from Wiley, 2015.

Abstract

The chemical composition and structure of NiMo sulfides supported on γ-Al₂O₃ and its properties for hydrogenation of polyaromatic compounds was explored. The presence of Ni favors the formation of disperse octahedrally coordinated Mo in the oxide precursors and facilitates its reduction during sulfidation. This decreases the particle size of MoS₂ (transmission electron microscopy) and increases the concentration of active sites up to a Ni/(Mo+Ni) atomic ratio



of 0.33. At higher Ni loadings, the size of the MoS₂ did not decrease further, while the concentration of adsorption sites and accessible Ni atoms decreased. This is attributed to the formation of NiS_x clusters at the edges of MoS₂. Nickel interacts also with the support forming separated NiS_x clusters and is partially incorporated into the γ-Al₂O₃ forming a Ni-spinel. The hydrogenation of phenanthrene follows two pathways, adding one or two H₂ molecules leading to 9,10-dihydrophenanthrene and 1,2,3,4-tetrahydrophenanthrene as primary products. Only symmetric hydrogenation leading to 9,10-dihydrophenanthrene was observed on unpromoted MoS₂/γ-Al₂O₃. In contrast, symmetric and deep hydrogenation (leading to 9,10-dihydrophenanthrene and 1,2,3,4-tetrahydrophenanthrene, respectively) occur with similar selectivity on Ni-promoted MoS₂/γ-Al₂O₃. The rates of both pathways increase linearly with the concentration of Ni atoms in the catalyst. The higher rates for symmetric hydrogenation is attributed to increasing concentrations of reactive species at the surface, while deep hydrogenation is concluded to be catalyzed by Ni at the edge of MoS₂ slabs.

2.1. Introduction

MoS₂- and WS₂-based materials are well-established catalysts in major industrial processes, ranging from coal liquefaction and the production of clean fuels in petroleum refineries (hydrotreating) to the synthesis of alcohols and thiols.¹⁻³ Addition of Ni or Co helps to increase the rate of hydrotreating reactions.⁴ In consequence, a wide body of information exists with respect to catalyst formulations and their catalytic properties. It has been established, for instance, that the maximum promoter effect is obtained at well-defined Ni or Co concentrations. Various structural models have been developed to explain this promotion on MoS₂/γ-Al₂O₃.⁵ The Co-Mo-S model⁶, nowadays widely accepted and adapted to Ni promotion, proposes substitution of individual Mo atoms by Co (or Ni) atoms at the edges of the MoS₂ slabs. Abundant evidence for this substitution has been provided by diverse methods, including STM⁷, STEM^{8,9}, DFT calculations¹⁰, IR spectroscopy^{11,12} and EXAFS studies.^{13,14} Despite this consensus, the nature of the interactions between active sites and reactant molecules is not fully understood qualitatively and quantitatively on an atomistic level. Thus, substantial efforts have been made towards this goal over the last years by imaging MoS₂-based systems, as well as by theoretical chemistry describing selected aspects of these catalytic materials, i.e., promoter effect, H₂-activation, desulfurization mechanisms¹⁵⁻¹⁷ and in developing synthesis procedures for well-controlled morphologies.^{18,19}

Most of the research described above has been stimulated by the mandate to reduce the sulfur levels in fuels.²⁰ Thus, the effects of promoters have been rationalized for hydrodesulfurization (HDS) by the presence of (Co)Ni-S-Mo sites with optimum metal-sulfur bond strength, which optimizes the rates of adsorption as well as of removal of sulfur.²¹⁻²⁵ Similar interpretations are

put forward for direct nitrogen removal in hydrodenitrogenation (HDN).^{26–28} Besides heteroatom removal, the catalysts enable hydrogenation, but the role of the promoter is not unequivocally elucidated.^{10,24} The conventional interpretation invokes adjacent vacancies as sites for adsorption of aromatic rings, but recent results indicate sites having metal-like character on the plane close to the edge of the sulfide particles.¹⁰

Most of the evidence for the Co-Mo-S model and recent advances on the understanding of sulfide catalysts has been obtained from model Co-promoted catalysts. This suggests that the nature of Ni promotion and its concomitant effect on hydrogenation must be explored in more detail. One of the questions that we address is related to the structural and local chemical impact of Ni on the MoS₂ structure. The second question addresses the correlation of the formation of the Ni-Mo-S phase with hydrogenation in the absence of defunctionalization pathways. Our target reaction, therefore, is the hydrogenation of polyaromatics.

To address these questions, we have synthesized a series of (Ni)MoS₂/γ-Al₂O₃ materials with varying Ni loading at a fixed Mo content. These materials were characterized by IR and X-ray spectroscopy and kinetically explored in the hydrogenation of phenanthrene as model compound for polyaromatic hydrocarbons. We provide models for the structure of the Ni-MoS₂ phase evolving with increasing concentrations of Ni and describe the consequences of different levels of promotion on the rates and depth of hydrogenation.

2.2. Experimental Section

2.2.1. Material Synthesis

The oxide catalyst precursors were prepared by incipient wetness impregnation of γ-Al₂O₃, provided by the Chevron Energy Technology Company. The support was treated in flowing synthetic air at 833 K for 2 h before impregnation. The two precursor salts, i.e., ammonium heptamolybdate ((NH₄)₆Mo₇O₂₄·4H₂O, Aldrich, ≥99.0%) and nickel nitrate (Ni(NO₃)₂·6H₂O, Aldrich, ≥98.5%) were deposited from aqueous solutions in two consecutive impregnation steps (first Mo and then Ni). After each impregnation step, the materials were dried at 393 K in static air and subsequently treated at 773 K in flowing synthetic air for 4 h. The nominal Mo content was kept constant (1 mmol Mo per gram of γ-Al₂O₃) in all prepared materials, while increasing the concentration of Ni in order to obtain NiMo materials with varying Ni/(Mo+Ni) ratios. Additionally, an oxide precursor containing 1 mmol of Ni per gram of γ-Al₂O₃ was prepared as reference material by impregnation with the Ni-salt and applying the described thermal treatments. Prior to activity tests and ex-situ characterization, the active, sulfide form of the catalysts was obtained by sulfidation of the oxide precursors in a plug flow reactor under a flow of 20 mL/min of 10 vol.-% H₂S in H₂ at 20 bar and 673 K for 8 h.

2.2.2. Catalyst characterization

N₂-physisorption isotherms were measured at liquid N₂ temperature using a Thermo Finnigan Sorptomatic 1990 series instrument. Prior to the measurements, the samples were outgassed at 523 K for 2 h. The texture of the oxide precursors including the specific surface area (BET analysis) and the specific pore volume (Gurvich analysis) were determined from the N₂ adsorption data. The elemental composition of the catalysts was determined by the Microanalytical Laboratory at TU München.

UV-Vis diffuse-reflectance (DR) spectra of the oxide materials were obtained in an Avantes Avaspec 2048 spectrometer. The samples were used as powders, placed in a PTFE sample holder and illuminated by UV light using an optical fiber (Avantes FCR-7UV400–2ME-HTX UV–Vis reflection probe) at room temperature. The UV–Vis DR spectra were collected with an integration time of 33 ms, and 30 scans were accumulated. All obtained spectra are presented in the supporting information in the form of the Kubelka–Munk function defined as $F(R) = (1-R)^2/(2R)$, where R is the reflectance of the sample.

The crystallinity of the oxide and sulfide materials was determined by powder X-ray diffraction (XRD) at a Phillips/PANalytical's X'Pert PRO system (Cu K_α radiation, 0.154056 nm) operating at 45 kV and 40 mA. The XRD patterns were recorded using a scan speed of 0.017 °/s. The samples were deposited on a silicon single crystal with a (111) surface for the analysis.

The transition of the oxides to the sulfide forms of the materials was studied by temperature programmed sulfidation (TPS). In a typical experiment, 0.1 g of the oxide catalyst precursor (250–355 μm) was placed in a quartz flow reactor inside a ceramic oven. The samples were treated for 2 h at 393 K in 10 mL/min He. Subsequently, the samples were sulfided in 10 mL/min of 2 vol.-% H₂S in H₂, heating with 5 K/min up to 673 K, where a final dwell time of 2 h was applied. The evolution and consumption of H₂, and H₂S was monitored by a mass spectrometer (Pfeiffer Vacuum QME 200) recording the signals of the masses (m/e) 2 (H₂) and 34 (H₂S).

The concentration of NO adsorbed on the sulfide materials at room temperature was determined by volumetric NO pulse experiments. The oxide precursors were sulfided *in situ* during a TPS experiment (vide supra) and, after cooling the reactor in sulfiding atmosphere to room temperature, purged thoroughly with He. Subsequently, pulses of 1.68 mL of 10 vol.-% NO in He were periodically introduced into the reactor until further NO uptake (followed by a mass spectrometer, m/e 30) was not observed. The concentration of NO adsorbed in a given pulse was determined as the integral difference between that NO signal and the NO signal at saturation. The total concentration of NO adsorbed was calculated as the sum of the NO uptake per pulse.

Transmission electron microscopy of the sulfide catalysts was performed in a JEOL JEM-2011 instrument using an acceleration voltage of 120 keV. Prior to the analysis, suspensions of the materials in ethanol were prepared and deposited on copper grids with supporting carbon films. The statistical analysis of the properties of the supported MoS₂ phase (length and stacking degree) was performed by measuring at least 300 slabs distributed in micrographs taken from different regions of the sample.

The adsorption of CO on the sulfide catalysts was followed by IR spectroscopy using a Nicolet 6700 FT-IR spectrometer equipped with a MCT detector using a resolution of 4 cm⁻¹. A dedicated flow/vacuum IR cell allowed the *in situ* sulfidation of the samples at high pressure and temperature (up to 20 bar and 673 K) and the subsequent adsorption of CO at ≤123 K in vacuum without any exposure of the sample to air. The samples were diluted with γ-Al₂O₃ (ratio 1:3) to improve the transmission of catalysts with high Ni content. The powders were pressed into self-supported wafers (10 mg/cm²), and placed inside the IR cell. Sulfidation was performed *in situ* at 673 K (heating rate 3 K/min) and 20 bar in 20 mL/min of 10 vol.-% H₂S in H₂. After sulfidation for two hours, the cell was flushed with He, evacuated to a residual pressure of 10⁻⁶ mbar and after 1 h cooled to 323 K. In order to perform the adsorption experiments, the IR cell was cooled with liquid nitrogen to 123 K in the presence of 3 mbar He. After taking a reference spectrum, the cell was evacuated and small doses of CO were admitted to the cell up to an equilibrium pressure of 1 mbar. The spectra reported here were background subtracted and were recorded in presence of 1 mbar CO and 2 mbar of He being present in the IR cell in order to reach a stable temperature. The intensities of the bands were quantitatively determined by deconvolution using the software GRAMS. Concentrations of adsorbed CO species were calculated using molar extinction coefficients reported in Refs.^{29,30}.

X-ray absorption spectroscopy (XAS) was employed on sulfide catalysts for a complete study of their structural properties. The data were recorded at two beamlines, the BM 26A - DUBBLE at ESRF (Grenoble, France), and the BL 22 – CLÆSS at ALBA (Barcelona, Spain). Prior to the experiments, samples of the catalysts were sulfided at 20 bar (vide supra), pressed into self-supporting wafers and re-sulfided *in situ* in the stainless-steel flow cell used for the XAS measurements. All spectra were recorded in transmission mode in flowing He, and at liquid N₂ temperature to minimize thermal vibrations. In the monochromator, a Si(311) crystal was used for the Mo K-edge (20000 eV) and a Si(111) crystal for the Ni K-edge (8333 eV). For energy calibration, Mo and Ni foils were measured simultaneously with each sample. Two spectra per sample were averaged in order to enhance the signal-to-noise ratio. The X-ray absorption near edge structure (XANES) and extended X-ray absorption fine structure (EXAFS) data was analyzed by using IFEFFIT together with the Demeter package (Athena and Artemis, version 0.9.20).³¹⁻³³ After removing the background absorption, the spectra were normalized to an average post-edge height of one. The XANES were analysed by linear combination fitting

(LCF) in the energy range of -20 eV to 50 eV relative to the absorption edge. For EXAFS analysis, the oscillations were weighted with k^3 and Fourier transformed (limits $k=3-12 \text{ \AA}$ for Ni-edge and $k=3-13 \text{ \AA}$ for Mo-edge). The local environment of Mo and Ni atoms was determined in k -space from the EXAFS. Single and multiple scattering contributions for Mo-S, Mo-Mo, Ni-S and Ni-Ni (phase shifts and backscattering amplitudes) were calculated with FEFF³³ based on crystallographic information files (cif) of the ICSD.³⁴ The amplitude reduction factor S_0^2 was determined from reference compounds and was for Mo 0.85 at ESRF and 0.98 at ALBA and 1.0 for Ni at both beamlines. For the Ni(x)MoS₂/γ-Al₂O₃ catalysts the Mo K-edge and Ni K-edge were fitted simultaneously in order to identify Mo-Ni and Ni-Mo contributions. The distance R for Mo-Ni and Ni-Mo were constrained to be equal and the coordination numbers N were defined by the molar ratio of Mo and Ni in the catalysts ($N_{\text{Mo-Ni}} = n(\text{Ni})/n(\text{Mo}) \cdot N_{\text{Ni-Mo}}$).

2.2.3. Kinetic measurements

The kinetic measurements were carried out in a continuous trickle bed reactor with a glass-coated stainless steel tube ($\varnothing \frac{1}{4}$ inches). High-pressure mass flow controllers (Bronkhorst EL--FLOW) and a HPLC pump (Gilson 307, pump head 5SC) were used to introduce gas and liquid feeds, respectively. The oxide catalyst precursor (250-355 μm) was diluted 1:20 with SiC (63-90 μm) and positioned in the middle of the reactor tube by filling up with SiC of the same size. Prior to each experiment, the oxide precursors were sulfided *in situ* (vide supra). The hydrogenation reactions were performed as space time dependent experiments at 573 K and 6 MPa total pressure after 20 h time on stream (in order to reach steady state). Space-time was defined as m_{cat}/F where m_{cat} is the mass of the catalyst precursor (40 mg) and F is the molar flow of phenanthrene. The reactions were performed keeping a H₂ to hydrocarbon ratio of 300 Ndm³/dm³. The reactant solution had a concentration of 1 wt.-% of phenanthrene (Alfa Aesar, 98%) and 1000 ppm S (present as dimethyl disulfide, Aldrich $\geq 99.0\%$) in decalin (Merck, $\geq 99.0\%$) and 2 wt.-% tetradecane (Alfa Aesar, 99+%) as internal standard. The absence of transport artifacts or incomplete wetting was verified by performing experiments using different amounts of catalyst, varying flow rates, and changing the catalyst and SiC particle sizes. The reactions were monitored by periodically collecting samples using a multiport sampling valve. The liquid samples were analyzed off-line by gas chromatography with a Shimadzu GC-2010 gas chromatograph equipped with a 50 m HP-1 column and a flame ionization detector.

2.3. Results

2.3.1. Catalyst characterization

The materials containing only Mo or Ni were denoted as MoO₃/γ-Al₂O₃ and NiO/γ-Al₂O₃ in their oxide form and as MoS₂/γ-Al₂O₃ and NiS_x/γ-Al₂O₃ when sulfided. The bimetallic materials were denoted as Ni(x)MoO₃, or Ni(x)MoS₂ in the oxide and sulfide form, respectively, where x is the nominal weight percentage of Ni in the sample. An overview of the elemental composition and textural properties of the γ-Al₂O₃ support and the oxide catalyst precursors is given in Table 2-1. The Mo content was very similar among all Mo-containing samples and was slightly lower than the nominal one. The four different bimetallic Ni(x)MoO₃ samples had Ni concentrations close to the nominal ones, and the Ni/(Mo+Ni) molar fractions increased from 0.19 to 0.62. The Ni content of NiO/γ-Al₂O₃ was 1 mmol/g, i.e., identical to the Mo content in the other samples.

The specific surface area of the γ-Al₂O₃ support was 248 m²/g with a pore volume of 0.67 cm³/g. Impregnation with Mo decreased the specific surface area to 216 m²/g, which corresponded to the value expected considering the density increase. The pore volume, in contrast, decreased by almost 20%, suggesting effective deposition of the sulfides in the mesopores of γ-Al₂O₃. Further addition of Ni to the Mo-containing materials decreased the surface area and pore volume insignificantly. Thus, we conclude that deposition of Mo and Ni occurred inside the pores without substantial pore blocking.

Considering the surface area of the support and the metal loadings, the concentration of Mo in all materials was around 2.3 Mo atoms per nm² (2.4 Ni atoms per nm² in NiO/γ-Al₂O₃). The total metal surface density (Mo+Ni) increased from 2.3 in MoO₃/γ-Al₂O₃ to 2.8, 3.4, 4.2 and 5.8 metal atoms per nm² in Ni(1.5)MoO₃, Ni(3)MoO₃, Ni(6)MoO₃, and Ni(10)MoO₃, respectively. Thus, in all catalysts the metal content was below the value of a monolayer on alumina.³⁵

Table 2-1. Elemental composition and textural properties of the γ-Al₂O₃ support and all investigated catalysts.

Catalyst	Metal content, wt.-% (mmol/g)		Ni/(Mo+Ni) mol/mol	BET surface area, m ² /g	Pore volume, cm ³ /g
	Mo	Ni			
γ-Al ₂ O ₃	-	-	-	248	0.67
MoO ₃ /γ-Al ₂ O ₃	9.1 (0.95)	-	-	216	0.52
Ni(1.5)MoO ₃	8.8 (0.92)	1.3 (0.22)	0.19	207	0.54
Ni(3)MoO ₃	9.1 (0.95)	2.7 (0.46)	0.33	198	0.53
Ni(6)MoO ₃	8.5 (0.89)	5.0 (0.85)	0.49	194	0.50
Ni(10)MoO ₃	8.7 (0.91)	8.8 (1.50)	0.62	187	0.47
NiO/γ-Al ₂ O ₃	-	5.8 (0.97)	-	210	0.58

The profiles of the H_2 and H_2S consumption and evolution recorded during selected temperature programmed sulfidation (TPS) experiments are compiled in Figure 2-1 (all profiles are presented in Figure 2-S15 of the supporting information). Four main sections were distinguished in the H_2S profiles: (i) a small peak below 373 K ascribed to the desorption of H_2S physisorbed at lower temperatures, (ii) a first region of H_2S consumption below 520-545 K, (iii) a sharp maximum of H_2S evolution with a temperature characteristic for the material, and (iv) a second consumption region.

The processes occurring in each of these steps are analyzed in accordance with an earlier report.^{37,38} During the low temperature H_2S consumption, section (ii), O is gradually exchanged by S at Mo^{6+} producing H_2O . The following section (iii) is characterized by a rapid H_2S evolution accompanying H_2 consumption and corresponds to the reduction of Mo^{6+} to Mo^{4+} coupled with formation of H_2S (reduction temperature T_{red}). In section (iv) the rest of O is exchanged for S.

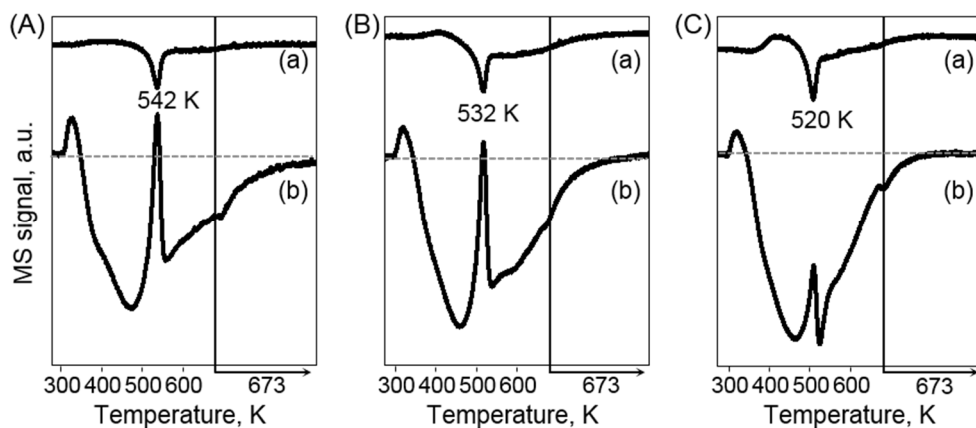


Figure 2-1. Profiles of H_2 (a) and H_2S (b) for the temperature programmed sulfidation of (A) $\text{MoO}_3/\gamma\text{-Al}_2\text{O}_3$, (B) $\text{Ni}(3)\text{MoO}_3$ and (C) $\text{Ni}(10)\text{MoO}_3$.

While the H_2S and H_2 consumption and evolution were similar, increasing concentrations of Ni reduced the reduction temperature (see Figure 2-2) and accelerated the H_2S consumption after the reduction was complete. Both observations suggest an easier reduction of Mo with increasing Ni loading. The TPS profile of reference $\text{NiO}/\gamma\text{-Al}_2\text{O}_3$ (see supporting information) exhibited a strong H_2S consumption signal at around 500 K. The total H_2S consumption of $\text{Ni}(x)\text{MoS}_2$ increased with the content of Ni in line with the higher overall metal loading. Further characterization of the oxide precursors is given in the supporting information. Results corresponding to sulfide materials are described in the following.

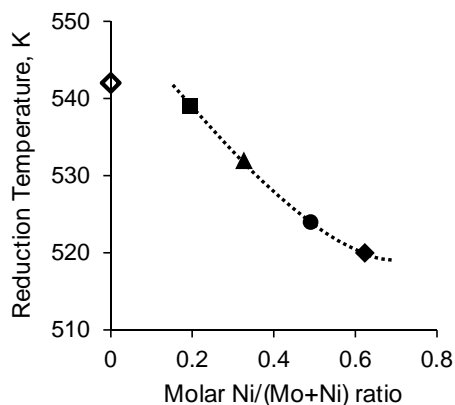


Figure 2-2. Reduction temperature T_{red} determined by temperature programmed sulfidation of $\text{MoO}_3/\gamma\text{-Al}_2\text{O}_3$ (\diamond), $\text{Ni}(1.5)\text{MoO}_3$ (\blacksquare), $\text{Ni}(3)\text{MoO}_3$ (\blacktriangle), $\text{Ni}(6)\text{MoO}_3$ (\bullet) and $\text{Ni}(10)\text{MoO}_3$ (\blacklozenge).

X-ray diffractograms of the sulfide catalysts are depicted in Figure 2-3. All samples showed the diffraction peaks characteristic for MoS_2 at 33 and 59 $^\circ 2\theta$. The absence of a peak at 14 $^\circ 2\theta$ corresponding to the (002) plane of MoS_2 with interplanar distance of 6.1 \AA indicated that stacking of MoS_2 was not significant.³⁶ The reflections at 36 and 66 $^\circ 2\theta$ appearing in some diffractograms (Figure 2-3a and 3e) result from the incomplete removal of SiC used for dilution in the sulfidation procedure.

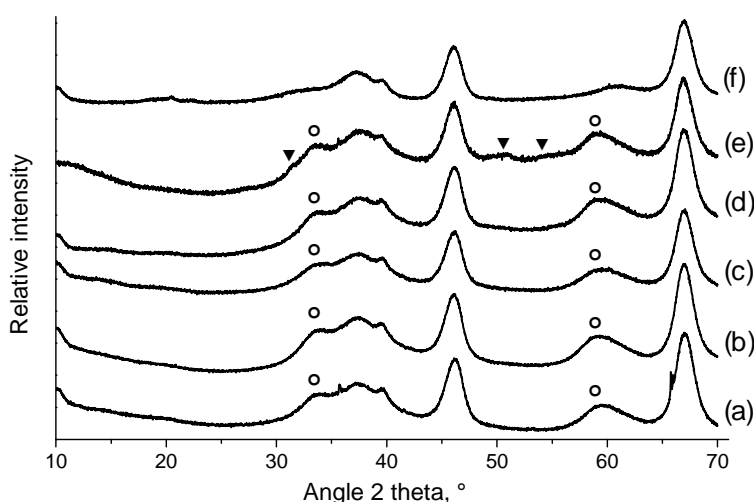


Figure 2-3. X-ray diffractograms of the sulfide catalysts. (a) $\text{MoS}_2/\gamma\text{-Al}_2\text{O}_3$, (b) $\text{Ni}(1.5)\text{MoS}_2$, (c) $\text{Ni}(3)\text{MoS}_2$, (d) $\text{Ni}(6)\text{MoS}_2$, (e) $\text{Ni}(10)\text{MoS}_2$, (f) $\text{NiS}_x/\gamma\text{-Al}_2\text{O}_3$. The marked reflections correspond to MoS_2 (\circ) and Ni_3S_2 (\blacktriangledown). Not marked reflections are assigned to the $\gamma\text{-Al}_2\text{O}_3$ support.

The sulfided $\text{NiO}/\gamma\text{-Al}_2\text{O}_3$ sample did not exhibit any reflection that can be assigned to a crystalline Ni sulfide phase, therefore we name them $\text{NiS}_x/\gamma\text{-Al}_2\text{O}_3$. Specifying the Ni and S stoichiometry implies that the corresponding phase has been identified by XRD (e.g., Ni_3S_2). Note that the value of x is between 0.7 and 1.3 as the Ni phases found in Ni-Mo sulfide catalysts are typically Ni_3S_2 , Ni_9S_8 , or Ni_3S_4 .²⁶ Reflections ascribed to Ni_3S_2 (22, 32, 50, 55 $^\circ 2\theta$, supporting information) appeared only for $\text{Ni}(10)\text{MoS}_2$.

Typical fringes of MoS₂ were observed in the transmission electron microscopy micrographs of all Mo-containing sulfide catalysts.³⁹ Most of the particles consist of 1 or 2 MoS₂ layers with a length range of 2-8 nm. Due to the flexible structure of MoS₂, the crystals bend (i.e., the slabs are not straight along the x and y axes) when the slabs grow longer in the x and y directions than in the z direction. However, significant differences of the degree of bending (other than those related to the length) were not observed among the MoS₂ particles on the different catalysts. Representative micrographs as well as distributions of slab length and stacking, resulting from the statistical analysis, are shown in Figure 2-S17 and 2-S18 of the supporting information. Table 2-2 presents the average slab length and stacking degree of the supported MoS₂ phase on all catalysts. The average length of the MoS₂ slabs decreased upon the addition of Ni from 5.5 nm for MoS₂/γ-Al₂O₃ to 4.7 nm for Ni(1.5)MoS₂. At the same time, the distribution of the slab length became narrower in presence of Ni, giving rise to a lower standard deviation (graphical display in the supporting information Figure 2-S18). Interestingly, increasing of the Ni/(Mo+Ni) ratio did not have a significant effect on the average slab length. The stacking degree, on the other hand, increased slightly with increasing Ni loading from 1.5 to 1.9 (MoS₂/γ-Al₂O₃ and Ni(3)MoS₂, respectively) and remained constant at higher loadings.

Table 2-2. Average slab length, stacking degree and dispersion f_{Mo} of the supported MoS₂ phase determined by statistical analysis of TEM micrographs (standard deviation given in brackets). NO adsorption measured by pulse experiments at room temperature.

Catalyst	Slab length, nm	Stacking degree	f_{Mo}	NO, μmol/g
MoS ₂ /γ-Al ₂ O ₃	5.5 (2.2)	1.5 (0.7)	0.22	151
Ni(1.5)MoS ₂	4.7 (1.9)	1.6 (0.8)	0.26	231
Ni(3)MoS ₂	4.5 (1.9)	1.9 (0.9)	0.26	298
Ni(6)MoS ₂	4.5 (1.9)	1.7 (0.9)	0.26	314
Ni(10)MoS ₂	4.6 (1.9)	1.8 (1.1)	0.26	407

Using the structural information obtained from the analysis of the TEM micrographs, we determined the fraction of Mo atoms at the edges of the sulfide slab, f_{Mo} , assuming a perfect hexagonal geometry for the MoS₂ crystals.^{40,41} Recent investigations suggest that the morphology of MoS₂ might deviate from a perfect hexagonal one.^{10,42} However, the assumption of hexagonal shape allows to determine the dispersion using the thermodynamically most stable structure of MoS₂ as a model. The f_{Mo} value reflects the dispersion of MoS₂ and, concomitantly, is a semi-quantitative measure of the active sites. The f_{Mo} values for all catalysts are reported in Table 2-2. The presence of Ni in MoS₂ slightly increased f_{Mo} from 0.22 to 0.26. The concentration of NO adsorbed on the sulfide catalysts at room temperature is compiled in Table 2-2. The reference NiS_x/γ-Al₂O₃ material adsorbed 351 μmol of NO per gram of material. Comparing MoS₂/γ-Al₂O₃ and Ni(1.5)MoS₂, it was evident that the addition of small concentrations of Ni (1.5 wt.-%) had a dramatic impact on the adsorption capacity of MoS₂,

increasing the uptake of NO by 50%, in agreement with literature.⁴³⁻⁴⁶ Further Ni addition steadily increased the NO uptake of the samples.

The concentration of adsorbed NO reflects the concentration of coordinatively unsaturated sites (CUS) in the MoS_2 phase.^{22,46-49} However, the $\text{NiS}_x/\gamma\text{-Al}_2\text{O}_3$ reference material also adsorbed a significant amount of NO. Thus, the concentration of adsorbed NO on $\text{Ni}(x)\text{MoS}_2$ requires some caution in interpretation, as increasing concentrations of NiS_x were observed with increasing Ni loading. In order to account for the effect of increasing concentrations of NiS_x species, the overall NO uptake was normalized per mol of metal in the samples. Figure 2-4 shows the dependence of the normalized concentration of adsorbed NO on the $\text{Ni}/(\text{Mo}+\text{Ni})$ fraction.

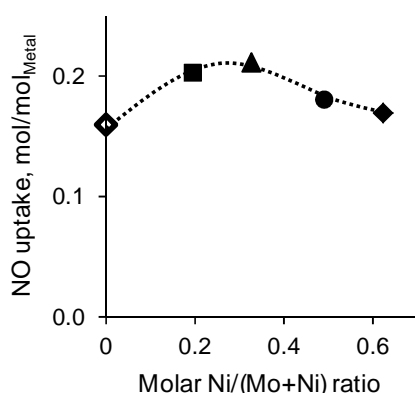


Figure 2-4. Concentration of NO adsorbed on the catalysts normalized to the metal content of each sample. $\text{MoS}_2/\gamma\text{-Al}_2\text{O}_3$ (\diamond), $\text{Ni}(1.5)\text{MoS}_2$ (\blacksquare), $\text{Ni}(3)\text{MoS}_2$ (\blacktriangle), $\text{Ni}(6)\text{MoS}_2$ (\bullet) and $\text{Ni}(10)\text{MoS}_2$ (\blacklozenge).

The NO uptake increased with the Ni content, peaking at 3 wt.-% Ni. This indicated that Ni promotion increased the concentration of CUS on the catalysts up to certain Ni content. The decrease in the concentration of adsorbed NO at higher loadings (instead of leveling off as expected from the small changes in dispersion observed by TEM) is attributed to the formation of large NiS_x particles, which reduce the fraction of surface available to adsorb NO per gram of catalyst. Therefore, NO adsorption can be considered as a method to probe the adsorption sites (concomitantly dispersion) of all phases present in the catalysts (e.g., Ni-MoS_2 and on NiS_x), not all of them catalytically active for hydrogenation.

The IR spectra of CO adsorbed on $\gamma\text{-Al}_2\text{O}_3$, $\text{MoS}_2/\gamma\text{-Al}_2\text{O}_3$ and $\text{NiS}_x/\gamma\text{-Al}_2\text{O}_3$ are shown in Figure 2-S19 of the supporting information. For alumina, two bands appeared at 2192 and 2156 cm^{-1} corresponding to CO adsorbed on Lewis ($\nu(\text{CO}/\text{Al}^{3+})$) and Brønsted acid sites ($\nu(\text{CO}/\text{OH})$), respectively.⁵⁰ The intensity of these bands decreased in the spectra of $\text{MoS}_2/\gamma\text{-Al}_2\text{O}_3$ and $\text{NiS}_x/\gamma\text{-Al}_2\text{O}_3$, most likely due to sulfide phases covering these sites on alumina. Regarding CO adsorbed on the sulfide phase, for $\text{MoS}_2/\gamma\text{-Al}_2\text{O}_3$ (Figure 2-S19 or Figure 2-5a) two bands, at 2106 (high intensity) and 2094 cm^{-1} (appearing as a shoulder) were observed. The former corresponded to CO adsorbed on Mo located at the edge of MoS_2

terminated by metal cations and the latter was attributed to CO adsorbed on Mo at the sulfur edge of MoS_2 .⁵⁰ Both were identified as active sites for hydrodesulfurization.^{51,52} In addition to the bands of CO adsorbed on the support, the spectra of $\text{NiS}_x/\gamma\text{-Al}_2\text{O}_3$ (Figure 2-S19 and Figure 2-5f) exhibited an intense asymmetric band at 2080 cm^{-1} with shoulders at 2056 and 2025 cm^{-1} . The main band (2080 cm^{-1}) is attributed to CO adsorbed on NiS_x , the shoulders to polycarbonyl species $(\text{Ni}(\text{CO})_x)$.^{12,53,54}

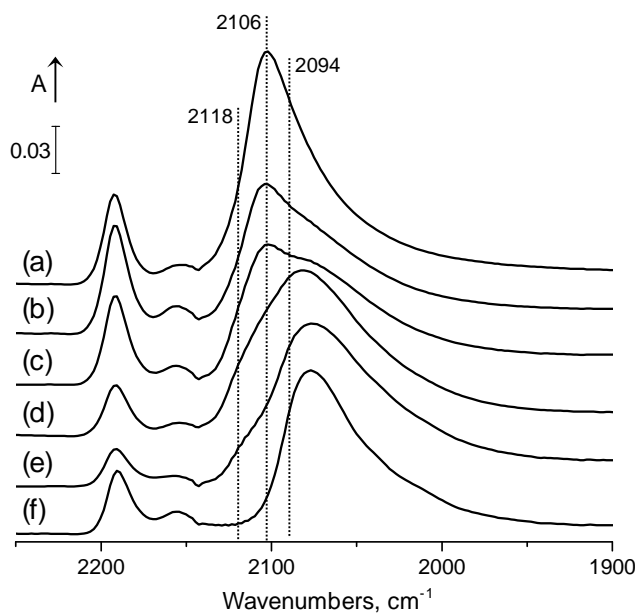


Figure 2-5. Spectra of CO adsorbed on $\text{Ni}(x)\text{MoS}_2/\gamma\text{-Al}_2\text{O}_3$. (a) $\text{MoS}_2/\gamma\text{-Al}_2\text{O}_3$, (b) $\text{Ni}(1.5)\text{MoS}_2$, (c) $\text{Ni}(3)\text{MoS}_2$, (d) $\text{Ni}(6)\text{MoS}_2$, (e) $\text{Ni}(10)\text{MoS}_2$, (f) $\text{NiS}_x/\gamma\text{-Al}_2\text{O}_3$.

The spectra of CO adsorbed on $\text{Ni}(x)\text{MoS}_2$ (Figure 2-5 b-e) were complex and cannot be understood by combinations of the spectra of the components (Figure 2-S19 or Figure 2-5 a/f). The spectra of $\text{Ni}(x)\text{MoS}_2$ had a complex group of bands between 2140 and 1950 cm^{-1} . Based on separate spectroscopic and DFT studies¹², as well as considering the spectra of reference materials, adsorption of CO on five different sites has been hypothesized to contribute to these bands. The adsorbed species identified were (i) CO adsorbed on Ni atoms decorating MoS_2 (2118 cm^{-1}), (ii) CO adsorbed on not-promoted Mo at the M-edge of MoS_2 (2106 cm^{-1}), (iii) between $2080 - 2020\text{ cm}^{-1}$ a group of CO bands were concluded to be adsorbed on NiS_x species, on Mo at the S-edge of MoS_2 , and on promoted Mo sites. The spectra of $\text{Ni}(x)\text{MoS}_2$ (Figure 2-5) showed clearly, how the increasing concentration of Ni shifted the maximum of CO adsorption from 2106 cm^{-1} (not-promoted MoS_2) to 2080 cm^{-1} (NiS_x and promoted MoS_2). This indicated that the accessible surface of the catalysts at high Ni loading was dominated by NiS_x . To quantify this, the areas of bands were fitted by deconvolution and the results of the deconvolution are summarized in detail in the supporting information (Figure 2-S20 and Table 2-S7).

In Figure 2-6 the concentrations of CO calculated from the intensities of the bands at 2118 cm^{-1} (associated to CO on Ni atoms decorating MoS_2), and at 2106 cm^{-1} (assigned to not-promoted Mo at the M-edge of MoS_2) are shown. The bands in the $2080\text{-}2020\text{ cm}^{-1}$ region were not quantitatively analyzed due to strong overlapping of bands from different species.

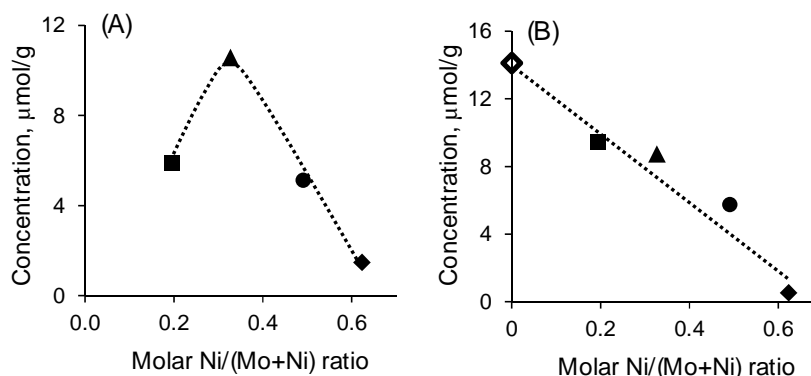


Figure 2-6. Relative concentrations of CO adsorbed on Ni atoms (A) and not-promoted Mo sites (B). $\text{MoS}_2/\gamma\text{-Al}_2\text{O}_3$ (\diamond), $\text{Ni}(1.5)\text{MoS}_2$ (\blacksquare), $\text{Ni}(3)\text{MoS}_2$ (\blacktriangle), $\text{Ni}(6)\text{MoS}_2$ (\bullet) and $\text{Ni}(10)\text{MoS}_2$ (\blacklozenge).

Figure 2-6 reveals that the concentration of CO on Ni atoms (2118 cm^{-1}) was the highest for $\text{Ni}(3)\text{MoS}_2$ indicating an optimum decoration of MoS_2 at a molar fraction of Ni of 0.33. The concentration of CO on not-promoted Mo (2106 cm^{-1}), however, decreased steadily with increasing Ni loading and reached values close to zero for $\text{Ni}(10)\text{MoS}_2$. This indicates that at $\text{Ni}/(\text{Mo}+\text{Ni})$ ratios above 0.33 both, the decoration of MoS_2 with Ni and the fraction of MoS_2 without contact to the Ni promoter decreased. These seemingly contradicting observations were related to changes in structure and diverse promotion mechanisms that were not related to Ni decoration (vide infra). Not surprisingly, the steady increase of the intensity of the bands at $2080\text{-}2020\text{ cm}^{-1}$ indicated that the concentration of CO adsorbed on promoted Mo and/or NiS_x species increased with increasing Ni loading.

The X-ray absorption near edge structure (XANES) and the Fourier transformed extended X-ray absorption fine structure (EXAFS) at the Mo K-edge are presented in Figure 2-7. The absorption edge energy and the local environment around Mo were almost identical between the sulfide catalyst samples and reference MoS_2 . According to the well-known 2H-MoS_2 structure, the first contribution at around 1.9 \AA (not phase corrected) belonged to Mo-S and the second at around 2.8 \AA (not phase corrected) to Mo-Mo distances.¹³ The Mo-Mo paths of the catalysts are less intense than those of bulk MoS_2 , because the reference material has a considerably larger crystal size and much less structural disorder (bending and low-coordinated Mo atoms) than the supported (Ni) MoS_2 particles. Thus, a large proportion of Mo atoms are positioned within well-defined bond distances and angles, which enhances the characteristic Mo-Mo scattering.

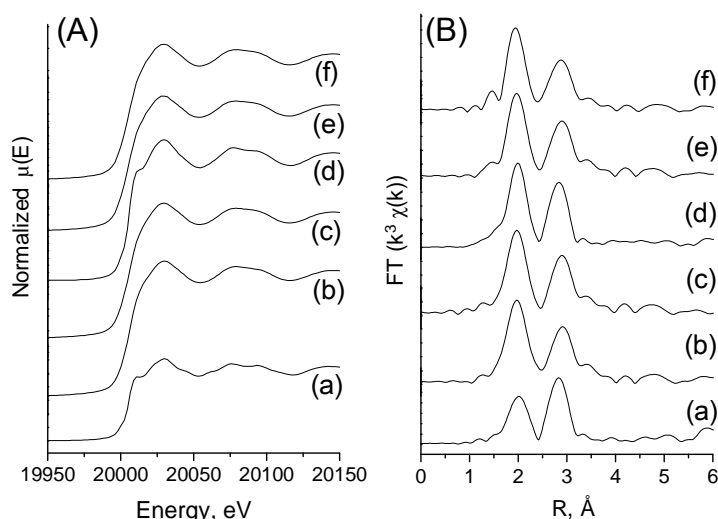


Figure 2-7. (A) Mo K-edge XANES and (B) FT of k^3 -weighted EXAFS of (a) reference MoS_2 , (b) $\text{MoS}_2/\gamma\text{-Al}_2\text{O}_3$, (c) $\text{Ni}(1.5)\text{MoS}_2$, (d) $\text{Ni}(3)\text{MoS}_2$, (e) $\text{Ni}(6)\text{MoS}_2$, (f) $\text{Ni}(10)\text{MoS}_2$.

Figure 2-8 depicts the XANES and EXAFS data at the Ni K-edge. The sample $\text{Ni}(1.5)\text{MoS}_2$ was omitted due to the inadequate quality of the spectra caused by the low concentration of Ni (see Figure 2-S21 in the supporting information). A small pre-edge at around 8333 eV was visible for Ni_3S_2 and the sulfide catalysts (shown in the inset of Figure 2-8), which is typical for tetrahedral or pentagonal coordinated Ni. The reference NiAl_2O_4 spinel displayed a quite sharp feature at the edge, which was observed to some extent also in $\text{NiS}_x/\gamma\text{-Al}_2\text{O}_3$ and in the $\text{Ni}(x)\text{MoS}_2$ materials with a lower intensity. This implied that a small fraction of Ni was always present as NiAl_2O_4 spinel, in line with the UV-Vis spectra (see supporting information).⁵⁵ The absorption edge energy and the local environment around Ni for the sulfide catalysts were similar to the Ni_3S_2 reference, in parallel to the results comparing the XRD of the present material and the sample with the highest Ni loading. The structure of Ni_3S_2 contains four tetrahedrally coordinated S atoms in the first shell at 2.3 Å, and four Ni atoms at 2.5 Å in a second coordination shell.³⁴ Due to the closeness of these contributions, one broad and intense backscatter signal appeared in EXAFS. The contributions observed for the sulfide catalysts had lower intensities and were shifted to shorter distances. Moreover, the Ni-Ni contribution of Ni_3S_2 at 3.7 Å (not phase corrected) was absent.

Linear combination fitting (LCF) was performed to obtain information on the chemical environment of the metal species in the catalysts, which is required during the EXAFS fitting. This analysis, shown in the supporting information, revealed a mixture of phases in the catalysts. Thus, the XANES was modeled with small fractions of oxide species and a new, bimetallic phase in addition to the sulfide phases MoS_2 or Ni_3S_2 . The unknown phase has been identified as the Ni-Mo-S phase with neighboring Mo and Ni atoms, which also contributed to the XANES of the sulfide catalysts.²⁶

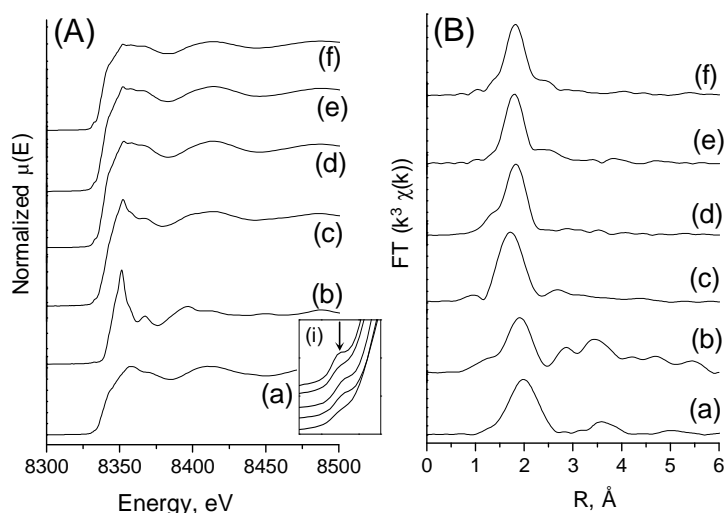


Figure 2-8. (A) Ni K-edge XANES and (B) FT of k^3 -weighted EXAFS of (a) reference Ni₃S₂, (b) reference NiAl₂O₄, (c) NiS_x/γ-Al₂O₃, (d) Ni(3)MoS₂, (e) Ni(6)MoS₂, (f) Ni(10)MoS₂. Inset (i) displays the pre-edge found for materials (a) and (c-f).

Therefore, Mo-Ni and Ni-Mo scattering contributions were included in the multi-edge fitting of the EXAFS data. Ni₃S₂ was described by four different contributions, whereas for the sulfide catalysts only one Ni-S path at ~2.3 Å and one Ni-Ni path at ~2.6 Å were distinguishable.²⁶ Moreover, a Ni O path at ~2.0 Å and a Ni-Ni path at ~3.1 Å were introduced to account for Ni-O interactions. The best-fit results for the k^3 -weighted EXAFS data at the Mo K-edge and the Ni K-edge are presented in Table 2-3 and Table 2-4, respectively. The corresponding fitted EXAFS spectra are depicted in the supporting information.

Table 2-3. Best-fit results for k^3 -weighted EXAFS data of sulfided catalysts at the Mo K-edge in k -space. N : coordination number; R : distance; σ^2 : Debye-Waller factor; E_0 : inner potential.

Catalyst	Path	N	R , Å	σ^2 , Å ²
MoS ₂ /γ-Al ₂ O ₃ ($R=0.019$) ($E_0=2.2\pm 1.0$)	Mo-S	4.8 ± 0.2	2.41 ± 0.01	0.0026 ± 0.0002
	Mo-Mo	3.9 ± 0.2	3.16 ± 0.01	0.0033 ± 0.0002
Ni(3)MoS ₂ ($R=0.038$) ($E_0=1.8\pm 1.1$)	Mo-S	6.0 ± 0.2	2.40 ± 0.01	0.0031 ± 0.0002
	Mo-Mo	4.8 ± 0.2	3.17 ± 0.01	0.0036 ± 0.0002
	Mo-Ni	0.2 ± 0.1	2.81 ± 0.05	0.0075 ± 0.0050
Ni(6)MoS ₂ ($R=0.01$) ($E_0=2.2\pm 1.4$)	Mo-S	5.5 ± 0.2	2.42 ± 0.01	0.0020 ± 0.0003
	Mo-Mo	4.4 ± 0.2	3.18 ± 0.01	0.0029 ± 0.0003
	Mo-Ni	0.2 ± 0.1	2.82 ± 0.06	0.0089 ± 0.0078
Ni(10)MoS ₂ ($R=0.01$) ($E_0=2.8\pm 1.5$)	Mo-S	5.4 ± 0.2	2.41 ± 0.01	0.0022 ± 0.0003
	Mo-Mo	4.3 ± 0.2	3.17 ± 0.01	0.0027 ± 0.0003
	Mo-Ni	0.2 ± 0.1	2.84 ± 0.06	0.0073 ± 0.0070

Table 2-4. Best-fit results for k³-weighted EXAFS data of sulfided catalysts at the Ni K-edge in k-space. *N*: coordination number; *R*: distance; σ^2 : Debye-Waller factor; *E*₀: inner potential.

Catalyst	Path	<i>N</i>	<i>R</i> , Å	σ^2 , Å ²
NiS _x /γ-Al ₂ O ₃ (<i>R</i> =0.030) (<i>E</i> ₀ =8.0±2.5)	Ni-S	1.6 ± 0.1	2.22 ± 0.02	0.0038 ± 0.0022
	Ni-Ni	1.0 ± 0.1	2.61 ± 0.02	0.0058 ± 0.0021
	Ni-O	4.4 ± 0.2	2.11 ± 0.02	0.0071 ± 0.0049
	Ni-Ni	0.7 ± 0.3	3.14 ± 0.04	0.0054 ± 0.0030
Ni(3)MoS ₂ (<i>R</i> =0.007) (<i>E</i> ₀ =1.0±2.9)	Ni-S	2.4 ± 0.1	2.21 ± 0.02	0.0042 ± 0.0005
	Ni-Ni	1.5 ± 0.2	2.58 ± 0.04	0.0067 ± 0.0046
	Ni-O	1.0 ± 0.2	2.00 ± 0.04	0.0079 ± 0.0052
	Ni-Ni	0.6 ± 0.1	3.07 ± 0.04	0.0070 ± 0.0028
Ni(6)MoS ₂ (<i>R</i> =0.031) (<i>E</i> ₀ =2.7±2.3)	Ni-S	2.7 ± 0.4	2.27 ± 0.02	0.0091 ± 0.0011
	Ni-Ni	0.3 ± 0.2	2.61 ± 0.02	0.0072 ± 0.0029
	Ni-O	1.6 ± 0.3	2.06 ± 0.01	0.0021 ± 0.0008
	Ni-Ni	0.5 ± 0.3	3.07 ± 0.07	0.0059 ± 0.0023
Ni(10)MoS ₂ (<i>R</i> =0.016) (<i>E</i> ₀ =9.1±1.3)	Ni-S	2.4 ± 0.2	2.28 ± 0.01	0.0091 ± 0.0011
	Ni-Ni	0.6 ± 0.1	2.57 ± 0.02	0.0072 ± 0.0021
	Ni-O	1.5 ± 0.1	2.08 ± 0.01	0.0021 ± 0.0008
	Ni-Ni	0.5 ± 0.2	3.14 ± 0.02	0.0056 ± 0.0023
	Ni-Mo	0.4 ± 0.2	2.84 ± 0.02	0.0078 ± 0.0021

The average coordination numbers $N_{\text{Mo-S}}=4.8$ and $N_{\text{Mo-Mo}}=3.9$ were found for MoS₂/γ-Al₂O₃, which are low compared to reference MoS₂ with $N_{\text{Mo-S}}=5.8$ and $N_{\text{Mo-Mo}}=6.0$ (see Table 2-S10 in the supporting information). The addition of Ni led to an increase of the coordination numbers of Mo. A maximum was observed for Ni(3)MoS₂ with $N_{\text{Mo-S}}=6.0$ and $N_{\text{Mo-Mo}}=4.8$. For all Ni containing catalysts a Mo-Ni contribution was found with $N_{\text{Mo-Ni}}=0.2$ at ~2.8 Å.

The first coordination shell of Ni in the sulfide catalysts consisted of oxygen, e.g., $N_{\text{Ni-O}}=1.0$ for Ni(3)MoS₂, and $N_{\text{Ni-O}}=4.4$ for NiS_x/γ-Al₂O₃. The Ni-Ni path corresponding to NiAl₂O₄ spinel was found as 0.6 ($N_{\text{Ni-Ni}}$) for Ni(3)MoS₂.²⁶ The second coordination shell of Ni consisted of S atoms at ~2.25 Å, which were attributed to Ni₃S₂. The $N_{\text{Ni-S}}$ for Ni(*x*)MoS₂ is between 2.4-2.7. The Ni-Ni distance of Ni₃S₂ followed in the third coordination shell at ~2.6 Å with coordination numbers ranging from 0.3 to 1.5. Hence, the coordination numbers for Ni-S and Ni-Ni are remarkably low for the sulfide catalyst materials compared to reference Ni₃S₂ ($N_{\text{Ni-S}}=N_{\text{Ni-Ni}}=4$, see Table 2-S10 in the supporting information). A Ni-Mo contribution was found for all Ni(*x*)MoS₂ catalysts at ~2.8 Å, being 0.3 for Ni(3)MoS₂ and Ni(6)MoS₂ and 0.4 for Ni(10)MoS₂.

2.3.2. Hydrogenation of Phenanthrene

The hydrogenation activity of series of (Ni)MoS₂ catalysts was evaluated through the conversion of phenanthrene as model compound with three condensed aromatic rings. The conversion of phenanthrene on all sulfide catalysts as function of space-time is presented in Figure 2-S25 of the supporting information (points represent experimental values, lines display the fitting model described below). The addition of Ni significantly increased the rate of phenanthrene hydrogenation (Table 2-5). For instance, at low conversions the rate of phenanthrene hydrogenation reached $0.58 \cdot 10^{-3} \text{ mol}_{\text{Phe}}/\text{h} \cdot \text{g}_{\text{cat}}$ on MoS₂/γ-Al₂O₃, and about twice that value on Ni(1.5)MoS₂ ($1.13 \cdot 10^{-3} \text{ mol}_{\text{Phe}}/\text{h} \cdot \text{g}_{\text{cat}}$). The most active catalyst was Ni(3)MoS₂ leading to a reaction rate of $1.54 \cdot 10^{-3} \text{ mol}_{\text{Phe}}/\text{h} \cdot \text{g}_{\text{cat}}$. Increasing further the concentration of Ni decreased the rates to $1.26 \cdot 10^{-3} \text{ mol}_{\text{Phe}}/\text{h} \cdot \text{g}_{\text{cat}}$ and $1.08 \cdot 10^{-3} \text{ mol}_{\text{Phe}}/\text{h} \cdot \text{g}_{\text{cat}}$ on Ni(6)MoS₂ and Ni(10)MoS₂, respectively. It is important to mention that NiS_x/γ-Al₂O₃ did not show any activity for phenanthrene hydrogenation at the applied reaction conditions.

Under the present experimental conditions, only hydrogenation was observed, ring opening and hydrogenolysis were not detected. The products observed during the activity tests were 9,10-dihydrophenanthrene (DiHPhe), 1,2,3,4-tetrahydrophenanthrene (TetHPhe), 1,2,3,4,5,6,7,8-octahydrophenanthrene (*sym*OHPhe) and 1,2,3,4,4a,9,10,10a-octahydrophenanthrene (*asym*OHPhe). The fully hydrogenated product, perhydro-phenanthrene, was not observed. In turn, the formation rates and hydrogenation depth of the products dramatically depended on the presence of Ni. In Figure 2-S26 of the supporting information, the yields on MoS₂/γ-Al₂O₃ and Ni(x)MoS₂ are shown. In the case of MoS₂/γ-Al₂O₃ only two products appeared, i.e., DiHPhe and TetHPhe. On Ni(x)MoS₂ the deeper hydrogenated products, *sym*OHPhe and *asym*OHPhe, were also produced.

In order to develop the reaction network, the experimental data was analyzed using the delplot technique.⁵⁶ The product yield and selectivity observed on MoS₂/γ-Al₂O₃, Ni(1.5)MoS₂ and Ni(6)MoS₂ are presented as function of phenanthrene conversion in Figure 2-9. The dependence of yield and selectivity on conversion for Ni(3)MoS₂ and Ni(10)MoS₂ were almost identical to those for Ni(6)MoS₂ and, therefore, not shown. The yield-conversion plots in Figure 2-9 (A-C) and the selectivity-conversion plots in Figure 2-9 (D-F) show that DiHPhe and TetHPhe are primary products, in agreement with previous studies.^{57,58} On MoS₂/γ-Al₂O₃, the selectivity to DiHPhe and TetHPhe remained constant at 90 and 10%, respectively, in the studied range of conversion. On Ni(3)MoS₂, Ni(6)MoS₂, and Ni(10)MoS₂ the initial selectivity towards DiHPhe and TetHPhe was almost 50% (Figure 2-9 (F)). The product distribution of Ni(1.5)MoS₂ was in between those of MoS₂/γ-Al₂O₃ and the other Ni(x)MoS₂ catalysts. The products *sym*- and *asym*OHPhe (detected on Ni(x)MoS₂ catalysts) were regarded as secondary products based on the yield- and selectivity-conversion plots in Figure 2-9 (their initial selectivities equal zero at extrapolated zero conversion).

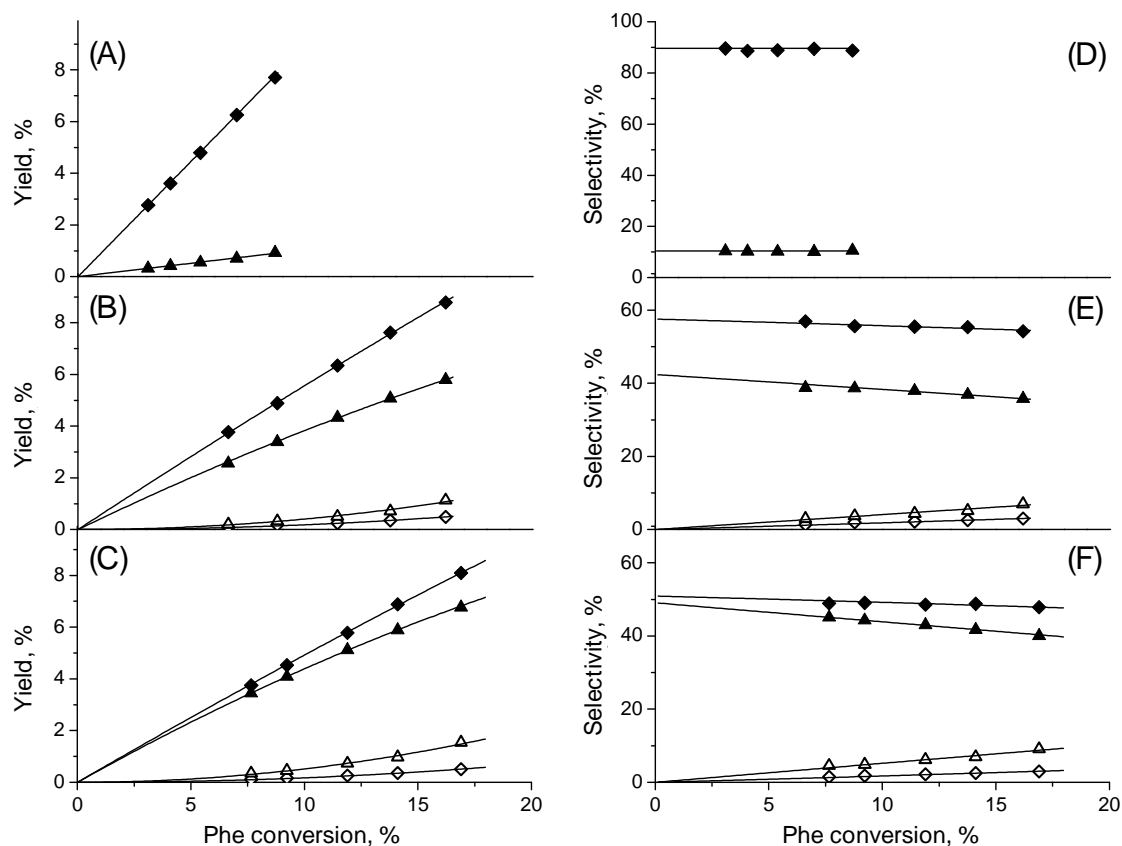


Figure 2-9. Yield and selectivity of the products of phenanthrene hydrogenation as a function of conversion. Yield: (A) MoS₂/γ-Al₂O₃, (B) Ni(1.5)MoS₂, (C) Ni(6)MoS₂. Selectivity: (D) MoS₂/γ-Al₂O₃, (E) Ni(1.5)MoS₂, (F) Ni(6)MoS₂. Phenanthrene hydrogenation products: DiHPhe (◆), TetHPhe (▲), *sym*OHPhe (Δ), *asym*OHPhe (◇)

To determine the origins of *sym*- and *asym*OHPhe, let us comment the selectivity-conversion plot of Ni(6)MoS₂ (Figure 2-S27 of the supporting information). The selectivity to DiHPhe and TetHPhe (primary products) decreased steadily with increasing phenanthrene conversion. Note that at, e.g., 17% of phenanthrene conversion, the decrease in the yield of DiHPhe (compared to the initial selectivity) was 3%, which perfectly corresponded to the increase in selectivity for *asym*OHPhe. On the other hand, the decrease of TetHPhe selectivity equaled the increase of *sym*OHPhe selectivity, the differences (compared to initial selectivities) being 9% each. These observations allowed concluding that phenanthrene was hydrogenated in two parallel reaction pathways. One, further referred to as “symmetric hydrogenation”, comprised consecutive hydrogenation to DiHPhe and *asym*OHPhe. The second pathway, “deep hydrogenation”, proceeded from phenanthrene to *sym*OHPhe *via* TetHPhe. Further hydrogenation was not observed, e.g., formation of perhydrophenanthrene, probably due to the low phenanthrene conversions accessed in this work. The low conversions also allowed neglecting reversible reactions, as the concentrations of the products were well below equilibrium compositions (supporting information). The reaction network corresponding to this description is shown in Figure 2-10.

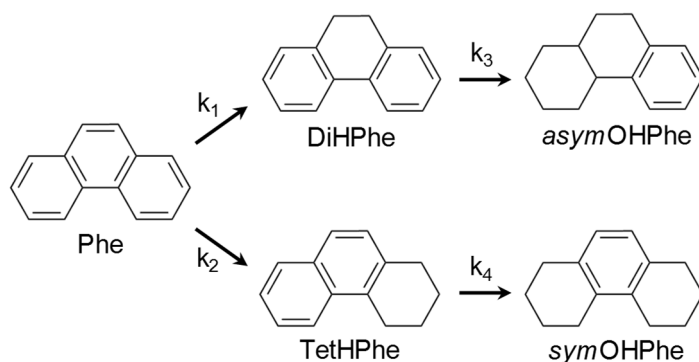


Figure 2-10. Reaction network for the hydrogenation of phenanthrene at the present reaction conditions. Phe: phenanthrene, DiHPhe: 9,10-dihydrophenanthrene, TetHPhe: 1,2,3,4-tetrahydrophenanthrene, *sym*OHPhe: 1,2,3,4,5,6,7,8-octahydrophenanthrene, *asym*OHPhe: 1,2,3,4,4a,9,10,10a-octahydrophenanthrene.

The apparent rate constants for each step of the reaction network were calculated assuming first order in the hydrocarbons and zero order in H₂ in all steps (the hydrogen was present in great excess).⁴ The network in Figure 2-10 was represented by the set of differential equations shown in the supporting information (3)-(7). The resulting rate constants are reported in Table 2-5. Over MoS₂/γ-Al₂O₃, the reaction toward DiHPhe (k_1) was considerably faster than that to TetHPhe (k_2), giving $k_1/k_2 = 8.6$. Upon addition of Ni, k_1 and k_2 increased. The former increased by 26%, 55%, 23% and 4% for Ni(1.5)MoS₂, Ni(3)MoS₂, Ni(6)MoS₂ and Ni(10)MoS₂, respectively. The increase of k_2 was much higher, i.e., 7, 12, 9 and 8 times for Ni(1.5)MoS₂, Ni(3)MoS₂, Ni(6)MoS₂ and Ni(10)MoS₂, respectively. This marked difference in the increase of k_2 led to the k_1/k_2 ratio of 1.4 for Ni(1.5)MoS₂ and 1.0 for the catalysts with higher Ni content. The effect of Ni addition on the formation of OHPhe (k_3 and k_4) was even more dramatic, as these products did not occur on MoS₂/γ-Al₂O₃.

Table 2-5. Reaction rate (r) and rate constants (k_i) determined for the hydrogenation of phenanthrene. The unit of r and k_i is mol_{Phe}/h·g_{cat}.

Catalyst	$r \cdot 10^3$	$k_1 \cdot 10^3$	$k_2 \cdot 10^3$	$k_3 \cdot 10^3$	$k_4 \cdot 10^3$	k_1/k_2
MoS ₂ /γ-Al ₂ O ₃	0.58	0.87	0.10	0	0	8.6
Ni(1.5)MoS ₂	1.13	1.10	0.81	1.14	3.63	1.4
Ni(3)MoS ₂	1.54	1.35	1.29	1.58	5.18	1.0
Ni(6)MoS ₂	1.26	1.07	1.03	1.35	4.42	1.0
Ni(10)MoS ₂	1.08	0.90	0.87	1.31	4.02	1.0

2.4. Discussion

2.4.1. State of Ni and its effect on the structure of MoS₂/γ-Al₂O₃

The chemical composition strongly influenced the physicochemical and catalytic properties of the mixed sulfides. The interactions between Ni and Mo were observed even in the oxide precursors. Ni disperses agglomerated MoO₃ species (in XRD reflections from MoO₃ are present in MoO₃/γ-Al₂O₃ but not in Ni(x)MoO₃/γ-Al₂O₃, see supporting information), and decreases its interaction with the support favoring the formation of O_h Mo species (UV-Vis spectroscopy).^{47,59} Weaker interactions with the support facilitated the reduction of Mo oxide as shown by the reduction at lower temperature during TPS. This suggests that proximity between Ni and Mo exists in the oxide precursors. This proximity is maintained in the sulfide form as all characterizations suggest.

The presence of Ni decreased the size of MoS₂ slabs (TEM), but slightly increased stacking. The concentration of Ni did not influence this effect. The fraction of Mo at the MoS₂-edges (f_{Mo}) followed this variation perfectly (Table 2-2). Thus the structural impact of Ni was confined to a slight reduction in size and an equally slight increase of the stacking degree. In contrast, the concentration of CUS increased linearly with increasing concentration of metals.

The IR spectra of adsorbed CO allowed to conclude that Ni decorated MoS₂ (Ni was incorporated at the edge of MoS₂ forming the so-called Ni-Mo-S phase), leading to a variety of adsorption sites, depending in concentration of Ni. The presence of Ni incorporated into the MoS₂ edge was further confirmed by the presence of Ni-Mo contributions in EXAFS. The distance and coordination number of this contribution was in good agreement to a model of direct substitution of Ni for Mo in the whole edge structure.^{14,26,55}

The concentration of incorporated Ni atoms reached a maximum at 3 wt.-% Ni, whereas the concentration of parent MoS₂ sites decreased with Ni concentration (see Figure 2-6). The quantitative variations did not complement each other, as one would expect that the concentrations of promoting Ni atoms and not-promoted Mo show opposite trends. Therefore, we conclude that further surface species must exist at high Ni loadings, and that at least a small fraction of the incorporated Ni atoms is negatively affected by high concentrations. The formation of this additional phase is concluded to begin already at relatively low concentrations of Ni because of the presence of a significant fraction of not-promoted Mo atoms. A simple mass balance points, therefore, to the existence of separate NiS_x clusters. The negative impact of this phase on the concentration of accessible Ni in the edge, suggests that at least a part of it grows from the edge of the MoS₂ crystals, not unlike early postulates by Delmon *et al.*⁶⁰ and van der Kraan *et al.*^{61,62} for Co-promoted catalysts. We hypothesize that Ni cations incorporated in the MoS₂ edge act as nucleation sites for NiS_x. This process would rapidly turn the Ni-decorated sites into NiS_x clusters, but would not hinder the promotion of nearby Mo

sites. Both, adsorption of CO and the EXAFS analysis confirm their presence. During the adsorption of CO, the intensity of the 2084 cm^{-1} band (carbonyls on NiS_x) strongly increased with the addition of Ni above 3 wt.-%. On the other hand, the rather low Ni-S and Ni-Ni coordination numbers in EXAFS analysis compared to reference Ni_3S_2 pointed to an important contribution of very small Ni_3S_2 particles.^{26,55} The coordination number $N_{\text{Ni-Ni}}$ decreased for high Ni concentrations. This was explained by the formation of NiS_x clusters with a broad distribution of particle sizes and Ni-Ni distances (many kinds of Ni sulfides are stable at the experimental conditions). It should also be emphasized at this point that an important fraction of Ni forms NiAl_2O_4 spinel (evidence from UV-Vis spectroscopy of the oxides and XAS measurements in the sulfide catalysts). Thus, Ni was present in three phases in the sulfided catalysts, i.e., Ni atoms incorporated into the edges of MoS_2 , NiS_x (segregated on the support or as small clusters at the MoS_2 edges) and NiAl_2O_4 spinel.

Visualizations constructed by Accelrys Material Studio 7.0 software (see Figure 2-11 and the supporting information) exemplify such a situation. The Ni-Mo-S phase in Ni(3)MoS_2 is considered to exhibit the highest proportion of decorating Ni atoms without full decoration or full replacement of Mo at the edges. The excess of Ni, which was not present in the spinel, formed mainly NiS_x clusters on the support. In the Ni(6)MoS_2 model, more Ni atoms were incorporated at the edges, which increased the concentration of Mo atoms adjacent to Ni. However, clusters of NiS_x species also formed at the edge, which reduced the net concentration of exposed Ni atoms. The Ni sulfide species not associated with the MoS_2 edges also grew in size and abundance. In the Ni(10)MoS_2 model, full decoration was virtually reached, as there was a minimum of Mo atoms exposed at the edges. However, it was far from an ideal decoration, as many of the decorating species were not single Ni atoms but NiS_x clusters. This drastically decreased the concentration of exposed Ni atoms. In addition, the concentration of Ni was so high that NiS_x species agglomerate to form crystalline species detectable by XRD.

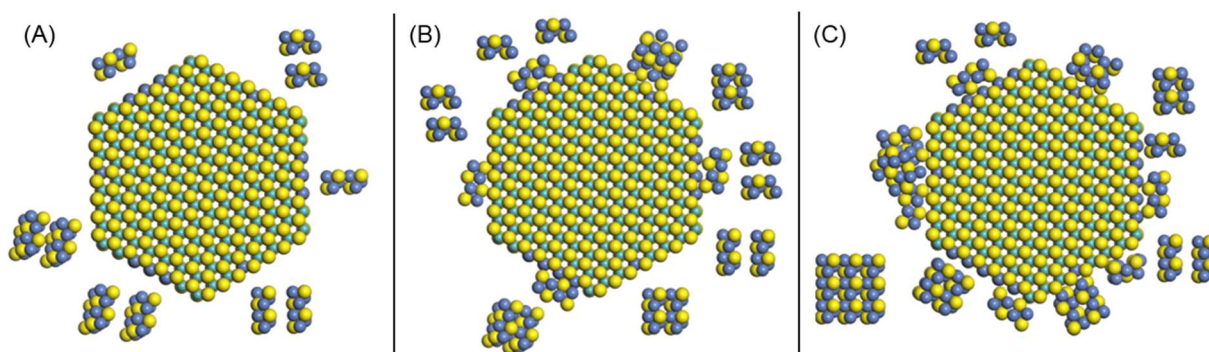


Figure 2-11. Visualization of the Ni-Mo-S and NiS_x phases in Ni(3)MoS_2 (A), Ni(6)MoS_2 (B), and Ni(10)MoS_2 (C). Yellow: S, light blue: Mo, dark blue: Ni.

The quantification of Mo and Ni atoms in the models is presented in Table 2-S13 of the supporting information. Table 2-S13 also showed a comparison of the Ni/(Mo+Ni) ratios determined by elemental analysis and those corresponding to the models in Figure 2-11 and 2-S29. The ratios of the models were lower than determined by elemental analysis, because a fraction of Ni is present in the NiAl₂O₄ spinel, which was not considered for the construction of the models. The deviation of the Ni/(Ni+Mo) ratios in the models and those from elemental content increased with Ni loading, because more Ni was engaged with the support. The atomic contents of the models (Table 2-S13), in combination with experimental elemental analysis, allowed an estimation of the concentration of decorating Ni atoms per gram of catalyst as 87, 46 and 15 μmol_{Ni}/g_{cat}, for Ni(3)MoS₂, Ni(6)MoS₂, and Ni(10)MoS₂, respectively. In contrast, the concentration of decorating Ni atoms observed by the IR spectra of adsorbed CO was 10.6, 5.1 and 1.5 μmol_{Ni}/g_{cat} (Figure 2-6), which indicates that by CO titration we observed about one tenth of the total decorating Ni atoms present under the probing conditions.

Comparison of the coordination numbers of the catalysts determined by EXAFS analysis and those of the models in Figure 2-11 and 2-S29 are given in Table 2-6. The N_{Ni-S} values of the models were in good agreement with the ones resulting from the EXAFS fitting, although the numbers for the models were slightly higher. The N_{Ni-Ni} values of the models exceed the values from EXAFS analysis, especially in case of Ni(6)MoS₂ and Ni(10)MoS₂. This was attributed to the large variety of NiS_x species that formed at the edges or on the support. Contributions of all those species (with different Ni-Ni distances) broadened the XAS spectra driving the fitting to underestimate the Ni-Ni coordination strongly. The N_{Mo-Ni} and N_{Ni-Mo} values of the models are generally in good accordance with the EXAFS fitting.

Table 2-6. Comparison of the coordination numbers determined by EXAFS fitting (a) and the coordination numbers calculated from the corresponding models in Figure 2-S29 and 2-11 (b).

Catalyst		N_{Mo-S}	N_{Mo-Mo}	N_{Ni-S}	N_{Ni-Ni}	N_{Mo-Ni}	N_{Ni-Mo}
MoS ₂ /Al ₂ O ₃	(a)	4.8±0.2	3.9±0.2	-	-	-	-
	(b)	5.5	5.8	-	-	-	-
Ni(3)MoS ₂	(a)	6.0±0.2	4.8±0.2	2.4±0.1	1.5±0.2	0.2±0.2	0.3±0.2
	(b)	5.8	5.3	2.9	2.2	0.3	0.6
Ni(6)MoS ₂	(a)	5.5±0.2	4.4±0.2	2.7±0.4	0.3±0.2	0.2±0.2	0.3±0.2
	(b)	5.9	5.3	2.9	2.4	0.3	0.4
Ni(10)MoS ₂	(a)	5.4±0.2	4.3±0.2	2.4±0.2	0.6±0.1	0.2±0.1	0.4±0.2
	(b)	5.9	5.3	3.0	2.7	0.4	0.6

The coordination numbers N_{Mo-Mo} were 5.7 and 5.8, for the MoS₂-14x14 and MoS₂-17x17 models, respectively (see Table 2-S12 in the supporting information). These values were higher than those determined in the EXAFS fitting, i.e., 3.9 (MoS₂/γ-Al₂O₃) and 4.3–4.8

(Ni(x)MoS₂/γ-Al₂O₃). This constant discrepancy was attributed to structural disorder of MoS₂ in the samples, which led to underestimation of $N_{\text{Mo-Mo}}$ values (correlated with the particle size).⁶³ The $N_{\text{Mo-S}}$ value of MoS₂/γ-Al₂O₃ was lower than that of the MoS₂-17x17 model ($N_{\text{Mo-S}}=5.5$), likely due to incomplete sulfidation of the MoS₂ phase in the sample.²⁶ The introduction of Ni eased reduction (TPS) leading to better sulfided catalysts and, therefore, the $N_{\text{Mo-S}}$ values of Ni(x)MoS₂ (5.4-6.0) were in better agreement with the value of 5.9 of the models.

2.4.2. Structure-activity correlations for (Ni)MoS₂/γ-Al₂O₃

The hydrogenation rate of phenanthrene on catalysts with varying Ni concentrations showed a maximum in activity on Ni(3)MoS₂ with a Ni/(Mo+Ni) ratio of 0.33. This optimum coincided with the maximum HDS and HDN activity on supported Ni-promoted MoS₂ catalysts reported at Ni/(Mo+Ni) ratios of 0.3 – 0.4.^{5,14,24,64,65}

The presence of Ni influenced, however, also the selectivity of phenanthrene hydrogenation. Deep hydrogenation was favored leading to a DiHPhe/TetHPhe (k_1/k_2) selectivity ratio of 1 (versus k_1/k_2 of 8.6 on MoS₂/γ-Al₂O₃). The formation rates of TetHPhe and OHPhe also increased dramatically. Interestingly, increasing Ni loading above 3 wt.-% did not influence the selectivity, but only the activity of the catalyst. This indicates that adding Ni to MoS₂/γ-Al₂O₃ increased the concentration of active sites and changed their intrinsic nature, while further variation of Ni only modified the concentration of sites.

The linear correlation between the rate constant k_1 (Phe to DiHPhe, symmetric hydrogenation) and the concentration of Ni atoms in the edge of MoS₂ slabs (Figure 2-12 A) indicates similar k_1 values for MoS₂/γ-Al₂O₃ and Ni(10)MoS₂ although both had very different sites, i.e., only not-promoted sites and only promoted sites (and NiS_x clusters), respectively. This demonstrates that hydrogenation of the middle ring in phenanthrene does not depend directly on the presence of Ni in the active site, but mainly on the total concentration of adsorption sites. A recent study demonstrated that the variation of Ni on (Ni)MoS₂ increased the concentration of active hydrogen by most 30% in Ni(3)MoS₂ compared to MoS₂/γ-Al₂O₃.⁶⁶ This increase was comparable to the increase in k_1 with the optimum promotion (55%). Indeed, the increase of k_1 is concluded to result from a combination of increased active hydrogen (30%) and increase in dispersion (f_{Mo} increases about 20% by adding 3 wt.-% Ni).

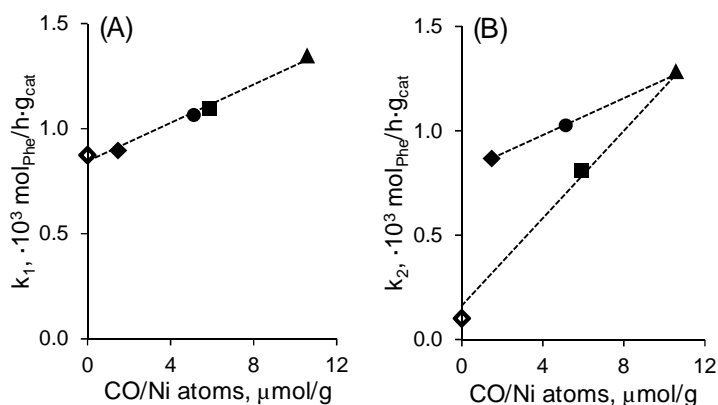


Figure 2-12. Correlation of the rate constants k_1 (A) and k_2 (B) with the concentration of CO adsorbed on Ni atoms decorating MoS_2 . $\text{MoS}_2/\gamma\text{-Al}_2\text{O}_3$ (◇), Ni(1.5)MoS₂ (■), Ni(3)MoS₂ (▲), Ni(6)MoS₂ (●), Ni(10)MoS₂ (◆).

Deep hydrogenation (k_2) showed a more complex dependence on the concentration of Ni atoms incorporated in the edge of the MoS_2 slab (Figure 2-12 B). The values for $\text{MoS}_2/\gamma\text{-Al}_2\text{O}_3$, Ni(1.5)MoS₂, and Ni(3)MoS₂ correlate well indicating that Ni(1.5)MoS₂ consisted of a mixture of not-promoted and Ni-promoted MoS_2 as suggested also by the selectivity (Figure 2-9). The values for Ni(3)MoS₂, Ni(6)MoS₂, and Ni(10)MoS₂ were correlated with a different function, one with a less pronounced slope and with an intercept way above the level of $\text{MoS}_2/\gamma\text{-Al}_2\text{O}_3$. This indicated that the presence of Ni in the active sites was mandatory for deep hydrogenation and that variations in the magnitude of k_2 depend mostly on the concentration of these sites. The same trend is observed for k_3 and k_4 (see Figure 2-S28 supporting information).

The mechanistic picture that arises from this work is presented in Figure 2-13. The adsorption of phenanthrene, driven by van der Waals forces, occurs on the basal plane of the (Ni)MoS₂ slab.⁶⁷ Hydrogenation is likely to occur, however, at regions close to the edge, where SH-groups provide hydrogen. The chemisorption through π -interactions is considered decisive for the selectivity due to the properties of phenanthrene. The angular arrangement of the three rings creates two electron sextets at the corners of the molecule, leaving a single double bond with high reactivity in the 9,10-position.⁶⁸ Therefore, adsorption of phenanthrene *via* the middle ring leads to fast hydrogenation towards DiHPhe (symmetric hydrogenation) even on not-promoted Mo sites. On the other hand, adsorption of phenanthrene *via* a lateral ring does not lead to a stable product (TetHPhe) unless four hydrogen atoms have been added to the adsorbed molecule. This seems to be difficult on not-promoted sites. We hypothesize that the deep hydrogenation is promoted by the stronger interaction of Ni cations with these sites, shifting from the more planar interaction in the parent MoS_2 .

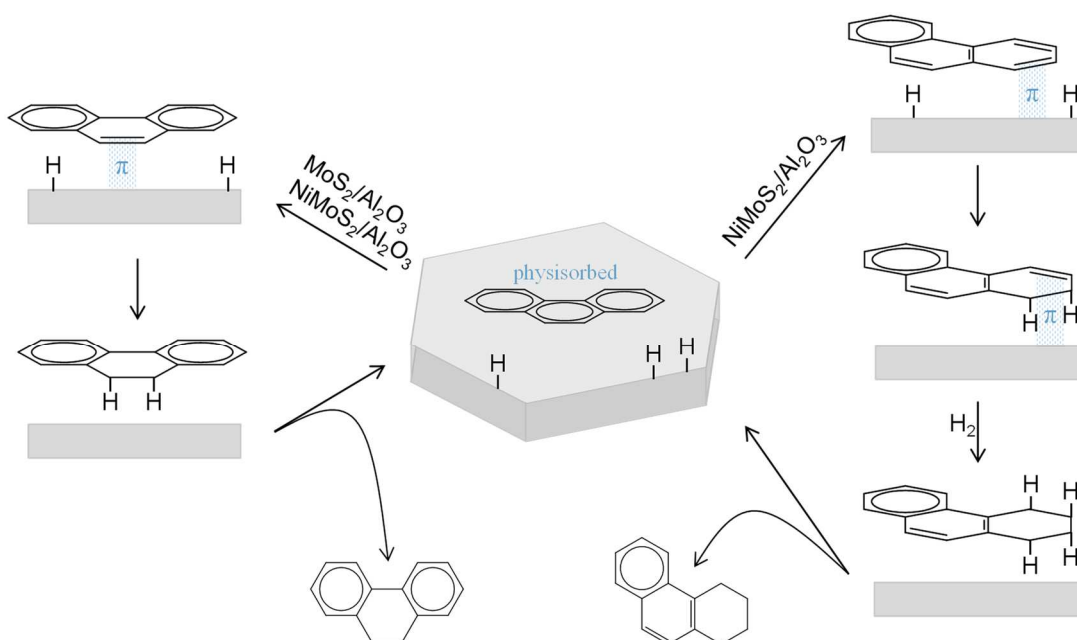


Figure 2-13. Illustration of the hydrogenation routes of phenanthrene on $(\text{Ni})\text{MoS}_2/\gamma\text{-Al}_2\text{O}_3$.

The adsorption of phenanthrene *via* the middle ring on promoted catalysts leads to faster symmetric hydrogenation than on $\text{MoS}_2/\gamma\text{-Al}_2\text{O}_3$ due to the higher edge fraction and concentration of SH-groups (available hydrogen). On the other hand, deep hydrogenation would occur if phenanthrene adsorbs *via* a lateral ring on a promoted site, where a Ni entity (atom or cluster according to correlations shown above) is indeed present.

2.5. Conclusions

Using a series of $(\text{Ni})\text{MoS}_2/\gamma\text{-Al}_2\text{O}_3$ catalysts it is shown that incorporation of Ni influences the state of Mo precursors and sulfides alike. Ni is concluded to weaken the interaction of Mo with the support. This increases the oligomerization of molybdate species at the expense of tetrahedral Mo species and concomitantly reduces the reduction temperature of Mo species during sulfidation. The dispersion of the MoS_2 phase is modestly increased by 20%, whereas the concentration of coordinatively unsaturated sites substantially increases with the Ni loading. Ni is incorporated in three forms, as spinel within the support, as Ni atoms decorating MoS_2 (Ni-Mo-S phase), and as NiS_x sulfide species ranging from NiS_x clusters to agglomerated Ni_3S_2 . A fraction of the small clusters grows at the edge of MoS_2 decreasing the concentration of single Ni atoms. These changes can be modeled perfectly, supporting feasibility of the conclusions derived from the physicochemical measurements.

Hydrogenation of phenanthrene occurs *via* two routes, “symmetric hydrogenation” (phenanthrene \rightarrow 9,10-dihydro-phenanthrene) and “deep hydrogenation” (Phe \rightarrow 1,2,3,4-tetrahydro-phenanthrene \rightarrow 1,2,3,4,5,6,7,8-octahydro-phenanthrene). Only symmetric

hydrogenation is observed on not-promoted MoS₂/γ-Al₂O₃. The addition of Ni increases the rate of symmetric hydrogenation and opens the route towards deep hydrogenation (the selectivity towards both routes is almost the same on Ni-containing catalysts). The activity for the hydrogenation of phenanthrene correlates with the concentration of exposed Ni atoms. The enhancement of symmetric hydrogenation (on adsorbing the middle ring with the reactive bond in the 9,10-position) by promotion is attributed to higher concentration of available hydrogen (SH-groups) at the surface, the presence of Ni at the active site is not needed. In contrast, Ni is part of the active site that performs deep hydrogenation after the adsorption of a lateral ring of phenanthrene.

2.6. References

- (1) Stanislaus, A.; Cooper, B. *Catal. Rev.* **1994**, 36 (1), 75–123.
- (2) Christensen, J. M.; Mortensen, P. M.; Trane, R.; Jensen, P. A.; Jensen, A. D. *Appl. Catal. A Gen.* **2009**, 366 (1), 29–43.
- (3) Gutiérrez, O. Y.; Zhong, L.; Zhu, Y.; Lercher, J. A. *ChemCatChem* **2013**, 5 (11), 3249–59.
- (4) Girgis, M. J.; Gates, B. C. *Ind. Eng. Chem. Res.* **1991**, 30, 2021–2058.
- (5) Topsøe, H.; Clausen, B. S.; Massoth, F. E. *Hydrotreating Catalysis*; Springer Verlag: Berlin, 1996.
- (6) Topsøe, H.; Clausen, B. S. *Catal. Rev.* **1984**, 26 (3), 395–420.
- (7) Lauritsen, J. V.; Helveg, S.; Lægsgaard, E.; Stensgaard, I.; Clausen, B. S.; Topsøe, H.; Besenbacher, F. *J. Catal.* **2001**, 197 (1), 1–5.
- (8) Zhu, Y.; Ramasse, Q. M.; Brorson, M.; Moses, P. G.; Hansen, L. P.; Kisielowski, C. F.; Helveg, S. *Angew. Chem. Int. Ed. Engl.* **2014**, 53 (40), 10723–10727.
- (9) Deepak, F. L.; Esparza, R.; Borges, B.; Lopez-Lozano, X.; Jose-Yacamán, M. *ACS Catal.* **2011**, 1, 537–543.
- (10) Besenbacher, F.; Brorson, M.; Clausen, B. S.; Helveg, S.; Hinnemann, B.; Kibsgaard, J.; Lauritsen, J. V.; Moses, P. G.; Nørskov, J. K.; Topsøe, H. *Catal. Today* **2008**, 130 (1), 86–96.
- (11) Topsøe, N.-Y.; Topsøe, H. *J. Catal.* **1982**, 75, 354–374.
- (12) Travert, A.; Dujardin, C.; Maugé, F.; Veilly, E.; Cristol, S.; Paul, J.-F.; Payen, E. *J. Phys. Chem. B* **2006**, 110 (3), 1261–1270.
- (13) Bouwens, S. M. A. M.; Prins, R.; de Beer, V. H. J.; Koningsberger, D. C. *J. Phys. Chem.* **1990**, 94, 3711–3718.
- (14) Louwers, S. P. A.; Prins, R. *J. Catal.* **1992**, 133, 94–111.
- (15) Dumcenco, D. O.; Kobayashi, H.; Liu, Z.; Huang, Y.-S.; Suenaga, K. *Nat. Commun.* **2013**, 4, 1–5.
- (16) Sun, M.; Nelson, a; Adjaye, J. *J. Catal.* **2005**, 233 (2), 411–421.
- (17) Byskov, L. S.; Nørskov, J. K.; Clausen, B. S.; Topsøe, H. *J. Catal.* **1999**, 187, 109–122.

- (18) Coleman, J. N.; Lotya, M.; O'Neill, A.; Bergin, S. D.; King, P. J.; Khan, U.; Young, K.; Gaucher, A.; De, S.; Smith, R. J.; Shvets, I. V.; Arora, S. K.; Stanton, G.; Kim, H.-Y.; Lee, K.; Kim, G. T.; Duesberg, G. S.; Hallam, T.; Boland, J. J.; Wang, J. J.; Donegan, J. F.; Grunlan, J. C.; Moriarty, G.; Shmeliov, A.; *et al.* *Science* **2011**, 331 (6017), 568–571.
- (19) Yonemoto, B. T.; Hutchings, G. S.; Jiao, F. *J. Am. Chem. Soc.* **2014**, 136 (25), 8895–98.
- (20) Leliveld, R. G.; Eijsbouts, S. *Catal. Today* **2008**, 130 (1), 183–189.
- (21) Bensch, W. Hydrotreating: Removal of Sulfur from Crude Oil Fractions with Sulfide Catalysts, In *Comprehensive Inorganic Chemistry II* (2nd Edition), edited by Reedijk J. and Poeppelemeier K.; Elsevier, Amsterdam; 2013, 287–321.
- (22) Gutiérrez, O. Y.; Singh, S.; Schachtl, E.; Kim, J.; Kondratieva, E.; Hein, J.; Lercher, J. A. *ACS Catal.* **2014**, 4 (5), 1487–1499.
- (23) Prins, R.; De Beer, V. H. J.; Somorjai, G. A. *Catal. Rev. Sci. Eng.* **1989**, 31 (1&2), 1–41.
- (24) Startsev, A. N. *Catal. Rev.* **1995**, 37 (3), 353–423.
- (25) Byskov, L. S.; Hammer, B.; Nørskov, J. K.; Clausen, B. S.; Topsøe, H. *Catal. Letters* **1997**, 47, 177–182.
- (26) Hein, J.; Hrabar, A.; Jentys, A.; Gutiérrez, O. Y.; Lercher, J. a. *ChemCatChem* **2014**, 6 (2), 485–499.
- (27) Prins, R.; Egorova, M.; Röthlisberger, A.; Zhao, Y.; Sivasankar, N.; Kukula, P. *Catal. Today* **2006**, 111 (1-2), 84–93.
- (28) Prins, R.; Jian, M.; Flechsenhar, M. *Polyhedron* **1997**, 16 (18), 3235–3246.
- (29) Maugé, F.; Lavalley, J.-C. *J. Catal.* **1992**, 137, 69–76.
- (30) Kondratieva, E. V.; Manoilova, O. V.; Tsyganenko, A. A. *Kinet. Catal.* **2008**, 49 (3), 451–6.
- (31) Ravel, B.; Newville, M. *J. Synchrotron Radiat.* **2005**, 12, 537–541.
- (32) Newville, M. *J. Synchrotron Radiat.* **2001**, 8, 322–324.
- (33) Zabinsky, S. I.; Rehr, J. J.; Ankudinov, A.; Albers, R. C.; Eller, M. J. *Phys. Rev. B* **1995**, 52, 2995–3009.
- (34) Belsky, A.; Hellenbrandt, M.; Karen, V. L.; Luksch, P. *Acta Crystallogr. Sect. B Struct. Sci.* **2002**, 58 (3), 364–369.
- (35) Wang, X.; Zhao, B.; Jiang, D.; Xie, Y. *Appl. Catal. A Gen.* **1999**, 188 (1-2), 201–209.
- (36) Wyckoff, R. W. G. *Crystal Structures, Vol. 1*; Interscience: New York, 1963.
- (37) Arnoldy, P.; van den Heijkant, J. A. M.; de Bok, G. D.; Moulijn, J. A. *J. Catal.* **1985**, 92, 35–55.
- (38) Scheffer, B.; Mangnus, P. J.; Moulijn, J. A. *J. Catal.* **1990**, 121, 18–30.
- (39) Eijsbouts, S.; van den Oetelaar, L. C. A.; van Puijenbroek, R. R. *J. Catal.* **2005**, 229 (2), 352–364.
- (40) Hensen, E. J. M.; Kooyman, P. J.; van der Meer, Y.; van der Kraan, A. M.; de Beer, V. H. J.; van Veen, J. A. R.; van Santen, R. A. *J. Catal.* **2001**, 199 (2), 224–235.
- (41) Kasztelan, S.; Toulhoat, H.; Grimblot, J.; Bonnelle, J. *Appl. Catal.* **1984**, 13, 127–159.
- (42) Chen, J.; Maugé, F.; El Fallah, J.; Oliviero, L., *J. Catal.* **2014**, 320, 170–179.
- (43) Topsøe, N.-Y.; Topsøe, H. *J. Catal.* **1983**, 84, 386–401.

- (44) Gutiérrez, O. Y.; Hrabar, A.; Hein, J.; Yu, Y.; Han, J.; Lercher, J. A. *J. Catal.* **2012**, *295*, 155–168.
- (45) Gutiérrez, O. Y.; Kaufmann, C.; Lercher, J. A. *ACS Catal.* **2011**, *1* (11), 1595–1603.
- (46) Hrabar, A.; Hein, J.; Gutiérrez, O. Y.; Lercher, J. A. *J. Catal.* **2011**, *281* (2), 325–338.
- (47) Gutiérrez, O. Y.; Klimova, T. *J. Catal.* **2011**, *281* (1), 50–62.
- (48) Koizumi, N.; Jung, S.; Hamabe, Y.; Suzuki, H.; Yamada, M. *Catal. Letters* **2010**, *135* (3-4), 175–181.
- (49) Topsøe, N.; Tuxen, A.; Hinnemann, B.; Lauritsen, J. V.; Knudsen, K. G.; Besenbacher, F.; Topsøe, H. *J. Catal.* **2011**, *279*, 337–351.
- (50) Travert, A.; Dujardin, C.; Maugé, F.; Cristol, S.; Paul, J.-F.; Payen, E.; Bougeard, D. *Catal. Today* **2001**, *70* (1-3), 255–269.
- (51) Dujardin, C.; Lélías, M.; van Gestel, J.; Travert, A.; Duchet, J.; Maugé, F. *Appl. Catal. A Gen.* **2007**, *322*, 46–57.
- (52) Vogelaar, B. M.; Kagami, N.; van der Zijden, T. F.; van Langeveld, A. D.; Eijsbouts, S.; Moulijn, J. A. *J. Mol. Catal. A Chem.* **2009**, *309* (1-2), 79–88.
- (53) Marceau, E.; Löfberg, A.; Giraudon, J.-M.; Négrier, F.; Che, M.; Leclercq, L. *Appl. Catal. A Gen.* **2009**, *362* (1-2), 34–39.
- (54) Poncelet, G.; Centeno, M. A.; Molina, R. *Appl. Catal. A Gen.* **2005**, *288* (1-2), 232–242.
- (55) Koizumi, N.; Hamabe, Y.; Jung, S.; Suzuki, Y.; Yoshida, S.; Yamada, M. *J. Synchrotron Radiat.* **2010**, *17* (3), 414–424.
- (56) Bhore, N. A.; Klein, M. T.; Bischoff, K. B. *Ind. Eng. Chem. Res.* **1990**, *29* (2), 313–316.
- (57) Girgis, M. J.; Gates, B. C. *Ind. Eng. Chem. Res.* **1994**, *33* (12), 2301–2313.
- (58) Beltramone, A. R.; Resasco, D. E.; Alvarez, W. E.; Choudhary, T. V. *Ind. Eng. Chem. Res.* **2008**, *47* (19), 7161–7166.
- (59) Williams, C. C.; Ekerdt, J. G.; Jehng, J. M.; Hardcastle, F. D.; Wachs, I. E. *J. Phys. Chem.* **1991**, *95* (22), 8791–8797.
- (60) Delmon, B. *Stud. Surf. Sci. Catal.* **1990**, *53*, 1–40.
- (61) Van der Kraan, A. M.; Crajé, M. W. J.; Gerkema, E.; Ramselaar, W. L. T. M.; de Beer, V. H. J. *Appl. Catal.* **1988**, *39*, 7–10.
- (62) Crajé, M. W. J.; Gerkema, E.; de Beer, V. H. J.; van der Kraan, A. M. *Stud. Surf. Sci. Catal.* **1989**, *50*, 165–179.
- (63) Shido, T.; Prins, R. *J. Phys. Chem. B* **1998**, *102*, 8426–8435.
- (64) Park, Y. C.; Rhee, H.-K. *Korean J. Chem. Eng.* **1998**, *15* (4), 411–416.
- (65) De Beer, V. H. J.; van Sint Fiet, T. H. M.; Engelen, J. F.; van Haandel, A. C.; Wolfs, M. W. J.; Amberg, C. H.; Schuit, G. C. A. *J. Catal.* **1972**, *27*, 357–368.
- (66) Schachtl, E.; Kondratieva, E.; Gutiérrez, O. Y.; Lercher, J. A. *J. Phys. Chem. Lett.* **2015**, *6* (15), 2929–2932.
- (67) Moses, P. G.; Mortensen, J. J.; Lundqvist, B. I.; Nørskov, J. K. *J. Chem. Phys.* **2009**, *130* (10), 104709.
- (68) Clar, E. *Polycyclic Hydrocarbons, Band I*; Academic Press: London-New York, 1964.

2.7. Supporting Information

UV-Vis DR spectroscopy and X-ray diffraction of oxide precursor

The UV-Vis DR spectra of the oxide precursors are shown in Figure 2-S14. The bands at 220-400 nm range are attributed to $\text{O}^{2-} \rightarrow \text{Mo}^{6+}$ charge transfer transitions.^{S1-S3} All spectra showed a band at 255 nm, which is assigned to isolated (tetrahedral, T_d) molybdate species. The bands at 300-330 nm were attributed to polymolybdate (octahedral, O_h) species. In the spectrum of $\text{MoO}_3/\gamma\text{-Al}_2\text{O}_3$, this band appeared at 300 nm and had low intensity. It shifted to higher wavenumbers and became better defined with increasing Ni content in the $\text{Ni}(x)\text{MoO}_3$ materials until a well-defined peak at 330 nm was observed for $\text{Ni}(10)\text{MoO}_3$. This implies that both, T_d and O_h Mo species were already present in $\text{MoO}_3/\gamma\text{-Al}_2\text{O}_3$. The systematic shift of the O_h Mo band for the Ni-modified samples indicated that Ni increased the proportion of O_h Mo species compared to $\text{MoO}_3/\gamma\text{-Al}_2\text{O}_3$. This was attributed to the increase of the oligomerization degree of the polymolybdate species in presence of increasing concentrations of Ni.^{S4}

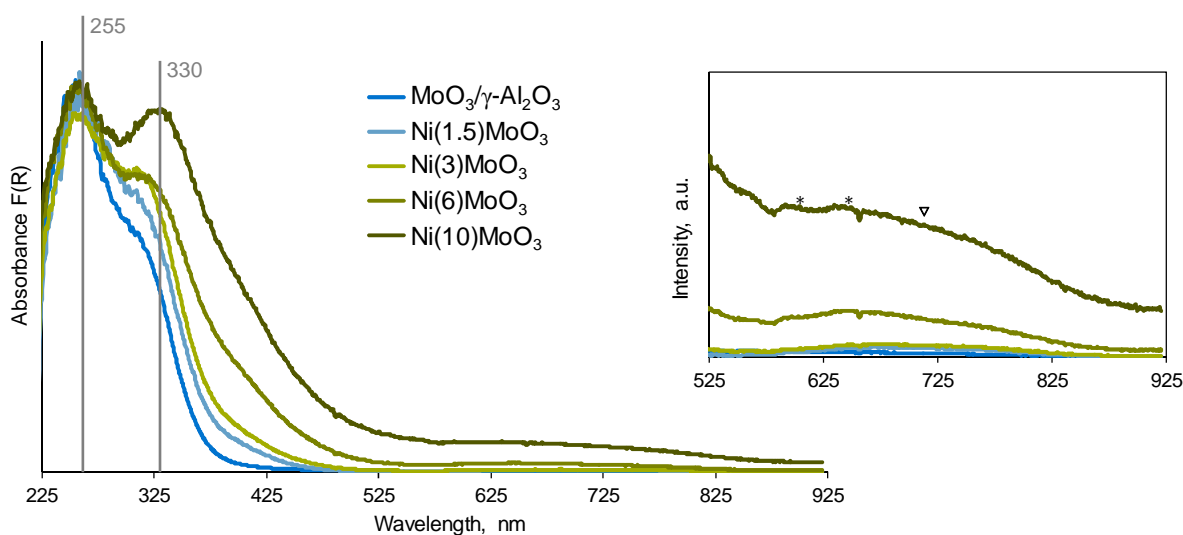


Figure 2-S14. UV-Vis DR spectra of the oxidic catalyst precursors. (*) NiAl_2O_4 , (∇) NiO .

The shoulder at 400 and 420 nm in the spectra of $\text{Ni}(6)\text{MoO}_3$ and $\text{Ni}(10)\text{MoO}_3$, respectively, as well as the broad bands between 600 and 850 nm observed for all Ni-containing materials (inset in Figure 2-S14) were assigned to Ni^{2+} species.^{S5} The intensity of these bands increased with increasing Ni loading, as expected from the concomitant formation of spinel. The shift of the band at 320 nm in $\text{Ni}(3)\text{MoO}_3$ and $\text{Ni}(6)\text{MoO}_3$ to 330 nm in $\text{Ni}(10)\text{MoO}_3$, and the intensity increase points to increasing contributions of NiO species as confirmed with X-ray diffraction (vide infra).

Temperature programmed sulfidation

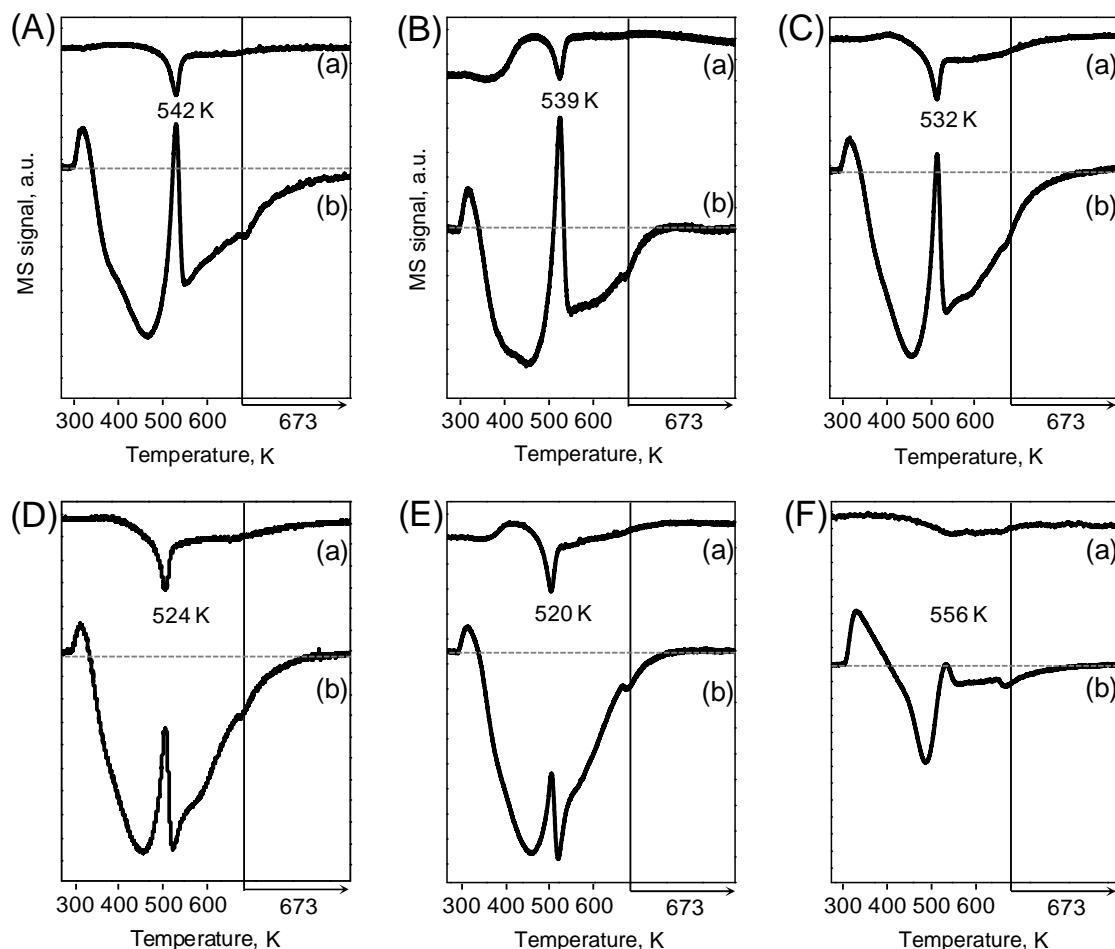


Figure 2-S15. Profiles of H₂ (a) and H₂S (b) for the temperature programmed sulfidation of (A) MoO₃/γ-Al₂O₃, (B) Ni(1.5)MoO₃, (C) Ni(3)MoO₃, (D) Ni(6)MoO₃, (E) Ni(10)MoO₃, (F) NiO/γ-Al₂O₃.

X-ray diffraction

X-ray diffractograms of the oxide precursors and reference materials are given in Figure 2-S16. All diffractograms showed well-defined reflections corresponding to the γ-Al₂O₃ support at 37, 40, 46, 61 and 67 °2θ (not marked) according to the reference diffractogram. An additional weak reflection assigned to MoO₃ appeared at 23 °2θ for MoO₃/γ-Al₂O₃. The other oxide precursors did not exhibit any characteristic reflections typical for crystalline Mo species. This observation suggests that a minor crystalline MoO₃ phase was formed on MoO₃/γ-Al₂O₃, which dispersed with the addition of Ni. Two reflections corresponding to NiO, at 44 and 63 °2θ, were observed for Ni(10)MoO₃, suggesting relatively large NiO particles as also concluded from UV-Vis DR (vide infra). Crystalline Ni species were not observed in other materials.

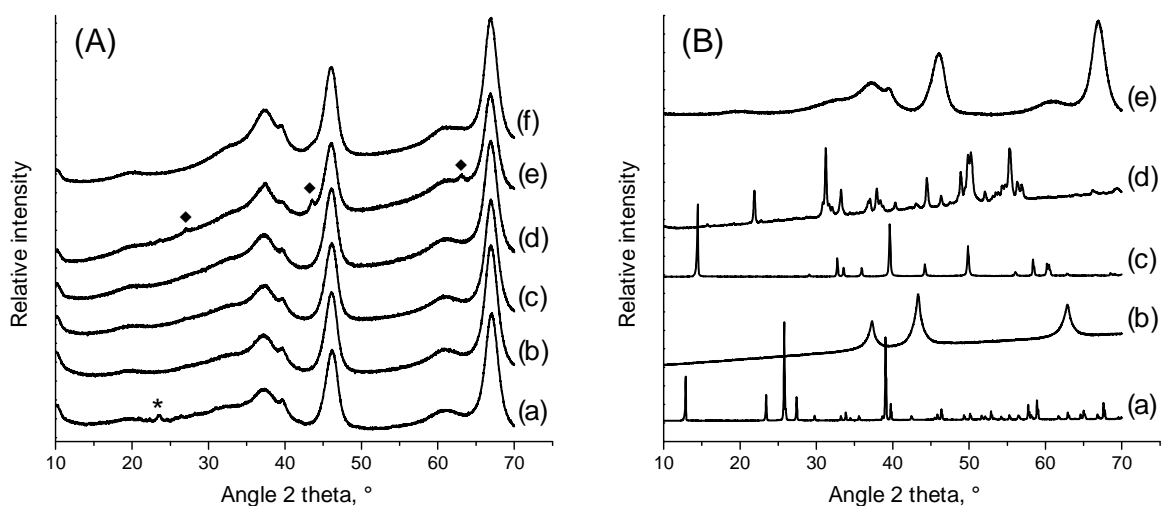


Figure 2-S16. X-ray diffractograms of (A) oxide precursors and (B) reference materials. (A,a) $\text{MoO}_3/\gamma\text{-Al}_2\text{O}_3$, (A,b) $\text{Ni}(1.5)\text{MoO}_3$, (A,c) $\text{Ni}(3)\text{MoO}_3$, (A,d) $\text{Ni}(6)\text{MoO}_3$, (A,e) $\text{Ni}(10)\text{MoO}_3$, (A,f) $\text{NiO}/\gamma\text{-Al}_2\text{O}_3$. (B,a) MoO_3 , (B,b) NiO , (B,c) MoS_2 , (B,d) Ni_3S_2 , (B,e) $\gamma\text{-Al}_2\text{O}_3$. The marked reflections in (A) correspond to MoO_3 (*) and NiO (◆).

Transmission electron microscopy

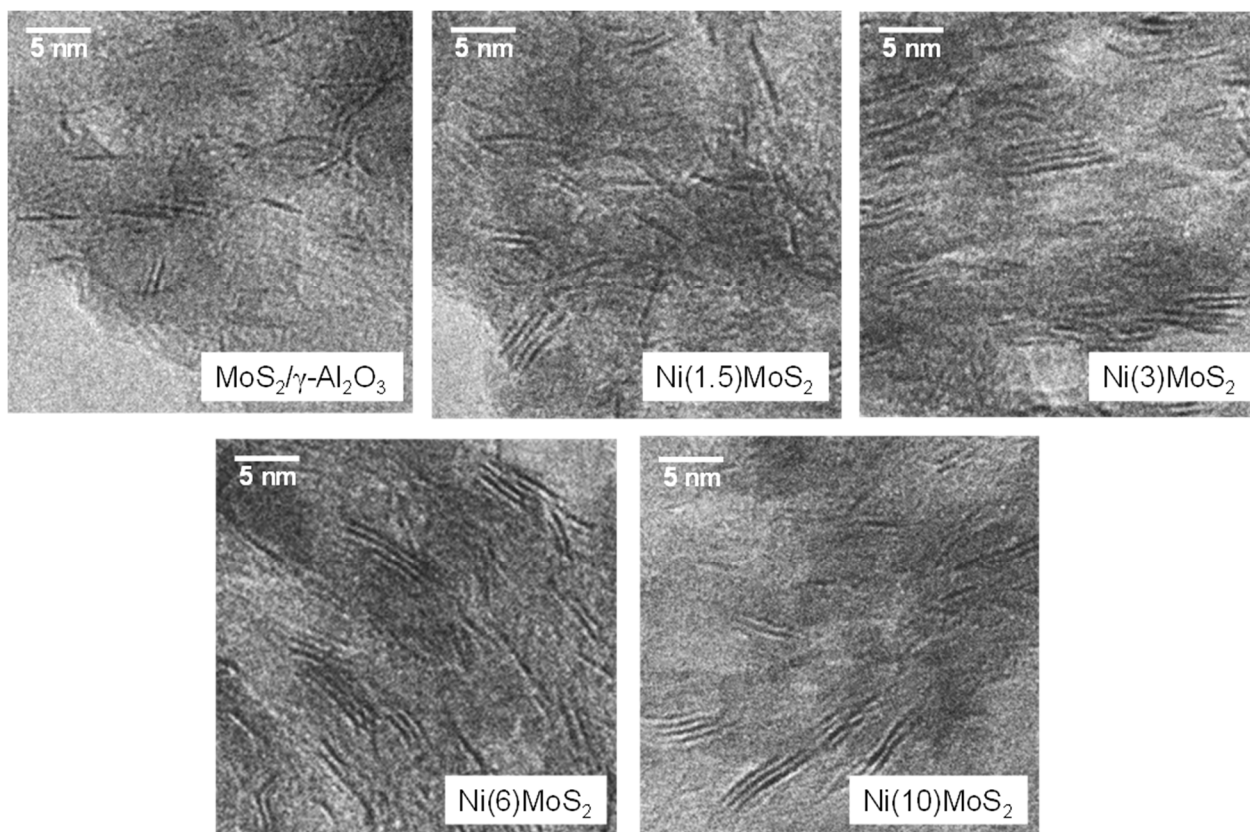


Figure 2-S17. Transmission electron micrographs of $\text{MoS}_2/\gamma\text{-Al}_2\text{O}_3$, $\text{Ni}(1.5)\text{MoS}_2$, $\text{Ni}(3)\text{MoS}_2$, $\text{Ni}(6)\text{MoS}_2$ and $\text{Ni}(10)\text{MoS}_2$.

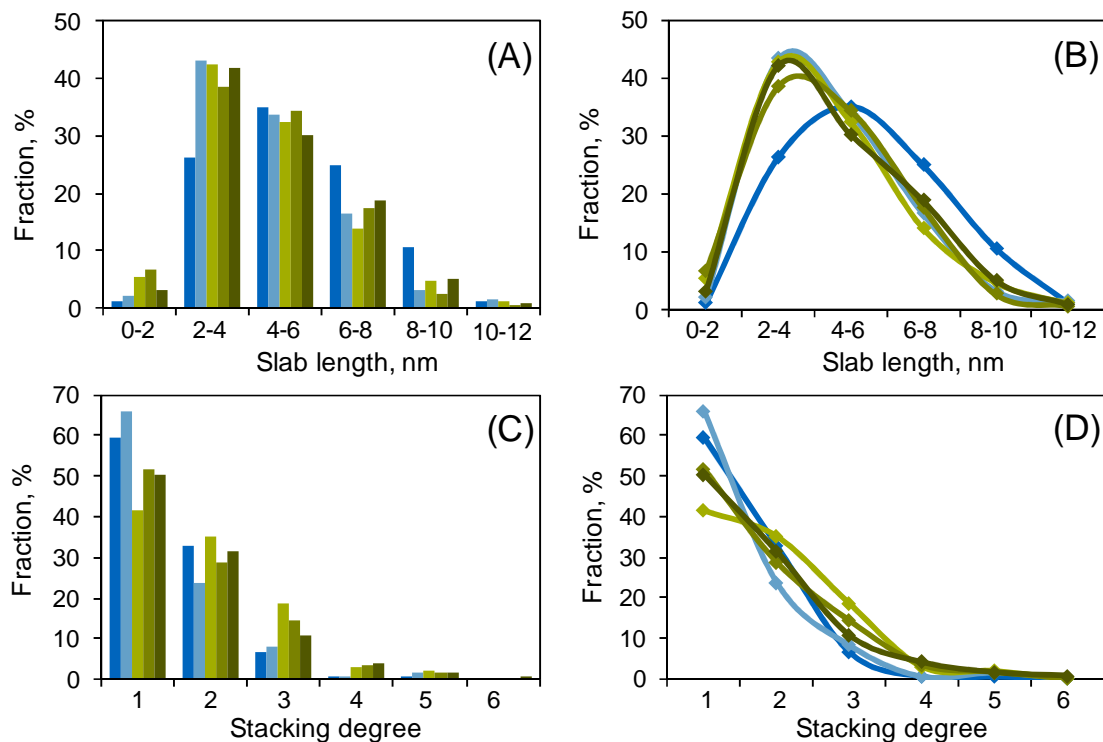


Figure 2-S18. Graphical displays of the distribution of slab length (A and B) and stacking degree (C and D) as derived from the statistical TEM analysis. Blue: $\text{MoS}_2/\gamma\text{-Al}_2\text{O}_3$; orange: $\text{Ni}(1.5)\text{MoS}_2$; green: $\text{Ni}(3)\text{MoS}_2$; yellow: $\text{Ni}(6)\text{MoS}_2$; red: $\text{Ni}(10)\text{MoS}_2$.

IR spectroscopy of adsorbed CO

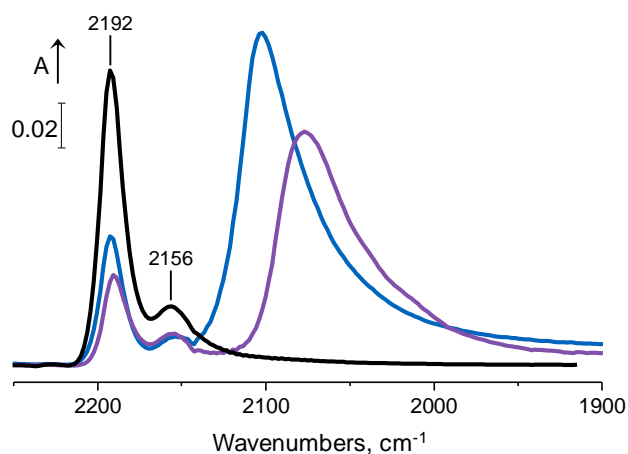


Figure 2-S19. IR Spectra of CO adsorbed on $\gamma\text{-Al}_2\text{O}_3$ (black), $\text{MoS}_2/\gamma\text{-Al}_2\text{O}_3$ (blue) and $\text{NiS}_x/\gamma\text{-Al}_2\text{O}_3$ (purple).

Discussion on the semi-quantitative analysis of the IR-CO adsorption data

The spectra of CO adsorbed on the sulfide catalysts (presented in Figure 2-5) were deconvoluted using the assignments presented in Table 2-S7 (the deconvoluted spectra are shown in Figure 2-S20). In turn, these assignments are based on the spectra of γ-Al₂O₃, MoS₂/γ-Al₂O₃ and NiS_x/γ-Al₂O₃ (see Figure 2-S19) and DFT calculations reported in Ref.^{S6}. The adsorption of CO on not-promoted MoS₂ leads to two kinds of adsorbed species, i.e., CO on Mo at the S-edge (2094 cm⁻¹) and on the M-edge (2106 cm⁻¹). The addition of Ni leads to a variety of species whose overlapping bands made it necessary to make some assumptions in order to perform the analysis of the results. The position of the bands of CO on not-promoted Mo sites at the S-edge and CO on NiS_x are very close (2094 versus 2080 cm⁻¹). It is expected that as the loading of Ni increases, the contribution of CO species adsorbed on not-promoted sites decreases, as it is, indeed, the case for the band at 2106 cm⁻¹ (CO on not-promoted Mo sites at the M-edge). In contrast the contribution of CO species adsorbed on NiS_x has to increase, as does the broad band at 2060 - 2020 cm⁻¹. Additionally, DFT calculations predict CO adsorbed on promoted Mo on the S- and M-edge to be located at ~2060 cm⁻¹, as well. Therefore, the deconvoluted band at 2084 cm⁻¹ in Ni(x)MoS₂ is attributed to three contributions, CO on not-promoted Mo sites at the S-edge, CO on promoted Mo and CO on NiS_x species, the latter presumably having the strongest influence at high Ni concentrations.

The concentrations of adsorbed CO were calculated from the deconvoluted peak areas using the molar extinction coefficient reported in Refs.^{S7,S8}. Those were ε = 4.5 cm·μmol⁻¹ for Ni on not-promoted MoS₂ and ε = 16 cm·μmol⁻¹ for Ni atoms incorporated in MoS₂.

Table 2-S7. Assignments of the spectra of CO adsorbed on the sulfide catalysts and area of the corresponding deconvoluted bands.

Catalysts	CO-Ni ^a (2118)	CO-MoS ₂ ^b (2106)	CO-MoS ₂ ^c (2094)	CO-NiS _x /CO-MoS ₂ ^d (2080-2020)
MoS ₂ /γ-Al ₂ O ₃	-	2.26	5.02	-
Ni(1.5)MoS ₂	0.27	1.52	-	2.78
Ni(3)MoS ₂	0.48	1.40	-	4.22
Ni(6)MoS ₂	0.23	0.92	-	6.41
Ni(10)MoS ₂	0.07	0.08	-	6.94

^a CO adsorbed on Ni atoms decorating the MoS₂ slabs.

^b CO adsorbed on not-promoted Mo sites at the Mo-edge.

^c CO adsorbed on not-promoted Mo sites at the S-edge.

^d CO adsorbed on the NiS_x phase, on not-promoted Mo at the S-edge and on promoted Mo sites at M- & S-edge.

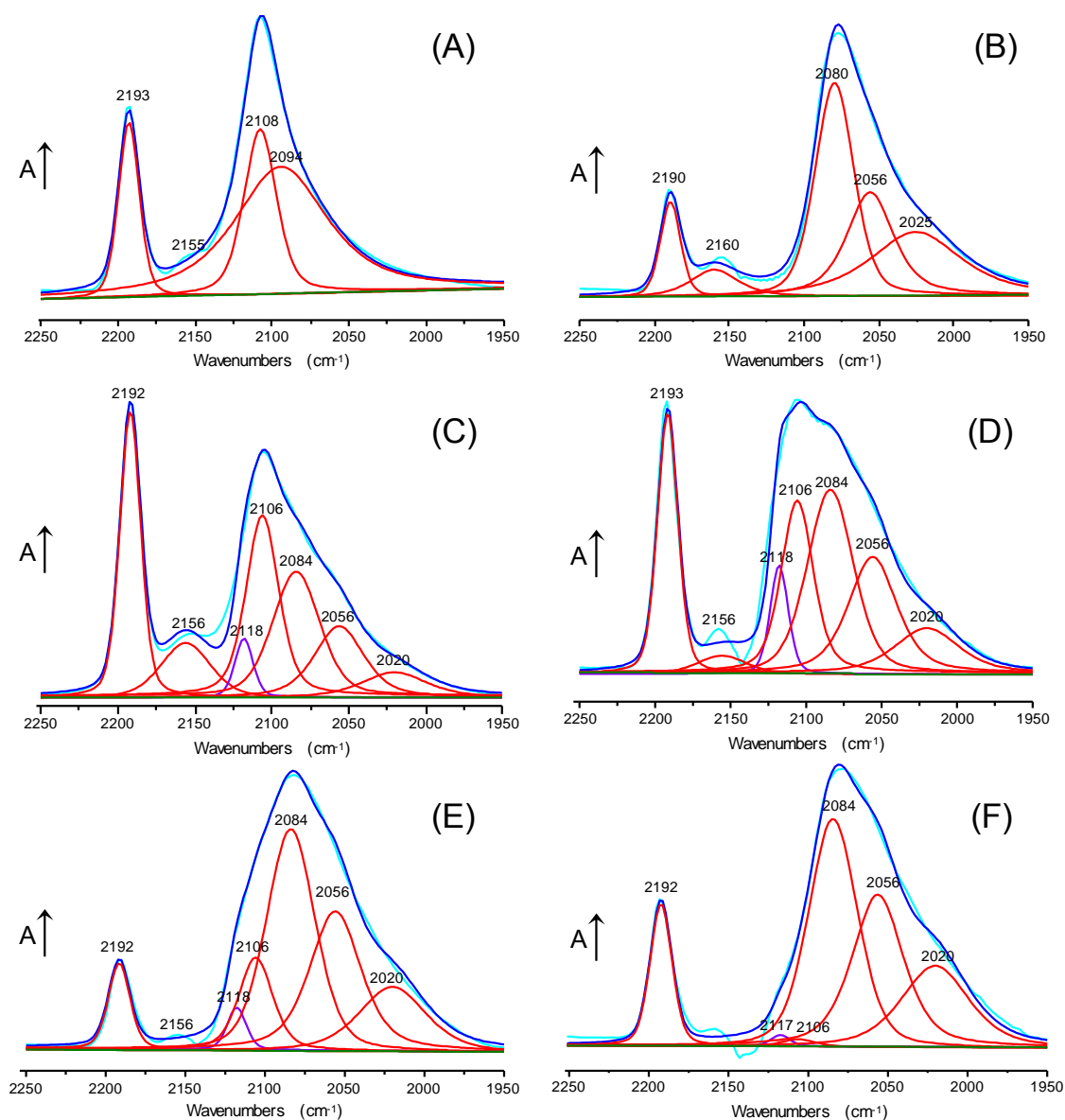


Figure 2-S20. Deconvoluted IR spectra of CO adsorbed on (A) $\text{MoS}_2/\gamma\text{-Al}_2\text{O}_3$, (B) $\text{Ni}_5/\gamma\text{-Al}_2\text{O}_3$, (C) $\text{Ni}(1.5)\text{MoS}_2$, (D) $\text{Ni}(3)\text{MoS}_2$, (E) $\text{Ni}(6)\text{MoS}_2$, and (F) $\text{Ni}(10)\text{MoS}_2$. Light blue: experimentally recorded data, dark blue: fitted curve, purple: contribution of Ni atoms decorating MoS_2 , red: contributions of the individual species as assigned in Table 2-S7.

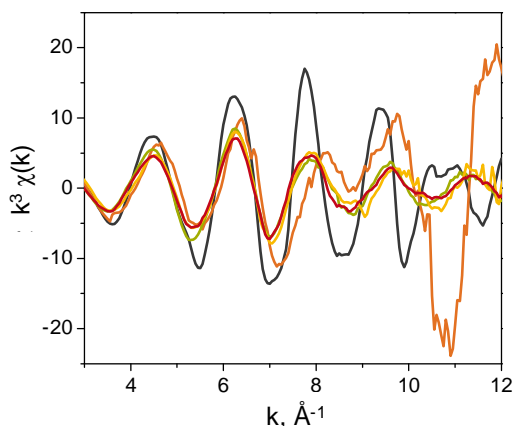
X-ray absorption spectroscopy of $(\text{Ni})\text{MoS}_2/\gamma\text{-Al}_2\text{O}_3$ 

Figure 2-S21. k^3 weighted EXAFS at the Ni K-edge. Black: Ni_3S_2 ; orange: $\text{Ni}(1.5)\text{MoS}_2$; green: $\text{Ni}(3)\text{MoS}_2$; yellow: $\text{Ni}(6)\text{MoS}_2$; red: $\text{Ni}(10)\text{MoS}_2$. Compared to the others, the amplitude of the oscillations of $\text{Ni}(1.5)\text{MoS}_2$ appears too high and in addition phase shifted at the higher k region. This is attributed to a very low intensity of the original spectrum, related to the very low concentration of Ni in the sample, which is why the sample $\text{Ni}(1.5)\text{MoS}_2$ was not considered for further analysis.

Discussion on the linear combination fitting (LCF) of the XANES at the Ni K-edge

Linear combination fitting (LCF) was applied and difference spectra were created to explore further the XANES at the Ni K-edge. LCF of the spectra of the sulfide catalysts was performed, using the reference spectra of Ni_3S_2 and the particular oxide precursor, in order to determine the proportion of Ni present as Ni_3S_2 on the sulfide catalysts (see Table 2-S8). In case of $\text{Ni}(3)\text{MoS}_2$, 92% of the XANES is reproduced by Ni_3S_2 . At higher Ni concentrations the share of Ni_3S_2 decreases to 89% for $\text{Ni}(6)\text{MoS}_2$ and 75% for $\text{Ni}(10)\text{MoS}_2$. These fitting results were not completely satisfactory because they showed significant discrepancies between the experimental and the modeled XANES (Figure 2-S22). Therefore, a second LCF was done by using Ni_3S_2 in combination with spinel NiAl_2O_4 and various other nickel oxide species (see Table 2-S9).^{S4} The proportion of Ni_3S_2 decreased hereby; however, it is still in the same range as following the approach described before. Moreover, the modeled XANES (presented in Figure 2-S22) is in very good agreement to the experimental one.

LCF of sulfide and oxide references revealed that in case of $\text{Ni}(3)\text{MoS}_2$, the XANES can be reproduced by a Ni_3S_2 contribution of 88%. At higher Ni concentrations the contribution of the XANES of Ni_3S_2 decreased to 84% for $\text{Ni}(6)\text{MoS}_2$, 75% for $\text{Ni}(10)\text{MoS}_2$ and to 71% for $\text{NiS}_x/\gamma\text{-Al}_2\text{O}_3$. In parallel, the percentages of the spinel NiAl_2O_4 XANES increased, from 1% for $\text{Ni}(3)\text{MoS}_2$ to 24% for $\text{NiS}_x/\gamma\text{-Al}_2\text{O}_3$. The remaining difference could be represented by the addition of the XANES of various oxides, i.e., NiO , $\text{Ni}(\text{OH})_2$ and NiMoO_4 . However, a perfect reproduction of the experimental XANES of $\text{Ni}(x)\text{MoS}_2$ by LCF with model references was not possible. This indicated the presence of the Ni-Mo-S phase with neighboring Mo and Ni atoms,

which also contributed to the XANES of the sulfide catalysts.^{S4} Note that LCF provides information on the average environment of the elements being analyzed, while it cannot provide an accurate phase composition. However, LCF can be applied to estimate the proportion of Ni in oxide and sulfide environments.

Table 2-S8. Linear combination fitting (LCF) results for the XANES at the Ni K-edge of the sulfide catalysts using the oxidic precursors and Ni₃S₂ for modelling. R factor: the goodness of LCF. Integrated area of the residual: area under the difference spectra (difference between the experimental and the modelled XANES).

Catalyst	Weight of the used XANES, %		R factor	Integrated area of the residual
	oxidic precursor	Ni ₃ S ₂		
Ni(3)MoS ₂	8.5	91.5	0.0046	-3.14
Ni(6)MoS ₂	10.9	89.1	0.0046	-3.55
Ni(10)MoS ₂	25.4	74.6	0.0046	-4.75

Table 2-S9. Linear combination fitting (LCF) results for XANES at the Ni K-edge of the sulfide catalysts using Ni₃S₂ and various oxidic references for modelling. R factor: the goodness of LCF. Integrated area of the residual: area under the difference spectra (difference between the experimental and the modelled XANES).

Catalyst	Weight of the used XANES, %				R factor	Integrated area of the residual
	Ni(OH) ₂ /NiO	Ni ₃ S ₂	NiMoO ₄	NiAl ₂ O ₄		
Ni(3)MoS ₂	3.6	87.5	7.8	1.0	0.0003	-3.14
Ni(6)MoS ₂	6.6	84.4	3.8	5.3	0.0002	-0.93
Ni(10)MoS ₂	8.0	75.0	4.5	12.5	0.0012	-2.16
NiS _x /γ-Al ₂ O ₃	5.3	70.7	-	24.1	0.0006	-2.22

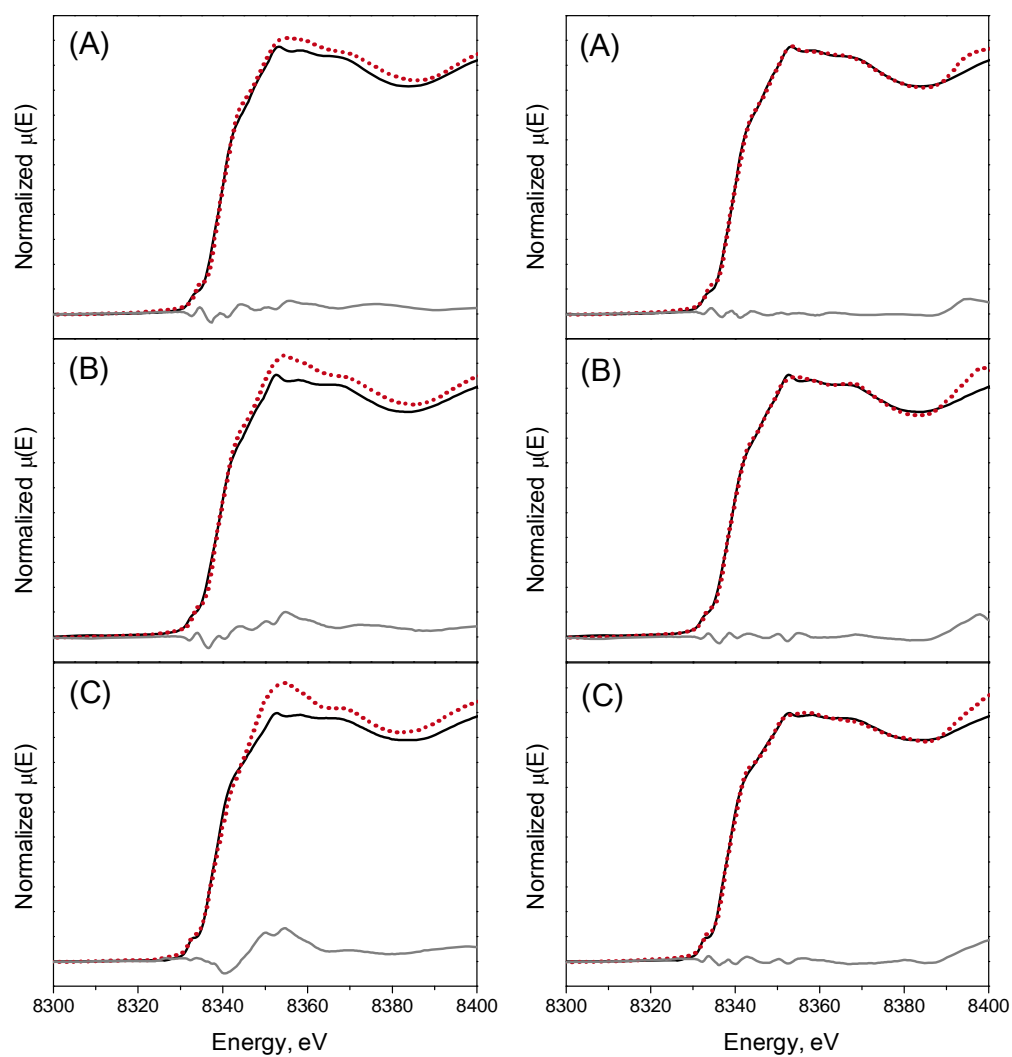


Figure 2-S22. Linear combination fitting (LCF) results for XANES at the Ni K-edge of the sulfide catalysts. Right: LCF using Ni_3S_2 and oxidic catalyst precursors; left: LCF using Ni_3S_2 and various oxide references (see Table 2-S9). Solid line: experimental XANES; dashed line: modeled XANES; gray line: residual of the difference spectra between the experimental and the modelled XANES. (A) $\text{Ni}(3)\text{MoS}_2$; (B) $\text{Ni}(6)\text{MoS}_2$; (C) $\text{Ni}(10)\text{MoS}_2$.

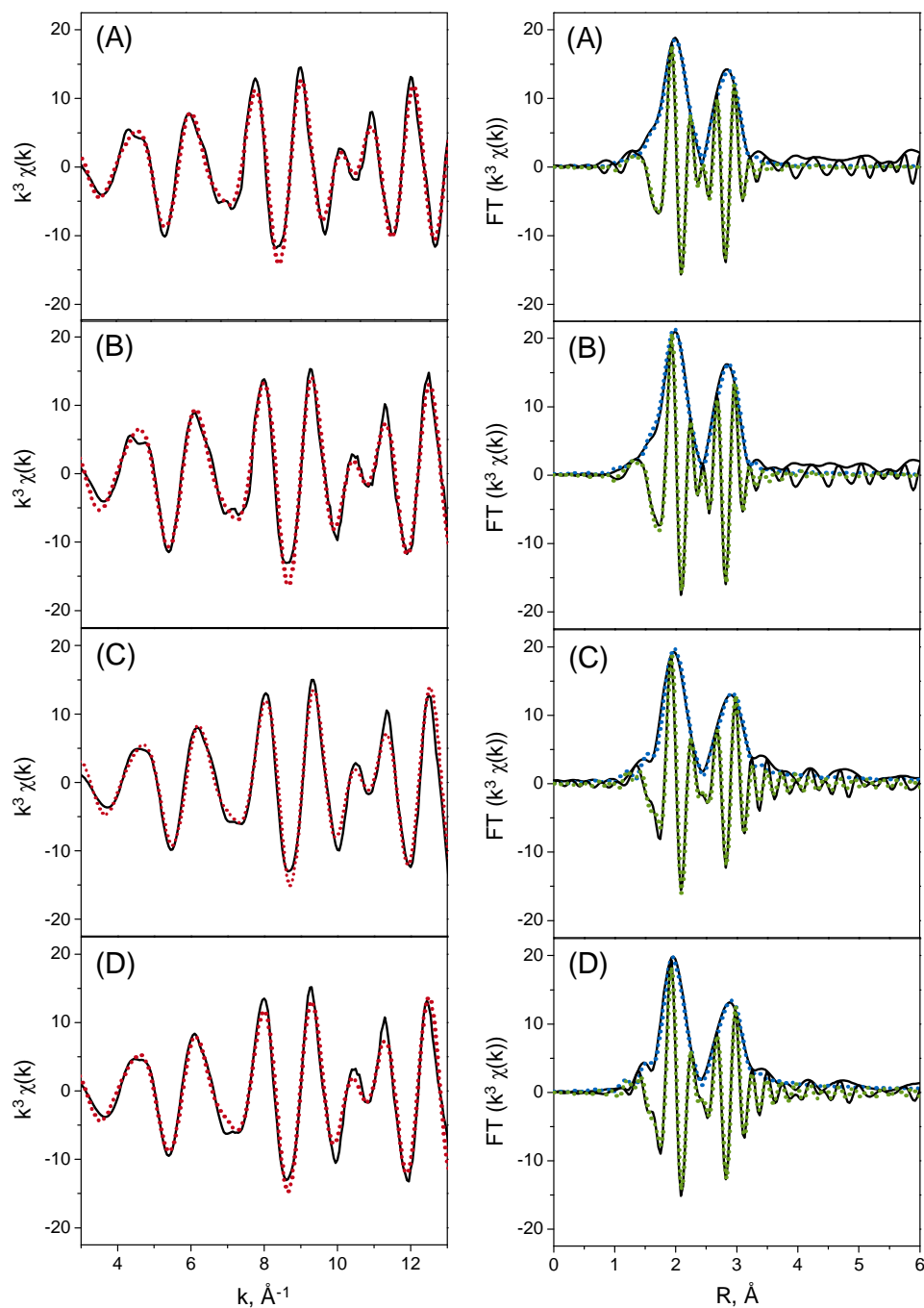


Figure 2-S23. k^3 weighted EXAFS (left) at the Mo K-edge and the corresponding Fourier transforms, magnitudes and imaginary part (right). Solid lines: experimental data, dashed lines: best fit results. (A) $\text{MoS}_2/\gamma\text{-Al}_2\text{O}_3$; (B) $\text{Ni}(3)\text{MoS}_2$; (C) $\text{Ni}(6)\text{MoS}_2$; (D) $\text{Ni}(10)\text{MoS}_2$.

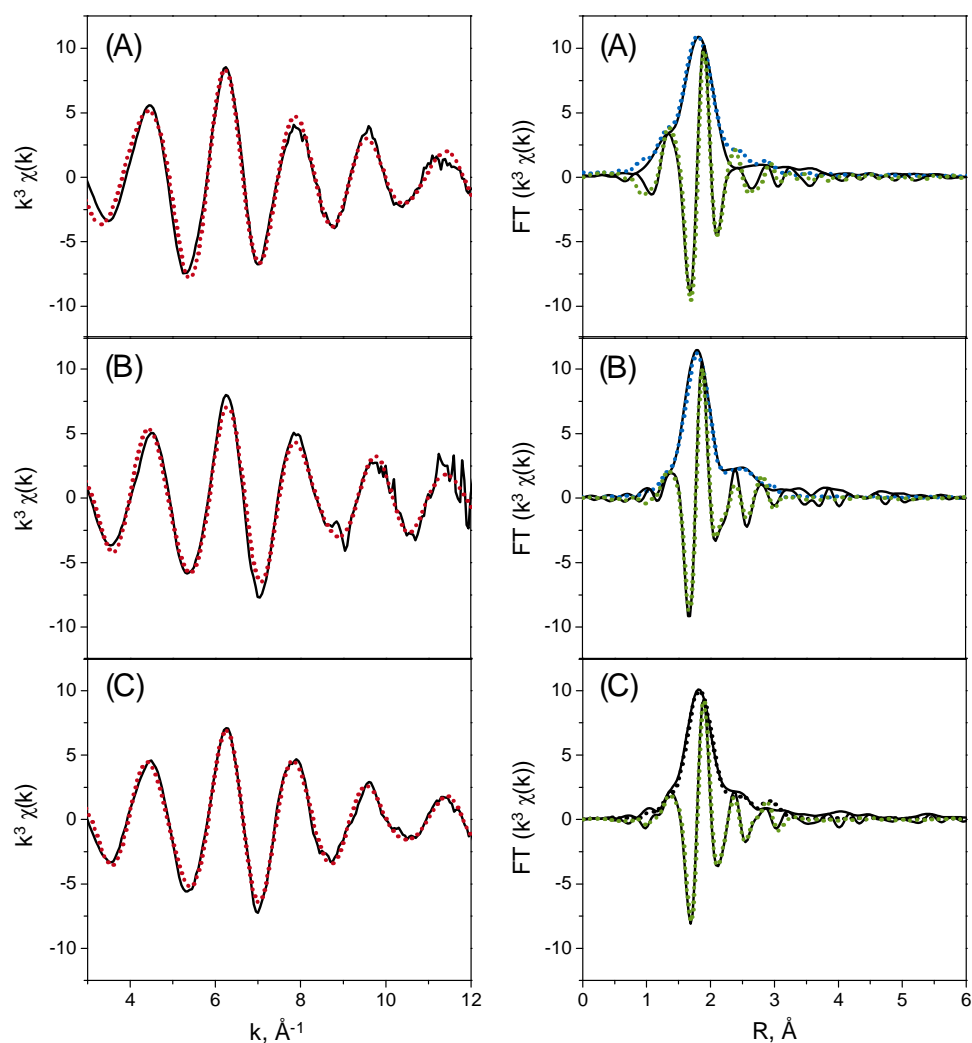


Figure 2-S24. k^3 weighted EXAFS (left) at the Ni K-edge and the corresponding Fourier transforms, magnitudes and imaginary part (right). Solid lines: experimental data, dashed lines: best fit results. (A) Ni(3)MoS₂; (B) Ni(6)MoS₂; (C) Ni(10)MoS₂.

Table 2-S10. Reference bulk materials MoS₂ and Ni₃S₂ taken from literature.^{S4}

Compound	Path	N	$R, \text{Å}$	$\sigma^2, \text{Å}^2$
MoS ₂ ($R=0.0093$) ($E_0=-0.50\pm 4.47$)	Mo-S	5.8 ± 0.6	2.40 ± 0.02	0.0019 ± 0.0007
	Mo-Mo	6.0 ± 0.6	3.16 ± 0.02	0.0014 ± 0.0005
Ni ₃ S ₂ *	Ni-S	2.0	2.23	
	Ni-S	2.0	2.27	
	Ni-Ni	2.0	2.47	
	Mo-Ni	2.0	2.49	

*The structural parameters of Ni₃S₂ correspond to the crystallographic data in ICSD #27521.^{S9}

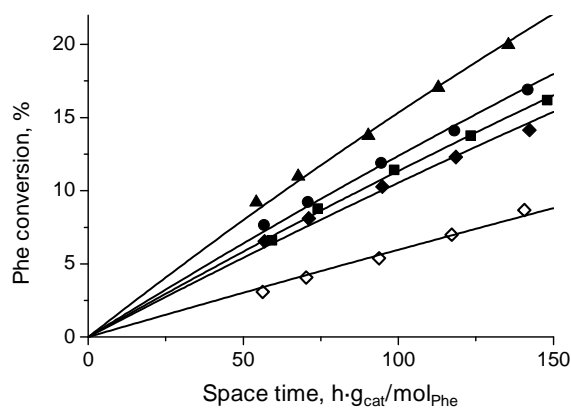
Hydrogenation of phenanthrene

Figure 2-S25. Conversion of phenanthrene as function of space time on $\text{MoS}_2/\gamma\text{-Al}_2\text{O}_3$ (\diamond), $\text{Ni}(1.5)\text{MoS}_2$ (\blacksquare), $\text{Ni}(3)\text{MoS}_2$ (\blacktriangle), $\text{Ni}(6)\text{MoS}_2$ (\bullet) and $\text{Ni}(10)\text{MoS}_2$ (\blacklozenge). The points represent experimental values, the lines correspond to values predicted by the model described in the discussion.

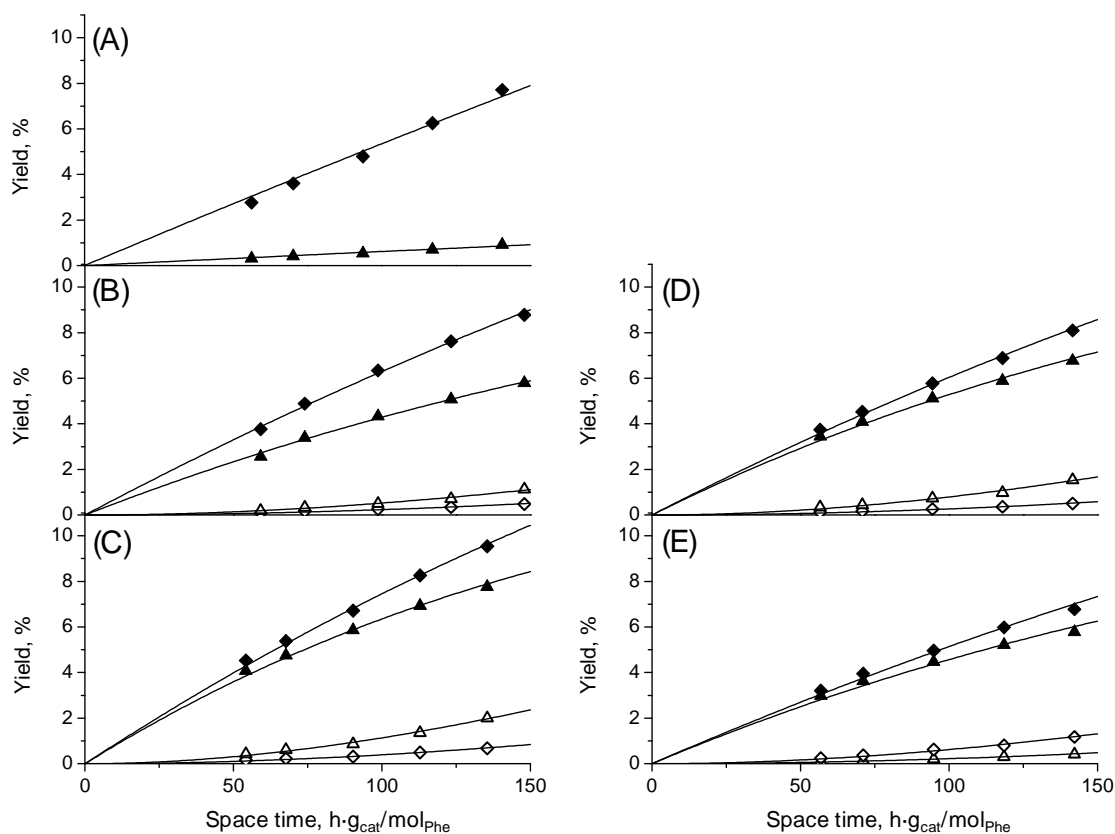


Figure 2-S26. Yield of DiHPhe (\blacklozenge), TetHPhe (\blacktriangle), *sym*OHPhe (\triangle) and *asym*OHPhe (\diamond) as a function of increasing space time. (A) $\text{MoS}_2/\gamma\text{-Al}_2\text{O}_3$, (B) $\text{Ni}(1.5)\text{MoS}_2$, (C) $\text{Ni}(3)\text{MoS}_2$, (D) $\text{Ni}(6)\text{MoS}_2$ (C) $\text{Ni}(10)\text{MoS}_2$.

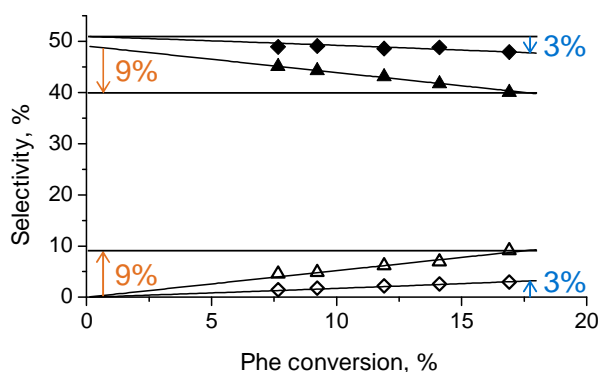


Figure 2-S27. Selectivity of phenanthrene hydrogenation over the catalyst Ni(6)MoS₂ as a function of conversion. DiHPhe (◆), TetHPhe (▲), symOHPhe (△) and asymOHPhe (◇). The arrows mark the corresponding decrease/increase of DiHPhe/asymOHPhe (blue) and TetHPhe/symOHPhe (orange).

Discussion on the equilibrium composition of phenanthrene hydrogenation

Hydrogenation reactions of aromatic hydrocarbons are generally reversible reactions, with equilibrium constants smaller than one at the employed reaction temperature.^{S10,S11} Equilibrium constants (K_{eq}) for phenanthrene hydrogenation at 573 K are taken from Refs.^{S12–S14} and given in Table 2-S11. The equilibrium constant for the hydrogenation of the first ring is generally the highest. However, the reaction to deeper hydrogenated products involves more moles of hydrogen, which results in a thermodynamic preference of deep hydrogenation and leaves the first ring hydrogenation as the least favored. To clarify this relation, an equilibrium concentration K_c is calculated by equation (1) and (2) and included in Table 2-S11. In the equations, $[Phe]$ corresponds to the concentration of phenanthrene and $[Product]$ to the concentration of each phenanthrene hydrogenation product (DiHPhe: 9,10-dihydrophenanthrene, TetHPhe: 1,2,3,4-tetrahydrophenanthrene, symOHPhe: 1,2,3,4,5,6,7,8-octahydrophenanthrene, asymOHPhe: 1,2,3,4,4a,9,10,10a-octahydrophenanthrene). The partial pressure of H₂ (40 bar) is denoted as p_{H_2} and n stands for the mol of hydrogen involved in each reaction.

$$K_{eq} = \frac{[Product]}{[Phe] \cdot p_{H_2}^n} \quad (1)$$

$$K_c = \frac{[Product]}{[Phe]} = K_{eq} \cdot p_{H_2}^n \quad (2)$$

Regarding phenanthrene, the reaction to DiHPhe is the thermodynamically least preferred, because only one mole of hydrogen is involved in the reaction. At 573 K the ratio of DiHPhe/Phe is found to be 1.1. At phenanthrene conversions below 20%, however, the concentration of DiHPhe never exceeds the concentration of Phe, giving DiHPhe/Phe ratios below unity. Hence, the influence of the thermodynamic equilibrium can be considered as insignificant and is neglected in the reaction network presented in Figure 2-10.

Table 2-S11. Equilibrium constants (K_{eq}) for the hydrogenation of phenanthrene at 573 K taken from Refs.^{S10,S11,S14}. K_c are the predicted equilibrium concentrations calculated by equation (1).

Reaction	log K_{eq} at 573 K	K_c at 573 K
Phe + H ₂ ⇌ DiHPhe	-1.57	1.1
Phe + 2 H ₂ ⇌ TetHPhe	-1.79	26
Phe + 4 H ₂ ⇌ OHPhe	-3.64	587
Phe + 7 H ₂ ⇌ PerHPhe	-6.02	156466

Set of differential equations derived from the reaction network of the hydrogenation of Phe

$$\frac{d[\text{Phe}]}{dt} = -k_1 \cdot [\text{Phe}] - k_2 \cdot [\text{Phe}] \quad (3)$$

$$\frac{d[\text{DiHPhe}]}{dt} = k_1 \cdot [\text{Phe}] - k_3 \cdot [\text{DiHPhe}] \quad (4)$$

$$\frac{d[\text{TetHPhe}]}{dt} = k_2 \cdot [\text{Phe}] - k_4 \cdot [\text{TetHPhe}] \quad (5)$$

$$\frac{d[\text{asymOHPhe}]}{dt} = k_3 \cdot [\text{DiHPhe}] \quad (6)$$

$$\frac{d[\text{symOHPhe}]}{dt} = k_4 \cdot [\text{TetHPhe}] \quad (7)$$

In the equations, ' k_i ' is the reaction constants of the step ' i ' as shown in Figure 2-10 and ' $[j]$ ' represents the concentration of compound ' j '. The experimental measurements were fitted using a CMA-ES algorithm programmed in the Matlab software. The resulting rate constants are reported in Table 2-5 of the main text. The fitting was very good as seen in Figure 2-9 (main text) and Figure 2-S25 and S26.

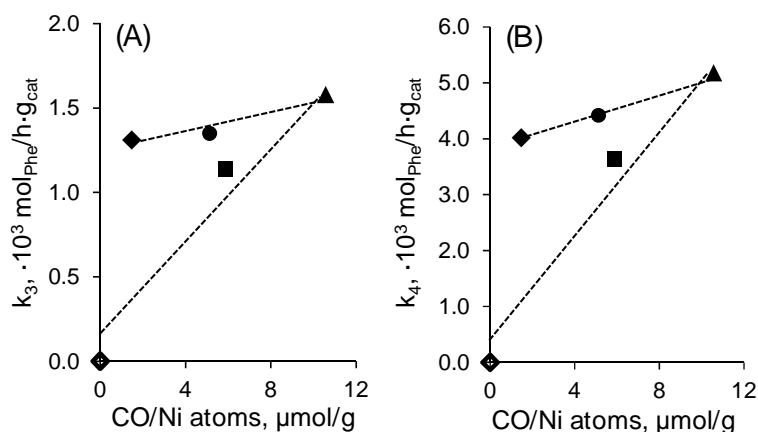


Figure 2-S28. Correlation of the rate constants k_3 (A) and k_4 (B) with the concentration of CO adsorbed on Ni atoms decorating MoS₂. MoS₂/γ-Al₂O₃ (◇), Ni(1.5)MoS₂ (■), Ni(3)MoS₂ (▲), Ni(6)MoS₂ (●) and Ni(10)MoS₂ (◆).

Development of model sulfide particles

According to TEM, the average slab length in MoS₂/γ-Al₂O₃ was 55 Å. This corresponded to 17 Mo atoms in the diagonal of a hexagonal particle. Moreover, the average stacking degree was 1.5, therefore, a single slab or two stacked slabs were representative of the MoS₂ phase. The distance between stacked slabs was 6.1 Å. Thus, EXAFS analysis did not provide further structural information in this respect. In case of Ni-containing catalysts, the average MoS₂ particle on the Ni(x)MoS₂ materials consisted of 2 stacked slabs with a length of 46 Å (Table 2-2), which corresponded to 14 Mo atoms in the diagonal of a hexagonal particle. The visualizations of the average MoS₂ particles for MoS₂/γ-Al₂O₃ and Ni(x)MoS₂ (denoted as “MoS₂-17x17” and “MoS₂-14x14”, respectively) are depicted in Figure 2-S29.

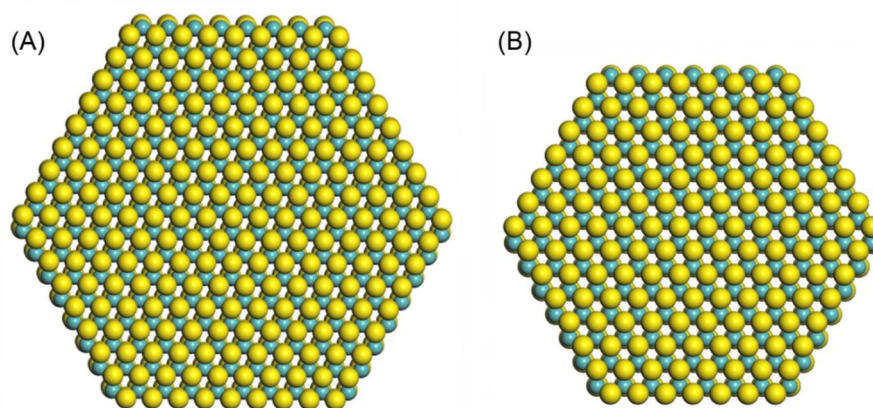


Figure 2-S29. Simulated MoS₂ hexagonal structure 17x17 (A) and 14x14 (B).

In order to visualize the Ni-containing species in Ni(x)MoS₂/γ-Al₂O₃, we have taken the MoS₂-14x14 model as base (according to TEM, the slab length did not vary to the extent of justifying a particular base MoS₂ slab per material). The first step in order to create the models has been to randomly exchange Mo by Ni atoms preferentially, but not exclusively, at the metal edge of MoS₂ as was suggested by DFT calculations.^{S15} The substitution was done until the Mo-Ni coordination numbers of the models was equal to the $N_{\text{Mo-Ni}}$ values produced by the EXAFS fitting. The values of $N_{\text{Ni-Mo}}$ were adjusted by introducing NiS_x clusters into the models constraining the amount of Ni in each model to the Ni to Mo molar ratio in the sulfide phases. In turn, the fraction of Ni in the sulfide phases was calculated subtracting the concentration of Ni in the NiAl₂O₄ spinel (LCF of the experimental XANES) from the total concentration of Ni (elemental analysis). In order to illustrate the changes in the concentration of decorating Ni atoms with increasing Ni loading, we assumed that the presence of small NiS_x clusters at the edges of MoS₂ in Ni(3)MoS₂ is negligible (this sample exhibited the highest concentration of NO uptake and CO adsorbed on decorating Ni atoms). Then small NiS_x clusters were added at the edges of Ni(6)MoS₂, and Ni(10)MoS₂ in order to decrease the number of single Ni atoms

proportionally to the decrease in the concentration of decorating Ni atoms observed by CO adsorption (IR spectroscopy).

Table 2-S12. Coordination numbers $N_{\text{Mo-S}}$ and $N_{\text{Mo-Mo}}$ calculated from simulated model particles.

Model compound	$N_{\text{Mo-S}}$	$N_{\text{Mo-Mo}}$
MoS ₂ 14x14	5.4	5.7
MoS ₂ 17x17	5.5	5.8
MoS ₂ 19x19	5.6	5.8

Table 2-S13. Comparison of the Ni/(Mo+Ni) ratios determined by elemental analysis, by LCF analysis and those corresponding to the models in Figure 2-S29 and 11. Differentiation between the number of Ni atoms substitution the edges of Ni(x)MoS₂/γ-Al₂O₃ ($N_{\text{atoms-edge}}$) and the total number of atoms, including the Ni₃S₂ crystals ($N_{\text{atoms-total}}$).

Catalyst	Elemental analysis	LCF analysis	$N_{\text{atoms-edge}}$ in models			decorating Ni atoms	$N_{\text{atoms-total}}$ in models		
	Ni/(Ni+Mo)	Ni/(Ni+Mo)	Mo	Ni*	Ni/(Ni+Mo)		Mo	Ni	Ni/(Ni+Mo)
MoS ₂ /Al ₂ O ₃	-	-	78	-	-	-	294	-	-
Ni(3)MoS ₂	0.33	0.30	54	24	0.31	24	269	127	0.32
Ni(6)MoS ₂	0.49	0.45	48	30	0.38	12	264	223	0.46
Ni(10)MoS ₂	0.62	0.55	42	36	0.46	4	258	310	0.54

* The Ni atoms ($N_{\text{atoms-edge}}$) substituting the edges of MoS₂ are partially blocked by growing NiS_x particles. This means that not all Ni atoms sitting at the edges of MoS₂ can be considered as “decorating Ni atoms”, which are exclusively those Ni atoms freely accessible and detected, e.g. by CO-IR.

References

- (S1) Gutiérrez, O. Y., Valencia, D., Fuentes, G., Klimova, T. *J. Catal.* **2007**, *249*, 140–153.
- (S2) Williams, C. C., Ekerdt, J. G., Jehng, J. M., Hardcastle, F. D., Wachs, I. E. *J. Phys. Chem.* **1991**, *95*, 8791–8797.
- (S3) Williams, C. C., Ekerdt, J. G., Jehng, J. M., Hardcastle, F. D., Turek, A. M., Wachs, I. E. *J. Phys. Chem.* **1991**, *95*, 8781–8791.
- (S4) Hein, J., Hrabar, A., Jentys, A., Gutiérrez, O. Y., Lercher, J. A. *ChemCatChem* **2014**, *6*, 485–499.
- (S5) Scheffer, B., Heijeinga, J. J., Moulijn, J. A. *J. Phys. Chem.* **1987**, *91*, 4752–4759.
- (S6) Travert, A., Dujardin, C., Maugé, F., Veilly, E., Cristol, S., Paul, J.-F., Payen, E. *J. Phys. Chem. B* **2006**, *110*, 1261–70.
- (S7) Maugé, F., Lavalley, J.-C. *J. Catal.* **1992**, *137*, 69–76.
- (S8) Kondratieva, E. V., Manoilova, O. V., Tsyganenko, A. A. *Kinet. Catal.* **2008**, *49*, 451–456.
- (S9) Belsky, A., Hellenbrandt, M., Karen, V. L., Luksch, P. *Acta Crystallogr. Sect. B Struct. Sci.* **2002**, *58*, 364–369.
- (S10) M. J. Girgis, B. C. Gates, *Ind. Eng. Chem. Res.* **1991**, *30*, 2021–2058.

- (S11) A. Stanislaus, B. Cooper, *Catal. Rev.* **1994**, 36, 75–123.
- (S12) C. G. Frye, *J. Chem. Eng. Data* **1962**, 7, 592–595.
- (S13) C. G. Frye, A. W. Weitkamp, *J. Chem. Eng. Data* **1969**, 14, 372–376.
- (S14) J. Ancheyta, J. G. Speight, *Hydroprocessing of Heavy Oils and Residua*, Taylor & Francis, **2007**.
- (S15) M. Sun, A. E. Nelson, J. Adjaye, *J. Catal.* **2004**, 226, 32–40.

Individual Contribution

E.S. prepared the catalytic materials, constructed and engineered the setup for IR spectroscopy, performed and evaluated the characterization experiments and kinetic reactions, conducted the XAS experiments, prepared and edited the manuscript. E.K. designed and performed experiments in the IR setup. L.Z. contributed to the analysis of IR and XAS spectra. J.H. contributed to the XAS experiments. O.Y.G. and A.J. assisted the IR setup construction, guided experiments, contributed to the scientific discussion and edited the paper. J.A.L. edited the manuscript and contributed to results discussion.

Chapter 3

Pathways for H₂ activation on (Ni)-MoS₂ catalysts

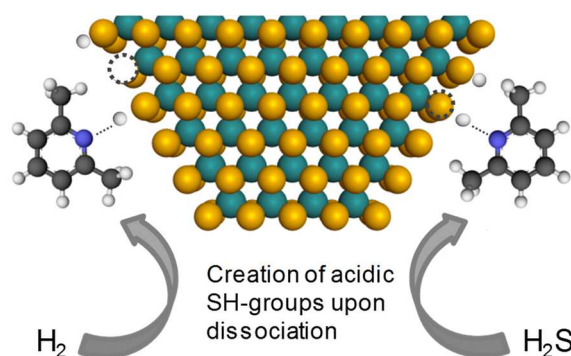
This chapter is based on:

Eva Schachtl, Elena Kondratieva, Oliver Y. Gutiérrez and Johannes A. Lercher “Pathways for H₂ activation on (Ni)-MoS₂ catalysts.” *J. Phys. Chem. Lett.*, **2015**, 6 (15), pp 2929–2932.
DOI: 10.1021/acs.jpcclett.5b01217

Reprinted with permission from American Chemical Society, Copyright 2015.

Abstract:

The activation of H₂ and H₂S on (Ni)MoS₂/Al₂O₃ leads to the formation of SH-groups with acid character able to protonate 2,6-dimethylpyridine. The variation in concentrations of SH-groups induced by H₂ and H₂S adsorption shows that both molecules dissociate on coordinatively unsaturated cations and neighboring S²⁻. In the studied materials one sulfur vacancy and four SH-groups per 10 metal atoms exist at the active edges of MoS₂ under the conditions studied. H₂-D₂ exchange studies



show that Ni increases the concentration of active surface hydrogen by up to 30 % at the optimum Ni loading, by increasing the concentration of H₂ and H₂S chemisorption sites.

3.1. Introduction

Molybdenum sulfide catalysts have been widely studied, because they are key catalysts in several processes including hydrotreating reactions, and synthesis of alcohols and thiols.¹⁻⁴ The interest to fundamentally understand the catalytic properties of MoS₂ has recently increased because of the potential of these materials in photoelectrochemical applications.^{5,6} In consequence, spectacular advances in imaging,⁷⁻⁹ preparation of sulfide materials,¹⁰ and DFT studies aiming to understand molecular mechanisms occurring on the sulfide materials have been achieved.¹¹⁻¹³ However, experiment-based insight into the routes in which H₂ is activated and (dissociatively) chemisorbed has not advanced at the same rate.

It was proposed early on that after dissociation, hydrogen atoms bond to S²⁻ anions to form SH-groups.¹⁴ It was established that these SH-groups are weakly acidic and located primarily at the edges of the MoS₂ slabs.¹⁵ Unfortunately, direct spectroscopic characterization of such groups is very challenging and has been reported scarcely.¹⁵⁻¹⁶ Titration with a base is, in contrast, a more practical approach to quantitatively characterize SH-groups. 2,6-dimethylpyridine (DMP) has been successfully applied for this purpose.¹⁷⁻¹⁸

To better understand the nature of sites dissociating H₂ in hydrotreating reactions, we explored the concentration of SH-groups created *via* activation of H₂ on Al₂O₃-supported MoS₂ promoted with different concentrations of Ni. Adsorption of H₂S was used to quantify the concentration of Lewis acid sites. The mechanism and nature of H₂ activation on the sulfide surface was further explored by H₂-D₂ isotope exchange experiments.

3.2. Results and Discussion

The series of Al₂O₃-supported Ni-promoted MoS₂ materials was prepared *via* impregnation with S-free precursors, calcination and sulfidation at 673 K and 20 bar H₂S/H₂ (10 vol.% of H₂S). The Mo content was kept constant at 1 mmol·g⁻¹ for all samples, whereas the Ni concentrations varied. The samples were denoted as MoS₂/Al₂O₃ and Ni(x)MoS₂/Al₂O₃, x being the nominal content of Ni in wt.-%. A detailed description of the synthesis and basic catalysts characterization is provided in chapter 2. For IR characterization, sulfidation was done inside the IR-cell for 2 h at high pressure, followed by evacuation to 10⁻⁶ mbar for 1 h. After cooling to 323 K, 2,6-dimethylpyridine (DMP) was adsorbed to determine the concentration of acid sites and compare to the concentration of DMP after admission of H₂ or H₂S.

Figure 3-1a shows the DMP spectra of a selected catalyst before and after adsorption of H₂S. The main bands of adsorbed DMP at 1650 and 1625 cm⁻¹ are assigned to the ring vibrations (ν_{8a} and ν_{8b} modes) of the protonated base. DMP interacting with Lewis acid sites is characterized by a band at 1618 cm⁻¹, whereas weakly, physisorbed DMP gives a band at 1602 cm⁻¹. The band at 1580 cm⁻¹ is caused by DMP adsorbed on Lewis acid and weakly interacting sites.¹⁸⁻¹⁹ The intensity of the bands at 1650 and 1625 cm⁻¹ increased after adsorption of H₂S. In parallel, the intensity of the bands between 1618 and 1580 cm⁻¹ decreased. This leads to the conclusion that by adsorption of H₂S a fraction of Lewis acid sites is converted to Brønsted acid sites. Table 3-1 shows the concentration of DMP, which is protonated on the sulfided materials and after adsorption of H₂S (spectra of all materials and examples of deconvolution are presented in the supporting information). As one DMP is adsorbed per SH-group, values in Table 3-1 correspond to the concentration of acid SH-groups protonating DMP. Al₂O₃ has some Brønsted acid sites able to protonate DMP, and after H₂S adsorption a low concentration of additional acidic SH-groups were formed. However, the initial concentration of acidic groups (only 20 μmol·gcat⁻¹) and the concentration of H₂S activated on alumina are less than 20 % of the average concentration of the Mo-containing catalysts. The contribution of the acid sites on Al₂O₃ in the supported (Ni)MoS₂ is expected to be even lower, because MoS₂ will cover a significant fraction of the specific surface area of Al₂O₃. Thus, we conclude that the observations discussed here mainly correspond to changes induced in the MoS₂ phase.

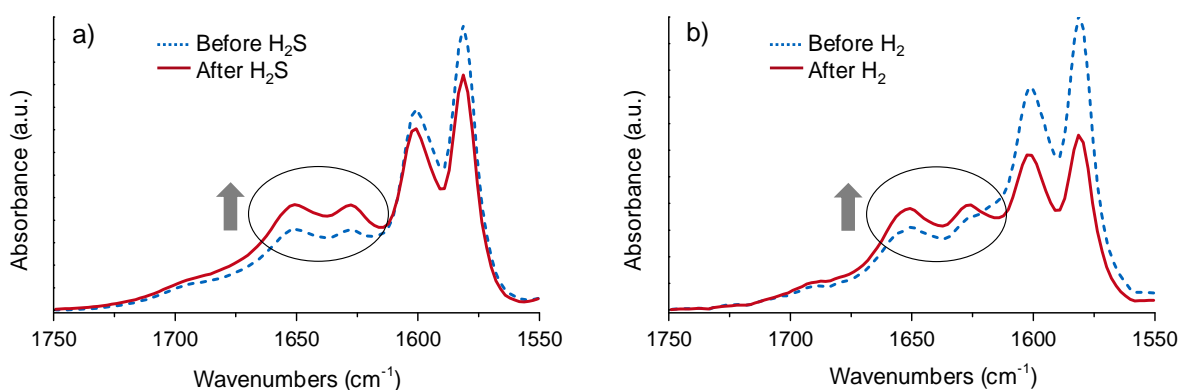


Figure 3-1. IR spectra of 2,6-dimethylpyridine (DMP) adsorbed on Ni(3)MoS₂/Al₂O₃ before (dashed line) and after (solid line) admission of H₂S (a) and H₂ (b). The equilibration pressure of DMP was 0.5 mbar, whereas the total pressure after admission of H₂S was 1 mbar and after H₂ was 1 bar.

The concentration of acidic SH-groups increased with the Ni loading until a Ni·(Mo+Ni)⁻¹ molar ratio of 0.33 (Ni(3)MoS₂/Al₂O₃) and decreased at higher loadings. This holds true for the as-sulfided samples, as well as for the samples after adsorption of H₂S (creating additional Brønsted acid sites). It indicates that the variations in the concentration of Lewis sites in the as-sulfided materials, where H₂S is activated, and the concentration of acidic SH-groups follow

the same trends. Furthermore, the maximum concentration of acidic SH-groups at a Ni molar ratio of 0.33 coincides with the optimum Ni loading (maximum promoter effect) reported for hydrotreating reactions (a comparison of reported catalytic activities is presented in the supporting information).

Table 3-1. Concentration of 2,6-dimethylpyridine protonated on as-sulfided catalysts and after H₂S adsorption ($\mu\text{mol}\cdot\text{g}^{-1}$).

Catalyst	As-sulfided	After H ₂ S adsorption	Difference
Al ₂ O ₃	20	21	1
MoS ₂ /Al ₂ O ₃	79	98	19
Ni(1.5)MoS ₂	93	114	21
Ni(3)MoS ₂	95	119	24
Ni(6)MoS ₂	87	109	22
Ni(10)MoS ₂	86	106	20

Figure 3-1b shows the spectra of DMP adsorbed on Ni(3)MoS₂/Al₂O₃ before and after the adsorption of H₂ (the spectra of all materials are presented in the supporting information). Adsorption of H₂ led to a decrease in DMP interacting weakly with the surface or with Lewis sites, while the concentration of DMP interacting with Brønsted sites increased. Table 3-2 compiles the concentration of 2,6-dimethylpyridine, which is protonated on the parent sulfided catalysts and after adsorption of H₂. As H₂ adsorption does not induce formation of acid sites in Al₂O₃, variations in the concentration of adsorbed DMP in the presence of MoS₂ are attributed to the activation of H₂ and the formation of SH-groups in the sulfide phase.

Table 3-2. Concentration of 2,6-dimethylpyridine protonated on as-sulfided catalysts and after H₂ adsorption ($\mu\text{mol}\cdot\text{g}^{-1}$).

Catalyst	As-sulfided	After H ₂ adsorption	Difference
Al ₂ O ₃	17	17	0
MoS ₂ /Al ₂ O ₃	76	88	12
Ni(1.5)MoS ₂	82	96	14
Ni(3)MoS ₂	91	107	16
Ni(6)MoS ₂	71	79	8
Ni(10)MoS ₂	75	83	8

The dependence in the formation of SH-groups on the Ni loading is identical for adsorption of H₂ as for H₂S. Indeed, there is a linear correlation between the concentration of acid sites created after H₂S and after H₂ adsorption on materials with Ni loading up to Ni·(Mo+Ni)⁻¹=0.33, as shown in Figure 3-2. Interestingly, the materials with high concentrations of Ni do not obey this relation. At present, we attribute this to the additional formation of a segregated Ni sulfide species at high Ni loadings.⁴ Direct evidence of increasing concentration of SH-groups after H₂

and H₂S activation is observed in the 3200-3900 cm⁻¹ region. The broadness of the corresponding band, however, hinders quantitative analysis (see the supporting information).

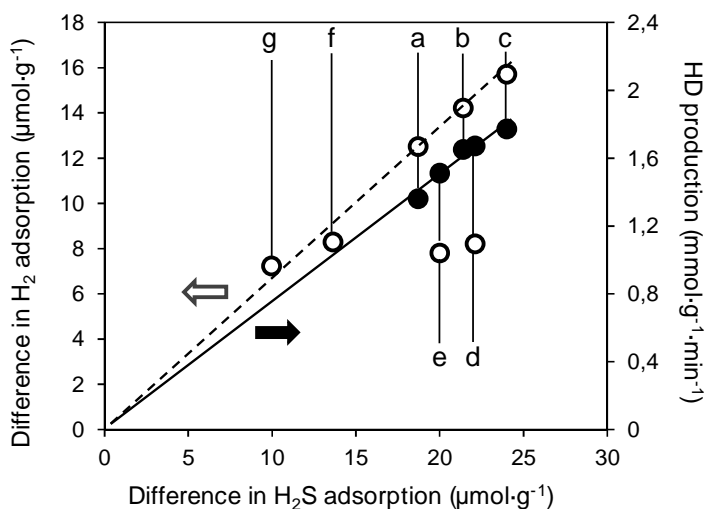


Figure 3-2. Correlation of the increase of Brønsted sites on adsorption of H₂S with the increase on adsorption of H₂ (dashed line, open circles, left y-axis) and the rates of HD production (continuous line, filled circles, right y-axis). The data correspond to MoS₂/Al₂O₃ (a), Ni(1.5)MoS₂/Al₂O₃ (b), Ni(3)MoS₂/Al₂O₃ (c), Ni(6)MoS₂/Al₂O₃ (d), Ni(10)MoS₂/Al₂O₃ (e), MoS₂/Al₂O₃-A (f), NiMoS₂/Al₂O₃-B (g). Information of the latter two samples is provided in the supporting information.

In order to better understand the nature of the SH-groups two types of H₂-D₂ scrambling experiments were performed. One of them was a transient experiment during which the catalysts were exposed to an atmosphere of H₂ after sulfidation, followed by a rapid transition to D₂. In the other experiment, samples of the catalysts were used to catalyze H₂-D₂ exchange by flowing an equimolar mixture of H₂ and D₂ at 1 bar and 353 K. Details of the experiments and the profiles of HD evolution in transient and continuous modes are shown in the supporting information. Table 3-3 compiles the concentrations of HD released during both kinds of experiments.

In general, the amount and rates of HD evolution on the sulfide catalysts varied in parallel with the concentration of acid sites induced by adsorption of H₂S and H₂. The rates of formation of HD increased with the content of Ni up to a Ni·(Mo+Ni)⁻¹ molar ratio of 0.33. Compared to MoS₂/Al₂O₃, the rate increased by 30 % on Ni(3)MoS₂/Al₂O₃.

Table 3-3. Evolution and production rates of HD determined by scrambling experiments.

Catalyst	HD concentration, μmol·g _{cat} ⁻¹	HD production rate, mmol·g _{cat} ⁻¹ ·min ⁻¹
MoS ₂ /Al ₂ O ₃	240	1.36
Ni(1.5)MoS ₂	250	1.65
Ni(3)MoS ₂	280	1.77
Ni(6)MoS ₂	280	1.67
Ni(10)MoS ₂	260	1.51

The values obtained here agree well with previous reports (quantitative comparisons are provided in the supporting information). The rates of HD formation correlate linearly with the concentration of Brønsted sites created by the adsorption of H₂S (Figure 3-2), indicating that the sites able to dissociatively adsorb H₂S are also able to react H₂ and D₂. The concentration of Brønsted sites able to protonate DMP was much lower than the amount of HD evolved in the site titrating transient experiments. This is attributed to the presence of two types of H₂ species on the materials, i.e., H₂ dissociatively adsorbed on the edges of MoS₂ (which is the one probed by DMP), and a hydrogen species that remains adsorbed or absorbed on the support and the sulfide phase and that, being replaced by D₂, might diffuse towards the active sites and react during the transient experiments. Differentiation of H₂ adsorbed on the sulfide phase and stored in Al₂O₃ has been reported.²⁰

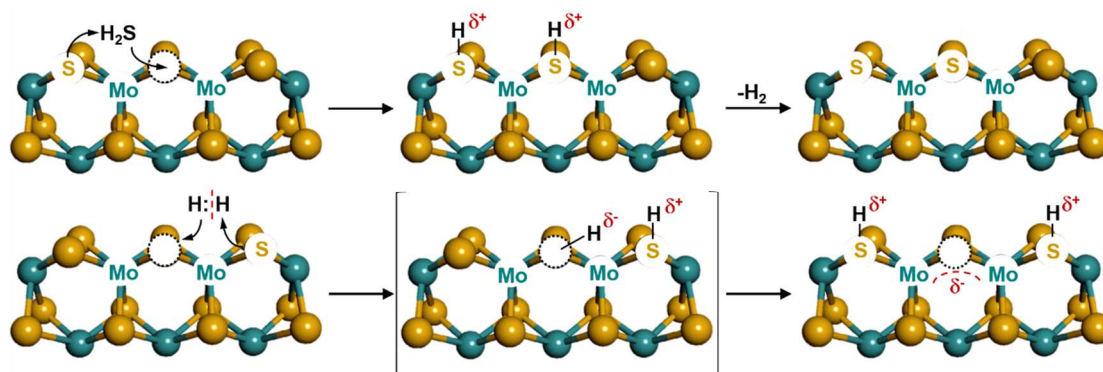
The effect of Ni on MoS₂ for hydrogen activation and scrambling is strikingly low, considering its strong impact on catalysis. The concentrations of acidic SH-groups increase first with Ni loading and pass a maximum, while the HD formation rates change similarly, exhibiting the same dependence on Ni loading. Therefore, we conclude that the main role of Ni in supported Ni-Mo sulfide is to increase the concentration of sites able to adsorb H₂ dissociatively.

The concentration of DMP protonated on the as-sulfided materials corresponds to the concentration of SH-groups produced during sulfidation (“as-sulfided” values in Table 3-1), whereas the increase in DMP concentration after adsorption of H₂S (“difference” values in Table 3-1) corresponds to the concentration of vacancies. Accordingly, the concentrations of sites in the as-sulfided materials are approximately 10 SH-groups and 3 vacancies per 100 Mo atoms in the sample, or 4 SH-groups and 1 vacancy per 10 Mo atoms at the edges of MoS₂ (see the supporting information for details and values corresponding to each sample).

3.3. Conclusions

Based on the present experiments, we propose that H₂ and H₂S are activated on identical sites in MoS₂, i.e., Lewis acid-base pairs (vacancies and S²⁻ anions, Scheme 3-1). The involvement of these paired sites suggests that the dissociative adsorption of H₂S and H₂ occurs heterolytically in the initial step. The dissociation of H₂S creates two SH-groups. As they are structurally identical, the nature of the SH-groups after dissociative adsorption is identical, both being acidic (represented as δ⁺ in Scheme 3-1). Not all SH-groups, however, may be able to protonate DMP due to steric hindrance induced by the size of DMP (Mo-Mo distance in MoS₂ is 3.17 Å, whereas the methyl groups of DMP are 4.83 Å apart).

Scheme 3-1. Visualization of the mechanisms proposed for the activation of H₂S and H₂ on (Ni)-MoS₂. In the case of H₂S (up), the formation of ideal MoS₂ after H₂ release is shown.

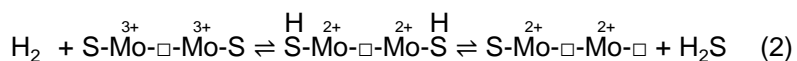
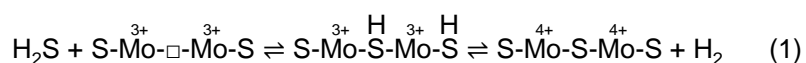


We propose that in the initial state H₂ dissociates, producing transiently an acidic SH-group and a hydride. Some authors have proposed the existence of metal-hydride species (e.g., Mo-H) and recent DFT calculations have suggested that their formation is feasible.^{11-13,21} However, DFT studies also indicate that Mo-H species are not thermodynamically favored. This leads to the conclusion that after the initial H₂ dissociation, the hydride species reacts further with the adjacent sulfur anions forming additional SH-groups.²² Thus, the overall process is homolytic dissociation with a heterolytic transition state (shown in brackets in Scheme 3-1).

During the transformation of the hydride to an SH-group (as during the creation of CUS itself), the excess electrons would partially reduce the adjacent cations. This could produce reduced Mo states at the edges (Mo^{<4+}), which has been displayed as a delocalized negative charge in Scheme 3-1. Accordingly, some studies have related the formation of vacancies to reduced states of Mo.²³ Alternatively, the negative charges might be delocalized due to the semiconductor nature of MoS₂ (with a band gap of 1.3 eV).

Dissociative adsorption of H₂S will not reduce the oxidation state of MoS₂. If followed by H₂ recombinative desorption, the formal oxidation state of the Mo cations involved will be increased to +4 (Scheme 3-2 (1)). In contrast, dissociation of H₂ would reduce the catalyst towards less favored formal oxidation states +2 (Scheme 3-2 (2)). In addition, the H-H bond has a higher energy than the S-H bond (436 vs. 339 kJ·mol⁻¹, respectively). These facts render demanding H₂ activation and, therefore, smaller concentrations of Brønsted acid sites after adsorption of H₂ than after H₂S.

Scheme 3-2. Dissociation of H₂S (1) and H₂ (2) on MoS₂ including formal oxidation states of MoS₂.



In conclusion, first experimental evidence for the formation of acidic SH-groups after H₂ chemisorption on supported (Ni)-MoS₂ is provided. Low to moderate concentrations of Ni increase the concentration of S vacancies and SH-groups. H₂-D₂ exchange experiments indicate a uniform reactivity of the sites involving accessible cations catalyzing this exchange. At the optimum Ni concentration, $\text{Ni} \cdot (\text{Mo} + \text{Ni})^{-1} = 0.33$, the concentration of active surface hydrogen increased approximately 30 % compared to not-promoted MoS₂/Al₂O₃.

3.4. References

- (1) Chianelli, R. R.; Berhault, G.; Torres, B. *Catal. Today* **2009**, *147*, 275–286.
- (2) Andersson, R.; Boutonnet, M.; Järås, S. *Appl. Catal. A Gen.* **2012**, *417-418*, 119–128.
- (3) Gutiérrez, O. Y.; Zhong, L.; Zhu, Y.; Lercher, J. A. *ChemCatChem* **2013**, *5*, 3249–3259.
- (4) Bensch, W. Hydrotreating: Removal of Sulfur from Crude Oil Fractions with Sulfide Catalysts, In *Comprehensive Inorganic Chemistry II* (2nd Edition), edited by Reedijk J. and Poeppelemeier K.; Elsevier, Amsterdam; 2013, 287-321.
- (5) Hinnemann, B.; Moses, P. G.; Bonde, J.; Jørgensen, K. P.; Nielsen, J. H.; Horch, S.; Chorkendorff, I.; Nørskov, J. K. *J. Am. Chem. Soc.* **2005**, *127*, 5308–5309.
- (6) Jaramillo, T. F.; Jørgensen, K. P.; Bonde, J.; Nielsen, J. H.; Horch, S.; Chorkendorff, I. *Science* **2007**, *317*, 100–102.
- (7) Zhu, Y.; Ramasse, Q. M.; Brorson, M.; Moses, P. G.; Hansen, L. P.; Kisielowski, C. F.; Helveg, S. *Angew. Chem. Int. Ed. Engl.* **2014**, *53*, 10723–10727.
- (8) Dumcenco, D. O.; Kobayashi, H.; Liu, Z.; Huang, Y.-S.; Suenaga, K. *Nat. Commun.* **2013**, *4*, 1–5.
- (9) Hansen, L. P.; Ramasse, Q. M.; Kisielowski, C.; Brorson, M.; Johnson, E.; Topsøe, H.; Helveg, S. *Angew. Chem. Int. Ed. Engl.* **2011**, *50*, 10153–10156.
- (10) Yonemoto, B. T.; Hutchings, G. S.; Jiao, F. A. *J. Am. Chem. Soc.* **2014**, *136*, 8895–8898.
- (11) Prodhomme, P.-Y.; Raybaud, P.; Toulhoat, H. *J. Catal.* **2011**, *280*, 178–195.
- (12) Sun, M.; Nelson, A. E.; Adjaye, J. *J. Catal.* **2005**, *233*, 411–421.
- (13) Travert, A.; Nakamura, H.; van Santen, R. A.; Cristol, S.; Paul, J.-F.; Payen, E. *J. Am. Chem. Soc.* **2002**, *124*, 7084–7095.
- (14) Ratnasamy, P.; Fripiat, J. J. *Trans. Faraday Soc.* **1970**, *66*, 2897–2910.
- (15) Topsøe, N.-Y.; Topsøe, H. *J. Catal.* **1993**, *139*, 641–651.
- (16) Wright, C. J.; Sampson, C.; Fraser, D.; Moyes, R. B.; Wells, P. B.; Riekel, C. *J. Chem. Soc. Faraday Trans. 1 Phys. Chem. Condens. Phases* **1980**, *76*, 1585–1598.
- (17) Gutiérrez, O. Y.; Hrabar, A.; Hein, J.; Yu, Y.; Han, J.; Lercher, J. A. *J. Catal.* **2012**, *295*, 155–168.
- (18) Travert, A.; Maugé, F. *Stud. Surf. Sci. Catal.* **1999**, *127*, 269–277.
- (19) Oliviero, L.; Vimont, A.; Lavalley, J.-C.; Romero, F.; Gaillard, M.; Maugé, F. *Phys. Chem. Chem. Phys.* **2005**, *7*, 1861–1869.

- (20) Thomas, C.; Vivier, L.; Travert, A.; Maugé, F.; Kasztelan, S.; Pérot, G. *J. Catal.* **1998**, *502*, 495–502.
- (21) Anderson, A. B.; Al-Saigh, Z. Y.; Hall, W. K. *J. Phys. Chem.* **1988**, *92*, 803–809.
- (22) Toulhoat, H.; Raybaud, P. *J. Catal.* **2003**, *216*, 63–72.
- (23) Leliveld, R. G.; van Dillen, A. J. V.; Geus, J. W.; Koningsberger, D. C. *J. Catal.* **1997**, *171*, 115–129.

3.5. Supporting Information

Experimental methods

Spectroscopic experiments

The adsorption of 2,6-dimethylpyridine (DMP, Aldrich, ≥99.0%) on the (Ni)MoS₂/Al₂O₃ materials was followed by IR spectroscopy using a Nicolet 6700 FT-IR spectrometer equipped with a MCT detector having a resolution of 4 cm⁻¹. A dedicated flow/vacuum IR cell allowed the *in situ* sulfidation of the samples at 20 bar and 673 K (3 K·min⁻¹) in flowing H₂S/H₂ (10 vol.-% of H₂S) and the subsequent adsorption of DMP, and H₂S or H₂ at 323 K in vacuum conditions without exposing the sample to air. The powders were pressed into self-supported wafers (10 mg·cm⁻²), and placed inside the IR cell. After two hours at sulfidation conditions, the cell was flushed with He for 10 min, evacuated to a residual pressure of 10⁻⁶ mbar keeping 673 K for another 1h and then cooled to 323 K. In order to perform the adsorption experiments, small doses of DMP were admitted to the cell up to an equilibrium pressure of 0.5 mbar. After recording the spectra at such conditions, H₂S or H₂ were admitted to the cell up to a total pressure of 1 mbar (or 1 bar for H₂) and another set of spectra was recorded. The intensities of the bands were quantitatively determined using the OMNIC software. The spectra were deconvoluted following the assignment of Ref.^{S1}. Five contributions, located between 1550 and 1700 cm⁻¹ were considered. The bands at 1650 and 1625 cm⁻¹ were assigned to protonated DMP, whereas DMP on Lewis acid sites was located at 1618 and 1580 cm⁻¹. Weakly interacting DMP was considered to appear at 1602 and 1580 cm⁻¹. For Ni(3)MoS₂/Al₂O₃ the deconvoluted spectra before and after admission of DMP, H₂S and H₂ are shown exemplary in Figure 3-S5. The concentration of protonated DMP was calculated using the molar extinction coefficient reported in Ref.^{S2} ($\epsilon_{\nu_{8a}} = 6.5 \text{ cm} \cdot \mu\text{mol}^{-1}$).

H₂-D₂ transient and continuous experiments

The H₂-D₂ experiments were carried out at atmospheric pressure in a quartz reactor inside a ceramic oven after drying of the oxidic sample at 773 K in synthetic air and *in situ* sulfidation at 673 K in 10 vol.-% of H₂S/H₂. In a typical experiment, a sample of the oxide precursor of 0.1 g (250-355 μm) was placed in the reactor, and hold in place by quartz wool. Mass flow controllers (Bronkhorst) were used to introduce the sulfidation mixture as well as H₂, D₂, and

N₂ (diluting gas). The effluent of the reactor was analyzed on-line with a mass spectrometer (Pfeiffer Vacuum QME 200) recording the signals of the masses (m/e) 2 (H₂), 3 (HD), 4 (D₂), and 34 (H₂S).

The transient experiments consisted of exposing the *in situ* sulfide materials to a flow of H₂ (10 vol.-% in N₂) for 1.5 h at 353 K (avoiding so reduction of the materials as confirmed by the absence of H₂S evolution). After flushing with N₂ for another 1.5 h, the flow was quickly changed to D₂ (10 vol.-% in N₂). The gas composition was monitored until HD evolution was not observed.

The continuous H₂-D₂ scrambling was performed as space time dependent experiments (defined as m_{cat}/F where m_{cat} is the mass of the catalyst and F is the molar flow of H₂ and D₂) at 353 K, keeping equimolar concentrations of H₂ and D₂.

Preparation of additional (Ni)MoS₂/Al₂O₃ materials

In order to demonstrate the correlation between the concentrations of acid sites created after adsorption of H₂S and H₂, additional sulfide materials were prepared. For MoS₂/Al₂O₃-A, the synthesis procedure described above was employed. The Mo content was 1.18 mmol·g⁻¹. The sample NiMoS₂/Al₂O₃-B contained 0.96 mmol·g⁻¹ Mo and 0.36 mmol·g⁻¹ Ni, giving a Ni·(Mo+Ni)⁻¹ ratio of 0.27. The oxide precursor of this sample was treated at 833 K in air.

Results

Spectra of 2,6-dimethylpyridine adsorbed on the (Ni)-MoS₂/Al₂O₃ materials before and after adsorption of H₂S or H₂

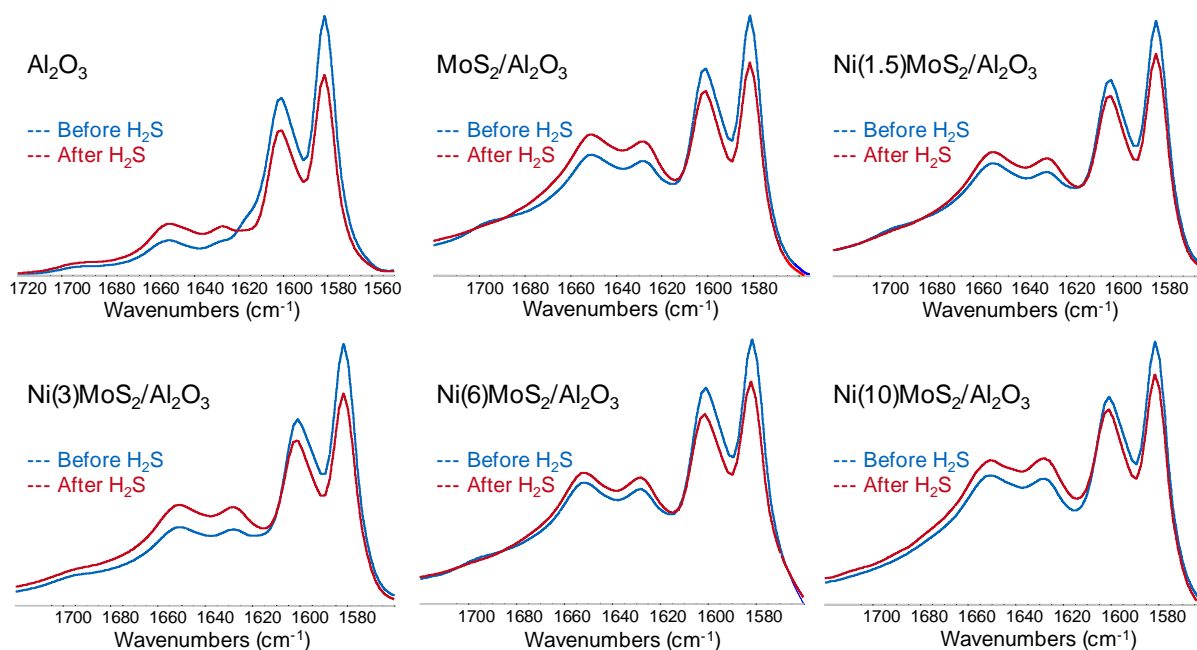


Figure 3-S3. Spectra of 2,6-dimethylpyridine (DMP) adsorbed on pure Al₂O₃ and on the (Ni)MoS₂/Al₂O₃ materials before (blue) and after (red) adsorption of H₂S at 323 K. The equilibration pressure of DMP was 0.5 mbar and 1 mbar for H₂S.

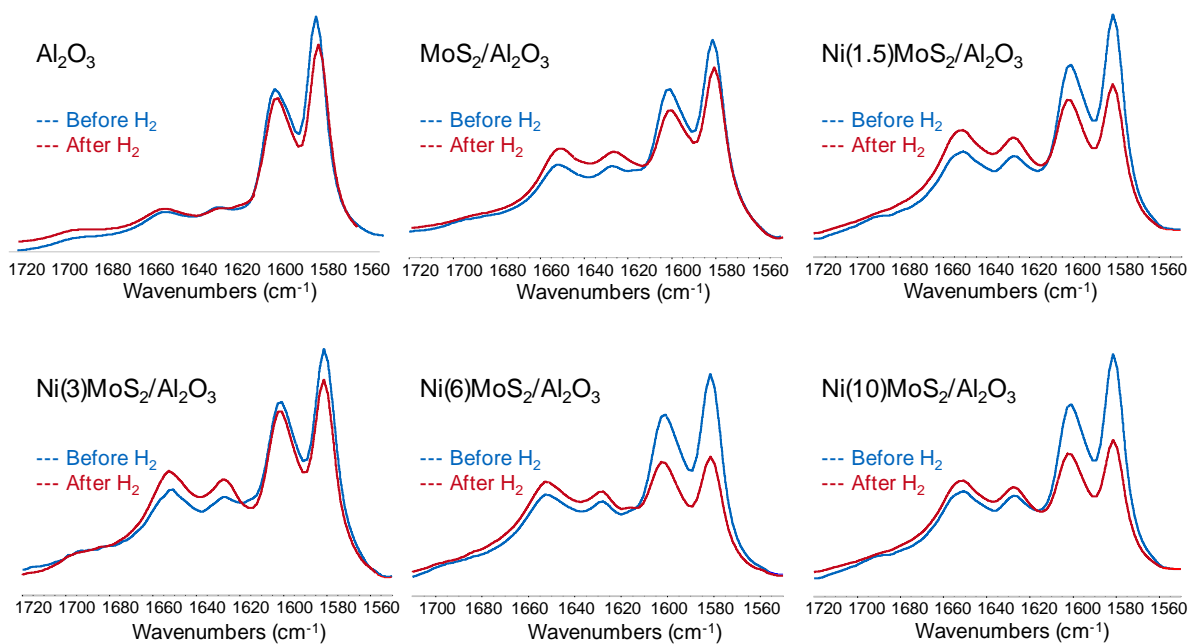


Figure 3-S4. Spectra of 2,6-dimethylpyridine (DMP) adsorbed on pure Al₂O₃ and on the (Ni)MoS₂/Al₂O₃ materials before (blue) and after (red) adsorption of H₂ at 323 K. The equilibration pressure of DMP was 0.5 mbar and 1 bar for H₂.

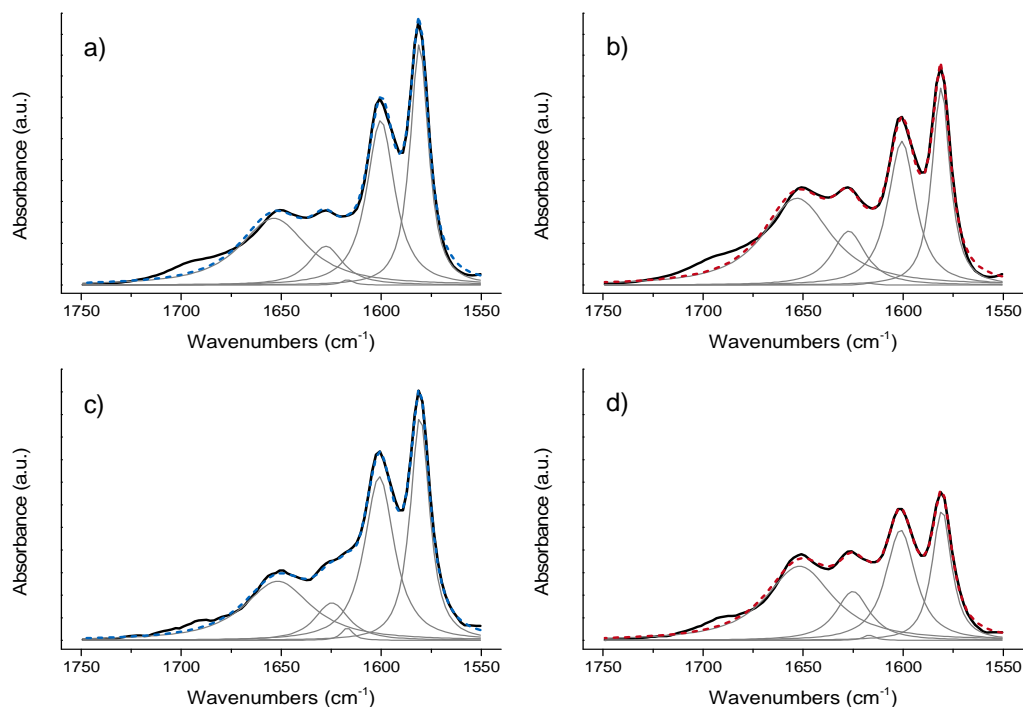


Figure 3-S5. Deconvoluted spectra of 2,6-dimethylpyridine (DMP) adsorbed on Ni(3)MoS₂. Adsorption of 0.5 mbar DMP (a, c), after addition of 1 mbar H₂S (b), after addition of 1 bar H₂ (d). Black: experimentally recorded data; dashed: fitted curve; gray: contributions of the individual species (vide supra).

IR spectra in the 3200-3900 cm^{-1} region

Direct evidence of increasing concentration of SH-groups after H_2 and H_2S activation is observed in the 3200-3900 cm^{-1} region with the band attributable to SH-groups (as shown in Figure 3-S6 for a selected catalyst). However, we have not analyzed this region because the bands are so broad that the subtle changes are not quantifiable. Tøpsoe *et al.*^{S5} performed a semiquantitative analysis of this SH band when varying the amount of Mo in the catalyst, which leads to appreciable changes in intensity.

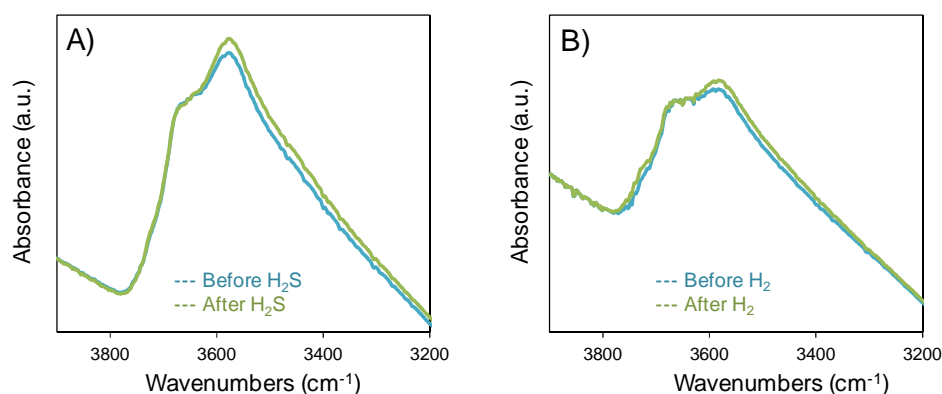


Figure 3-S6. IR spectra showing the SH-region (3200-3900 cm^{-1}) after adsorption of 2,6-dimethylpyridine on $Ni(3)MoS_2/Al_2O_3$ - before (blue) and after (green) admission of H_2S (A) and H_2 (B).

H_2 - D_2 isotopic transient and continuous experiments

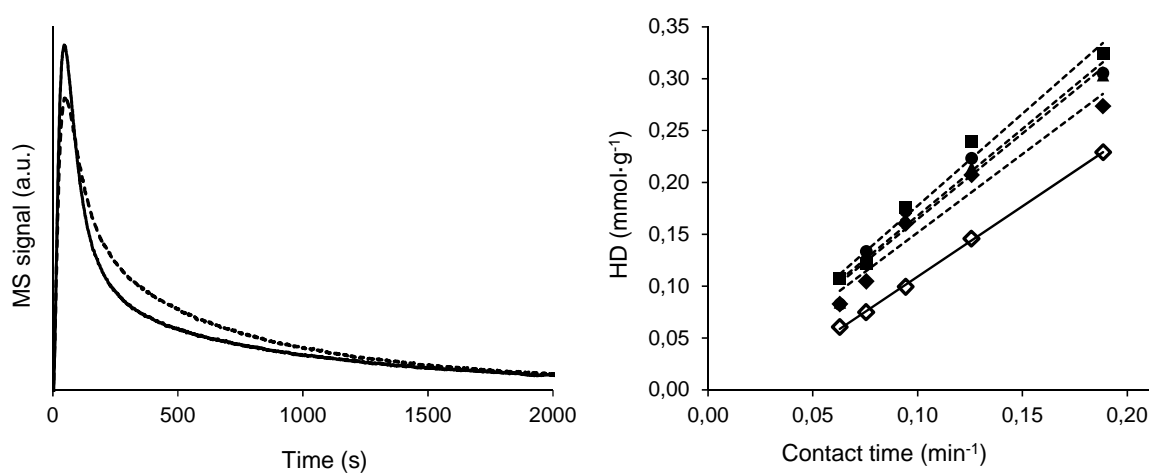


Figure 3-S7. Profiles of HD evolution on the $(Ni)MoS_2/Al_2O_3$ materials (A) during the switch transient experiments, and (B) during the continuous reaction $H_2+D_2\rightarrow 2HD$ as a function of contact time. Conditions: 353 K, atmospheric pressure. Solid line: MoS_2/Al_2O_3 ; dashed line: $(Ni)MoS_2/Al_2O_3$. (\diamond) MoS_2/Al_2O_3 , (\blacktriangle) $Ni(1.5)MoS_2$, (\blacksquare) $Ni(3)MoS_2$, (\bullet) $Ni(6)MoS_2$, (\blacklozenge) $Ni(10)MoS_2$.

Discussion

Comparison of the results in this work with previous studies

The research on MoS₂-based catalysts has a long history and many groups have made important contributions to the understanding of their catalytic chemistry. Isotopic exchange has been a valuable tool to investigate the rates of reaction involving hydrogen on sulfide materials (although the studies are not as abundant as one would have expected). In this section we compare previous insightful reports on H-D exchange with the results of the isotope experiments in this work.^{S4, S6-S9} The comparisons are summarized in Table 3-S4. For the sake of clarity, the data has been recalculated to be presented in the same units.

The rates of HD formation determined for our series of catalysts is in excellent agreement with the values previously determined for similar catalysts although some scatter exists. The concentrations of adsorbed hydrogen and the molar H/Mo ratios calculated in this work are in general lower than those reported before. However, given the important contribution of hydrogen stored in the support,^{S6,S9} comparisons of these values are difficult due to the different thermal treatments applied to the supports.

Table 3-S4. Summary of rates of HD production (r_{HD}), adsorbed H amounts (n_H), and atomic H/Mo ratios (considering total Mo content) calculated in this work and in other reports.

Sulfided material ¹	Ref.	r_{HD} , $10^{-6} \text{ mol}_{HD} \cdot (\text{s} \cdot \text{g}_{cat})^{-1}$	n_H , $10^{-3} \text{ mol}_H \cdot \text{g}_{cat}^{-1}$	H/Mo
Mo(9)/Al ₂ O ₃	This work ²	22.7	0.48	0.05
Ni(1.3)Mo(9)/Al ₂ O ₃	This work ²	27.5	0.50	0.06
Ni(3)Mo(9)/Al ₂ O ₃	This work ²	29.5	0.56	0.07
Ni(5)Mo(9)/Al ₂ O ₃	This work ²	27.8	0.56	0.06
Ni(9)Mo(9)/Al ₂ O ₃	This work ²	25.2	0.52	0.06
NiO(3)-MoO ₃ (12)/Al ₂ O ₃	S6 ² , S7 ²	1.98	2.40	2.8
Mo(8)/Al ₂ O ₃	S8 ²	25	-	-
Ni(3)Mo(8)/Al ₂ O ₃	S8 ²	22	-	-
Mo(9)/Al ₂ O ₃	S9 ³	4-11	-	0.1-1.1
Ni(3)Mo(9)/Al ₂ O ₃	S9 ³	11-28	-	0.5-1.3
Mo(8)/C	S10 ⁴	0.62	6.3	-
Co(1.3)Mo(6)/C	S10 ⁴	2.00	7.0	-

¹ The numbers in brackets indicate the content (wt.-%) of the metal/compound on the left.

² The H₂-D₂ reactions were performed at 353 K and 1 bar.

³ The H₂-D₂ reactions were performed at 273 K.

⁴ The H₂-D₂ reactions were performed at 673 K.

Correlation of spectroscopic observations with Mo content and TEM analysis

Let us correlate the concentration of protonated 2,6-dimethylpyridine (DMP) determined during the spectroscopic experiments with the total concentration of Mo (Mo_{Total}) and the fraction of Mo at the edges (Mo_{Edge}) of MoS₂ determined from TEM analysis (vide supra). Table 3-S5 shows the DMP/Mo ratios (for total Mo and edge Mo) before, and after H₂S adsorption. Table 3-S5 shows the ratios corresponding to the experiments of H₂ activation. As expected, in both cases (activation of H₂S and H₂) the DMP/Mo_{Total} ratios clearly follow the same trend as observed with the concentration per gram of catalyst (as the Mo content is very similar on all samples). In contrast, the differences among the catalysts fade when the DMP/Mo_{Edge} ratios are calculated. We attribute these remarkably similar values to compensation of both effects of Ni observed in this work: increasing dispersion and increasing the concentration of vacancies. In any case, within the experimental error the trends are preserved and the small differences in the H/Mo_{Edge} ratios confirm that the effect of Ni on the interaction of (Ni)-MoS₂ with H₂ is a very subtle one.

The comparison between TEM and IR spectroscopy allows the quantification of adsorption sites in the sulfide catalysts. We assume that the concentration of DMP protonated on the as-sulfided materials corresponds to the concentration of SH-groups produced during sulfidation, whereas the increase in its concentration after adsorption of H₂S corresponds to the concentration of vacancies. With these considerations we can estimate that the concentrations of sites in the as-sulfided materials are ca. 10 SH-groups (“DMP/Mo_{Total}-Ante H₂S” in Table 3-S5) and 2 vacancies per 100 Mo atoms in the sample (“DMP/Mo_{Total}-Difference” in Table 3-S5), or 4 SH-groups (“DMP/Mo_{Edge}-Ante H₂S” in Table 3-S5) and 1 vacancy (“DMP/Mo_{Edge}-Difference” in Table 3-S5) per 10 Mo atoms at the edges of MoS₂.

Table 3-S5. Ratios of protonated 2,6-dimethylpyridine (DMP) to Mo calculated from the spectroscopic experiments before the adsorption of H₂S, after the adsorption of H₂S and the difference of those values. DMP/Mo_{Total} is based on the total amount of Mo in the sample, whereas DMP/Mo_{Edge} is based on the amount of Mo at the edges of the corresponding MoS₂ phase as determined from TEM analysis.

Catalyst	DMP/Mo _{Total} Before H ₂ S	DMP/Mo _{Total} After H ₂ S	DMP/Mo _{Total} Difference	DMP/Mo _{Edge} Before H ₂ S	DMP/Mo _{Edge} After H ₂ S	DMP/Mo _{Edge} Difference
MoS ₂ /Al ₂ O ₃	0.083	0.103	0.020	0.381	0.473	0.090
Ni(1.5)MoS ₂	0.101	0.124	0.023	0.395	0.485	0.091
Ni(3)MoS ₂	0.100	0.125	0.025	0.377	0.472	0.095
Ni(6)MoS ₂	0.098	0.122	0.025	0.373	0.467	0.095
Ni(10)MoS ₂	0.095	0.117	0.022	0.364	0.448	0.085

Table 3-S6. Ratios of protonated 2,6-dimethylpyridine (DMP) to Mo calculated from the spectroscopic experiments before the adsorption of H₂, after the adsorption of H₂ and the difference of those values. DMP/Mo_{Total} is based on the total amount of Mo in the sample, whereas DMP/Mo_{Edge} is based on the amount of Mo at the edges of the corresponding MoS₂ phase as determined from TEM analysis.

Catalyst	DMP/Mo _{Total}			DMP/Mo _{Edge}		
	Before H ₂	After H ₂	Difference	Before H ₂	After H ₂	Difference
MoS ₂ /Al ₂ O ₃	0.079	0.093	0.013	0.364	0.425	0.060
Ni(1.5)MoS ₂	0.089	0.104	0.015	0.347	0.407	0.060
Ni(3)MoS ₂	0.096	0.112	0.017	0.361	0.423	0.062
Ni(6)MoS ₂	0.079	0.088	0.009	0.302	0.337	0.035
Ni(10)MoS ₂	0.082	0.091	0.009	0.316	0.349	0.033

Comparison of the catalytic performance of MoS₂-based catalysts with varying Ni loadings

Molar Ni·(Mo+Ni)⁻¹ ratios of about 0.3 are usually accepted as the optimum Ni loading for Ni-promoted MoS₂. However, studies reporting systematic variations of Ni loading in MoS₂-based catalysts and its effect on activity are scarce. Hydrodesulfurization of thiophene and dibenzothiophenes has been reported in Refs.^{S11-S12}, hydrogenation of *o*-xylene and phenanthrene has been reported in Refs.^{S13-S14}. Figure 3-S8 shows the variation of the activity of MoS₂/Al₂O₃ promoted with varying Ni loadings. For the sake of comparison, the values presented in Figure 3-S8 have been normalized with respect to the maximum activities. The optimum Ni loadings are indeed around 0.3 for hydrodesulfurization and hydrogenation.

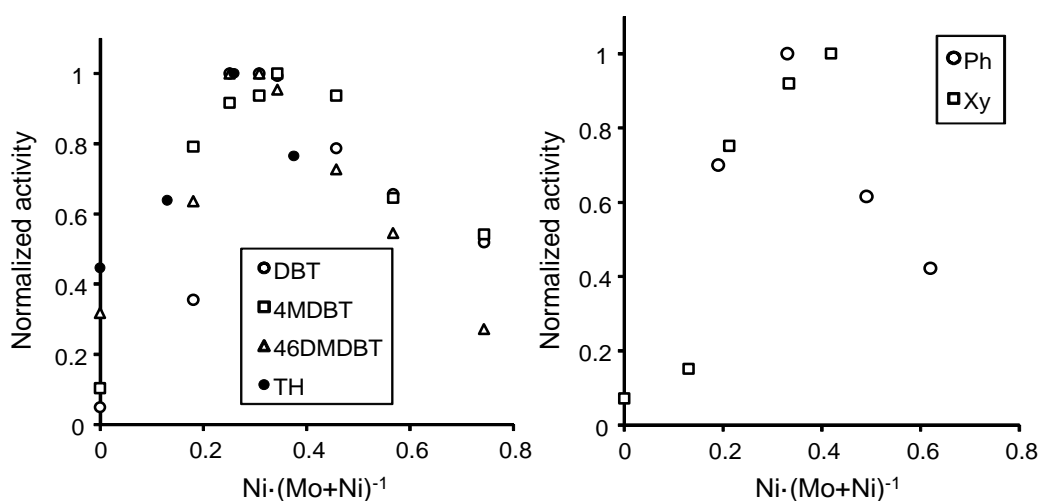


Figure 3-S8. Normalized activity of (Ni)MoS₂/Al₂O₃ with varying Ni·(Mo+Ni)⁻¹ molar ratios for hydrodesulphurization (left) of dibenzothiophene (DBT), 4-methyldibenzothiophene (4MDBT), 4,6-dimethyldibenzothiophene (46DMDBT), and thiophene (TH), and hydrogenation (right) of phenanthrene (Ph) and *o*-xylene (Xy).

Note that the differences in activity between the optimal promoted catalyst and not-promoted MoS₂ are from a factor of 2 to one order of magnitude. That is, much more than the registered increase in the concentration of acidic SH-groups (~30%). Thus, we speculate that the increase in concentration of SH produced by Ni promotion do not contribute to a large extent to the changes in catalytic performance (at least for the reactions reported in Figure 3-S8).

References

- (S1) Travert, A., Maugé, F. *Stud. Surf. Sci. Catal.* **1999**, 127, 269–277.
- (S2) Gaillard, M. PhD-Thesis, University of Caen, France 2005.
- (S3) Hensen, E. J. M., Kooyman, P. J., van der Meer, Y., van der Kraan, A. M., de Beer, V. H. J., van Veen, J. A. R., van Santen, R. A. *J. Catal.* **2001**, 199, 224–235.
- (S4) Kasztelan, S., Toulhoat, H., Grimblot, J., Bonnelle, J. A. *Appl. Catal.* **1984**, 13, 127–159.
- (S5) Topsøe, N.-Y., Topsøe, H. *J. Catal.* **1993**, 139, 641–651.
- (S6) Thomas, C., Vivier, L., Lemberon, J. L., Kasztelan, S., Pérot, G. *J. Catal.* **1997**, 167, 1–11.
- (S7) Thomas, C., Vivier, L., Travert, A., Maugé, F., Kasztelan, S., Pérot, G. *J. Catal.* **1998**, 179, 495–502.
- (S8) Thomas, C., Vivier, L., Lescanne, M., Kasztelan, S., Pérot, G. *Catal. Letters* **1999**, 58, 33–35.
- (S9) Lacroix, M., Dumonteil, C., Breyse, M., Kasztelan, S. *J. Catal.* **1999**, 185, 219–222.
- (S10) Hensen, E. J. M., Lardinois, G. M. H. J., de Beer, V. H. J., van Veen, J. A. R., van Santen, R. A. *J. Catal.* **1999**, 187, 95–108.
- (S11) Gao, Q., Ofosu, T. N. K., Ma, S.-G., Komvokis, V. G., Williams, C. T., Segawa, K. *Catal. Today* **2011**, 164 (1), 538–543.
- (S12) Tétényi, P., Schnörch, P., Tellingner, O. *React. Kinet. Lett.* **2009**, 97, 141-150.
- (S13) Fischer, L., Harlé, V., Kasztelan, S. *Stud. Surf. Sci. Catal.* **1999**, 127, 261-268.
- (S14) Schachtl, E., Wuttke, E., Gutiérrez, O.Y., Lercher, J. A. 'Effect of Ni on the Characteristics and Hydrogenation Activity of Sulfide Mo/ γ -Al₂O₃.' *DGMK-Tagungsbericht 2012-3*, Germany, 2012, 227-233, ISBN 978-3-941721-26-5.

Individual Contribution

E.S. prepared the catalytic materials, constructed and engineered the setup for IR spectroscopy, performed and evaluated the reactions and IR experiments, prepared and edited the manuscript. E.K. designed and performed experiments in the IR setup. O.Y.G. and J.A.L. guided experiments, contributed to the scientific discussion and edited the paper.

Chapter 4

Mechanistic implications of Ni promotion on the hydrogenation of phenanthrene over MoS₂/γ-Al₂O₃

Abstract:

Hydrogenation on phenanthrene (Phe) and 9,10-dihydrophenanthrene (DiHPhe) is carried out on γ-Al₂O₃ supported MoS₂ and Ni-MoS₂ catalysts in order to interrogate the overall and elementary reaction steps taking place during the hydrogenation of polycyclic aromatic compounds. Two main routes prevail for the hydrogenation of Phe at 553-583 K and conversions below 15%, i.e, path 1: Phe → DiHPhe → 1,2,3,4,4a,9,10,10a-octahydrophenanthrene (*asym*OHPhe), and path 2: Phe → 1,2,3,4-tetrahydrophenanthrene (TetHPhe) → 1,2,3,4,5,6,7,8-octahydrophenanthrene (*sym*OHPhe). On MoS₂/Al₂O₃, the hydrogenation of Phe proceeds preferentially *via* path 1 (with a path 1/path 2 selectivity ratio of 9), whereas the reaction of DiHPhe follows mainly dehydrogenation to Phe. In contrast, during the hydrogenation of Phe on Ni-MoS₂/Al₂O₃, the selectivities towards path 1 and path 2 are similar, and during the reaction of DiHPhe hydrogenation steps increase considerably. In turn, Ni addition increases the overall hydrogenation activity by a factor of 2.5. With increasing conversions, both, the hydrogenation of Phe and the dehydrogenation of DiHPhe are enhanced, and the reaction steps TetHPhe → *asym*OHPhe (hydrogenation), and DiHPhe → TetHPhe (hydrogenation-isomerization) become evident. During the hydrogenation of Phe, the

reaction orders in H_2 increase from ~ 0.7 and ~ 0.9 (paths 1 and 2, respectively) for MoS_2/Al_2O_3 to ~ 1.1 and ~ 1.3 (paths 1 and 2) for $Ni-MoS_2/Al_2O_3$. In contrast, the reaction orders in Phe do not change to a large extent with Ni promotion (0.5-0.7 for both pathways), while the reaction orders in H_2S are zero on MoS_2/Al_2O_3 and slightly negative on $Ni-MoS_2/Al_2O_3$. The reaction mechanism proposed for the hydrogenation process considers quasi-equilibrated adsorption of the reactants followed by consecutive addition of hydrogen pairs to the adsorbed hydrocarbon. The addition of the first and second hydrogen is the rate determining step for the formation of DiHPhe, whereas the addition of the third and fourth hydrogen is the rate determining step for the formation of TetHPhe. Ni promotion changes the electronic properties of MoS_2 and increases the concentration of sites for the activation of H_2 , which increases the rates of hydrogenation. The changes in reaction mechanisms and associated changes in selectivity are attributed to accelerated hydrogen addition to adsorbed hydrocarbon intermediates.

4.1. Introduction

Hydrogenation of polycyclic aromatic compounds on (Ni-) MoS_2 is needed to adjust the H to C ratio in fuels and is a mandatory step for defunctionalization *via* hydrotreating, e.g., hydrodesulfurization, hydrodenitrogenation, and hydrodeoxygenation.¹⁻³ Rational catalyst design of sulfides for hydrogenation requires the description of the elemental steps that lead to the addition of hydrogen to adsorbed hydrocarbons, and the effect of promoters on such steps.

The overall hydrogenation activity may be governed by the adsorption and activation of hydrogen and hydrocarbons or the barriers of hydrogen addition at the active sites. Activation of hydrogen on sulfides has received a great deal of attention due to its relevance for many catalytic applications.⁴⁻¹³ Heterolytic and homolytic mechanism on paired sites containing S^{2-} anions and exposed cations (coordinatively unsaturated sites, CUS) have been put forward.¹⁰ Density functional theory (DFT) calculations suggest that formation of hydrides at cationic sites is feasible upon heterolytic H_2 splitting, followed by the formation of SH groups.⁵⁻⁷ Homolytic hydrogen dissociation on S_2^- groups at fully sulfided edges also would yield SH groups. Hence, it is accepted that SH is the stable form of activated H on the sulfide surface. Correlations between the concentration of activated hydrogen and CUS at the edges of MoS_2 have been found in previous experimental studies.^{14,15}

In contrast, the adsorption of polycyclic aromatics and the subsequent reductive steps towards hydrogenated products have not been addressed in detail. DFT calculations show that aromatics can adsorb at the basal plane of MoS_2 with strong contribution from van der Waals interactions, although the effect of Ni on the adsorption processes has not been discussed.^{16,17}

On the other hand, proposals on the nature of the hydrogen addition steps and their correlation with macroscopic transformations are rare, although detailed studies of polyaromatic hydrogenation on sulfides are reported.^{18–26}

Thus, the goal of our investigation was to determine the mechanistic steps for the hydrogenation of phenanthrene (as model compound for polycyclic aromatic compounds) on γ -Al₂O₃ supported MoS₂ and Ni-MoS₂, and their consequences for the overall reaction network. In order to achieve this goal, we have performed series of catalytic experiments at differential and not-differential conditions. Different models have been applied to draw quantitative comparisons, ranging from simple first order kinetics, over Langmuir-Hinshelwood models, to detailed mechanisms at differential conditions. Analysis of the kinetic data in combination with previous structural characterization^{15,27} allowed us to describe the active sites and the surface processes that define the performance of the catalyst.

4.2. Experimental part

4.2.1. Material synthesis and characterization

Oxide Mo and Ni-Mo catalyst precursors were prepared by incipient wetness impregnation of γ -Al₂O₃ (248 m²/g, provided by the Chevron Energy Technology Company). Ammonium heptamolybdate ((NH₄)₆Mo₇O₂₄·4H₂O, Aldrich, ≥99.0%) and nickel nitrate (Ni(NO₃)₂·6H₂O, Aldrich, ≥98.5%) were employed as precursor salts. The γ -Al₂O₃ support was mixed with an aqueous solution containing the Mo salt, followed by thermal treatment of the impregnated material at 773 K in a synthetic air flow. This procedure yielded the oxide precursor of MoS₂/Al₂O₃. In order to prepare the bimetallic NiMo catalyst precursor, the precursor of MoS₂/Al₂O₃ was impregnated with a solution of the Ni salt, followed by thermal treatment at 773 K in a synthetic air flow. The corresponding sulfide catalysts were obtained by sulfidation of the oxide precursors in a plug flow reactor under 20 mL/min of 10 vol.-% H₂S in H₂ at 20 bar and 673 K for 8 h. The catalyst containing only Mo is denoted as MoS₂/Al₂O₃ and the bimetallic catalyst as Ni-MoS₂/Al₂O₃. Detailed characterization of these catalysts has been reported in Ref.²⁷.

4.2.2. Kinetic measurements

Kinetic measurements were carried out in a continuous flow trickle bed reactor equipped with high-pressure mass flow controllers (Bronkhorst EL-FLOW) and a HPLC pump (Gilson 307, pump head 5SC). The oxide catalyst precursor (250–355 μ m) was diluted 1:20 with SiC (63–90 μ m) and sulfided *in situ* (vide supra) for each experiment. The hydrogenation reactions were performed at 6 MPa total pressure. Kinetic measurements were done after 20 h time on stream, when steady state was reached. Liquid samples were taken periodically by a multiport

sampling valve and analyzed off-line by gas chromatography with a Shimadzu GC-2010 instrument using a 50 m HP-1 column and a flame ionization detector.

The model compounds in this study were phenanthrene and 9,10-dihydrophenanthrene. Reactant solutions contained 1 wt.-% of phenanthrene (Alfa Aesar, 98%) or 9,10-dihydrophenanthrene (Aldrich, 94%) in addition to 1000 ppm S present as dimethyl disulfide (Aldrich $\geq 99.0\%$). Decalin (Merck, $\geq 99.0\%$) was used as solvent, with 2 wt.-% n-tetradecane (Alfa Aesar, 99+%) as internal standard. The reactions were performed as space time dependent experiments, defined as m_{cat}/F , where m_{cat} is the mass of the catalyst precursor and F is the molar flow of aromatic reactant. The temperatures ranged from 553 K to 583 K and a H_2 to hydrocarbon ratio of $300 \text{ Ndm}^3/\text{dm}^3$ was kept. For the calculation of activation energies, experimental data up to 15% phenanthrene conversion was considered.

Experiments to determine the reaction order in H_2 were done by dilution of the gas flow with N_2 , varying the proportion of N_2 in the range of 0–25 vol.-%. The reaction orders in phenanthrene and H_2S were determined by varying the concentration of the liquid feed. The phenanthrene concentration ranged from 0.6 to 1.2 wt.-% and the sulfur concentration from 500 to 1500 ppm (using CS_2 as H_2S source). Each reaction order was measured independently at phenanthrene conversions below 10%, at 553 – 583 K. The kinetic data was fitted to diverse models using the Matlab software utilizing a CMA-ES algorithm. For the analysis of the phenanthrene reaction network, the whole data range was used, whereas only data up to 10% phenanthrene conversion was taken to derive a surface reaction mechanism.

4.3. Results

4.3.1. Catalyst characterization

This work focuses on two metal sulfide catalysts, $\text{MoS}_2/\text{Al}_2\text{O}_3$ and $\text{Ni-MoS}_2/\text{Al}_2\text{O}_3$. The Mo content of both materials was 9.1 wt.-% (0.95 mmol/g). The bimetallic catalyst contained 2.7 wt.-% (0.46 mmol/g) of Ni, yielding a $\text{Ni}/(\text{Mo}+\text{Ni})$ molar ratio of 0.33. The surface areas of the catalysts were $216 \text{ m}^2/\text{g}$ for $\text{MoS}_2/\text{Al}_2\text{O}_3$ and $207 \text{ m}^2/\text{g}$ for $\text{Ni-MoS}_2/\text{Al}_2\text{O}_3$. X-ray diffraction and transmission electron microscopy indicated good dispersion of Mo and Ni sulfide species on $\gamma\text{-Al}_2\text{O}_3$. Slab length and stacking degree of MoS_2 were 5.5 nm and 1.5, respectively, for $\text{MoS}_2/\text{Al}_2\text{O}_3$. Slab length and stacking degree of 4.5 nm and 1.9, respectively, were observed for $\text{Ni-MoS}_2/\text{Al}_2\text{O}_3$. Infrared spectroscopy of adsorbed CO and X-ray absorption spectroscopy confirmed the incorporation of Ni atoms in the MoS_2 structure, forming a Ni-Mo-S mixed phase. At $\text{Ni}/(\text{Mo}+\text{Ni})$ molar ratio of 0.33, the promoted catalyst exhibited the optimum degree of Ni promotion, as a maximum concentration of sulfur vacancies (Lewis acidic) and SH groups (Brønsted acidic) was reached. For details of the characterization and determination of functional groups, see Refs.^{15,27}.

4.3.2. Hydrogenation of phenanthrene and dihydrophenanthrene

Investigations on the reaction network of phenanthrene hydrogenation were conducted by performing reactions at up to 40% phenanthrene (Phe) conversion at 573 K. In presence of Ni the rate of phenanthrene hydrogenation increased by a factor of 2.5, from $0.58 \cdot 10^{-3} \text{ mol}_{\text{Phe}}/\text{h} \cdot \text{g}_{\text{cat}}$ to $1.54 \cdot 10^{-3} \text{ mol}_{\text{Phe}}/\text{h} \cdot \text{g}_{\text{cat}}$ on $\text{MoS}_2/\text{Al}_2\text{O}_3$, and $\text{Ni-MoS}_2/\text{Al}_2\text{O}_3$, respectively. Figure 4-1 (A, B) shows the product yields of Phe hydrogenation on $\text{MoS}_2/\text{Al}_2\text{O}_3$ and $\text{Ni-MoS}_2/\text{Al}_2\text{O}_3$ as function of conversion. The main product on both catalysts was 9,10-dihydrophenanthrene (DiHPhe). For $\text{MoS}_2/\text{Al}_2\text{O}_3$ only one more product was formed, namely 1,2,3,4-tetrahydrophenanthrene (TetHPhe). These products were formed with a DiHPhe:TetHPhe concentration ratio of 9:1. Over $\text{Ni-MoS}_2/\text{Al}_2\text{O}_3$, the yield of TetHPhe was much higher than on $\text{MoS}_2/\text{Al}_2\text{O}_3$, which led to an initial DiHPhe:TetHPhe concentration ratio of almost 1:1. The formation of higher hydrogenated products, i.e. 1,2,3,4,5,6,7,8-octahydrophenanthrene (*sym*OHPhe) and 1,2,3,4,4a,9,10,10a-octahydrophenanthrene (*asym*OHPhe) was significant only on $\text{Ni-MoS}_2/\text{Al}_2\text{O}_3$. The fully hydrogenated product, perhydrophenanthrene, was not observed even at 40% Phe conversion.

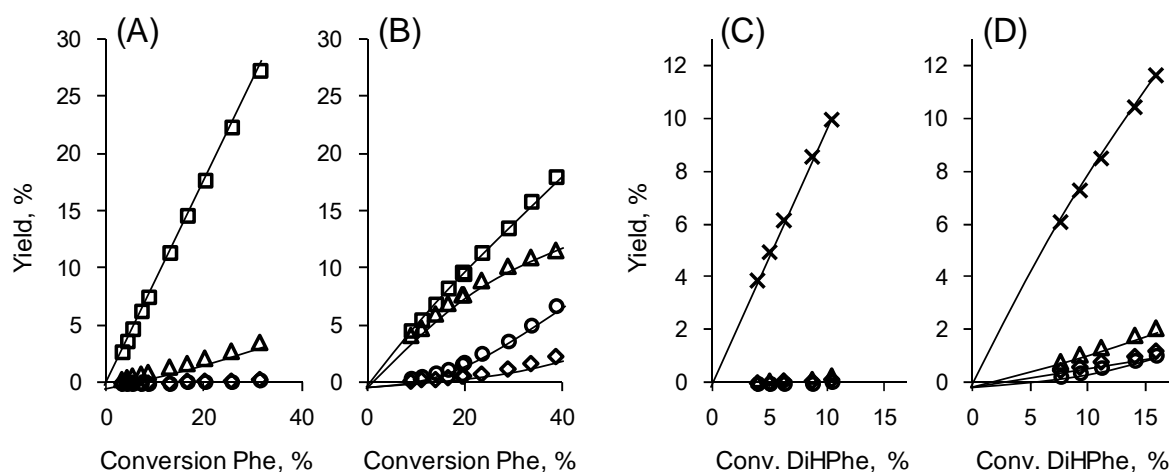


Figure 4-1. Product yields as function of conversion for the hydrogenation of phenanthrene over $\text{MoS}_2/\text{Al}_2\text{O}_3$ (A) and $\text{Ni-MoS}_2/\text{Al}_2\text{O}_3$ (B) at 573 K, 60 bar and space times varying from 50 to 670 $\text{h} \cdot \text{g}_{\text{cat}}/\text{mol}_{\text{Phe}}$. Hydrogenation of 9,10-dihydrophenanthrene over $\text{MoS}_2/\text{Al}_2\text{O}_3$ (C) and $\text{Ni-MoS}_2/\text{Al}_2\text{O}_3$ (D) at 573 K, 60 bar and varying space times between 50 and 130 $\text{h} \cdot \text{g}_{\text{cat}}/\text{mol}_{\text{DiHPhe}}$. (x) phenanthrene/Phe, (□) 9,10-dihydrophenanthrene/DiHPhe, (Δ) 1,2,3,4-tetrahydrophenanthrene, (○) 1,2,3,4,5,6,7,8-octahydrophenanthrene, and (◇) 1,2,3,4,4a,9,10,10a-octahydrophenanthrene.

Hydrogenation of aromatic hydrocarbons is reversible under typical hydrotreating conditions.¹⁸ At 573 K and 60 bar, the lowest equilibrium concentration ratio (K_c) among the compounds present in the reaction was found between Phe and DiHPhe ($K_c = 1.1$).²⁷ On the other hand, DiHPhe was the main product for Phe hydrogenation on $\text{MoS}_2/\text{Al}_2\text{O}_3$ and $\text{Ni-MoS}_2/\text{Al}_2\text{O}_3$. Therefore, hydrogenation reactions with DiHPhe as reactant were undertaken at the same conditions as those applied for the hydrogenation of phenanthrene. The reaction rates were $0.79 \cdot 10^{-3} \text{ mol}_{\text{DiHPhe}}/\text{h} \cdot \text{g}_{\text{cat}}$ on $\text{MoS}_2/\text{Al}_2\text{O}_3$ and $1.39 \cdot 10^{-3} \text{ mol}_{\text{DiHPhe}}/\text{h} \cdot \text{g}_{\text{cat}}$ on $\text{Ni-MoS}_2/\text{Al}_2\text{O}_3$, i.e., a

factor of 1.8 faster in the presence of Ni than on $\text{MoS}_2/\text{Al}_2\text{O}_3$. The product yields observed over $\text{MoS}_2/\text{Al}_2\text{O}_3$ and $\text{Ni-MoS}_2/\text{Al}_2\text{O}_3$ are given as function of DiHPhe conversion in Figure 4-1 (C, D). The main product on both catalysts was Phe. Higher hydrogenated products were obtained to a significant extent only on $\text{Ni-MoS}_2/\text{Al}_2\text{O}_3$, TetHPhe being the most abundant, followed by *asym*OHPhe and *sym*OHPhe. The fully hydrogenated product, perhydrophenanthrene, was not observed.

The product selectivities observed during the hydrogenation of Phe and DiHPhe on $\text{Ni-MoS}_2/\text{Al}_2\text{O}_3$ are presented as function of conversion in Figure 4-2. Product selectivity observed on $\text{MoS}_2/\text{Al}_2\text{O}_3$ is given in the supporting information. DiHPhe and TetHPhe are identified as primary products during the hydrogenation of Phe because their extrapolated initial selectivity is different to zero.²⁸ In contrast, *sym*OHPhe and *asym*OHPhe are secondary products with selectivities of zero at conversion zero. To determine the origin of the *sym*OHPhe and *asym*OHPhe, selectivities to all products are compared in Figure 4-S8 of the supporting information. The decrease in selectivity to DiHPhe was 4% and to TetHPhe was 19%, compared to their initial selectivity, while the increase in selectivity to *asym*OHPhe was 6% and to *sym*OHPhe was 17%. Hence, *sym*OHPhe is formed from TetHPhe, whereas *asym*OHPhe originates mainly from DiHPhe.

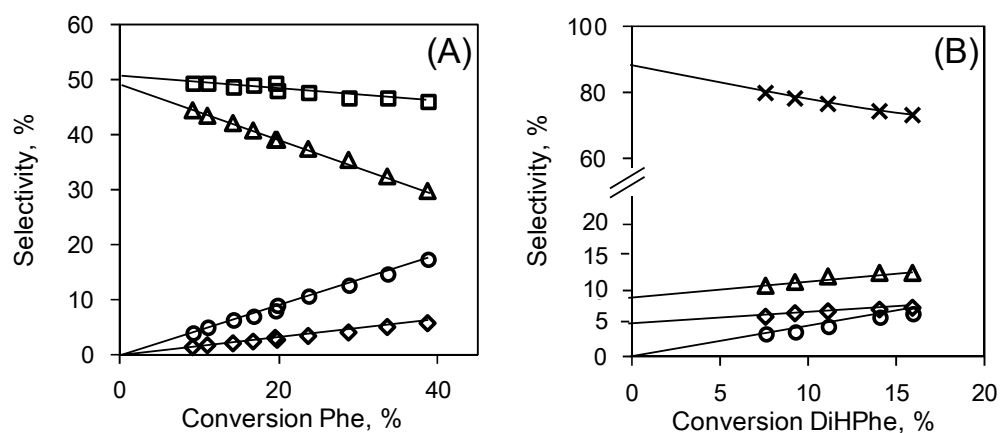


Figure 4-2. Product selectivity for the hydrogenation of phenanthrene (A) and 9,10-dihydrophenanthrene (B) over $\text{Ni-MoS}_2/\text{Al}_2\text{O}_3$, at 573 K, 60 bar and varying space time. (x) phenanthrene/Phe, (□) 9,10-dihydrophenanthrene/DiHPhe, (Δ) 1,2,3,4-tetrahydrophenanthrene, (O) 1,2,3,4,5,6,7,8-octahydrophenanthrene, and (◇) 1,2,3,4,4a,9,10,10a-octahydrophenanthrene.

In the case of 9,10-dihydrophenanthrene hydrogenation, Phe, TetHPhe and *asym*OHPhe are identified as primary products (Figure 4-2B). However, TetHPhe displays an up-curved trend line in the yield-conversion plot (enlarged view in the supporting information), which is typical for secondary products. Hence, TetHPhe originates from two different pathways, as primary product directly from DiHPhe and as secondary product *via* Phe. *Sym*OHPhe is clearly

identified as secondary product from the selectivity-conversion plot in Figure 4-2B, as its selectivity equals zero at extrapolated zero conversion.

The reaction network corresponding to the observations described for Phe and DiHPhe hydrogenation is shown in Figure 4-3. Seven reaction steps are considered relevant at our reaction conditions. An overall first order rate constant (k_i) is assigned to each step: k_1 and k_{-1} describe the (de-)hydrogenation reactions between Phe and DiHPhe, k_2 and k_5 describe the formation of TetHPhe from Phe and DiHPhe, respectively; k_3 is associated to the reaction of DiHPhe to *asym*OHPhe, whereas k_4 and k_6 represent the formation of *sym*- and *asym*OHPhe, respectively, from TetHPhe.

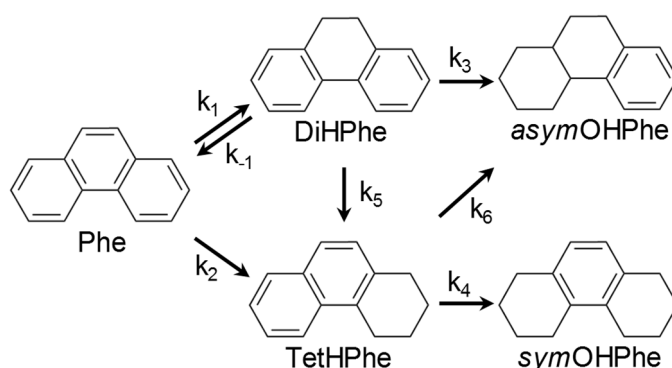


Figure 4-3. Reaction network derived from hydrogenation of Phe and DiHPhe as reactants at 573 K, 20 bar and conversions up to 40%. Phe: phenanthrene, DiHPhe: 9,10-dihydrophenanthrene, TetHPhe: 1,2,3,4-tetrahydrophenanthrene, *sym*OHPhe: 1,2,3,4,5,6,7,8-octahydrophenanthrene, *asym*OHPhe: 1,2,3,4,4a,9,10,10a-octahydrophenanthrene.

First order reaction rate constants for the reaction network shown in Figure 3 were determined by fitting each data set independently (Phe and DiHPhe hydrogenation) to the corresponding system of differential equations (shown in the supporting information). An overview of all rate constants is given in Table S1. In the following discussion only constants derived from primary reaction pathways are considered as the values of the constants of secondary pathways are overestimated.

For Ni-MoS₂/Al₂O₃, k_1 was $1.43 \cdot 10^{-3}$ mol/h·g_{cat} and k_{-1} $1.96 \cdot 10^{-3}$ mol/h·g_{cat}, leading to a k_1/k_{-1} ratio of 0.73. The value of k_2 was $1.27 \cdot 10^{-3}$ mol/h·g_{cat} and that of k_5 was $0.26 \cdot 10^{-3}$ mol/h·g_{cat} (as determined from the hydrogenation of Phe and DiHPhe, respectively, on Ni-MoS₂/Al₂O₃). The k_1/k_3 ratio was 9.5 ($1.43 \cdot 10^{-3}$ mol/h·g_{cat} and $0.15 \cdot 10^{-3}$ mol/h·g_{cat} for k_1 and k_3 , respectively), showing that the hydrogenation of Phe is one order of magnitude faster than the deep hydrogenation of DiHPhe towards *asym*OHPhe. The k_3/k_5 ratio was 0.6 ($0.15 \cdot 10^{-3}$ mol/h·g_{cat} and $0.26 \cdot 10^{-3}$ mol/h·g_{cat} for k_3 and k_5 , respectively), which means that the addition of six hydrogens to form *asym*OHPhe is slower than isomerization and further hydrogenation from DiHPhe to TetHPhe. Interestingly, k_5 was zero during hydrogenation with Phe as starting reactant. Qualitative comparisons of the values of k_3 , k_4 and k_6 (secondary reaction steps),

derived from the fitting of Phe hydrogenation on Ni-MoS₂/Al₂O₃ indicated that the hydrogenation of TetHPhe to *sym*OHPhe is faster than to *asym*OHPhe. Furthermore, the production of *asym*OHPhe from DiHPhe (k_3) was faster than from TetHPhe (k_6).

For MoS₂/Al₂O₃, the first order rate constants k_1 and k_{-1} were $0.9 \cdot 10^{-3}$ mol/h·g_{cat} and $1.36 \cdot 10^{-3}$ mol/h·g_{cat}, respectively, leading to a k_1/k_{-1} ratio of 0.66. The formation of TetHPhe on MoS₂/Al₂O₃ occurred exclusively from Phe (k_2 was $0.1 \cdot 10^{-3}$ mol/h·g_{cat}, while k_5 was 0), and was almost one order of magnitude slower than the reaction to DiHPhe ($k_1/k_2=9$). Further hydrogenation to *asym*OHPhe was very slow on MoS₂/Al₂O₃, even starting from DiHPhe as reactant, with k_3 being $0.01 \cdot 10^{-3}$ mol/h·g_{cat}.

Comparing not- and Ni-promoted MoS₂/Al₂O₃, an increase of k_1 and k_{-1} of about 45% was observed in the presence of Ni, leading to quite similar k_1/k_{-1} ratios (0.66 for MoS₂/Al₂O₃ and 0.73 for Ni-MoS₂/Al₂O₃). The main difference induced by addition of Ni was in the formation higher hydrogenated products. For instance, the k_1/k_2 ratio changed from 9 on MoS₂/Al₂O₃ to 1.1 on Ni-MoS₂/Al₂O₃. The effect on hydrogenation to *sym*- and *asym*OHPhe was even more dramatic, as they only form in significant concentrations over Ni-MoS₂/Al₂O₃.

The fastest reaction step in the reaction network was dehydrogenation (k_{-1}) from DiHPhe to Phe, followed by hydrogenation of Phe to DiHPhe (k_1) and further hydrogenation from Phe to TetHPhe (k_2). As the k_1/k_{-1} ratio was about 0.7 in average (over MoS₂/Al₂O₃ and Ni-MoS₂/Al₂O₃), which is lower than the predicted equilibrium concentration ratio ($K_c=1.1$)²⁷, equilibrium between DiHPhe and Phe was not reached at low Phe or DiHPhe conversion. The reaction of DiHPhe to TetHPhe (k_5) was slow and only important at high concentrations of DiHPhe. Among secondary reaction steps, k_3 and k_4 were dominant, whereas the contribution of k_6 was minor. Therefore, a reaction network containing only four first order rate constants (k_1 , k_2 , k_3 and k_4) would suffice to describe the hydrogenation of phenanthrene at low conversions. Fitting of the experimental results with four reaction constants instead of seven is presented in the supporting information. Comparison of the fittings of complete and simplified networks reveals minor differences, whereas the general trends are maintained.

First order kinetics are a valuable tool to quantitatively analyse the effects of Ni promotion on the overall hydrogenation steps of the studied aromatics. However, it does not explicitly account for the effect of different concentration of surface species, which is rather different when using either Phe or DiHPhe as starting reactant. Therefore, a Langmuir-Hinshelwood (L-H) model was applied to the kinetic data, considering the surface concentrations of Phe and DiHPhe and fitting the data sets of Phe and DiHPhe hydrogenation simultaneously.^{20,21,24,25} The hydrogenation pathways k_4 and k_6 of the reaction network in Figure 4-3 were neglected because Phe and DiHPhe were the dominating species. Furthermore, the concentrations of *sym*OHPhe and TetHPhe were lumped together. This approach led to four differential

equations, given in eqs. (1)-(4). Therein, k_i is the reaction rate constant for hydrogenation step i as indicated in Figure 4-3, c_j is the concentration of compound j and K_i is the adsorption equilibrium constant of Phe or DiHPhe. The obtained rate and adsorption constants are summarized in Table 4-1. Experimental and predicted concentrations are compared in the supporting information.

The rate constants k_1 and k_{-1} on Ni-MoS₂/Al₂O₃ were about 1.3 times large than on MoS₂/Al₂O₃. The effect of Ni on k_2 , k_3 and k_5 was more pronounced, the increase being more than one order of magnitude. The adsorption constants K_{Phe} and K_{DiHPhe} were almost equal for MoS₂/Al₂O₃ and Ni-MoS₂/Al₂O₃ ($K_{\text{Phe}}/K_{\text{DiHPhe}} = 1.1$). The k_1/k_{-1} ratios were 0.73 over Ni-MoS₂/Al₂O₃ and 0.67 over MoS₂/Al₂O₃, which are similar to the ratios obtained in the first order kinetic model (vide supra). Further comparison of the different fitting approaches showed identical ratios for k_1/k_2 . The k_3/k_5 ratio was <1 , which means that relative fast isomerization, is preserved. The ratio $(k_1 \cdot K_{\text{Phe}}) \cdot (k_3 \cdot K_{\text{DiHPhe}})^{-1}$ of the L-H model was 9.4, which is similar to k_1/k_3 (9.5) of the first order kinetics approach. Thus, the trends yielded by the different fitting approaches are consistent. In addition, the L-H model fitting revealed that rates of Phe and DiHPhe hydrogenation are very close because the adsorption strength of both molecules on the catalyst is very similar.

$$\frac{dc_{\text{Phe}}}{dt} = \frac{(-k_1 - k_2) \cdot K_{\text{Phe}} \cdot c_{\text{Phe}} + k_{-1} \cdot K_{\text{DiHPhe}} \cdot c_{\text{DiHPhe}}}{1 + K_{\text{Phe}} \cdot c_{\text{Phe}} + K_{\text{DiHPhe}} \cdot c_{\text{DiHPhe}}} \quad (1)$$

$$\frac{dc_{\text{DiHPhe}}}{dt} = \frac{(-k_{-1} + k_3 + k_5) \cdot K_{\text{DiHPhe}} \cdot c_{\text{DiHPhe}} + k_1 \cdot K_{\text{Phe}} \cdot c_{\text{Phe}}}{1 + K_{\text{Phe}} \cdot c_{\text{Phe}} + K_{\text{DiHPhe}} \cdot c_{\text{DiHPhe}}} \quad (2)$$

$$\frac{dc_{\text{TetHPhe}}}{dt} = \frac{k_2 \cdot K_{\text{Phe}} \cdot c_{\text{Phe}} + k_5 \cdot K_{\text{DiHPhe}} \cdot c_{\text{DiHPhe}}}{1 + K_{\text{Phe}} \cdot c_{\text{Phe}} + K_{\text{DiHPhe}} \cdot c_{\text{DiHPhe}}} \quad (3)$$

$$\frac{dc_{\text{asymOHPhe}}}{dt} = \frac{k_3 \cdot K_{\text{DiHPhe}} \cdot c_{\text{DiHPhe}}}{1 + K_{\text{Phe}} \cdot c_{\text{Phe}} + K_{\text{DiHPhe}} \cdot c_{\text{DiHPhe}}} \quad (4)$$

Table 4-1. Reaction rate and adsorption constants derived from a combined fitting of Phe and DiHPhe hydrogenation data according to a Langmuir-Hinshelwood mechanism. The unit of k_i is mol/h·g_{cat}, K_i is dimensionless.

Catalyst	k_1	k_{-1}	k_2	k_3	k_5	K_{Phe}	K_{DiHPhe}
MoS ₂ /Al ₂ O ₃	0.73	1.08	0.08	$0.14 \cdot 10^{-3}$	0.02	0.00132	0.00118
Ni-MoS ₂ /Al ₂ O ₃	0.99	1.37	0.93	0.12	0.24	0.00144	0.00132

4.3.3. Determination of activation energies for phenanthrene hydrogenation

The hydrogenation of phenanthrene was performed at varying temperatures in order to derive activation energies. The rate constants of the main reaction steps are presented in the supporting information. The corresponding Arrhenius plots of the primary routes are presented in Figure 4-4. The apparent activation energies for the formation of DiHPhe (k_1) and TetHPhe (k_2) were identical on each catalyst. That is, 138 kJ/mol on $\text{MoS}_2/\text{Al}_2\text{O}_3$, and 127 kJ/mol on $\text{Ni-MoS}_2/\text{Al}_2\text{O}_3$.

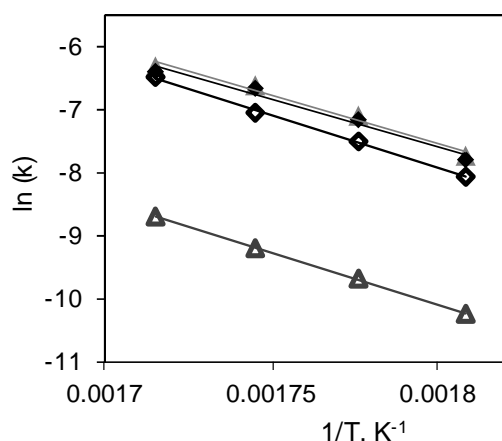


Figure 4-4. Arrhenius plot for the hydrogenation of phenanthrene on $\text{MoS}_2/\text{Al}_2\text{O}_3$ to DiHPhe (\diamond) and TetHPhe (\triangle) and on $\text{Ni-MoS}_2/\text{Al}_2\text{O}_3$ to DiHPhe (\blacklozenge) and TetHPhe (\blacktriangle). Reactions were conducted at 60 bar, with temperatures from 553 to 583 K, and space times between 30 and 140 $\text{h}\cdot\text{g}_{\text{cat}}/\text{mol}_{\text{Phe}}$.

4.3.4. Determination of reaction orders

The reaction orders in H_2 , Phe and H_2S determined for phenanthrene hydrogenation are presented in Table 4-2. The corresponding plots of rates along partial pressures are depicted in the supporting information. The experiments were conducted in the kinetic regime with a maximum phenanthrene conversion of 10% at 583 K. At these conditions the selectivities towards DiHPhe, TetHPhe, *sym*OHPhe and *asym*OHPhe were 49%, 41%, 7% and 3%, respectively. Hence, two parallel reaction pathways were analyzed, “path 1” including the consecutive formation of DiHPhe (k_1) and *asym*OHPhe (k_3) and “path 2” containing the consecutive reactions to TetHPhe (k_2) and *sym*OHPhe (k_4). Reaction orders were determined merging the concentrations of *asym*OHPhe and DiHPhe, as well as the concentrations of *sym*OHPhe and TetHPhe.

Reaction orders can be interpreted as relative coverages because the dependence of reaction rates on the surface concentration of a given species increases with lower coverage of that species. Namely, increases in reaction order reflect decreasing coverages, whereas decreasing reaction order reflects high coverage. The overall reaction order in H_2 for

hydrogenation over $\text{MoS}_2/\text{Al}_2\text{O}_3$ was 0.7, which increased in presence of Ni to 1.2, in average. This increase of the H_2 reaction orders with the addition of Ni suggests that the coverage of surface H is relatively low in the presence of Ni. This seems reasonable, as much more deeply hydrogenated products are formed on Ni- $\text{MoS}_2/\text{Al}_2\text{O}_3$ than on $\text{MoS}_2/\text{Al}_2\text{O}_3$. Thus, less free hydrogen is available on the promoted catalyst. A similar increase was observed when comparing the reaction order in H_2 for path 1 (DiHPhe) and path 2 (TetHPhe), the latter reaction being more hydrogen demanding and consequently showing higher dependence on H_2 pressure. At varying temperatures clear changes of the H_2 order were not observed for Ni- $\text{MoS}_2/\text{Al}_2\text{O}_3$. For $\text{MoS}_2/\text{Al}_2\text{O}_3$, however, the reaction orders in H_2 decreased at increasing temperatures. This decrease was accompanied by increasing reaction order in Phe, which indicates that the relative coverage of Phe increased at the expense of the H_2 coverage (although in absolute terms, both coverages are expected to decrease with increasing temperature). Furthermore, the reaction orders in Phe were the same for both pathways, being only slightly higher, in average, on Ni- $\text{MoS}_2/\text{Al}_2\text{O}_3$ than on $\text{MoS}_2/\text{Al}_2\text{O}_3$. The H_2S reaction order for $\text{MoS}_2/\text{Al}_2\text{O}_3$ was close to zero, showing that the influence of H_2S on the adsorption sites of MoS_2 was negligible. Over Ni- $\text{MoS}_2/\text{Al}_2\text{O}_3$, however, a negative influence of H_2S was observed with average reaction order of -0.25.

Table 4-2. Reaction orders for H_2 , Phe and H_2S for the hydrogenation of phenanthrene.

Reaction order		$\text{MoS}_2/\text{Al}_2\text{O}_3$				Ni- $\text{MoS}_2/\text{Al}_2\text{O}_3$			
		553	563	573	583	553	563	573	583
H_2	path 1 ^a	0.97	0.66	0.66	0.61	1.08	1.18	1.09	1.17
H_2	path 2 ^b	1.17	0.84	0.87	0.66	1.38	1.35	1.26	1.33
Phe	path 1 ^a	0.49	0.59	0.63	0.69	0.55	0.71	0.64	0.71
Phe	path 2 ^b	0.48	0.54	0.54	0.53	0.55	0.71	0.69	0.73
H_2S	path 1 ^a	-0.03	-0.02	-0.09	-0.06	-0.17	-0.13	-0.18	-0.21
H_2S	path 2 ^b	-0.09	-0.09	-0.14	-0.12	-0.30	-0.26	-0.30	-0.32

^a path 1: phenanthrene \rightarrow 9,10-dihydrophenanthrene \rightarrow 1,2,3,4,4a,9,10,10a-octahydrophenanthrene.

^b path 2: phenanthrene \rightarrow 1,2,3,4-tetrahydrophenanthrene \rightarrow 1,2,3,4,5,6,7,8-octahydrophenanthrene.

The kinetic data that allowed deriving the reaction orders was further used to propose reaction mechanisms of phenanthrene hydrogenation by fitting the experimental rates of DiHPhe and TetHPhe formation at varying reactant and H_2S concentrations. Different mechanisms were tried, comprising dissociative or associative adsorption of H_2 and H_2S , one or two kind of adsorption sites, and different rate determining steps. The models that fit the best the experimental data of DiHPhe production on $\text{MoS}_2/\text{Al}_2\text{O}_3$ and Ni- $\text{MoS}_2/\text{Al}_2\text{O}_3$, and TetHPhe on Ni- $\text{MoS}_2/\text{Al}_2\text{O}_3$ are surprisingly simple. The assumptions of the mechanisms, shown in Table 3, are the following. One kind of adsorption site for Phe, H_2 and H_2S , whereas H_2 dissociates upon adsorption. The adsorption of these three species is relatively fast, and therefore, quasi-

equilibrated (reactions (1)-(3) in Table 4-3). The rate determining step (rds) for the formation of DiHPhe is the hydrogenation of phenanthrene, which takes place by the simultaneous addition of two H at the surface to the adsorbed hydrocarbon (Table 4-3, reaction (4)). Similarly, the hydrogenation of Phe to TetHPhe proceeds through consecutive additions of H pairs. The addition of the first pair is reversible and quasi-equilibrated, whereas the addition of the second hydrogen pair is the rds (Table 4-3 reaction (4a) and (4b)). In the final step, Table 4-3 reaction (5), the hydrogenated products are desorbed and the initial state of the catalyst is restored.

The rate equations derived from the proposed mechanisms for the formation of DiHPhe and TetHPhe are given in equations (5) and (6), respectively. The derivation of these equations further assumes that the surface is covered only by the species contained in the feed, and a hydrogenated intermediate in the case of equation (6) (path 2). The surface concentrations of the products are considered negligible. In equations (5) and (6) k_r is the reaction rate constant of the rds, K_i is the adsorption equilibrium constant for H_2 , Phe or H_2S , and P_i is the partial pressure of either of these compounds. K_4 is the equilibrium constant of the surface reaction (4a) in Table 4-3, corresponding to the addition of the first two H to the adsorbed hydrocarbon. Analysis of Phe hydrogenation to TetHPhe on MoS_2/Al_2O_3 was not performed, because the concentration of TetHPhe was too low.

Fitting parameters, that is, enthalpies (ΔH°) and entropies (ΔS°) of adsorption, as well as, activation energies (E_A) and pre-exponential factors (A_0), were obtained with the Van't Hoff ($\ln K = -\Delta H^\circ/RT + \Delta S^\circ/R$) and Arrhenius ($\ln k = -E_A/RT + \ln A_0$) equations. These mathematical expressions allowed determining adsorption constants (K_i) and rate constants (k_r) at each target temperature in order to fit the experimental rates for hydrogenation. The experimental and fitted rates are compared in the parity plots given in the supporting information. The fitting parameters and the values of the constants at 573 K are given in Table 4-4. The values of the constants for all temperatures are shown in Table 4-S8.

Table 4-3. Elementary steps proposed for the formation of DiHPhe (path 1) and TetHPhe (path 2) as products of Phe hydrogenation.

Reaction	path 1 - DiHPhe	Reaction	path 2 - TetHPhe
(1)	$Phe + * \rightleftharpoons Phe^*$	(1)	$Phe + * \rightleftharpoons Phe^*$
(2)	$H_2 + 2* \rightleftharpoons 2H^*$	(2)	$H_2 + 2* \rightleftharpoons 2H^*$
(3)	$H_2S + * \rightleftharpoons H_2S^*$	(3)	$H_2S + * \rightleftharpoons H_2S^*$
(4)	$Phe^* + 2H^* \rightarrow PheH_2^* + 2*$	(4a)	$Phe^* + 2H^* \rightleftharpoons PheH_2^* + 2*$
		(4b)	$PheH_2^* + 2H^* \rightarrow PheH_4^* + 2*$
(5)	$PheH_2^* \rightleftharpoons PheH_2 + *$	(5)	$PheH_4^* \rightleftharpoons PheH_4 + *$

$$r_{\text{DiHPhe}} = \frac{k_r K_{\text{Phe}} K_{\text{H}_2} P_{\text{Phe}} P_{\text{H}_2}}{(1 + K_{\text{Phe}} P_{\text{Phe}} + (K_{\text{H}_2} P_{\text{H}_2})^{1/2} + K_{\text{H}_2\text{S}} P_{\text{H}_2\text{S}})^3} \quad (5)$$

$$r_{\text{TetHPhe}} = \frac{k_r K_{\text{Phe}} K_{\text{H}_2}^2 K_4 P_{\text{Phe}} P_{\text{H}_2}^2}{[1 + K_{\text{Phe}} P_{\text{Phe}} + (K_{\text{H}_2} P_{\text{H}_2})^{1/2} + K_{\text{H}_2\text{S}} P_{\text{H}_2\text{S}} + K_{\text{Phe}} K_{\text{H}_2} K_4 P_{\text{Phe}} P_{\text{H}_2}]^3} \quad (6)$$

Table 4-4. Fitting parameters for the hydrogenation of phenanthrene.

	path 1 - DiHPhe MoS ₂ /Al ₂ O ₃	path 1 - DiHPhe Ni-MoS ₂ /Al ₂ O ₃	path 2 - TetHPhe Ni-MoS ₂ /Al ₂ O ₃
K _{Phe} ^a	0.16	0.14	0.41
ΔH° [kJ·mol ⁻¹]	-72	-78	-50
ΔS° [kJ·mol ⁻¹ ·K ⁻¹]	-0.14	-0.15	-0.10
K _{H₂} ^b	1.5·10 ⁻⁵	8.0·10 ⁻⁷	3.0·10 ⁻⁷
ΔH° [kJ·mol ⁻¹]	-50	-51	-40
ΔS° [kJ·mol ⁻¹ ·K ⁻¹]	-0.18	-0.21	-0.20
K _{H₂S} ^c	1.3·10 ⁻³	6.2·10 ⁻³	10.2·10 ⁻³
ΔH° [kJ·mol ⁻¹]	-26	-40	-39
ΔS° [kJ·mol ⁻¹ ·K ⁻¹]	-0.10	-0.11	-0.11
K ₄ ^d			3.9·10 ⁻²
ΔH° [kJ·mol ⁻¹]			-15
ΔS° [kJ·mol ⁻¹ ·K ⁻¹]			-0.05
k _r ^e	0.13	1.99	0.28
E _A [kJ·mol ⁻¹]	170	157	169
A _o	3.3·10 ¹⁴	4.0·10 ¹⁴	6.7·10 ¹⁴

^a Parameters for the adsorption of phenanthrene at 573 K derived from Table 4-3, reaction (1).

^b Parameters for the adsorption of H₂ at 573 K derived from Table 4-3, reaction (2).

^c Parameters for the adsorption of H₂S at 573 K derived from Table 4-3, reaction (3).

^d Parameters for first hydrogenation step at 573 K in the TetHPhe reaction pathway derived from Table 4-3, reaction (4a).

^e Parameter k_r at 573 K derived from Table 4-3, reaction (4) for the DiHPhe reaction pathway, and from Table 4-3, reaction (4b) for the TetHPhe reaction pathway.

4.4. Discussion

First order kinetics showed that the rate constants k_1 and k_{-1} ($\text{Phe} \rightleftharpoons \text{DiHPhe}$) are similar on $\text{MoS}_2/\text{Al}_2\text{O}_3$, with dehydrogenation being slightly faster. Promotion of MoS_2 by Ni leads to an increase of the rates for hydrogenation and dehydrogenation to the same extent. Furthermore, on $\text{Ni-MoS}_2/\text{Al}_2\text{O}_3$, the direct conversion of DiHPhe to TetHPhe, involving isomerization and hydrogen addition (k_5) became relevant. Indeed, k_5 was larger than k_3 , which corresponds to hydrogenation by addition of six hydrogen atoms to DiHPhe.

The acceleration of the hydrogenation paths k_2 to k_6 by Ni promotion was much stronger than for k_1 , leading to a dramatic change in product selectivity compared to $\text{MoS}_2/\text{Al}_2\text{O}_3$. The formation of higher hydrogenated products, i.e. TetHPhe, *sym*- and *asym*OHPhe, was clearly favored on $\text{Ni-MoS}_2/\text{Al}_2\text{O}_3$. In the following we rationalize the results and discuss the possible changes in the reaction mechanism that might lead to the described effects of Ni promotion.

The electronic properties of phenanthrene determine to a large extent the selectivity observed on $\text{MoS}_2/\text{Al}_2\text{O}_3$. The angular arrangement of the three fused aromatic rings of Phe leads to two π -electron sextets at the terminal rings, leaving the middle ring with only 2 π -electrons. This leads to high reactivity at the bond in the 9,10-position.²⁹ Hence, activation of the middle ring of Phe occurs readily and hydrogenation to DiHPhe is fast. Activation of the lateral rings, on the contrary, is more demanding and only leads to a stable product (TetHPhe) when four H atoms are added to the adsorbed molecule. This seems to be difficult on $\text{MoS}_2/\text{Al}_2\text{O}_3$ and require the presence of Ni.

Promotion of MoS_2 by Ni reduces the average diameter of the MoS_2 slabs, which increases the dispersion of MoS_2 and active edge area by 20% compared to not-promoted MoS_2 .²⁷ Coordinatively unsaturated sites (CUS) located at the edges of (Ni-) MoS_2 are the accepted active sites for hydrogenolysis reactions. They can be probed by adsorption of probe molecules, e.g. NO and CO. The Ni promotion of MoS_2 increases significantly the concentration of NO adsorption sites as the concentration of adsorbed NO per mol of metal increases up to 33% for the catalysts studied in this contribution.^{27,30–34} Co-adsorption of 2,6-dimethylpyridine (DMP) and H_2S allowed for the quantification of CUS as 18.7 $\mu\text{mol/g}$ on $\text{MoS}_2/\text{Al}_2\text{O}_3$ and 24.0 $\mu\text{mol/g}$ on $\text{Ni-MoS}_2/\text{Al}_2\text{O}_3$, which corresponds to an increase of CUS by almost 30%.²² The increase of CUS concentration studied by IR of adsorbed CO and XAS could be attributed to the incorporation of Ni atoms at the MoS_2 edge substituting 30% of the Mo atoms at the perimeter forming a mixed Ni-Mo-S phase.^{27,35}

The concentration of SH-groups and its variation with Ni promotion is closely related to the presence of CUS. Co-adsorption of DMP and H_2 monitored by IR revealed the formation of SH-groups upon hydrogen dissociation taking place at Lewis acid-base pairs (sulfur vacancies and neighboring S^{2-}). Indeed, a linear correlation of the concentration of SH-groups with Ni

atoms at MoS₂ edges was found based on previous studies (supporting information).^{15,27} According to that correlation, the concentration of active surface H increased by 30% for Ni-MoS₂/Al₂O₃ compared to MoS₂/Al₂O₃.

Thus, the Ni-Mo-S phase exhibits higher dispersion and higher concentration of active sites than the not-promoted MoS₂. The increase in concentration of active sites (CUS and SH groups) is higher than that of dispersion, i.e., 30% and 20% according to the previous discussion. These increase does not account for the boost in activity observed in hydrotreating reactions, e.g., up to one orders of magnitude for hydrodesulfurization (HDS) and hydrodenitrogenation.³³ In this study we show that the increase in hydrogenation activity is also larger (more than twice) than the increase in dispersion, CUS and active H on Ni-MoS₂/Al₂O₃ compared to MoS₂/Al₂O₃. Differentiating between DiHPhe formation (k_1) and deep hydrogenation (k_2, k_3, k_4), indeed only the increase of k_1 (55% with Ni promotion) can be explained by the increase in dispersion and active sites. The increases of k_2, k_3 and k_4 exceed mere structural effects.²⁷ Thus, changes in hydrogenation depth and product selectivity have to be rationalized in terms of intrinsic activity of the active sites and concomitant changes in the reaction mechanism.

The increase of hydrogen coverage (concentration of SH groups) with Ni promotion correlates linearly with the rates of H₂-D₂ scrambling. This is in line with the conclusion that the rates of single hydrogenation follows the concentration of hydrogen on the surface and also indicates that the enhancement of hydrogenation depth is not related with hydrogen activation. Similar conclusions have been reached for HDS, where the increase in desulfurization rates with promotion is attributed to changes in Mo-S bond energy rather than to H₂ activation.^{36,37}

In a similar fashion, the absorption of phenanthrene under reaction conditions does not seem to be affected by the presence of Ni as the Phe reaction orders are hardly influenced by Ni promotion. In line with this inference, the apparent activation energies (identical for single and deep hydrogenation) on MoS₂/Al₂O₃ and Ni-MoS₂/Al₂O₃ have a difference of only ~10 kJ/mol, which suggests negligible changes in adsorption enthalpies (ΔH°) as corroborated by the fitting parameters derived from the L-H models (i.e., -75 kJ/mol and -50 kJ/mol for Phe and H₂, respectively for path 1). In terms of adsorption sites, this probably means that the adsorption of the aromatic does not depend on the changes of the properties of the material produced by Ni. In turn, primary adsorption of the aromatic compounds on the basal planes of MoS₂ is energetically favorable and the adsorption strength, strongly depending on van der Waals interactions, increases with the number of atoms in the molecule.¹⁷ On this primary adsorption, the interaction of adsorbed Phe with the surface must be different on MoS₂ and Ni-MoS₂ as promotion with Ni is known to change the electronic properties of MoS₂ and to increase the metal like character at the edge.^{16,38} The electron-donation from Ni into the 4d orbital of Mo changes its configuration from d^2 (MoS₂) to d^4 (Ni-MoS₂). This shifts the density of states (DOS)

of Ni-MoS₂ towards the configuration of RuS₂ and Rh₂S₃ (*d*⁶), which are the most active transition metal sulfide catalysts for hydrotreating.³⁷ From catalysis on metals it is known that electron-rich metals bind aromatics weakly.³⁹ Therefore, we hypothesize that phenanthrene adsorbs more loosely on Ni-MoS₂ than on MoS₂ resulting in a higher mobility on the surface.

Although phenanthrene is likely to adsorb at the basal plane of (Ni-)MoS₂, the hydrogenation of phenanthrene is likely to take place at the perimeter of (Ni-)MoS₂, where the activation of H₂ takes place and SH groups are located.^{10,12,40,41} High mobility of phenanthrene on the catalyst surface, as induced by Ni promotion, therefore could contribute to the formation of TetHPhe on Ni-MoS₂. This interpretation also explains why the kinetic models that fit the best the experimental data involves only one kind of adsorption site for Phe, H₂ and H₂S.

Changes in the electron density of the MoS₂ edge with Ni promotion also lower the binding energy of SH groups increasing the reactivity of H.⁴¹⁻⁴⁴ The lower apparent activation energy on Ni-MoS₂/Al₂O₃ compared to MoS₂/Al₂O₃ reflects this change in hydrogenation barriers. This conclusion is drawn after neglecting promoting effects on hydrocarbon adsorption as indicated by the small changes of Phe orders, similar adsorption constants of Phe (*K*_{phe} in the L-H model), and identical *E*_{A,app} for DiHPhe and TetHPhe formation on MoS₂ and Ni-MoS₂. The conclusion of decreasing hydrogenation barriers, leading to the shift towards deep hydrogenated products on Ni-MoS₂/Al₂O₃, is further supported by the change in rds concluded for the production of TetHPhe. In line with this conclusion, lower barriers for hydrogenation of thiophene were calculated on Co-promoted MoS₂.⁴²

The proposed mechanism for DiHPhe and TetHPhe formation on not- and Ni-promoted MoS₂/Al₂O₃ is given in Figure 4-5 and Figure 4-6. Phe is adsorbed on the basal plane of the catalyst surface due to strong van der Waals interactions. However, the molecules that undergo hydrogenation are those located near the edges of the sulfide slabs, or that move there, as active hydrogen (SH-groups) is present there. DiHPhe is formed when the middle ring of Phe is activated. In a first hydrogenation step a proton from an acidic SH-group is added to Phe. The charge developed in Phe is stabilized and compensated by MoS₂ *via* π–interaction. Subsequently, the carbocation is reduced and the catalyst oxidized yielding a partially hydrogenated intermediate. Finally, another H⁺ is added in a second hydrogenation step followed by reduction and desorption of DiHPhe. Note the addition of hydrogen may occur as described, i.e., by consecutive protonation and reduction or by addition of an H radical (interpreted as simultaneous addition of proton and electron) as expected on a metallic surface. The real nature of this event depends on the metallic character of the sulfide edge and remains unanswered in this study.

In the mechanistic model that describes the kinetic experiments, the rate limiting step was the addition of hydrogen, which was postulated as simultaneous addition of two H atoms. This

does not contradict the mechanism shown in Figure 4-5 and Figure 4-6 as the real determining barrier is likely a first hydrogen addition (which disrupts the aromaticity of the molecule), whereas addition of the second hydrogen might be too fast to be differentiated as a separate step. This rationale is well in line with DFT calculations for thiophene hydrogenation, where only the addition of the first H showed a barrier, whereas the second H-addition is non-activated.^{9,42}

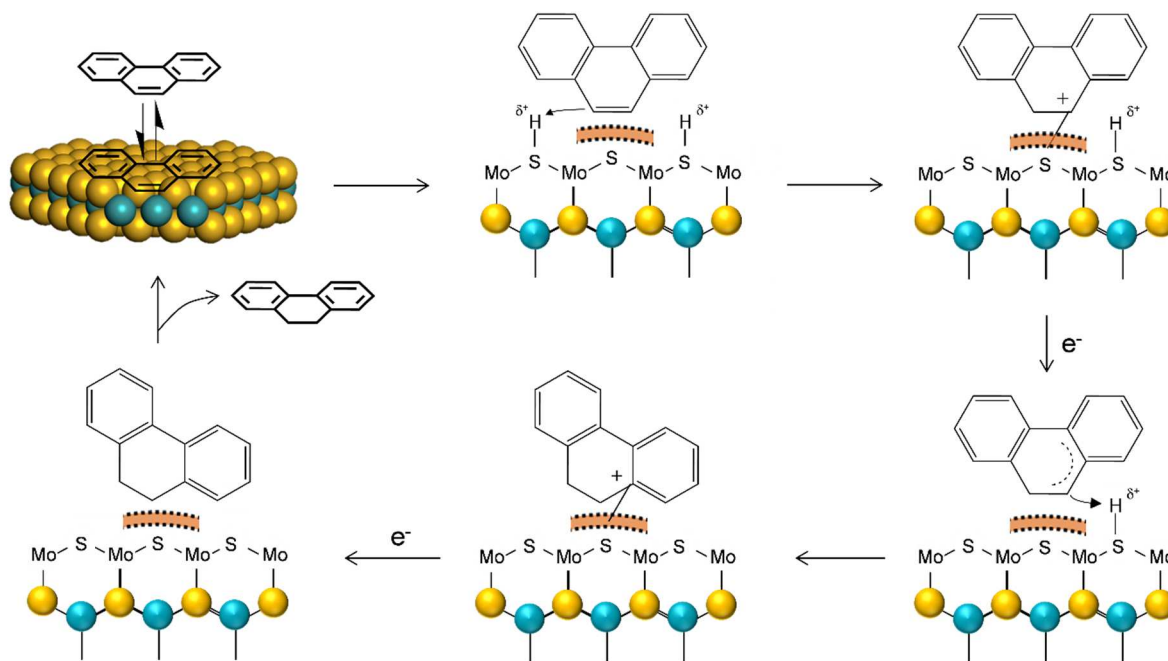


Figure 4-5. Surface mechanism for phenanthrene hydrogenation on MoS₂/Al₂O₃ resulting in the formation of 9,10-dihydrophenanthrene. Blue: Mo, yellow: S, red: π -interaction.

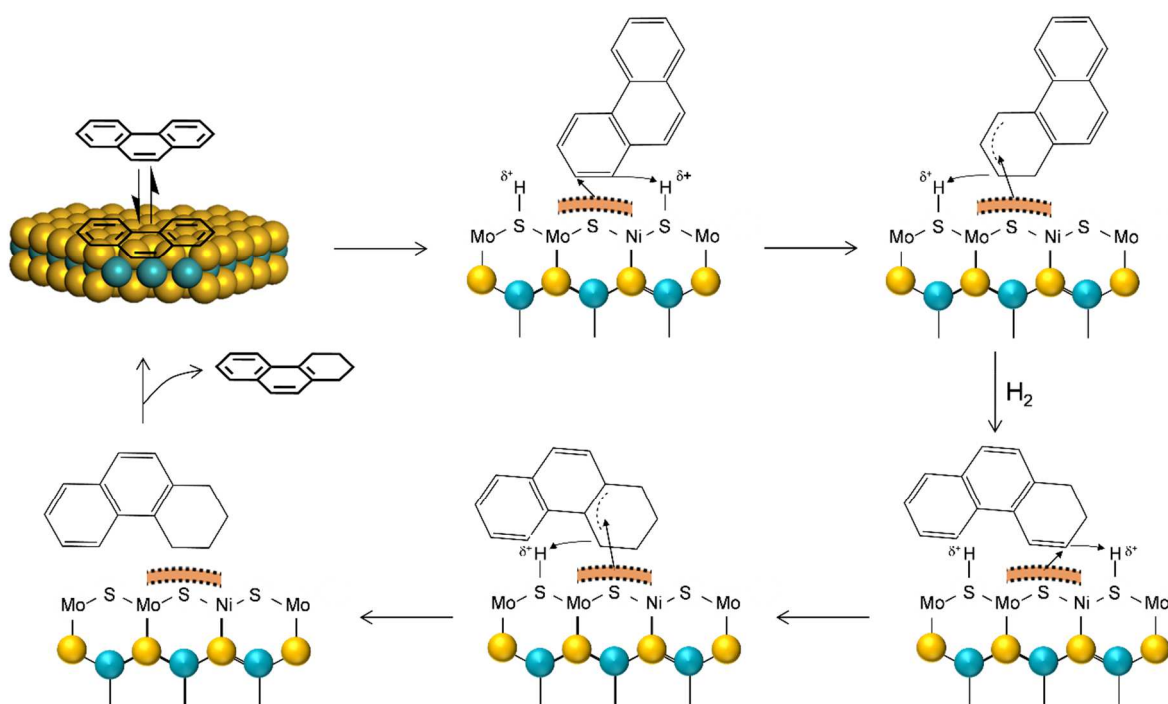


Figure 4-6. Surface mechanism for phenanthrene hydrogenation on Ni-MoS₂/Al₂O₃ resulting in the formation of 1,2,3,4-tetrahydrophenanthrene. Blue: Mo, yellow: S, red: π -interaction.

The formation of TetHPhe requires activation of the terminal ring of Phe, which supposedly invokes an orientation of Phe with the terminal ring towards the (Ni-)MoS₂ edge. The addition of hydrogen proceeds *via* successive addition of H⁺ from acidic SH-groups followed by charge compensation by the π -interaction of the cationic intermediate with the sulfide surface and reduction. The rate limiting step was concluded to be the addition of the second hydrogen pair. In line with the rational described above we conclude that the first and third H additions are the activated processes (or the steps with the highest barriers), whereas the second and fourth H additions are energetically much less demanding. Furthermore, the third H addition might be the one with the largest barrier. After the first two H atoms are added to phenanthrene, the addition of the second H pair needs to be very fast, otherwise dehydrogenation will prevail as all hydrogenation steps are reversible. For this reason the increase of hydrogen addition rates by Ni promotion is crucial for the formation of TetHPhe and further to *sym*- and *asym*OHPhe.

4.5. Conclusions

The mechanistic consequences of Ni promotion of MoS₂/Al₂O₃ were explored for the hydrogenation of polycyclic aromatic compounds using phenanthrene as model reactant. The decoration of MoS₂ with Ni atoms increases the dispersion of the active phase and the concentration of active sites at the perimeter (coordinatively unsaturated sites and SH groups). These effects account for the increase in hydrogenation rates of the middle ring of phenanthrene (Phe) producing 9,10-dihydrophenanthrene (DiHPhe), path 1. The hydrogenation of the lateral ring of Phe yielding 1,2,3,4-tetrahydrophenanthrene (TetHPhe), path 2, also depends on the concentration of surface hydrogen, however, the increase exceeds mere structural effects. Ni promotion also enables the catalyst to perform deep hydrogenation forming 1,2,3,4,5,6,7,8-octahydrophenanthrene (*sym*OHPhe) and 1,2,3,4,4a,9,10,10a-octahydrophenanthrene (*asym*OHPhe), and opens a direct pathway comprising isomerization and hydrogenation from DiHPhe to TetHPhe.

Changes of hydrocarbon adsorption and coverages by Ni promotion are very subtle and do not account for the change in catalytic performance. Thus, the variations in selectivity (deep hydrogenation favored with Ni) are interpreted as faster hydrogen addition of activated H to adsorbed hydrocarbons and associated changes in the rate determining steps. In turn, the hydrogenation of phenanthrene is postulated to occur via consecutive additions of hydrogen, with the first and the third hydrogen addition being the rate determining steps for the formation of DiHPhe and TetHPhe, respectively, and the addition of the second and fourth hydrogen atoms being much faster.

4.6. References

- (1) Topsøe, H.; Clausen, B. S.; Massoth, F. E. *Hydrotreating Catalysis*; Springer Verlag: Berlin, 1996.
- (2) Chianelli, R. R.; Berhault, G.; Torres, B. *Catal. Today* **2009**, *147* (3-4), 275–286.
- (3) Bensch, W. Hydrotreating: Removal of Sulfur from Crude Oil Fractions with Sulfide Catalysts, In *Comprehensive Inorganic Chemistry II* (2nd Edition), edited by Reedijk J. and Poeppelmeier K.; Elsevier, Amsterdam; 2013, 287-321.
- (4) Breyse, M.; Furimsky, E.; Kasztelan, S.; Lacroix, M.; Perot, G. *Catal. Rev.* **2002**, *44* (4), 651–735.
- (5) Byskov, L. S.; Bollinger, M.; Nørskov, J. K.; Clausen, B. S.; Topsøe, H. *J. Mol. Catal. A* **2000**, *163*, 117–122.
- (6) Hensen, E. J. M.; Lardinois, G. M. H. J.; de Beer, V. H. J.; van Veen, J. A. R. V; van Santen, R. A. *J. Catal.* **1999**, *187*, 95–108.
- (7) Sun, M.; Nelson, A. E.; Adjaye, J. *J. Catal.* **2005**, *233* (2), 411–421.
- (8) Kogan, V. M.; Nikulshin, P. a. *Catal. Today* **2010**, *149* (1-2), 224–231.
- (9) Moses, P. G.; Hinnemann, B.; Topsøe, H.; Nørskov, J. K. *J. Catal.* **2007**, *248* (2), 188–203.
- (10) Prodhomme, P.-Y.; Raybaud, P.; Toulhoat, H. *J. Catal.* **2011**, *280* (2), 178–195.
- (11) Thomas, C.; Vivier, L.; Lemberon, J. L.; Kasztelan, S.; Pérot, G. *J. Catal.* **1997**, *167*, 1–11.
- (12) Topsøe, N.-Y.; Topsøe, H. *J. Catal.* **1993**, *139*, 641–651.
- (13) Travert, A.; Nakamura, H.; van Santen, R. A.; Cristol, S.; Paul, J.-F.; Payen, E. *J. Am. Chem. Soc.* **2002**, *124* (24), 7084–7095.
- (14) Thomas, C.; Vivier, L.; Lemberon, J. L.; Kasztelan, S.; Pérot, G. *J. Catal.* **1997**, *167*, 1–11.
- (15) Schachtl, E.; Kondratieva, E.; Gutiérrez, O. Y.; Lercher, J. A. *J. Phys. Chem. Lett.* **2015**, *6* (15), 2929–2932.
- (16) Lauritsen, J. V.; Besenbacher, F. *J. Catal.* **2015**, *328*, 49–58.
- (17) Moses, P. G.; Mortensen, J. J.; Lundqvist, B. I.; Nørskov, J. K. *J. Chem. Phys.* **2009**, *130* (10), 104709.
- (18) Girgis, M. J.; Gates, B. C. *Ind. Eng. Chem. Res.* **1991**, *30* (9), 2021–2058.
- (19) Korre, S. C.; Klein, M. T.; Quann, R. J. *Ind. Eng. Chem. Res.* **1995**, *34* (1), 101–117.
- (20) Korre, S. C.; Neurock, M.; Klein, M. T.; Quann, R. J. *Chem. Eng. Sci.* **1994**, *49* (24A), 4191–4210.
- (21) Romero, C. M. C.; Thybaut, J. W.; Marin, G. B. *Catal. Today* **2008**, *130* (1), 231–242.
- (22) Stanislaus, A.; Cooper, B. *Catal. Rev.* **1994**, *36* (1), 75–123.
- (23) Girgis, M. J.; Gates, B. C. *Ind. Eng. Chem. Res.* **1994**, *33* (12), 2301–2313.
- (24) Beltramone, A. R.; Resasco, D. E.; Alvarez, W. E.; Choudhary, T. V. *Ind. Eng. Chem. Res.* **2008**, *47* (19), 7161–7166.

- (25) Ishihara, A.; Lee, J.; Dumeignil, F.; Takashi, M.; Qian, E. W.; Kabe, T. *Energy & Fuels* **2003**, *17* (5), 1338–1345.
- (26) Yang, H.; Wang, Y.; Jiang, H.; Weng, H.; Liu, F.; Li, M. *Ind. Eng. Chem. Res.* **2014**, *53* (31), 12264–12269.
- (27) Schachtl, E.; Zhong, L.; Kondratieva, E.; Hein, J.; Gutiérrez, O. Y.; Jentys, A.; Lercher, J. A. *ChemCatChem* **2015**.
- (28) Bhore, N. A.; Klein, M. T.; Bischoff, K. B. *Ind. Eng. Chem. Res.* **1990**, *29* (2), 313–316.
- (29) Clar, E. *Polycyclic Hydrocarbons, Band I*; Academic Press: London-New York, 1964.
- (30) Gutiérrez, O. Y.; Klimova, T. *J. Catal.* **2011**, *281* (1), 50–62.
- (31) Hrabar, A.; Hein, J.; Gutiérrez, O. Y.; Lercher, J. A. *J. Catal.* **2011**, *281* (2), 325–338.
- (32) Topsøe, N.-Y.; Topsøe, H. *J. Catal.* **1983**, *84*, 386–401.
- (33) Gutiérrez, O. Y.; Singh, S.; Schachtl, E.; Kim, J.; Kondratieva, E.; Hein, J.; Lercher, J. A. *ACS Catal.* **2014**, *4* (5), 1487–1499.
- (34) Hein, J.; Hrabar, A.; Jentys, A.; Gutiérrez, O. Y.; Lercher, J. a. *ChemCatChem* **2014**, *6* (2), 485–499.
- (35) Travert, A.; Dujardin, C.; Maugé, F.; Veilly, E.; Cristol, S.; Paul, J.-F.; Payen, E. *J. Phys. Chem. B* **2006**, *110* (3), 1261–1270.
- (36) Thomas, C.; Vivier, L.; Lescanne, M.; Kasztelan, S.; Pérot, G. *Catal. Letters* **1999**, *58*, 33–35.
- (37) Chianelli, R. R. *Oil Gas Sci. Technol. - Rev. l'IFP* **2006**, *61* (4), 503–513.
- (38) Lauritsen, J. V.; Kibsgaard, J.; Olesen, G. H.; Moses, P. G.; Hinnemann, B.; Helveg, S.; Nørskov, J. K.; Clausen, B. S.; Topsøe, H.; Laegsgaard, E.; Besenbacher, F. *J. Catal.* **2007**, *249* (2), 220–233.
- (39) Szymanski, R.; Charcosset, H.; Gallezot, P.; Massardier, J.; Tournayan, L. *J. Catal.* **1986**, *97* (2), 366–373.
- (40) Bollinger, M.; Jacobsen, K.; Nørskov, J. K. *Phys. Rev. B* **2003**, *67* (8), 085410.
- (41) Byskov, L. S.; Nørskov, J. K.; Clausen, B. S.; Topsøe, H. *J. Catal.* **1999**, *187*, 109–122.
- (42) Moses, P. G.; Hinnemann, B.; Topsøe, H.; Nørskov, J. K. *J. Catal.* **2009**, *268* (2), 201–208.
- (43) Guernalec, N.; Geantet, C.; Cseri, T.; Vrinat, M.; Toulhoat, H.; Raybaud, P. *Dalt. Trans.* **2010**, *39*, 8420–8422.
- (44) Moses, P. G.; Grabow, L. C.; Fernandez, E. M.; Hinnemann, B.; Topsøe, H.; Knudsen, K. G.; Nørskov, J. K. *Catal. Letters* **2014**, *144* (8), 1425–1432.

4.7. Supporting Information

Hydrogenation of phenanthrene and 9,10-dihydrophenanthrene at 573 K

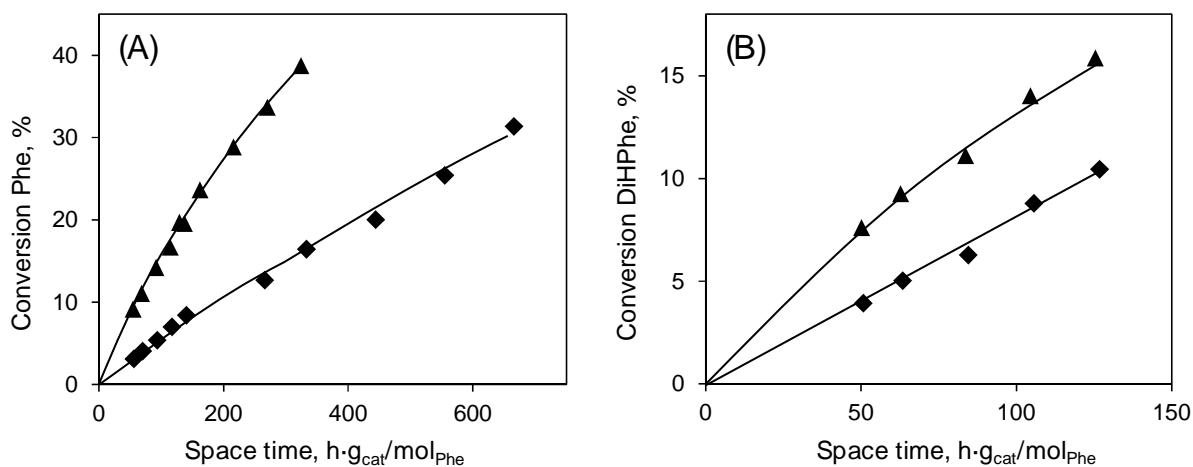


Figure 4-S7. Conversion of phenanthrene (Phe, A) and 9,10-dihydrophenanthrene (DiHPhe, B) at 573 K and 60 bar as a function of space time on MoS₂/Al₂O₃ (▲) and Ni-MoS₂/Al₂O₃ (◆).

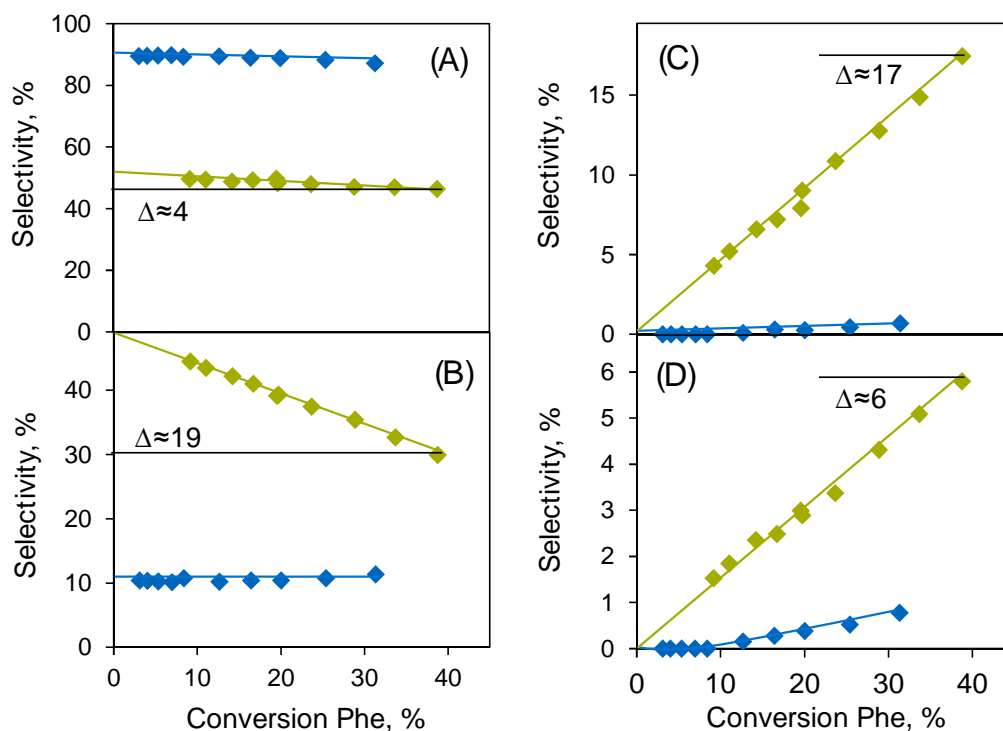


Figure 4-S8. Product selectivity in phenanthrene hydrogenation as function of conversion at 573 K, 60 bar and varying space time. Blue: MoS₂/Al₂O₃, Green: Ni-MoS₂/Al₂O₃. (A) DiHPhe, (B) TetHPhe, (C) *sym*OHPhe, (D) *asym*OHPhe.

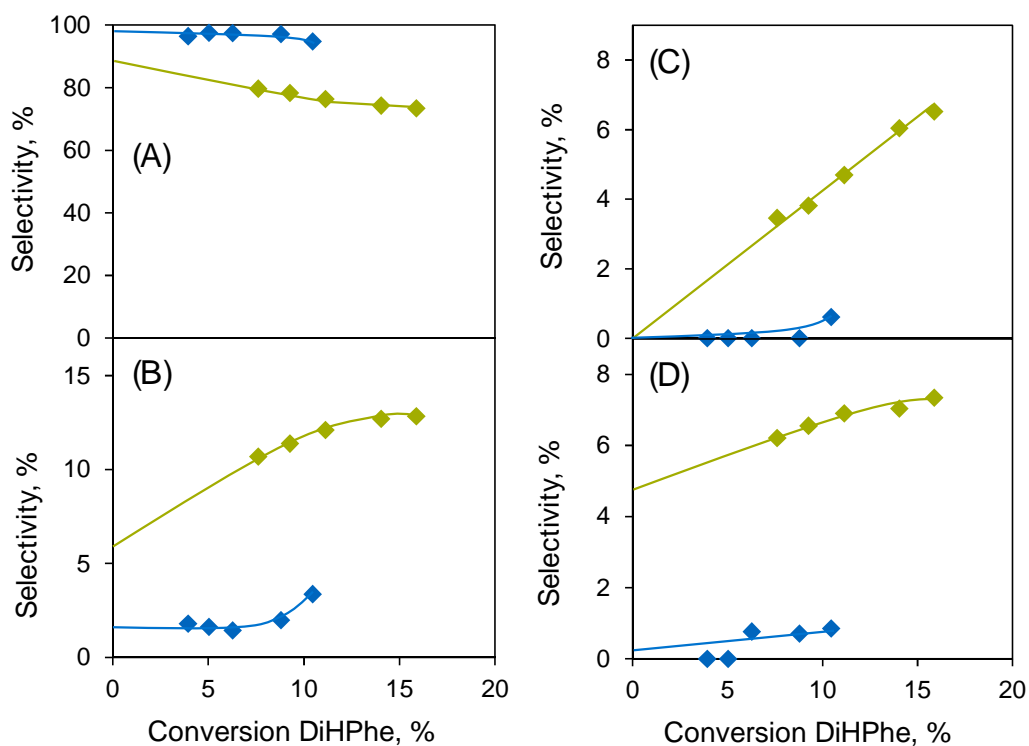


Figure 4-S9. Product selectivity in 9,10-dihydrophenanthrene hydrogenation as function of conversion at 573 K, 60 bar and varying space time. Blue: MoS₂/Al₂O₃, Green: Ni-MoS₂/Al₂O₃. (A) Phe, (B) TetHPhe, (C) *sym*OHPhe, (D) *asym*OHPhe.

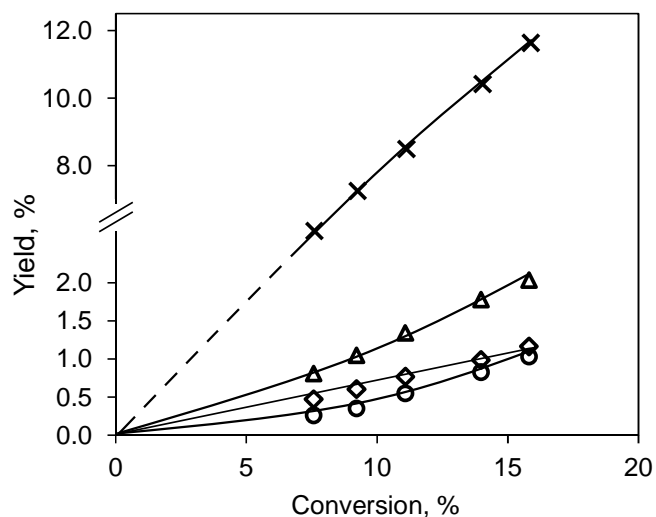


Figure 4-S10. Product yield in 9,10-dihydrophenanthrene hydrogenation as function of conversion on Ni-MoS₂/Al₂O₃ at 573 K, 60 bar and varying space time. (x) Phe, (Δ) TetHPhe, (○) *sym*OHPhe, (◇) *asym*OHPhe.

First order kinetic fitting

The experimental data obtained for hydrogenation of phenanthrene (Phe) and 9,10-dihydrophenanthrene (DiHPhe) were fitted with first order kinetic models using the Matlab software and a CMA-ES algorithm. Sets of differential rate equations were established according to the two reaction networks presented in Figure 4-S11. Network (A) was derived by the combined analysis of results of Phe and DiHPhe hydrogenation on $\text{MoS}_2/\text{Al}_2\text{O}_3$ and $\text{Ni-MoS}_2/\text{Al}_2\text{O}_3$. Seven rate constants describe the reaction network, $k_1 - k_6$ for hydrogenation steps (k_5 for lumped isomerization and hydrogenation), and k_{-1} for the dehydrogenation of DiHPhe.

Preliminary fitting results showed that four reaction steps are dominant during Phe hydrogenation, allowing a simplification of the reaction network using only four rate constants, i.e., k_1 - k_4 (network (B)). This results in two separate pathways, one including hydrogenation of Phe to DiHPhe (k_1) and *asym*OHPhe (k_3) - path 1 -, and a second one involving formation of TetHPhe (k_2) and *sym*OHPhe (k_4) - path 2 -. For low phenanthrene conversions, the reaction is satisfactorily described by this simplified reaction network, which was used also in a previous study.^{S1}

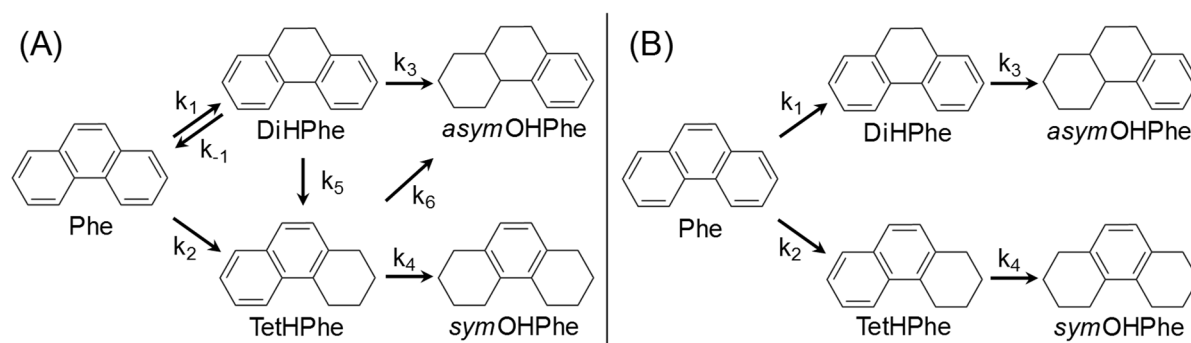


Figure 4-S11. Reaction networks (A) and (B) for hydrogenation of phenanthrene, Phe. DiHPhe: 9,10-dihydrophenanthrene, TetHPhe: 1,2,3,4-tetrahydrophenanthrene, *sym*OHPhe: 1,2,3,4,5,6,7,8-octahydrophenanthrene, *asym*OHPhe: 1,2,3,4,4a,9,10,10a-octahydrophenanthrene.

The differential equations derived from the reaction network (A) are given in equations (S1)-(S5) and for network (B) in equations (S6)-(S10). Therein, k_i is the reaction rate constant for the hydrogenation step ' i ' as indicated in Figure 4-S11 and c_j is the concentration of compound ' j '. The reactions are assumed to be pseudo-first-order in the hydrocarbons in all steps.^{S2} The results of the fitting for network (A) and (B) are comprised in Table 4-S5 and Table 4-S6. Comparisons of experimental and predicted concentration profiles are shown in Figure 4-S12, Figure 4-S13 and Figure 4-S14.

$$\frac{dc_{\text{Phe}}}{dt} = (-k_1 - k_2) \cdot c_{\text{Phe}} + k_{-1} \cdot c_{\text{DiHPhe}} \quad (\text{S1})$$

$$\frac{dc_{\text{DiHPhe}}}{dt} = (-k_{-1} - k_3 - k_5) \cdot c_{\text{DiHPhe}} + k_1 \cdot c_{\text{Phe}} \quad (\text{S2})$$

$$\frac{dc_{\text{TetHPhe}}}{dt} = (-k_4 - k_6) \cdot c_{\text{TetHPhe}} + k_2 \cdot c_{\text{Phe}} + k_5 \cdot c_{\text{DiHPhe}} \quad (\text{S3})$$

$$\frac{dc_{\text{asymOHPhe}}}{dt} = k_3 \cdot c_{\text{DiHPhe}} + k_6 \cdot c_{\text{TetHPhe}} \quad (\text{S4})$$

$$\frac{dc_{\text{symOHPhe}}}{dt} = k_4 \cdot c_{\text{TetHPhe}} \quad (\text{S5})$$

$$\frac{dc_{\text{Phe}}}{dt} = -k_1 \cdot c_{\text{Phe}} - k_2 \cdot c_{\text{Phe}} \quad (\text{S6})$$

$$\frac{dc_{\text{DiHPhe}}}{dt} = k_1 \cdot c_{\text{Phe}} - k_3 \cdot c_{\text{DiHPhe}} \quad (\text{S7})$$

$$\frac{dc_{\text{TetHPhe}}}{dt} = k_2 \cdot c_{\text{Phe}} - k_4 \cdot c_{\text{TetHPhe}} \quad (\text{S8})$$

$$\frac{dc_{\text{asymOHPhe}}}{dt} = k_3 \cdot c_{\text{DiHPhe}} \quad (\text{S9})$$

$$\frac{dc_{\text{symOHPhe}}}{dt} = k_4 \cdot c_{\text{TetHPhe}} \quad (\text{S10})$$

Table 4-S5. Kinetic constants k_i determined by fitting the experimental hydrogenation reaction data of Phe and DiHPhe according to network (A) using equations (S1)-(S5). Unit of k_i : mol/h·g_{cat}.

Ni-MoS ₂ /Al ₂ O ₃	$k_1 \cdot 10^3$	$k_{-1} \cdot 10^3$	$k_2 \cdot 10^3$	$k_3 \cdot 10^3$	$k_4 \cdot 10^3$	$k_5 \cdot 10^3$	$k_6 \cdot 10^3$
Phe ^a	1.43	1.96	1.27	3.30	4.29	0	0.86
DiHPhe ^b	1.43	1.96	2.63	0.15	13.20	0.26	0.89
MoS ₂ /Al ₂ O ₃	$k_1 \cdot 10^3$	$k_{-1} \cdot 10^3$	$k_2 \cdot 10^3$	$k_3 \cdot 10^3$	$k_4 \cdot 10^3$	$k_5 \cdot 10^3$	$k_6 \cdot 10^3$
Phe ^a	0.90	1.36	0.10	-	-	-	-
DiHPhe ^b	0.90	1.36	0.72	0.01	-	0	-

^a These values were fitted using the experimental data of phenanthrene hydrogenation.

^b These values were fitted using the experimental data of 9,10-dihydrophenanthrene hydrogenation.

A comparison of the reaction rate constants of reaction networks (A) and (B) derived from the experiments of phenanthrene hydrogenation is given in Table 4-S6. Only minor differences were observed for k_1 and k_2 , leading to similar k_1/k_2 ratios for both networks. k_3 and k_4 were slightly different between the two fittings because they tend to be over-estimated by this first order kinetic approach. Therefore, at low conversions, modelling of Phe hydrogenation according to network (A) is deemed sufficient, as the activity trends are well represented.

Table 4-S6. Comparison of the kinetic constants k_i fitted according to the reaction networks (A) and (B) (Figure 4-S11) for Phe hydrogenation. Unit of k_i : mol/h·g_{cat}.

Ni-MoS ₂ /Al ₂ O ₃	$k_1 \cdot 10^3$	$k_{-1} \cdot 10^3$	$k_2 \cdot 10^3$	$k_3 \cdot 10^3$	$k_4 \cdot 10^3$	$k_5 \cdot 10^3$	$k_6 \cdot 10^3$
network (A)	1.43	1.96	1.27	3.30	4.29	0	0.86
network (B)	1.36	-	1.28	1.40	4.77	-	-
MoS ₂ /Al ₂ O ₃	$k_1 \cdot 10^3$	$k_{-1} \cdot 10^3$	$k_2 \cdot 10^3$	$k_3 \cdot 10^3$	$k_4 \cdot 10^3$	$k_5 \cdot 10^3$	$k_6 \cdot 10^3$
network (A)	0.90	1.36	0.10	-	-	-	-
network (B)	0.86	-	0.10	-	-	-	-

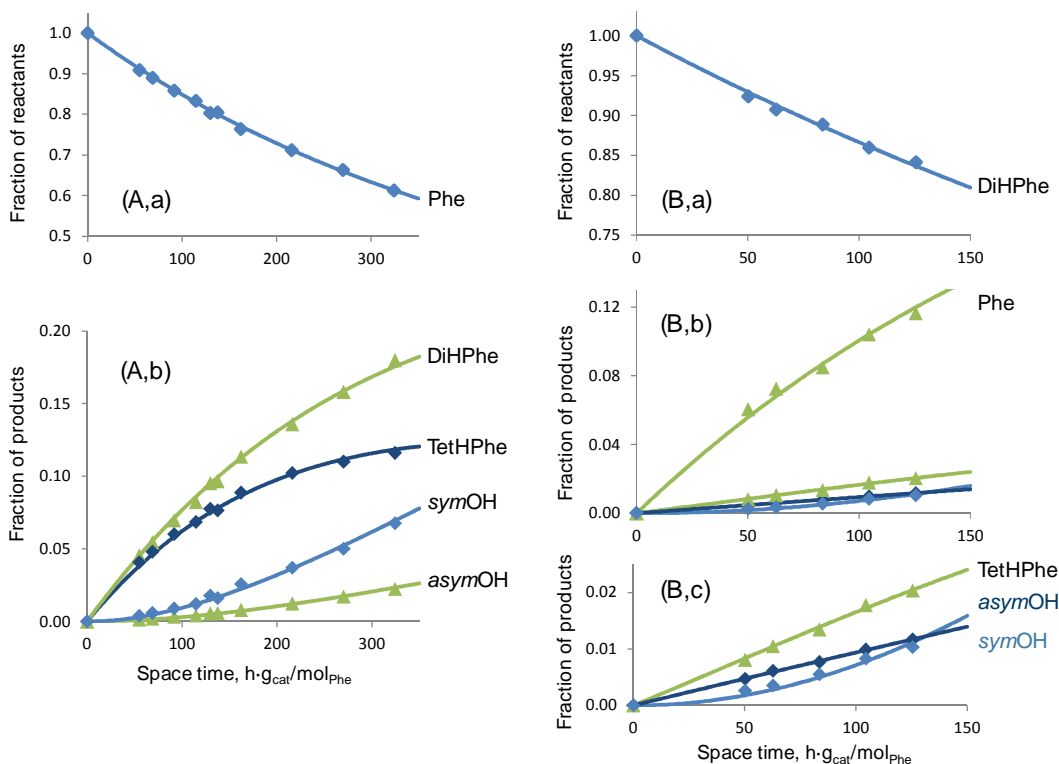


Figure 4-S12. Comparison of experimental (points) and predicted (line) concentration profiles on Ni-MoS₂/Al₂O₃ employing the network (A) presented in Figure 4-S11 for the hydrogenation of phenanthrene (Phe, left, A) and dihydrophenanthrene (DiHPhe, right, B). TetHPhe: 1,2,3,4-tetrahydro-, symOHPh: 1,2,3,4,5,6,7,8-octahydro-, asymOHPh: 1,2,3,4,4a,9,10,10a-octahydro- phenanthrene.

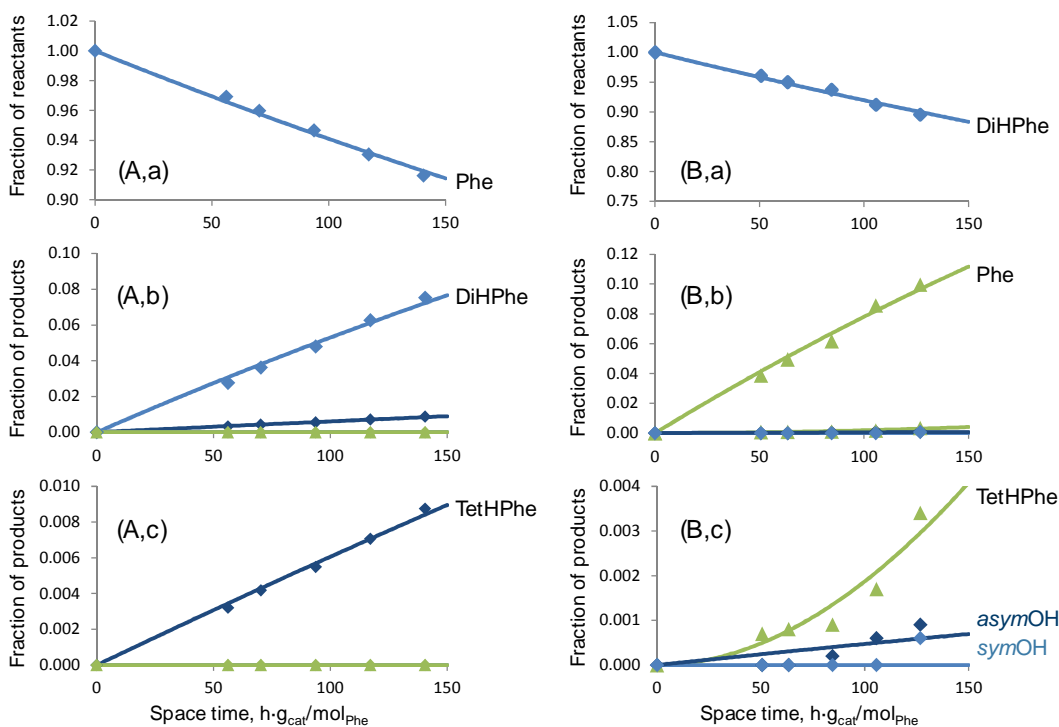


Figure 4-S13. Comparison of experimental (points) and predicted (line) concentration profiles on MoS₂/Al₂O₃ employing the network (A) presented in for the hydrogenation of phenanthrene (Phe, left, A) and dihydrophenanthrene (DiHPhe, right, B). TetHPhe: 1,2,3,4-tetrahydrophenanthrene, symOHPh: 1,2,3,4,5,6,7,8-octahydrophenanthrene, asymOHPh: 1,2,3,4,4a,9,10,10a-octahydro-phe.

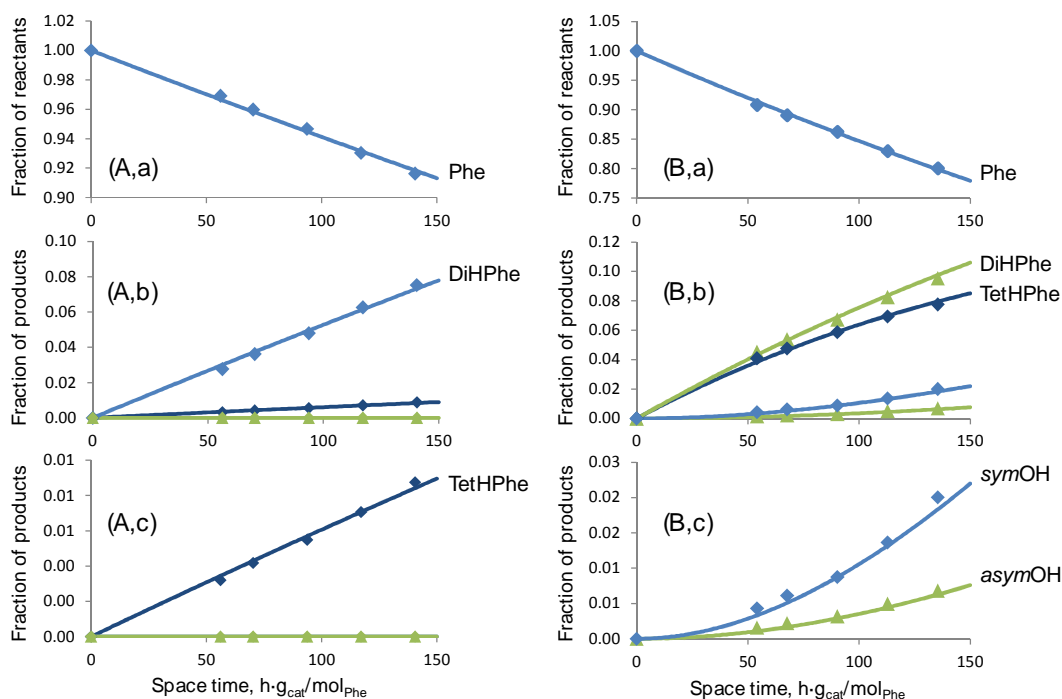


Figure 4-S14. Comparison of experimental (points) and predicted (line) concentration profiles of phenanthrene hydrogenation on MoS₂/Al₂O₃ (left, A) and Ni-MoS₂/Al₂O₃ (right, B) employing the network (B) presented in Figure 4-S11. Phe: phenanthrene, DiHPhe: 9,10-dihydrophenanthrene, TetHPhe: 1,2,3,4-tetrahydrophenanthrene, *sym*OH: 1,2,3,4,5,6,7,8-octahydrophenanthrene, *asym*OH: 1,2,3,4, 4a,9,10,10a-octahydrophenanthrene.

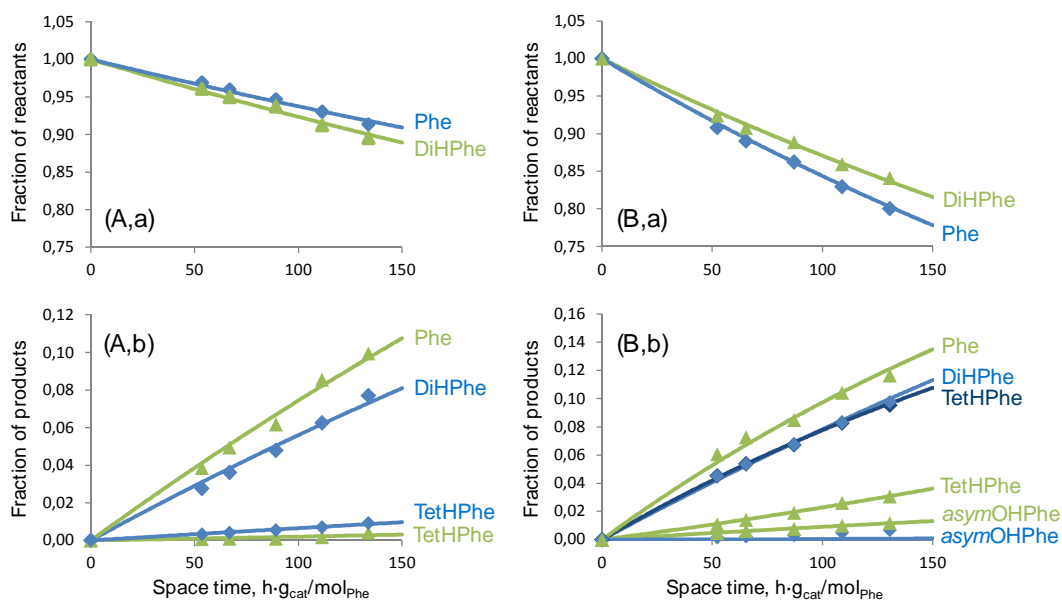


Figure 4-S15. Comparison of experimental (points) and predicted (line) concentration profiles on MoS₂/Al₂O₃ (left, A) and Ni-MoS₂/Al₂O₃ (right, B) employing the network (A) presented in Figure 4-S11 applying a Langmuir-Hinshelwood approach. Blue: phenanthrene (Phe) as reactant, Green: 9,10-dihydrophenanthrene (DiHPhe) as reactant. TetHPhe: 1,2,3,4-tetrahydrophenanthrene, *sym*OH: 1,2,3,4,5,6,7,8-octahydrophenanthrene, *asym*OH: 1,2,3,4,4a,9,10,10a-octahydrophenanthrene.

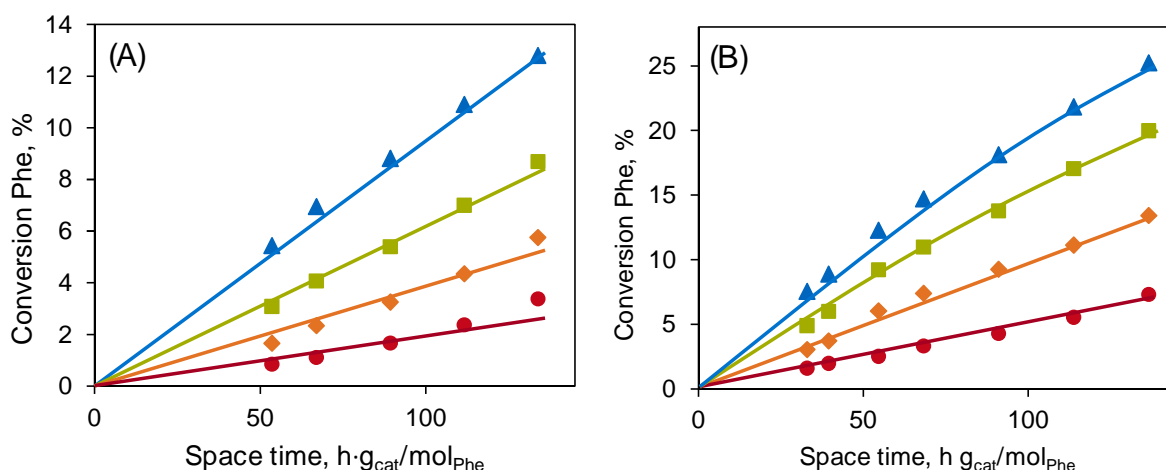
Hydrogenation of phenanthrene at varying temperatures

Figure 4-S16. Conversion of phenanthrene as a function of space time at 60 bar on MoS₂/Al₂O₃ (A) and Ni-MoS₂/Al₂O₃ (B) at different temperatures. Red: 553 K, orange: 563 K, green: 573 K, blue: 583 K.

Activation energies $E_{A,app}$ for the hydrogenation of phenanthrene were determined from reactions at four different temperatures, reaching from 553 to 583 K. The experimental data was fitted according to the reaction network (B) presented in Figure 4-S11, containing four rate constants - k_1 , k_2 , k_3 , and k_4 . Due to the overestimation of secondary pathways, only the rate constants k_1 and k_2 are employed to determine $E_{A,app}$ by Arrhenius plots as presented in Figure 4-4 in the main text. The dependence of Phe conversion on temperature is shown in Figure 4-S16, whereas the values of k_1 and k_2 are compiled in Table 4-S7.

Table 4-S7. Reaction rate constants k_i for phenanthrene hydrogenation at different temperatures. Unit of k_i : mol_{Phe}/h·g_{cat}.

T, K	MoS ₂ /Al ₂ O ₃		Ni-MoS ₂ /Al ₂ O ₃			
	$k_1 \cdot 10^3$	$k_2 \cdot 10^3$	$k_1 \cdot 10^3$	$k_2 \cdot 10^3$	$k_3 \cdot 10^3$	$k_4 \cdot 10^3$
553	0.316	0.036	0.439	0.414	1.116	2.951
563	0.552	0.063	0.829	0.777	1.312	3.857
573	0.871	0.102	1.343	1.278	1.596	5.191
583	1.530	0.168	1.808	1.669	2.107	7.857

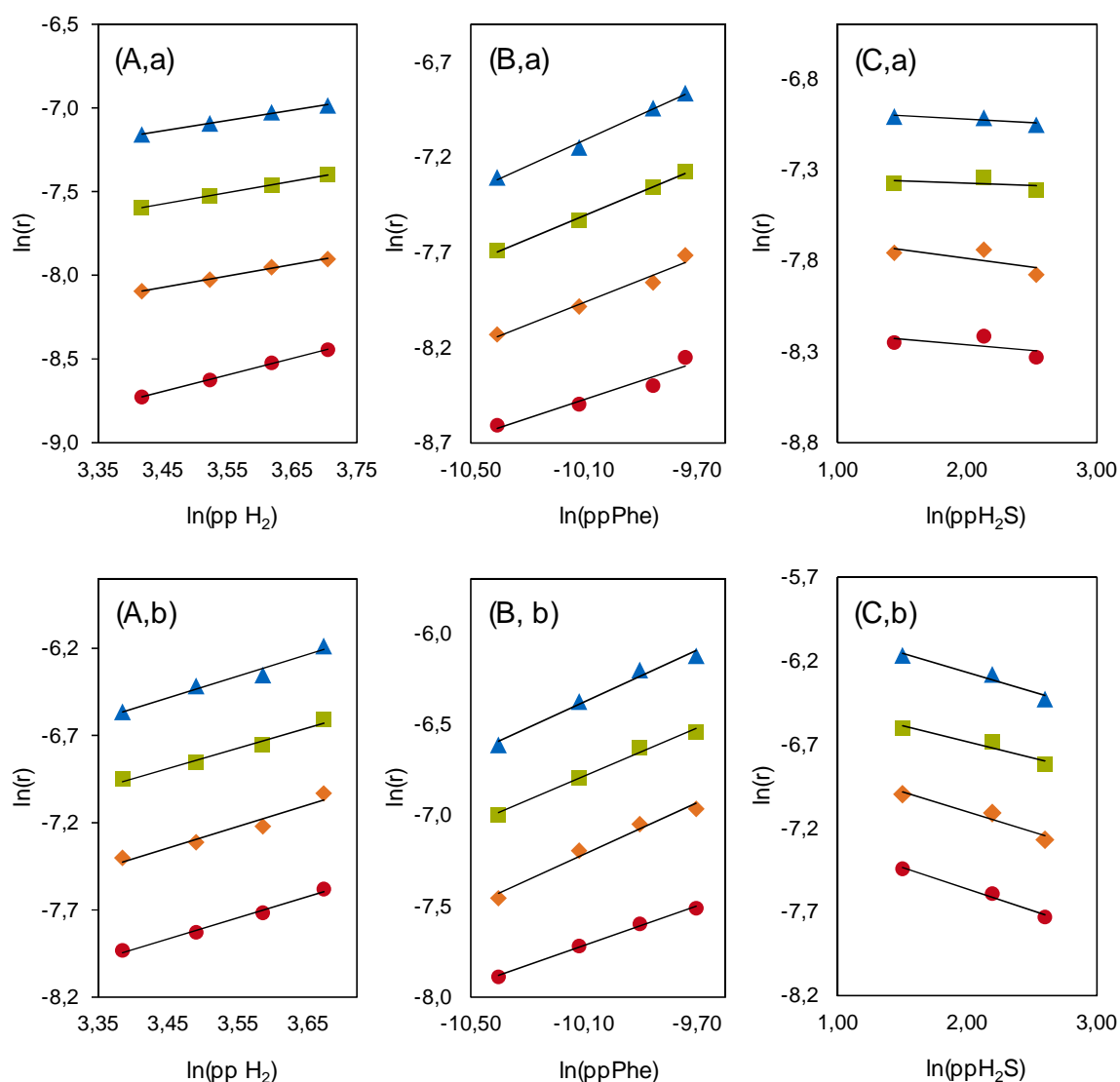
Reaction orders for H_2 , Phe and H_2S 

Figure 4-S17. Logarithmic plots of reaction rates versus concentrations of H_2 (A), Phe (B) and H_2S (C) for MoS_2/Al_2O_3 (top, a) and $Ni-MoS_2/Al_2O_3$ (bottom, b).

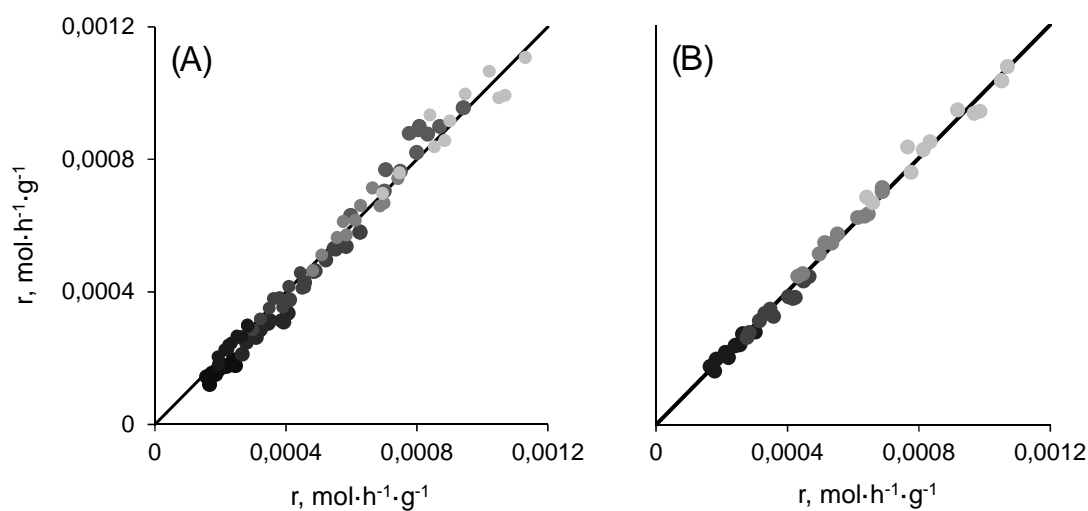


Figure 4-S18. Parity plots for the formation rates of (A) DiHPhe-path 1, and (B) TetHPhe-path 2.

Table 4-S8. Fitting parameters for the formation of 9,10-dihydrophenanthrene (DiHPhe) and 1,2,3,4-tetrahydrophenanthrene (TetHPhe) according to the mechanisms presented in the main text.

Catalyst	T, K	553	563	573	583	
MoS ₂ /Al ₂ O ₃	K _{Phe} ^{*1}	0.275	0.208	0.160	0.123	
	DiHPhe	K _{H₂} ^{*2}	2.20·10 ⁻⁵	1.81·10 ⁻⁵	1.50·10 ⁻⁵	1.25·10 ⁻⁵
		K _{H₂S} ^{*3}	1.60·10 ⁻³	1.45·10 ⁻³	1.32·10 ⁻³	1.20·10 ⁻³
	k _r ^{*5}	0.035	0.067	0.126	0.232	
Ni-MoS ₂ /Al ₂ O ₃	K _{Phe} ^{*1}	0.254	0.188	0.140	0.106	
	DiHPhe	K _{H₂} ^{*2}	11.8·10 ⁻⁷	9.71·10 ⁻⁷	8.04·10 ⁻⁷	6.70·10 ⁻⁷
		K _{H₂S} ^{*3}	8.36·10 ⁻³	7.16·10 ⁻³	6.17·10 ⁻³	5.35·10 ⁻³
	k _r ^{*5}	0.608	1.114	1.999	3.516	
Ni-MoS ₂ /Al ₂ O ₃	K _{Phe} ^{*1}	0.604	0.497	0.412	0.344	
	TetHPhe	K _{H₂} ^{*2}	4.00·10 ⁻⁷	3.42·10 ⁻⁷	2.95·10 ⁻⁷	2.55·10 ⁻⁷
		K _{H₂S} ^{*3}	1.37·10 ⁻²	1.18·10 ⁻²	1.02·10 ⁻²	0.88·10 ⁻²
	K ₄ ^{*4}	0.044	0.041	0.039	0.037	
k _r ^{*5}	0.078	0.149	0.280	0.515		

*1 Parameters for the adsorption of phenanthrene according to reaction no.(1) shown in Table 4-3.

*2 Parameters for the adsorption of H₂ according to reaction no.(2) shown in Table 4-3.

*3 Parameters for the adsorption of H₂S according to reaction no.(3) shown in Table 4-3.

*4 Parameters for the first hydrogenation step in the TetHPhe reaction pathway, reaction no.(4a), as shown in Table 4-3.

*5 Parameters for the rate determining steps, reaction no.(4) for DiHPhe, and reaction no.(4b) for TetHPhe as shown in Table 4-3.

Correlation of SH-groups and coordinatively unsaturated sites (CUS)

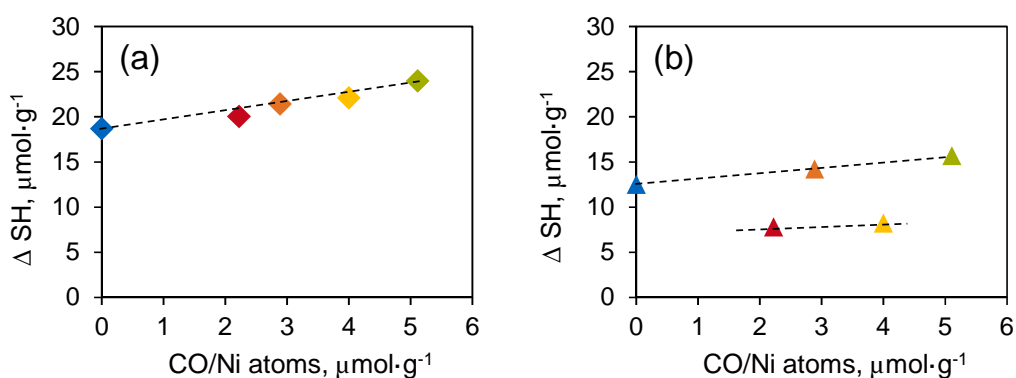


Figure 4-S19. Correlation of SH groups determined by co-adsorption of 2,6-dimethylpyridine with (a) H₂S and (b) H₂ with the amount of CO adsorbed on Ni atoms incorporated at the edge of MoS₂. Blue: MoS₂/Al₂O₃, orange: Ni(1.5)MoS₂/Al₂O₃, green: Ni(3)MoS₂/Al₂O₃, yellow: Ni(6)MoS₂/Al₂O₃, red: Ni(10)MoS₂/Al₂O₃. Based on results published in Refs.^{S1,S3}.

References

- (S1) Schachtl, E.; Zhong, L.; Kondratieva, E.; Hein, J.; Gutiérrez, O. Y.; Jentys, A.; Lercher, J. A. *ChemCatChem* **2015**.
- (S2) Stanislaus, A.; Cooper, B. *Catal. Rev.* **1994**, 36 (1), 75–123.
- (S3) Schachtl, E.; Kondratieva, E.; Gutiérrez, O. Y.; Lercher, J. A. *J. Phys. Chem. Lett.* **2015**, 6 (15), 2929–2932.

Chapter 5

Summary and Conclusions

Hydrotreating is one of the largest industrial processes worldwide and a key step in oil refining. The removal of metals, S, N, O, and hydrogenation of heavy fractions is gaining importance as the quality of crude oil declines while environmental regulations for fuels become stricter. The catalysts of choice are transition metal sulfides, mostly MoS₂ and WS₂ promoted by Ni or Co. Despite the long history of research in this field, the active sites and mechanistic steps of the reactions occurring on the sulfides are still under debate. Therefore, these topics are tackled in this thesis.

The structure of various NiMo sulfides supported on γ -Al₂O₃ was investigated, focusing especially on the location of the promoter. The molar ratio of Ni/(Mo+Ni) ranged from 0 to 0.7. Ni was in close contact with Mo, leading to the formation of octahedrally coordinated Mo in the oxide precursors and facilitating the reduction of Mo⁶⁺ to Mo⁴⁺ during sulfidation. As a result, also the dispersion of MoS₂ increased in presence of Ni, whereas Ni/(Mo+Ni) ratios above 0.33 had no significant influence on the slab length and stacking degree of MoS₂. For all Ni(x)MoS₂/Al₂O₃ catalysts, an increase of sulfur vacancies (coordinatively unsaturated sites, CUS) was detected, which could be attributed to decoration of MoS₂ by Ni atoms. A maximum concentration of CUS appeared for Ni(3)MoS₂/Al₂O₃ with a Ni/(Mo+Ni) ratio of 0.33. Nickel was shown to be present in three different phases, i.e., as Ni atoms incorporated in the edges on MoS₂ slabs forming a mixed Ni-Mo-S phase, as NiS_x clusters close to the perimeter of MoS₂,

and as spinel NiAl_2O_4 inside $\gamma\text{-Al}_2\text{O}_3$. Models were constructed by combining all structural information, e.g., EXAFS analysis, CO-IR spectroscopy, TEM. The models include the presence of segregated NiS_x clusters already at low Ni concentrations. For $\text{Ni}/(\text{Mo}+\text{Ni})$ ratios above 0.33, the NiS_x clusters grow, blocking active sites of $\text{Ni}(x)\text{MoS}_2$ because the Ni atoms at the MoS_2 edges can act as nucleation points for the formation of NiS_x . As a consequence, the accessibility of the active sites decreases for high Ni concentrations, as well as their activity in hydrogenation declines (*Chapter 2*).

The active sites of Ni- and not-promoted $\text{MoS}_2/\text{Al}_2\text{O}_3$ were further investigated by adsorption of the base 2,6-dimethylpyridine. Evidence for Lewis acidic (CUS) and Brønsted acidic sites (SH-groups) on the sulfide catalysts was reported. The activation of H_2 was concluded to be similar to that of H_2S , proceeding *via* heterolytic dissociation at pairs of sulfur vacancies and neighboring S^{2-} . Upon heterolytic splitting of H_2 , a SH-group and a hydride are formed. The hydride is regarded as not stable and transforms in another SH-group by transferring its electrons to MoS_2 . In the presence of Ni, the amount of active surface hydrogen increased by up to 30% (for $\text{Ni}(3)\text{MoS}_2/\text{Al}_2\text{O}_3$) compared to $\text{MoS}_2/\text{Al}_2\text{O}_3$ (*Chapter 3*).

Hydrogenation of phenanthrene (Phe), a model polycyclic aromatic hydrocarbon, exhibited a maximum in activity for $\text{Ni}(3)\text{MoS}_2/\text{Al}_2\text{O}_3$. In addition, the product distribution changed in presence of Ni. On not-promoted $\text{MoS}_2/\text{Al}_2\text{O}_3$ the main product was 9,10-dihydrophenanthrene (DiHPhe), followed by 1,2,3,4-tetrahydrophenanthrene (TetHPhe), giving a ratio of DiHPhe to TetHPhe of 9:1. On $\text{Ni}(x)\text{MoS}_2/\text{Al}_2\text{O}_3$ equal amounts of DiHPhe and TetHPhe were formed, and highly hydrogenated products were observed, i.e., 1,2,3,4,5,6,7,8-octahydrophenanthrene (*sym*OHPhe) and 1,2,3,4,4a,9,10,10a-octahydrophenanthrene (*asym*OHPhe). First order kinetic fitting revealed that Ni accelerates all reaction steps, but in particular favors deep hydrogenation pathways. A direct correlation between the Phe hydrogenation activity and Ni atoms decorating MoS_2 was derived. The increase, induced by the presence of Ni, on the kinetic constant k_1 ($\text{Phe} \rightarrow \text{DiHPhe}$) can be attributed to structural changes of MoS_2 , i.e. increasing dispersion and the resulting higher concentration of active sites. However, the acceleration of k_2 ($\text{Phe} \rightarrow \text{TetHPhe}$) exceeds mere structural effects, and therefore is attributed to an intrinsic change of the active site, involving the Ni-Mo-S phase (*Chapter 2*).

More insight into the surface reaction mechanism of Phe hydrogenation was gained by determining reaction orders in Phe, H_2 and H_2S . The reaction orders in H_2 increased in presence of Ni, from ~ 0.7 for $\text{MoS}_2/\text{Al}_2\text{O}_3$ to ~ 1.2 for $\text{Ni}(3)\text{MoS}_2/\text{Al}_2\text{O}_3$, indicating a relatively low H coverage on the latter. In addition, the H_2 reaction order was higher for the formation of TetHPhe than for DiHPhe. Both observations were rationalized by an increased H demand, for $\text{Ni}(3)\text{MoS}_2/\text{Al}_2\text{O}_3$ as well as TetHPhe formation, which in turn leads to a decrease in H coverage

and consequently an increase of the respective H₂ orders. In contrast, the adsorption of Phe was not affected by the presence of Ni as the Phe reaction orders for Ni(3)MoS₂/Al₂O₃ hardly changed compared to MoS₂/Al₂O₃ (0.5-0.7 for both). This was corroborated by only marginal changes of the apparent activation energy $E_{A,app}$ and adsorption constant K_{Phe} , which was determined by applying a Langmuir-Hinshelwood model. The reaction orders in H₂S were zero on MoS₂/Al₂O₃ and slightly negative on Ni(3)MoS₂/Al₂O₃ (*Chapter 4*).

Finally, a surface reaction mechanism for the hydrogenation of Phe was proposed. The best fitting model comprised one kind of adsorption site for Phe, H₂ and H₂S, with H₂ dissociating upon adsorption. Phe is assumed to strongly adsorb *via* van der Waals interactions at the basal plane of MoS₂. The hydrogenation reaction, however, takes place at the edges of the MoS₂ particles, where SH-groups and CUS are located. In turn, the hydrogenation of Phe is postulated to occur *via* consecutive addition of H and charge compensation *via* π -interaction of Phe with MoS₂. The rate determining step (rds) for the hydrogenation of Phe to DiHPhe was found to be the same for both catalysts, i.e., the addition of the first H pair. The rds for TetHPhe formation was the addition of the second hydrogen pair. However, the barriers for the first and third H addition step are speculated to be large, whereas the additions of the second and fourth H are regarded fast (*Chapter 4*).

The thorough physicochemical characterization in this work allowed providing structural models of the active phase present in series of Ni-promoted MoS₂ catalysts. Detailed mechanisms for H₂ activation and quantification of the functional groups relevant for hydrogenation of polycyclic aromatic compounds were provided. In turn, mechanistic insight into the hydrogenation processes and the influence of Ni on them was described. Thus, this thesis shed light into novel aspects of the catalytic chemistry of sulfides that are seldom explored, and definitively not with the depth reached in this work.

Chapter 6

Zusammenfassung

Hydrotreating ist einer der größten und bedeutendsten Industrieprozesse weltweit. Eine zentrale Rolle spielt das Hydrotreating bei der Aufarbeitung von Erdöl, wo durch Hydrierung unerwünschte Komponenten wie Metalle, S, N, O oder Aromaten aus dem Rohöl entfernt werden. Als Katalysatoren sind dafür besonders Übergangsmetallsulfide geeignet, vor allem MoS_2 und WS_2 , versetzt mit Ni oder Co als Promotoren. Die aktiven Zentren dieser sulfidischen Materialien sind jedoch trotz jahrelanger Forschung nach wie vor nicht eindeutig identifiziert und sind daher, ebenso wie ein detaillierter Reaktionsmechanismus der Hydrierung, Gegenstand dieser Arbeit.

Die beiden Übergangsmetalle Mo und Ni wurden auf $\gamma\text{-Al}_2\text{O}_3$ als Trägermaterial aufgebracht und strukturell untersucht, wobei ein besonderes Augenmerk auf den Einfluss des Promoters Ni gelegt wurde. Das molare Verhältnis $\text{Ni}/(\text{Mo}+\text{Ni})$ reichte dabei von 0 bis 0,7. Für die oxidischen Katalysatormaterialien konnte in Gegenwart von Ni vermehrt oktaedrisch koordiniertes Mo nachgewiesen werden, was ein Zeichen für eine unmittelbare Nachbarschaft von Ni und Mo ist. Der Kontakt der beiden Metalle führte zu einer Beschleunigung des Sulfidierungsprozesses, bedingt durch eine vereinfachte Reduktion von Mo^{6+} zu Mo^{4+} , und in der Folge zu einer stärkeren Dispersion von MoS_2 . Bei allen $\text{Ni}(x)\text{MoS}_2/\text{Al}_2\text{O}_3$ Proben konnte dadurch eine Zunahme an Fehlstellen im Schwefelgitter (coordinatively unsaturated sites, CUS) nachgewiesen werden, was einem Einbau einzelner Ni Atome auf Mo-Plätzen an den

Kanten der MoS_2 Partikel zugeordnet wird. Die höchste Konzentration an CUS hatte $\text{Ni(3)MoS}_2/\text{Al}_2\text{O}_3$ mit einem molaren $\text{Ni}/(\text{Mo}+\text{Ni})$ Verhältnis von 0,33. Es konnte gezeigt werden, dass Ni in drei unterschiedlichen Phasen auf der Katalysatoroberfläche vorliegt, nämlich als Ni Atome an den Kanten von MoS_2 (Ni-Mo-S Phase), als NiS_x Cluster in der Nähe der MoS_2 Partikel, und als Spinell NiAl_2O_4 im Gitter des $\gamma\text{-Al}_2\text{O}_3$. Durch die Kombination aller strukturellen Informationen, z.B. aus TEM, Röntgenabsorptions- und CO-IR Spektroskopie, wurden atomare Modelle der Sulfide kreiert und evaluiert. Bereits bei geringen Ni Konzentrationen kommt es zur Bildung kleiner NiS_x Cluster, die bei molaren $\text{Ni}/(\text{Mo}+\text{Ni})$ Verhältnissen über 0,33 weiter wachsen und schließlich aktive Zentren des Katalysators blockieren. Die Ni Atome an den Kanten des MoS_2 können dabei als Kristallisationskeime für die Ausbildung der NiS_x Cluster dienen. Dadurch wird die Zugänglichkeit zu den aktiven Zentren der (Ni-) MoS_2 Partikel weiter eingeschränkt, was bei zunehmenden Ni Konzentrationen zu einer Verringerung der katalytischen Aktivität führt (*Kapitel 2*).

Die aktiven Zentren der $\text{Ni(x)MoS}_2/\text{Al}_2\text{O}_3$ Proben konnten durch Adsorption der Base 2,6-Dimethylpyridin indirekt im IR-Spektrometer charakterisiert werden. Die Existenz Lewis-saurer (CUS) und Brønsted-saurer (SH-Gruppen) Zentren konnte nachgewiesen werden. Die Aktivierung von H_2 verlief dabei ähnlich zur Spaltung von H_2S , durch heterolytische Dissoziation an benachbarten Schwefelfehlstellen und S^{2-} Ionen, und führte zur Bildung einer SH-Gruppe und eines Hydrids. Da Hydridionen instabil sind, übertragen sie ihre Elektronen umgehend an MoS_2 und wandeln sich dabei in weitere SH-Gruppen um. Die Menge an aktivem Oberflächenwasserstoff stieg im Vergleich zu $\text{MoS}_2/\text{Al}_2\text{O}_3$ um bis zu 30% für $\text{Ni(3)MoS}_2/\text{Al}_2\text{O}_3$ (*Kapitel 3*).

Die höchste Aktivität bei der Hydrierung von Phenanthren (Phe), welches eine typische Modellverbindung für polyzyklische aromatische Kohlenwasserstoffe ist, zeigte $\text{Ni(3)MoS}_2/\text{Al}_2\text{O}_3$. Zudem änderte sich in Gegenwart von Ni das Produktspektrum. Das Hauptprodukt der Hydrierung von Phe mit $\text{MoS}_2/\text{Al}_2\text{O}_3$ war 9,10-Dihydrophenanthren (DiHPhe). 1,2,3,4-Tetrahydrophenanthren (TetHPhe) war das am zweithäufigsten gebildete Produkt und trat in einem DiHPhe:TetHPhe Verhältnis von 9:1 auf. Mit $\text{Ni(x)MoS}_2/\text{Al}_2\text{O}_3$ als Katalysator hingegen traten DiHPhe und TetHPhe zu gleichen Teilen auf. Zudem wurden noch zwei stärker hydrierte Produkte gebildet, 1,2,3,4,5,6,7,8-Octahydrophenanthren (*sym*OHPhe) und 1,2,3,4,4a,9,10,10a-Octahydrophenanthren (*asym*OHPhe). Durch Fitting der kinetischen Reaktionsdaten konnte gezeigt werden, dass Ni alle Reaktionsschritte beschleunigt, insbesondere jedoch die Reaktionswege, die zu höher hydrierten Produkten führen. Es wurde eine direkte Korrelation zwischen der Hydrieraktivität und der Anzahl an Ni Atomen an den MoS_2 Kanten festgestellt. So konnte der Ni induzierte Anstieg der Ratenkonstante k_1 ($\text{Phe} \rightarrow \text{DiHPhe}$) den strukturellen Veränderungen von MoS_2 , genauer gesagt der stärkeren Dispersion und der daraus resultierenden höheren Anzahl an aktiven Zentren zugeordnet

werden. Die Ni induzierte Beschleunigung von k_2 (Phe \rightarrow TetHPhe) überstieg jedoch die strukturellen Effekte und wird deshalb einer intrinsischen Veränderung der aktiven Zentren unter Einbezug der Ni-Mo-S Phase zugeordnet (*Kapitel 2*).

Um einen tieferen Einblick in den Mechanismus der Oberflächenreaktionen der Phe Hydrierung zu erhalten, wurden die Reaktionsordnungen für Phe, H_2 und H_2S bestimmt. Die Wasserstoffreaktionsordnung ist in Gegenwart von Ni von ~ 0.7 für MoS_2/Al_2O_3 auf ~ 1.2 für $Ni(3)MoS_2/Al_2O_3$ angestiegen, was auf eine relativ niedrige Wasserstoffbedeckung des Letzteren schließen lässt. Zudem wurden unterschiedliche Wasserstoffreaktionsordnungen für die Bildung von DiHPhe und TetHPhe gefunden. Beide Beobachtungen können durch einen erhöhten Wasserstoffbedarf erklärt werden, was eine Verringerung der Wasserstoffbedeckung zur Folge hat und schließlich zu einem Anstieg der jeweiligen Wasserstoffreaktionsordnung führt. Im Gegensatz dazu ist die Reaktionsordnung und somit die Adsorption von Phe auf $Ni(3)MoS_2/Al_2O_3$ unverändert gegenüber MoS_2/Al_2O_3 . Bekräftigt wird dieses Ergebnis durch lediglich minimale Veränderungen der scheinbaren Aktivierungsenergie $E_{A,app}$ und der Adsorptionskonstanten K_{Phe} , welche mit Hilfe eines Langmuir-Hinshelwood Modells ermittelt wurde. Die Reaktionsordnungen für H_2S waren für MoS_2/Al_2O_3 gleich null und für $Ni(3)MoS_2/Al_2O_3$ negativ (*Kapitel 4*).

Abschließend wurde ein Mechanismus für die Oberflächenreaktionen der Hydrierung von Phe aufgestellt. Das am besten passende Modell beinhaltet nur eine Art von aktivem Zentrum für die Adsorption von Phe, H_2 und H_2S , wobei der Wasserstoff bei der Adsorption dissoziativ gespalten wird. Die Adsorption von Phe erfolgt über van-der-Waals-Wechselwirkungen und findet hauptsächlich auf der Basisfläche des MoS_2 statt. Da jedoch die SH-Gruppen und CUS an den Kanten von MoS_2 sitzen, findet die Reaktion mit Wasserstoff vermutlich nur an den Rändern der MoS_2 Partikel statt. Die Hydrierung von Phe verläuft dabei über mehrere aufeinanderfolgende Wasserstoff-Additionsschritte, jeweils gefolgt von einem Ladungsaustausch zwischen Phe und MoS_2 über die Wechselwirkung ihrer π -Elektronensysteme. Der ratenbestimmende Schritt (rds) für die Hydrierung von Phe zu DiHPhe war für beide Katalysatoren die Addition des ersten Wasserstoffpaares. Der rds für die Bildung von TetHPhe hingegen war die Reaktion mit dem zweiten Wasserstoffpaar. Dabei wird angenommen, dass die energetischen Hürden für das Hinzufügen des ersten und dritten Wasserstoffatoms wesentlich größer sind als jeweils für das Zweite und Vierte, weshalb die Addition der letzten beiden Wasserstoffatome verhältnismäßig schnell verlaufen sollte (*Kapitel 4*).

Die gründliche physikalisch-chemische Charakterisierung der $Ni(x)MoS_2/Al_2O_3$ Katalysatoren in dieser Arbeit hat es mir ermöglicht strukturelle Modelle der aktiven Phase zu erstellen. Zudem konnten detaillierte Mechanismen für die H_2 Aktivierung und eine Quantifizierung der

funktionellen Gruppen, die maßgeblich an der Hydrierung polyzyklischer aromatischer Kohlenwasserstoffe beteiligt sind, erstellt werden. Es wurden außerdem Einblicke in den Reaktionsmechanismus der Hydrierung gegeben, wobei ein besonderes Augenmerk auf den Einfluss von Ni als Promoter gelegt wurde. Mit einer selten erreichten Tiefe konnte ich somit im Zuge dieser Arbeit verschiedene Aspekte der Katalyse sulfidischer Materialien beleuchten und neue strukturelle sowie mechanistische Einblicke gewähren.

Appendix

IR spectroscopy setup

The experimental requirements to investigate sulfide catalysts in situ are very demanding as very harsh conditions are needed for activation and probing. In the specific case of IR characterization with probe molecules, the two extreme cases are:

- in-situ sulfidation at 673 K (400°C) in 20 bar flowing H₂S/H₂ (10 vol.-% H₂S),
- CO adsorption at liquid N₂ temperature (LNT, <123 K or -150°C) after evacuation to around 10⁻⁷ mbar.

To meet these demands, a new IR setup with a novel cell combining flow and vacuum operations was planned, built and put in operation. The IR instrument is a Nicolet 6700 FT-IR spectrometer from Thermo Fisher Scientific equipped with a MCT detector. The new IR cell is the heart of the setup and is schematically illustrated in Figure A1 and depicted in Figure A2. The whole setup is shown in Figure A3 and Figure A4.

The material used for the IR cell body is austenitic stainless steel with grade 316 (SAE-grade standard). The admixture of Cr, Ni and Mo leads to a good corrosion resistance, which is important when working in an H₂S/H₂ environment and especially at strongly differing temperature and pressure ranges. Further, all parts connected to the flow system are made out of 316 stainless steel (high pressure section), and all parts of the vacuum system are made of 304 stainless steel (low pressure section). Stainless steel with grade 304 does not contain Mo and so is less corrosion resistant, but is the standard for vacuum systems.

As shown in Figure A1, the cell body has one gas inlet, a stainless steel tube with size 1/8 inch, and one cell outlet, with 1/2 inch in diameter and a 1/8 inch tube welded to its side. The small exit is used in flow conditions, whereas the large exit is connected to a vacuum pump. Each tube, inlet and outlet, are connected to a bellows-type valve (Swagelok, green handles in Figure A2) and can be sealed “steel-on-steel” against high and low pressure. The optical path is perpendicular to the flow path, the window material is CaF₂ and each window is 5 mm thick and 25 mm in diameter. The windows are sealed by Teflon rings.

For the IR cell top a standard CF40 flange is used, which is made of the less corrosion resistant 304 stainless steel, but as the top part is not usually heated or cooled excessively it is sufficient. The sealing of the CF40 flange is copper and is exchanged before each experiment. The other parts of the cell top are exposed to more stress, and therefore, stainless steels with higher grade are needed. Hence, the sample holder and the liquid N₂ cooling system are made of 316 stainless steel, whereas the thermocouple and the heating wires consist of Inconel 600, which has an especially good heat corrosion resistance.

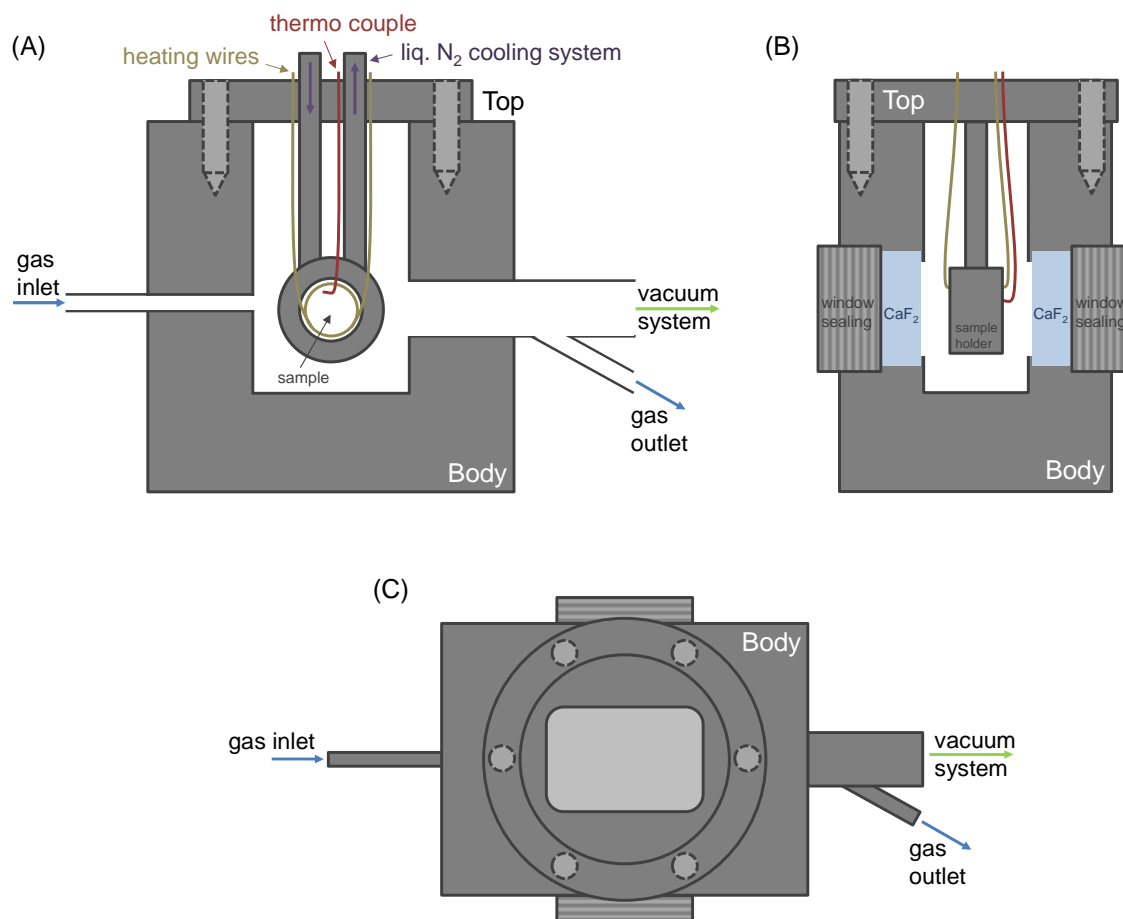


Figure A1. Schematic drawing of the combined flow-vacuum IR cell. (A) and (B) are cross sections of the cell body and top, (C) is a top-view of the cell body.

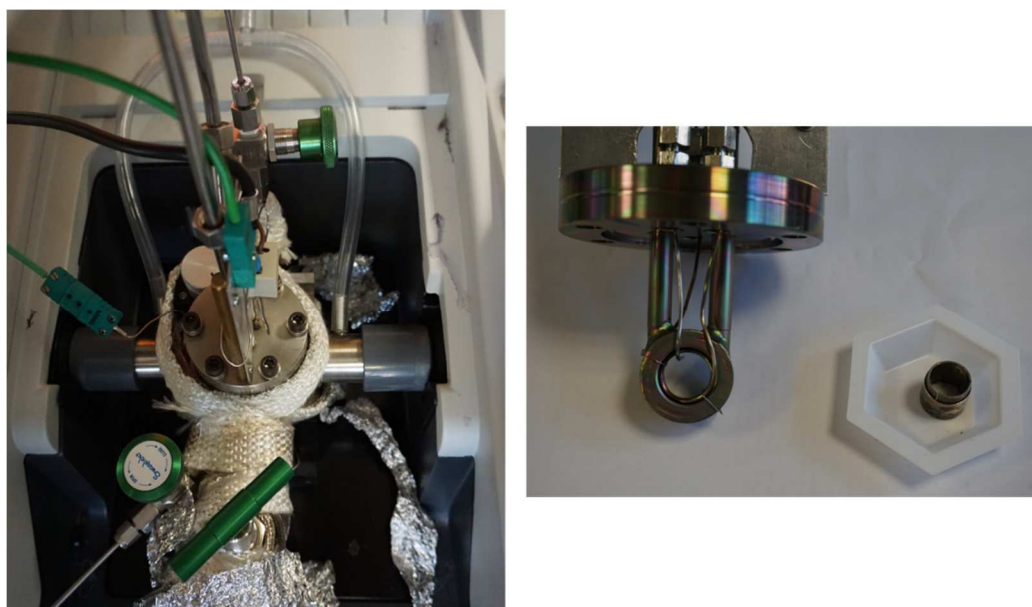


Figure A2. Picture of the IR cell body (left) and the IR cell top (right).

The samples (oxide precursor or sulfide sample) are placed inside the sample holder as self-supported wafers held in place by two stainless steel rings as shown in the right lower corner

of Figure A2 (B). The wafers are 10 mm in diameter, have about 2.5-5 mg total weight and are compacted by exerting a pressure of about 20 N/m² for about ½ min. The heating wires circumvent the sample, the thermocouple has to be placed close to the catalyst wafer and in contact with the stainless steel sample holder to ensure accurate temperature measurement. An Eurotherm is used for temperature control.

The inlet of the IR cell is connected to the flow system of the IR setup, marked blue in Figure A3. The flow system consists of three mass flow controllers (MFC, Bronkhorst), for He, H₂ and H₂S/H₂. The maximum flow for each MFC is 50 mL/min, the pressure limits are 5 bar for He and 20 bar for H₂ and H₂S/H₂. One of the gases can be chosen and conducted to the IR cell by a four-way valve (Swagelok, V1) passing through the inlet bellow-type valve (Swagelok, V2). The gas exit is connected to another bellow-type valve (Swagelok, V3), followed by a backpressure regulator (Swagelok, KCB series, BPR) with a pressure limit of 25 bar. Before releasing the gas to the vent, two 1 L glass bottles have to be passed. The first bottle is empty and its sole purpose is to protect the IR cell from back-flow during vacuum conditions. The second bottle is filled with a saturated NaOH-solution in order to neutralize H₂S.

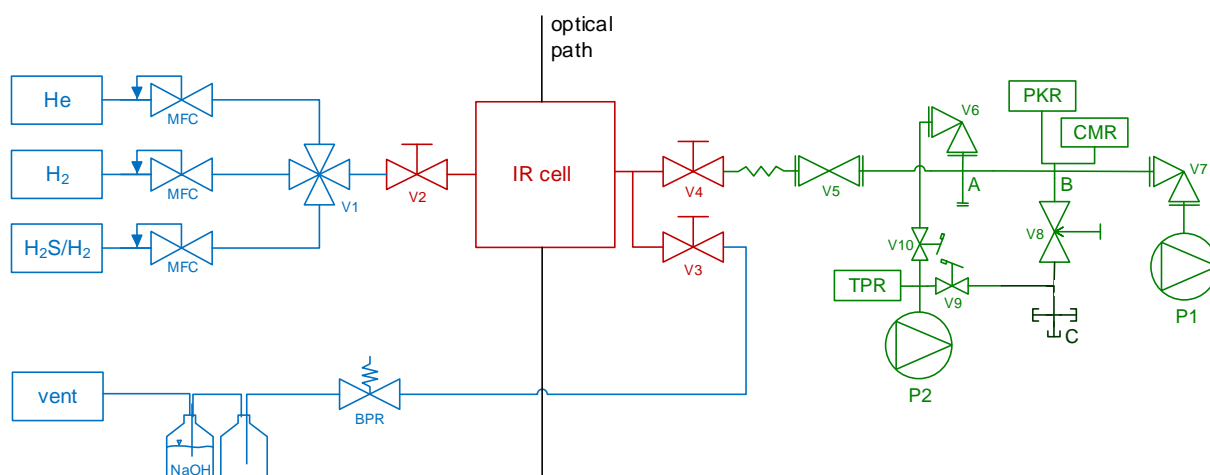


Figure A3. Schematic flow diagram of the IR setup. Blue: flow system, red: IR cell, green: vacuum part, black: optical path.

The vacuum part is linked to the IR cell *via* a bellow-type valve (Swagelok, V4) by a flexible hose (Trinos Vacuum, DN 16 CF), to protect the pumps from vibrations arising during sample replacement. Since every valve has a certain leak rate, a second pressure step is created between the cell and the vacuum system by inserting an all-metal inline-valve (MDC Vacuum, DN 40 CF, V5). A 4-way and a 5-way crosspart (Trinos Vacuum, DN 40 CF, A and B in Figure A3) are connected in a row to valve V5, leading at the rear to the turbo pumping station HiCube 80 Eco (Pfeiffer Vacuum, DN 63 CF, P1). A sealing gas valve protects the pump from corrosion. At cross part B (Figure A3) a FullRange Gauge (PKR 261, Active Pirani/Cold Cathode Transmitter, Pfeiffer Vacuum) measures the pressure of the vacuum system, indicated by a DualGauge Controller (TPG 262, Pfeiffer Vacuum). For accurate adsorption of probe

molecules, an Active Capacitive Transmitter (CMR 363, 0.001 – 11 mbar range, Pfeiffer Vacuum) is used. On top of cross part B an all-metal precision leak valve (MDC Vacuum, sapphire sealed, V8) is connected, that leads further on to the adsorption section (dark green in Figure A3). At another cross part (1/4 inch tubing, Swagelok, C) up to three different gas bottles or liquids (in glass flasks) can be put for adsorption *via* the vacuum system. The adsorption part is evacuated by an oil-free roots vacuum pump (ACP 15G, Adixen, Alcatel Hochvakuum Technik, P2) with a flushing gas connection for corrosion protection. It is linked to the adsorption line by a flexible hose (Trinos Vacuum, DN 16 KF) and can be closed off by a vacuum angle valve (VAT Vakuumventile, DN 16 KF). The same oil-free pump is employed to create pre-vacuum in the vacuum system (before the turbo pump is opened), and therefore, is connected also to cross part A (Figure A3) *via* an all-metal angle valve (MDC Vacuum, DN 40 CF, V6). The pressure of the pre-vacuum pump can be controlled by an Active Pirani Transmitter (TPR, Pfeiffer Vacuum) placed directly at the pump. All CF flanges are sealed by silver coated copper rings and all KF flanges are fit by FKM centering rings made of stainless steel grade 304.

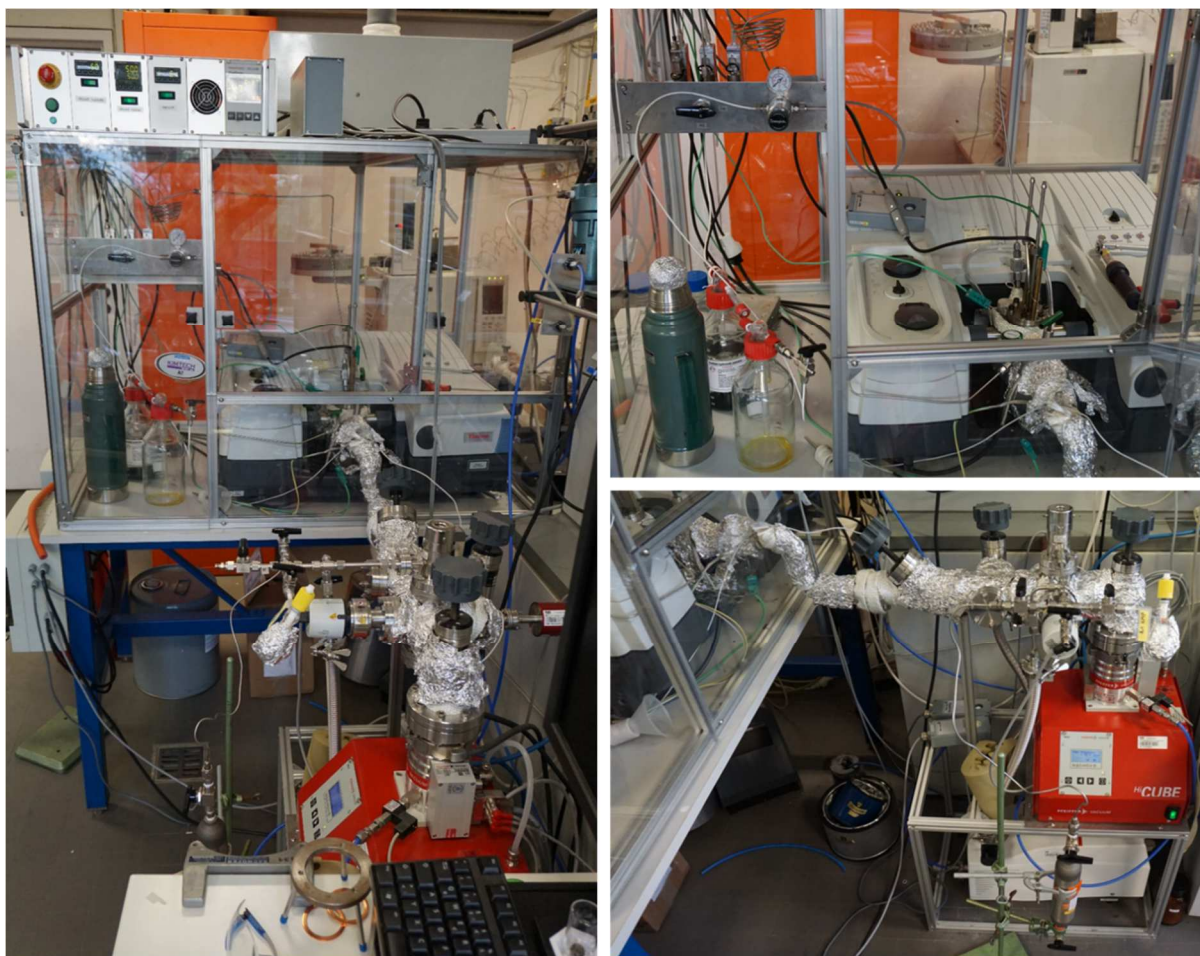


Figure A4. Picture of the whole IR setup (left), the flow (right, top) and the vacuum part (right, bottom).

Curriculum Vitae

Name	Eva Christina Schachtl
Birth	21.02.1986, Landshut
Citizenship	German
Education	
since 02/2011	TU München, Technische Chemie II, Catalysis Research Center Ph.D. candidate Supervisor: Prof Johannes A. Lercher
04/2009 – 11/2010	Master of Science in Chemistry, TU München Main subject: organic chemistry Side subject: catalysis and reaction technology Thesis: "Synthesis of Mesostructured Mixed Oxide Spheres" (1.3) Final grade: 1.6
10/2005 – 03/2009	Bachelor of Science in Chemistry, TU München Thesis: "Isobutane/2-butene alkylation on LaX catalysts" (1.3) Final grade: 2.3
until 06/2005	Abitur, Karl-Ritter-von-Frisch Gymnasium, Moosburg Main subjects: math, chemistry Final grade: 1.9
Internships	
08/2009 – 09/2009	Haldor Topsøe, Copenhagen, Denmark Topic: "Investigations on the sulphuric acid catalyst VK38 by in-situ Raman spectroscopy under industrial-like conditions" Duration: 8 weeks
08/2005	BASF AG, Ludwigshafen Topic: "Präparation und Stabilität von Microemulsionen" Duration: 4 weeks
08/2004 – 09/2004	Süd-Chemie AG, Moosburg Topic: "Intensität und Lichtbeständigkeit von Inkjetfarben auf neuen Pigmenten im Strich" Duration: 8 weeks

List of Publications

Journal Articles

Eva Schachtl, Elena Kondratieva, Lei Zhong, Jennifer Hein, Oliver Y. Gutiérrez, Andreas Jentys, Johannes A. Lercher, 'Understanding Ni promotion of $\text{MoS}_2/\gamma\text{-Al}_2\text{O}_3$ and its implications for the hydrogenation of phenanthrene' in *ChemCatChem*, **2015**, 7 (24), 4118-4130. DOI: 10.1002/cctc.201500706R1.

Jennifer Hein, Oliver Y. Gutiérrez, Eva Schachtl, Pinghong Xu, Nigel D. Browning, Andreas Jentys, Johannes A. Lercher, 'Distribution of Metal Cations in Ni-Mo-W Sulfide Catalysts' in *ChemCatChem*, **2015**, 7 (22), 3692-3704. DOI: 10.1002/cctc.201500788.

Eva Schachtl, Elena Kondratieva, Oliver Y. Gutiérrez and Johannes A. Lercher, 'Pathways for H_2 activation on (Ni)- MoS_2 catalysts' in *The Journal of Physical Chemistry Letters*, **2015**, 6 (15), 2929–2932, DOI: 10.1021/acs.jpcllett.5b01217.

Oliver Y. Gutiérrez, Srujan Singh, Eva Schachtl, Jeongnam Kim, Elena Kondratieva, Jennifer Hein, Johannes A. Lercher, 'Effects of the Support on the Performance and Promotion of (Ni) MoS_2 Catalysts for Simultaneous Hydrodenitrogenation and Hydrodesulfurization' in *ACS Catalysis*, **2014**, 4 (5), 1487-1499, DOI: 10.1021/cs500034d.

Pablo Beato, Eva Schachtl, Katia Barbera, Francesca Bonino, Silvia Bordiga, 'Operando Raman spectroscopy applying novel fluidized bed micro-reactor technology' in *Catalysis Today*, **2013**, 205, 128-133, DOI: 10.1016/j.cattod.2012.09.030.

Eva Schachtl, Elena Wuttke, Oliver Y. Gutiérrez, Johannes A. Lercher, 'Effect of Ni on the Characteristics and Hydrogenation Activity of Sulfide $\text{Mo}/\gamma\text{-Al}_2\text{O}_3$ ' Preprints of the DGMK Conference "Reducing the Carbon Footprint of Fuels and Petrochemicals", DGMK, Germany, **2012**, 227-233. ISBN 978-3-941721-26-5.

Oral presentations

Eva Schachtl, Oliver Y. Gutiérrez, Jong Suk Yoo, Felix Studt, Johannes A. Lercher, 'Effect of Ni on the hydrogenation mechanism of polyaromatic hydrocarbons over (Ni-) $\text{MoS}_2/\text{Al}_2\text{O}_3$ ' at the XIIth European Congress on Catalysis, Kazan, Russia, 2015.

Eva Schachtl, Jong Suk Yoo, Felix Studt, Oliver Y. Gutiérrez, Johannes A. Lercher, 'Mechanistic consequences of Ni-promotion on the hydrogenation of phenanthrene over (Ni) $\text{MoS}_2/\text{Al}_2\text{O}_3$ ' at 24th North American Catalysis Society Meeting, Pittsburgh (PA), USA, 2015.

Eva Schachtl, Elena Wuttke/Kondratieva, Oliver Y. Gutiérrez, Johannes A. Lercher, 'Active sites for hydrogenation of aromatic hydrocarbons on Ni-Mo sulfides' at 248th ACS National Meeting and Exposition, San Francisco (CA), USA, 2014.

Eva Schachtl, Elena Wuttke/Kondratieva, Oliver Y. Gutiérrez, Johannes A. Lercher, *'Mechanism and Active Sites of Phenanthrene Hydrogenation on Supported NiMoS Catalysts'* at the 23rd North American Catalysis Society Meeting, Louisiana (KY), USA, 2013.

Elena Wuttke/Kondratieva, Eva Schachtl, Oliver Y. Gutiérrez, Johannes A. Lercher, *'Effect of Ni on MoS₂/γ-Al₂O₃: characterization of active sites and activity for phenanthrene hydrogenation'* at VIth International Symposium on Molecular Aspects of Catalysis by Sulfides (MACS), Satillieu, France, 2013.

Poster presentations

Eva Schachtl, Elena Kondratieva, Oliver Y. Gutiérrez, Johannes A. Lercher, *'How does H₂S and H₂ activation occur on Ni-MoS₂/γ-Al₂O₃?'*, 48. Jahrestreffen Deutscher Katalytiker, Weimar, Germany, 2015.

Eva Schachtl, Ana Hrabar, Oliver Y. Gutiérrez and Johannes A. Lercher, *'Influence of Ni on the active sites of MoS₂/γ-Al₂O₃ and the activity for hydrogenation of phenanthrene'* at 47. Jahrestreffen Deutscher Katalytiker, Weimar, Germany, 2014.

Jennifer Hein, Oliver Y. Gutiérrez, Eva Schachtl, Johannes A. Lercher, *'Understanding of hydrodenitrogenation on unsupported Ni-Mo, Ni-W and Ni-Mo-W sulfide catalysts'* at 47. Jahrestreffen Deutscher Katalytiker, Weimar, Germany, 2014.

Eva Schachtl, Elena Wuttke/Kondratieva, Oliver Y. Gutiérrez, Johannes A. Lercher, *'Influence of Ni on the activity of MoS₂/γ-Al₂O₃ for hydrogenation of phenanthrene'*, at XIth European Congress on Catalysis, Lyon, France, 2013.

Eva Schachtl, Elena Wuttke/Kondratieva, Oliver Y. Gutiérrez and Johannes A. Lercher, *'Effect of Ni on the mechanism and activity for phenanthrene hydrogenation over sulfide (Ni)Mo/γ-Al₂O₃ catalysts'* at 46. Jahrestreffen Deutscher Katalytiker, Weimar, Germany, 2013.

Eva Schachtl, Elena Wuttke/Kondratieva, Oliver Y. Gutiérrez and Johannes A. Lercher, *'Effect of Ni on the Characteristics and Hydrogenation Activity of Sulfide Mo/γ-Al₂O₃'* at DGMK-Conference - Reducing the Carbon Footprint of Fuels and Petrochemicals, Berlin, Germany, 2012. (Preprints 2012-3, ISBN 978-3-941721-26-5)

Eva Schachtl, Ana Hrabar, Oliver Y. Gutiérrez and Johannes A. Lercher, *'Hydrogenation of phenanthrene on NiMo-sulfide catalysts supported on γ-Al₂O₃'* at 45. Jahrestreffen Deutscher Katalytiker, Weimar, Germany, 2012.